

# **Modeling a diversity of salamander motor behaviors with coupled abstract oscillators and a robot**

THÈSE N° 5709 (2013)

PRÉSENTÉE LE 23 AVRIL 2013

À LA FACULTÉ DES SCIENCES ET TECHNIQUES DE L'INGÉNIEUR

LABORATOIRE DE BIOROBOTIQUE

PROGRAMME DOCTORAL EN INFORMATIQUE, COMMUNICATIONS ET INFORMATION

ÉCOLE POLYTECHNIQUE FÉDÉRALE DE LAUSANNE

POUR L'OBTENTION DU GRADE DE DOCTEUR ÈS SCIENCES

PAR

**Jérémie KNÜSEL**

acceptée sur proposition du jury:

Prof. B. Moret, président du jury  
Prof. A. Ijspeert, directeur de thèse  
Prof. Ö. Ekeberg, rapporteur  
Prof. D. Floreano, rapporteur  
Prof. A. Ishiguro, rapporteur



ÉCOLE POLYTECHNIQUE  
FÉDÉRALE DE LAUSANNE

Suisse  
2013



# Acknowledgements

First, I want to thank my supervisor Auke Ijspeert for the opportunity of working on this thesis, and for his guidance without which this work would not have been possible. I also thank my colleagues at BioRob for making this a pleasant experience through their company that I will miss very much. My thesis has built on the work of André Guignard, Alessandro Crespi and Kostas Karakasiliotis who designed and constructed the robot *Salamandra robotica II*, and helped me with the robotic experiments. I am also indebted to Jean-Marie Cabelguen and Dimitri Ryczko for providing me with biological data and answering many questions. I have received invaluable help from Jesse van den Kieboom who provided me with splendid software libraries and tools for the implementation of my models. Finally I want to thank my family for their understanding in busy times. And a very special thank to Cécile, who supported me more than I could wish during these years.

*Lausanne, 6 April 2013*

J. K.





# Abstract

Salamanders are capable of a variety of locomotor behaviors including swimming, underwater stepping, and forward and backward land stepping. According to electromyographic and kinematic recordings of the trunk, each of these behaviors is characterized by a pattern of muscle activation and body curvature with specific values of cycle duration and trunk intersegmental phase lag. A wider, continuous range of intersegmental phase lags is also observed in recordings of isolated spinal cords. Previous models have typically been limited to the generation of two stereotypical behaviors and transitions between them. In contrast, the present work specifically addresses the flexibility of the spinal cord locomotor networks. We investigate how a flexible central pattern generator (CPG) can be modulated by a higher regulation mechanism to generate appropriate patterns of muscle activation. We then look at the effect of the muscles properties and interactions with the environment on the kinematic pattern, and how local proprioceptive feedback can shape the CPG activity. We propose a CPG model based on abstract oscillators that reproduces the main features of recordings from isolated spinal cords, and that scales well to the higher frequencies of locomotion in the intact animal. The model reproduces the distribution of intersegmental phase lags, the correlation between phase lags and cycle frequencies, and the spontaneous switches between slow and fast rhythms. Using numerical simulations of a salamander robot with a simple muscle model and proprioceptive sensory feedback, we show that the CPG model can reproduce the different motor behaviors of the animal. We find that local proprioceptive feedback, together with the mechanical properties of the muscles, can play an important role in reducing the variability of intersegmental phase lags towards values appropriate for locomotion. To validate the simulation results in the real world, we implement the CPG model as a completely distributed controller on a salamander robot. We show that the animal behaviors can be reproduced using only two simple drive signals and local sensory feedback. We find that local proprioceptive sensory feedback can reduce or replace the need for different levels of drive. In particular, good swimming gaits are achieved with the robot using only one level of drive by introducing a strong proprioceptive feedback in the axial oscillators. The model suggests that the same principles govern the shaping of the motor pattern by descending drive signals and local sensory feedback.

**Keywords :** salamander, locomotion, central pattern generator, multifunctional circuits, sensory feedback, coupled oscillators, robotics.



# Résumé

Les salamandres sont capables d'une variété de comportements locomoteurs, dont notamment la nage, la marche aquatique, et la marche avant et arrière sur terre. Les enregistrements myographiques et cinématiques montrent que chacun de ces comportements est caractérisé par un déphasage intersegmental et une fréquence de cycle spécifiques. Une gamme de déphasages, plus large et continue, est également observée dans les enregistrements de la moelle épinière isolée. Les travaux de modélisation précédents se sont typiquement limités à la génération de deux comportements stéréotypés et aux transitions entre ces comportements. La présente étude se démarque en s'intéressant spécifiquement à la flexibilité des réseaux locomoteurs de la moelle épinière. Nous explorons les principes par lesquels un générateur central de rythme ou CPG (central pattern generator) peut voir son activité modulée par des commandes descendantes afin de générer les séquences d'activation musculaire appropriées à la reproduction du comportement désiré. Nous étudions ensuite l'influence des propriétés musculaires et des interactions avec l'environnement sur la cinématique et, à travers un retour sensoriel proprioceptif local, sur le CPG. Nous proposons un modèle de CPG basé sur des oscillateurs abstraits, capable de reproduire les caractéristiques principales des enregistrements effectués sur la moelle épinière isolée, ainsi que les rythmes nettement plus rapides observés durant la locomotion. Le modèle reproduit la distribution des déphasages intersegmentaux, la corrélation entre déphasage et fréquence de cycle, et les transitions spontanées entre rythmes lents et rapides. À l'aide de simulations numériques d'un robot de salamandre doté d'un modèle de muscle et de retour sensoriel proprioceptif, nous montrons que le modèle de CPG peut reproduire les différents comportements moteurs observés chez l'animal. Nous trouvons que le retour sensoriel local et les propriétés mécaniques des muscles peuvent jouer un rôle important dans la réduction de la variabilité du déphasage intersegmental vers des valeurs appropriées à la locomotion. Afin de valider les résultats obtenus en simulation, nous implémentons le modèle de CPG sur un robot de salamandre sous forme de contrôleur distribué. Nous montrons que les comportements de l'animal peuvent être reproduits à l'aide de seulement deux signaux de commande descendants ainsi que du retour sensoriel. Nous trouvons que le retour sensoriel proprioceptif local peut réduire la différence nécessaire entre les deux signaux de contrôle, voire s'y substituer. En particulier, des nages efficaces sont obtenues à l'aide d'un unique signal de commande suite à l'introduction d'un retour sensoriel proprioceptif relativement fort sur les oscillateurs axiaux. Le modèle suggère que les mêmes principes gouvernent la modulation de l'activité motrice par les signaux de commande descendants et par le retour sensoriel local.

## Résumé

---

**Mots-clés :** salamandre, locomotion, générateur central de rythme, circuits multifonctionnels, retour sensoriel, oscillateurs couplés, robotique.

# Contents

<b>Acknowledgements</b>	<b>iii</b>
<b>Abstract (English/Français)</b>	<b>v</b>
<b>List of figures</b>	<b>xi</b>
<b>List of tables</b>	<b>xv</b>
<b>1 Introduction</b>	<b>1</b>
1.1 Central Pattern Generators . . . . .	2
1.2 Our Approach . . . . .	3
1.3 Organization of the Thesis . . . . .	4
<b>2 Experimental Data on the Salamander</b>	<b>7</b>
2.1 Some Definitions . . . . .	7
2.2 A Diversity of Motor Behaviors . . . . .	8
2.3 A Flexible Central Pattern Generator . . . . .	10
2.4 Analysis of the <i>in vitro</i> Recordings . . . . .	13
2.4.1 Distribution of Phase Lags <i>in vitro</i> . . . . .	14
2.4.2 Rhythm Switches . . . . .	22
2.4.3 Phase Lag and Frequency . . . . .	25
<b>3 State of the Art</b>	<b>27</b>
3.1 Lamprey Models . . . . .	27
3.2 Salamander Models . . . . .	29
3.3 Related Work in Robotics . . . . .	33
3.4 Outstanding issues . . . . .	35
3.4.1 A More Flexible Network . . . . .	36
3.4.2 The Mechanisms of Regulation . . . . .	36
3.4.3 The Role of the Body Viscoelastic Properties . . . . .	37
<b>4 Flexible Models of the Isolated CPG</b>	<b>39</b>
4.1 Features Required of the Model . . . . .	39
4.2 Difficulties with a Previous Model . . . . .	40
4.2.1 General Approach . . . . .	40

4.2.2	Random Intrinsic Frequencies . . . . .	41
4.2.3	Flexibility by Brainstem Input . . . . .	43
4.2.4	Random Walks on the Frequencies . . . . .	43
4.2.5	Conclusions on the Ijspeert et al. [2007] Model . . . . .	44
4.3	A Radically Different Approach to Flexibility . . . . .	48
4.3.1	Polar Coordinates . . . . .	48
4.3.2	Cartesian Coordinates . . . . .	51
4.3.3	Simulation Results . . . . .	52
4.3.4	Conclusions on the Flexible Couplings . . . . .	53
4.4	A Flexible Network that is Robust to Variations in Frequencies . . . . .	57
4.4.1	Design Considerations . . . . .	57
4.4.2	Model Description . . . . .	58
4.4.3	Results . . . . .	59
4.4.4	Discussion . . . . .	60
4.4.5	Application to the Swimming-Walking Transition . . . . .	64
4.5	Modeling Spontaneous Rhythm Switches . . . . .	68
4.5.1	Rhythm Switches in the Asymmetric Model . . . . .	68
4.5.2	Network Loops . . . . .	70
4.5.3	Other Possibilities . . . . .	72
<b>5</b>	<b>The Flexible CPG in its Body: A Diversity of Behaviors</b>	<b>75</b>
5.1	Virtual Muscles . . . . .	77
5.1.1	Relation to a PD Controller . . . . .	78
5.2	The Mechanical Model in Simulation . . . . .	81
5.2.1	The Hydrodynamic Model . . . . .	81
5.3	Integrating Local Sensory Feedback in the CPG . . . . .	84
5.3.1	The Nature of the Feedback . . . . .	84
5.3.2	Incorporating a Cartesian Feedback in a Polar Oscillator . . . . .	85
5.4	Systematic Exploration of the Muscle and Feedback Parameter Space . . . . .	87
5.4.1	Fitness Measurements . . . . .	88
5.4.2	Selection of the Muscle Damping Constant . . . . .	89
5.4.3	Selection of the Muscle Stiffness and Feedback Strength . . . . .	93
5.4.4	Selection of the Muscle Gain . . . . .	97
5.5	Salamander Behaviors in Simulation . . . . .	97
5.5.1	Swimming . . . . .	98
5.5.2	Forward Land Stepping . . . . .	100
5.5.3	Underwater Stepping . . . . .	102
5.5.4	Backward Stepping . . . . .	103
5.5.5	Struggling . . . . .	104
5.6	Turning . . . . .	104
5.7	Gait Transitions . . . . .	105
5.8	Robot Experiments . . . . .	107

5.9	Discussion . . . . .	111
<b>6</b>	<b>Understanding the Effect of Local Sensory Feedback</b>	<b>117</b>
6.1	A Mathematical Analysis . . . . .	121
6.2	Contributions to Feedback-Induced Modulations of Phase Lags . . . . .	124
6.3	Conclusion . . . . .	126
<b>7</b>	<b>Robotic Platform</b>	<b>129</b>
7.1	Robot Hardware . . . . .	129
7.1.1	Mechanical Design . . . . .	129
7.1.2	Electronics . . . . .	130
7.2	Characterization of the PI Torque Controller . . . . .	130
7.2.1	Static Calibration . . . . .	130
7.2.2	Lag between Setpoint and Torque . . . . .	131
7.3	A Distributed Robot Controller . . . . .	134
7.3.1	First Implementation . . . . .	136
7.3.2	Second Implementation . . . . .	137
7.3.3	CPG Slow-down Induced by Communication Delays . . . . .	138
7.3.4	Controller Time-Step . . . . .	141
7.3.5	Concluding Remarks . . . . .	142
7.4	External Video Tracking . . . . .	144
<b>8</b>	<b>Conclusion</b>	<b>145</b>
<b>A</b>	<b>CPG and Kinematic Patterns in Robot Experiments</b>	<b>149</b>
<b>B</b>	<b>Conversion Factors for Internal Robot Units</b>	<b>153</b>
B.1	Position Units . . . . .	153
B.2	Torque Units . . . . .	154
B.3	Speed Units . . . . .	156
	<b>Bibliography</b>	<b>165</b>
	<b>Curriculum Vitae</b>	<b>167</b>





# List of Figures

2.1	Kinematic recordings of a salamander during swimming and forward stepping	9
2.2	Five motor behaviors in the salamander	11
2.3	Kinematic and EMG patterns for the five motor behaviors	12
2.4	Burst identification in recordings <i>in vitro</i>	13
2.5	Variability of intersegmental phase lags <i>in vitro</i>	15
2.6	Histograms of intersegmental phase lags <i>in vitro</i> (1)	16
2.7	Histograms of intersegmental phase lags <i>in vitro</i> (2)	17
2.8	Standard deviation of intersegmental phase lag	18
2.9	Intersegmental phase lag for two long recordings	20
2.10	Standard deviation of intersegmental phase lag timeseries	21
2.11	Activity pattern during a back-and-forth switch	22
2.12	Cycle to cycle periods during a switch	23
2.13	Intersegmental phase lag during a switch	23
2.14	Duty cycles during a switch	24
2.15	Period as a function of the intersegmental phase lag	26
3.1	Models of the salamander spinal circuitry for locomotion	30
3.2	Previously published salamander robots	34
4.1	Original Hemicord model with random intrinsic frequencies	42
4.2	Distribution of phase lags in the Original Hemicord model with random frequencies	43
4.3	Distribution of phase lags in the Original Hemicord model with random frequencies and $k = 0$	44
4.4	Original Hemicord model with random frequencies and $k = 0$	45
4.5	Original Hemicord model with different frequency in the first segment	46
4.6	Original Hemicord model with damped random walk	47
4.7	Network topologies for flexible hemicord models	49
4.8	Ranges of phase lags in the intrinsically flexible hemicord networks	54
4.9	Distribution of phase lags in the intrinsically flexible hemicord	55
4.10	Flexible hemicord network with random intrinsic frequencies	56
4.11	Control of phase lag by a transient perturbation in a flexible hemicord network	56
4.12	Connectivity in the asymmetric model	62

## List of Figures

---

4.13	Distribution of intersegmental phase lags in the asymmetric model . . . . .	63
4.14	Correlation between intersegmental phase lag and cycle duration in the asymmetric model . . . . .	63
4.15	Simplified model with asymmetric couplings . . . . .	64
4.16	Controllability in the simplified asymmetric model . . . . .	66
4.17	Swim-to-walk transition in the simplified asymmetric model . . . . .	67
4.18	Rhythm switch in the asymmetric model . . . . .	69
4.19	Loop network . . . . .	71
4.20	50 simulations in the loop network . . . . .	73
5.1	Control architecture for the simulation of <i>in vivo</i> behaviors . . . . .	76
5.2	Spring-damper muscle model . . . . .	78
5.3	Simulations of swimming and forward land stepping in Webots . . . . .	83
5.4	Systematic exploration of the $(\beta, w^{\text{ipsi}})$ parameter space in swimming simulations with $\delta = 0.05$ . . . . .	90
5.5	Systematic exploration of the $(\beta, w^{\text{ipsi}})$ parameter space in swimming simulations with $\delta = 0.1$ . . . . .	91
5.6	Systematic exploration of the $(\beta, w^{\text{ipsi}})$ parameter space in swimming simulations with $\delta = 0.15$ . . . . .	92
5.7	Systematic exploration of the $(\beta, \gamma)$ parameter space in swimming simulations with $\alpha = 0.4$ , $\delta = 0.1$ and $w^{\text{ipsi}} = 19$ . . . . .	94
5.8	Systematic exploration of the $(\beta, \gamma)$ parameter space in swimming simulations with $\alpha = 0.4$ , $\delta = 0.1$ and $w^{\text{ipsi}} = 21$ . . . . .	95
5.9	Systematic exploration of the $(\beta, \gamma)$ parameter space in swimming simulations with $\alpha = 0.4$ , $\delta = 0.1$ and $w^{\text{ipsi}} = 24$ . . . . .	96
5.10	Swimming patterns in simulation . . . . .	99
5.11	Open-loop forward stepping in simulation . . . . .	100
5.12	Feedback effect in forward land stepping . . . . .	101
5.13	Comparison of hydrodynamic forces during water stepping in simulation with active vs. passive tail. . . . .	102
5.14	Underwater stepping in simulation . . . . .	103
5.15	Backward stepping in simulation . . . . .	103
5.16	Struggling in simulation . . . . .	104
5.17	Turning during swimming in simulation . . . . .	105
5.18	Walk-swim transition in simulation . . . . .	106
5.19	Effect of axial proprioceptive feedback during swimming . . . . .	109
5.20	CPG activity pattern during swimming . . . . .	110
5.21	Optimization of the limb→body phase bias in the robot . . . . .	111
5.22	Intersegmental phase lag in the robot mid-trunk in 5 simulated individuals . .	112
5.23	Differential drive signals used to reproduce the 5 motor behaviors . . . . .	113
5.24	Speed of locomotion in the five individuals for each motor behavior . . . . .	114

5.25	Effect of proprioceptive feedback on the intersegmental phase lag during forward land stepping . . . . .	115
6.1	Scaling of appropriate feedback strength with the drive during swimming . . .	118
6.2	Effect of local sensory feedback on a variety of open-loop patterns in presence of neck feedback during swimming . . . . .	120
6.3	Local effect of sensory feedback . . . . .	123
6.4	Contributions to the feedback-induced acceleration during swimming . . . . .	125
7.1	The <i>Salamandra robotica II</i> amphibious robot . . . . .	129
7.2	Torque calibration . . . . .	131
7.3	Rectified sine setpoints and torque values read back from the PI controller . . .	132
7.4	Torque setpoints and values read back from the PI controller in the robot swimming with the muscle model at 1.1 Hz. . . . .	133
7.5	Control architecture for experiments with <i>Salamandra robotica II</i> . . . . .	135
7.6	Phase lags and average coupling effects in the first implementation of the distributed controller . . . . .	136
7.7	Phase lags and average coupling effects in the distributed controller with coupling extrapolation . . . . .	138
7.8	Solutions of the in-phase synchronous oscillations with coupling delays . . . .	140
7.9	CPG slow-down induced by communication delays . . . . .	141
7.10	Real-time duration of a CPG integration step using unwrapped phases . . . . .	142
7.11	External video tracking setup . . . . .	144
A.1	Swimming pattern obtained with the first simulated individual, with feedback $w^{\text{ipsi}} = 10$ . . . . .	149
A.2	Underwater stepping pattern obtained with the first simulated individual. . . .	150
A.3	Forward land stepping pattern obtained with the first simulated individual. . .	150
A.4	Backward stepping pattern obtained with the first simulated individual. . . . .	151
A.5	Struggling pattern obtained with the first simulated individual . . . . .	151



## List of Tables

4.1	Coupling parameters in the asymmetric model . . . . .	59
4.2	Other parameters in the asymmetric model . . . . .	59
4.3	Four regimes in a simple network loop . . . . .	70
5.1	CPG parameters adjusted for <i>in vivo</i> simulations. . . . .	75
5.2	Muscle and feedback parameters for robot experiments . . . . .	108



# 1 Introduction

Animal locomotion relies on the constant interactions between the neural centers, the muscles, the passive tissues such as the bones, skin and tendons, and the environment. The interactions occur at many levels. The nervous system activates the muscles, and its own activity is modulated by the muscle response through sensing of the muscle force, length, and contraction rate. The muscles exert a force on the passive body parts, and the interactions between these parts and the environment will determine the contraction rate and future length of the muscles, which will in turn affect the activity of the neural centers. Given these complex interaction loops, locomotion cannot be fully understood by studying the individual components in isolation. Numerical and physical models that integrate all components of the control loops are essential to the formulation and validation of hypotheses regarding the interactions between these components.

The same principles of interaction between the control centers, the actuators, the passive parts and the environment apply to robotic locomotion. Mechanical designs and control principles of robots are often inspired by biology [Pfeifer et al., 2007, Floreano and Mattiussi, 2008]. Reciprocally, biologically inspired robots can bring new insights in biology [Webb, 2002]. While the present work is mainly concerned with the understanding of animal locomotion control, we hope that some of the principles outlined in our models can find a use in robotics.

The object of this thesis is to investigate the general principles that underlie the coordination of the trunk and tail muscles and the limbs in the salamander. We seek to understand how a single neural circuit in the spinal cord can generate a variety of behaviors, each of them requiring a different kind of muscle coordination; how the body mechanics and interactions with the environment affect the spinal circuits through sensory feedback; and how the brain can control the activity of these circuits and select between different coordination patterns to achieve the desired behavior. We mostly limit ourselves to the control of locomotion; we will address to a small extent other motor behaviors by including struggling among the behaviors we reproduce.<sup>1</sup>

---

1. Here, struggling refers to a motor behavior where the animal tries to escape a hand holding it at the pelvic girdle.

The salamander is a particularly interesting subject for the study of locomotion control, for several reasons. As one of the living animals closest to the early tetrapods—its morphology has been relatively stable for the last 150 million years [Gao and Shubin, 2001]—and as an amphibian, it constitutes a good opportunity to investigate the neural and morphological changes that accompanied the transition of vertebrates from the sea to the land. Its nervous system is relatively simple for a tetrapod [Nieuwenhuys et al., 1998], showing remarkable similarities to that of the lamprey [Ryczko et al., 2010b], a primitive jaw-less fish that uses an anguilliform swimming gait close to that of the salamander. These similarities allow us to build on a lot of research done on the lamprey, which has one of the best documented and most extensively modeled central nervous system among vertebrates. The simplicity of these nervous systems makes them more tractable for modeling, and yet much of the knowledge gained from these studies applies to all vertebrates [Grillner et al., 2003]. Finally, salamanders have impressive regenerating capabilities. They are the only adult limbed vertebrates that are known to recover completely from a lesion at any level of the spinal cord [Chevallier et al., 2004, Davis et al., 1990, Piatt, 1955].

The general architecture of locomotion control in vertebrates is known [Grillner et al., 2008]: the brain selects a motor program and activates the central pattern generator (CPG) in the spinal cord, as described in the next section. The CPG coordinates the activation of the muscles that enable locomotion. The resulting motion determines the sensory feedback signals that are received by the CPG and modulate its activity. The brain also receives sensory inputs e.g. from the vestibular system, affecting the commands it sends to the CPG. However, while the main information pathways are known, as well as many details of the interactions between particular components, a global understanding of the interaction between the CPG, the descending commands from the brain and sensory feedback is still missing.

### 1.1 Central Pattern Generators

Neural networks capable of generating a rhythmic output signal without receiving a rhythmic input are called central pattern generators (CPG). Such networks play an important role in the generation of rhythmic movements in most animals [Grillner and Wallen, 1985], but there is only indirect evidence for locomotor CPGs in humans—see Duysens and van de Cromment [1998] and MacKay-Lyons [2002] for reviews. The part of our work concerned with the nervous system consists essentially in a high level model of the salamander CPG.

CPGs are particularly well documented in the spinal cord of the lamprey and, to a smaller extent, the salamander. For example, an isolated salamander spinal cord can be pharmacologically stimulated by bath application of N-methyl-D-aspartate (NMDA), a molecule that activates specific neural receptors. The global excitation of the spinal network by NMDA leads to periodic bursts of activity in the spinal neurons, similar to the bursts of activity that cause the contraction of muscles during locomotion in an intact animal [Delvolvé et al., 1999]. Moreover, the bursts observed in different parts of the isolated spinal cord are coordinated in



a way that closely mirrors the activity of the network during locomotion: in each segment of the spinal cord,<sup>2</sup> the activity alternates between the neural populations on the left and right side of the cord. The coordination is also observed between segments, with waves of activity propagating from one end of the spinal cord to the other, as observed in the intact animal during swimming. These locomotor activity patterns in an unmoving preparation are referred to as *fictive locomotion*.

Experiments have shown that the activity of the salamander CPG can be controlled by electrical stimulation of a part of the brain called the mesencephalic locomotor region (MLR): The frequency of a swimming gait can be increased or decreased by adjusting the strength of the electrical stimulation. Below a certain stimulation threshold, a transition to a walking gait is observed [Cabelguen et al., 2003].

There is a scarcity of experimental data regarding the role of proprioceptive feedback in salamander locomotion. We are only aware of one study that identified stretch receptors in the limb muscles [Bone et al., 1976], but their effect on locomotion was not investigated. In contrast, there are many studies investigating the influence of intraspinal stretch-sensitive neurons on the lamprey CPG (see section 5.3). These studies show that proprioceptive feedback can have an accelerating or decelerating effect on the CPG rhythm.

These biological data motivated our investigation into the principles of interaction between the CPG, descending signals from the brain and proprioceptive sensory feedback.

## 1.2 Our Approach

In Ijspeert et al. [2007], a salamander robot driven by a model of the salamander spinal cord could reproduce swimming and walking gaits, and the corresponding gait transitions. The model led to new hypotheses that were verified in biological experiments, e.g. that neural centers controlling the limbs tend to generate slower rhythms than the neural centers controlling the axial muscles, at the same level of excitation.

In the present thesis, we build on this work to create a more flexible model that reproduces the variety of behaviors documented in the animal: Recent recordings of the kinematics and muscle activities during swimming, underwater stepping, forward land stepping, backward land stepping and struggling show that the CPG produces specific intersegmental coordination patterns in each case. These biological data are summarized in chapter 2. We incorporate virtual muscles and sensory feedback in the model, in order to specifically address the question of the interactions between the CPG, the descending commands from the brain, and sensory feedback, and how they change from one motor behavior to another. We consider exclusively *local proprioceptive* feedback. By local, we mean feedback that affects directly only the neural

---

2. The spinal cord can be divided in a number of segments, each segment corresponding to a vertebra. The salamander species that we model, *Pleurodeles waltl*, has about 40 segments.

centers close to the source of the signal.<sup>3</sup> While proprioceptive feedback refers to the sensing of joint positions, joint velocities and muscle forces, in this work we limit ourselves to the sensing of joint positions.

Our general approach is to first build a model of the isolated CPG that reproduces the main observations made in the isolated spinal cord; then to interface this model with a musculo-mechanical model of the salamander in simulation to reproduce the behaviors of the intact animal; finally to validate these results by using the CPG and muscle models to control a salamander robot. The validation of simulation results with a real physical model—the robot—is important due to the difficulty of simulating accurately the interactions with the environment, for example the friction effects and the hydrodynamic forces.

The compliance introduced by the virtual muscles increases the sensitivity of our model to environmental interactions, compared with typical robotic systems that control directly the position of the motors. These interactions determine the sensory feedback signals that are sent to the CPG; their accuracy is therefore particularly important in our case, and the tests with an actual robot particularly useful to validate the simulations. The robot platform, with its limitations in the maximal motor torques and in the reliability of inter-module communication, also serves to demonstrate the robustness of the control architecture.

Finally, we should note that while we address the integration of sensory feedback and descending signals in the CPG of the salamander, these questions are of great importance for all vertebrates. Sensory feedback has been shown to play a significant role in locomotion control in many vertebrates, not only as a mechanism to respond to external perturbations, but also as a contributor to the generation of the normal locomotor pattern [Rossignol et al., 2006]. Gait transitions induced by MLR stimulation have also been observed in all classes of vertebrates [Grillner et al., 1997].

### 1.3 Organization of the Thesis

We begin in chapter 2 with the presentation of recent biological data showing that the various coordination patterns observed during fictive locomotion correspond to distinct behaviors in the intact animal. The state of the art in the modeling of salamander locomotion is reviewed in chapter 3, together with relevant work in lamprey modeling and robotics.

In chapter 4, we propose different approaches to the modeling of the salamander CPG, with a focus on the flexibility of muscle activation patterns. One approach seeks to maximize the flexibility of the network by redefining the role of the CPG: The activity pattern, rather than being defined by the network parameters, would be part of the state of the dynamical system. The CPG would not resist a change to the activity pattern triggered e.g. by higher neural centers, but memorize the new pattern and strive to preserve its consistency across the whole network. Another approach takes a more conservative route, extending the model of

---

3. Long-range indirect influences are not excluded.

Ijspeert et al. [2007] to support a variety of activity patterns and to include a mechanism for the independent control of cycle frequency and intersegmental coordination by higher neural centers. This second approach is successful in reproducing important features from biological recordings of the isolated salamander spinal cord. In particular, the model reproduces the distribution of intersegmental coordination patterns and their correlation with the cycle frequency.

In chapter 5, we show how the second approach was used to drive the virtual muscles actuating a salamander robot. Sensory feedback was included in the form of axial proprioceptive feedback and—to a small extent—excitatory proprioceptive feedback from the limbs. Numerical simulations were used to explore the muscle and feedback parameter space and verify that the model could reproduce the different behaviors observed in the salamander. The simulation results were validated by reproducing the salamander behaviors on a real robot.

The mechanisms by which sensory feedback interacts with the CPG are analyzed in detail in chapter 6. We show that the principles governing the regulation of the CPG activity by higher neural centers, detailed in chapter 4, also apply to the modulation of the CPG pattern by local sensory feedback. We also find that local feedback can correct a variety of inappropriate activity patterns in the CPG during swimming. This optimizing effect of sensory feedback relies on increasing delays, from the head to the tail, between muscle activation and body curvature. These increasing delays, which are a consequence of the mechanical properties of muscles, and of the interactions with the environment, are also observed in the animal (see section 3.1).

Finally, the robotic platform is described in detail in chapter 7. In particular, we present the design of our distributed controller, in which the relevant part of the CPG model and the muscle model are calculated locally in each module. The distributed architecture allows us to distribute the cost of computation among the robot modules, and to minimize the communications between the different parts of the robot. It also improves the reliability of the muscle model, as it is not subject to inter-module transmission errors.



## 2 Experimental Data on the Salamander

In this chapter, we present the experimental data that motivated our work and defined our objectives. We begin with some definitions. Section 2.2 reviews the experimental data on the behaviors in the intact animal. Section 2.3 describes the organization of the salamander CPG and reviews data from experiments on the isolated spinal cord.

### 2.1 Some Definitions

We use mainly two measurements to characterize the CPG and kinematic patterns: the *intersegmental phase lag* and the *cycle frequency*. The intersegmental phase lag is a quantification of the intersegmental coordination. It corresponds to the delay between events occurring in consecutive spinal segments, expressed as a percentage of the cycle duration. For electromyographic (EMG) recordings,<sup>1</sup> we measure the delay between the bursts in two segments  $i$  and  $j$  (numbered from head to tail) and divide the result by  $j - i$ . For kinematic recordings, we measure the times of zero or maximal body curvature at different sites along the body and divide the result by the approximate number of segments separating these sites.

Most of the data presented here and used for modeling concern the salamander *mid-trunk*, which comprises the 6th to 12th segments of the spinal cord. One advantage of this approach is that the intersegmental phase lag is relatively uniform in this region of the trunk.

Animal experiments are of two kinds: *in vivo* and *in vitro*. The former refers to an intact, living animal. The latter refers for example to an isolated spinal cord preparation.

Head-to-tail and tail-to-head directions are referred to as *rostrocaudal* and *caudorostral* respectively. Body parts or neural connections relating to the same side (left or right) of the body are described as *ipsilateral*. Parts or connections relating to opposite sides are described as *contralateral*.

---

1. Electromyographic recordings are obtained by implanting small electrodes in the muscles of the salamander and recording their electrical activity.

### 2.2 A Diversity of Motor Behaviors

The kinematics of salamander locomotion has been documented for several behaviors including swimming, forward stepping and backward stepping, as reviewed by Karakasiliotis et al. [2012]. Most studies have focused on the axial bending and hindlimb kinematics.

During swimming, salamanders fold their limbs backward and use an anguilliform gait like the lamprey: axial undulations are such that a wave of body curvature propagates from the head to the tail (rostrocaudal wave, figure 2.1 left), with approximately one full wave visible on the body at any time [Frolich and Biewener, 1992, Delvolvé et al., 1997]. Backward swimming has never been reported.

When stepping on land, salamanders typically use a walking trot: diagonal limbs move in phase, with a duty factor<sup>2</sup> above 70% [Ashley-Ross, 1994, Ashley-Ross and Bechtel, 2004, Ashley-Ross et al., 2009]. A walking gait with only one limb at a time in the swing phase has also been reported [Edwards, 1976, Frolich and Biewener, 1992], but is less common. In the remainder of this chapter, “walking” will always refer to the walking trot.

In this gait, the body axis displays an S-shaped standing wave with nodes<sup>3</sup> at the girdles: the trunk joints between the girdles bend in unison and in anti-phase with respect to the tail joints (figure 2.1 right). The timing of forelimb protraction coincides with ipsilateral stretching of the trunk. This coordination of the limb and trunk motion maximizes the stride length [Roos, 1964, Daan and Belterman, 1968].

The kinematic patterns observed in the trunk are reflected in EMG recordings, where traveling and standing waves of muscle activation are observed during swimming and forward stepping respectively [Frolich and Biewener, 1992, Delvolvé et al., 1997]. The EMG patterns however show additional complexity compared to the kinematics. During walking, double bursting is observed in the neck and tail regions. During swimming, the rostrocaudal wave of muscle activation shows discontinuities around the shoulder and pelvic girdles [Delvolvé et al., 1997]. This is in contrast to the lamprey where smooth traveling waves of muscle activation are observed during swimming [Wallen and Williams, 1984, Williams et al., 1989].

During underwater stepping, salamanders use either a slight rostrocaudal traveling or a standing wave of muscle activation and body curvature [Ashley-Ross et al., 2009, Deban and Schilling, 2009]. In this case the duty factor is reduced to about 40%, and periods of suspension with no ground contact are observed [Ashley-Ross et al., 2009].

Recently, systematic EMG and kinematic recordings were obtained of the salamander *Pleurodeles walt* for five motor behaviors: swimming, underwater stepping, forward land stepping, backward land stepping and struggling. These five behaviors are illustrated with image sequences in figure 2.2. The results of the EMG and kinematic recordings are summarized in

---

2. The percentage of time that a given limb spends touching the ground.

3. The nodes of a standing wave are the points where the oscillation amplitude is minimal.

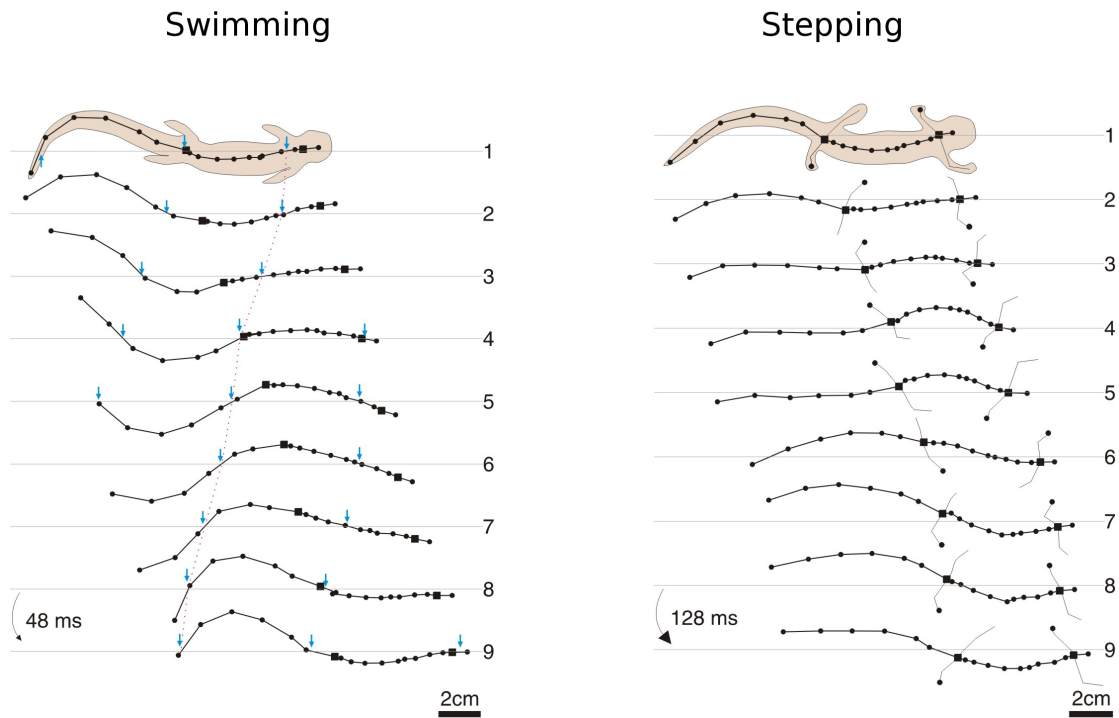


Figure 2.1 – Kinematic recordings of a salamander (*Pleurodeles waltlii*), reconstructed from individual video frames. Squares indicate the girdles. Dots at the limb extremities indicate estimated foot contacts. Body configurations from successive frames are aligned according to the direction of overall forward motion. **Left:** Swimming gait. Arrows indicate the points of minimal displacement from the overall forward direction. A traveling wave of body curvature propagates down the body. **Right:** Walking gait. The body displays a standing wave of body curvature with nodes close to the girdles. Adapted from Ijspeert et al. [2007].

figure 2.3. In addition to the behaviors already described, we see that backward stepping and struggling are characterized by strong rostrocaudal and caudorostral traveling waves respectively. They both show significantly lower cycle frequencies than the other motor behaviors. We note that tail muscles are mostly silent during underwater stepping.

### 2.3 A Flexible Central Pattern Generator

As in other vertebrates, the coordinated activation of muscles in the salamander is generated by neural networks called central pattern generators (CPG) located in the spinal cord [Wheatley et al. [1994], Delvolvé et al. [1999], see also section 1.1). A CPG network can be decomposed into several oscillatory units, where each unit corresponds to a group of neurons that exhibit periodic bursting. In the salamander, these oscillatory units are distributed along the spinal cord, as in the lamprey [Cohen and Wallen, 1980, Grillner et al., 1995]. Recent experiments on the salamander suggest that an oscillatory unit might be as small as a hemisegment [Ryczko et al., 2010a]. In the next section, we will show that the isolated salamander CPG can produce many different patterns of coordination between oscillatory units that control trunk muscles. This range of coordination patterns includes and exceeds the range of EMG patterns observed in the intact animal.

The neural centers that control the limb movements are located between the first and fifth segments (for the forelimbs) and between the fourteenth and eighteenth segments (for the hindlimbs) of the spinal cord [Székely and Czéh, 1976, Wheatley et al., 1992, Cheng et al., 1998]. Each of these regions can be decomposed in left and right parts that control the corresponding limb [Brändle and Székely, 1973, Székely and Czéh, 1976]. It has been suggested that the neural center for a given forelimb can further be decomposed into independent flexor and extensor centers [Cheng et al., 1998, 2002].

The salamander brainstem<sup>4</sup> includes a mesencephalic locomotor region (MLR). This region is involved in locomotion control and in particular gait selection in many vertebrates [Ryczko and Dubuc, 2013]. In the salamander, electrical stimulation of the MLR can control the transition between swimming and stepping [Cabelguen et al., 2003]. A low intensity stimulus yields a stepping gait. Increasing the current or frequency of the electrical stimulus causes an increase of the stepping frequency. Above a certain stimulation threshold, the preparation switches to a swimming gait. Further increases of the stimulus strength lead to faster swimming. These results are consistent with the observations in the intact animal, where swimming frequencies are always higher than walking frequencies for a particular individual [Delvolvé et al., 1997] (see figure 2.3).

---

4. The lower part of the brain in vertebrates, adjoining the spinal cord.



### 2.3. A Flexible Central Pattern Generator

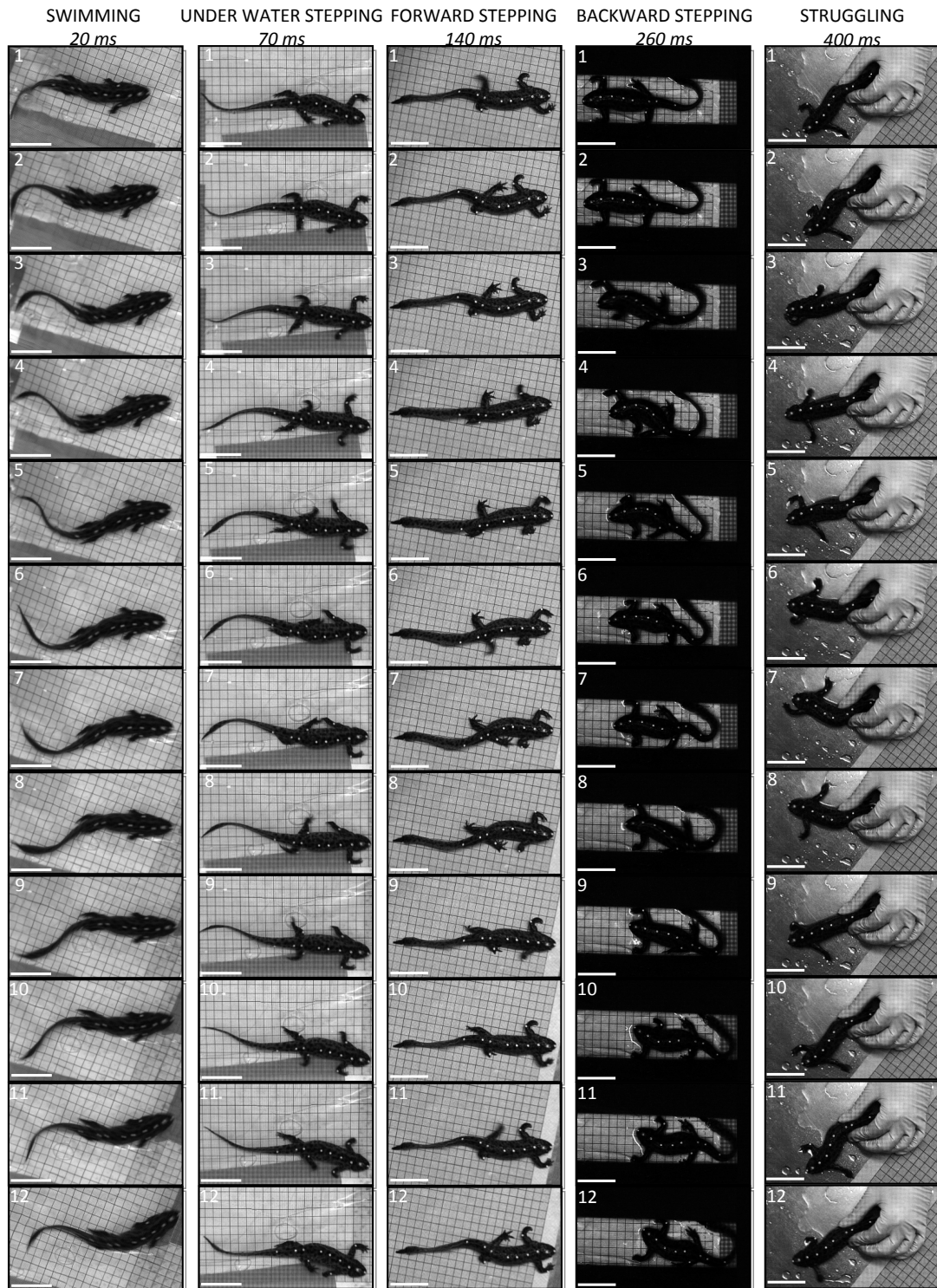


Figure 2.2 – Five motor behaviors in the salamander *Pleurodeles waltl*. The time lapse between two pictures is indicated at the top of each series. The white markers used to record the kinematic patterns are visible on the back of the animal. From Ryczko et al. [in preparation].

## Chapter 2. Experimental Data on the Salamander

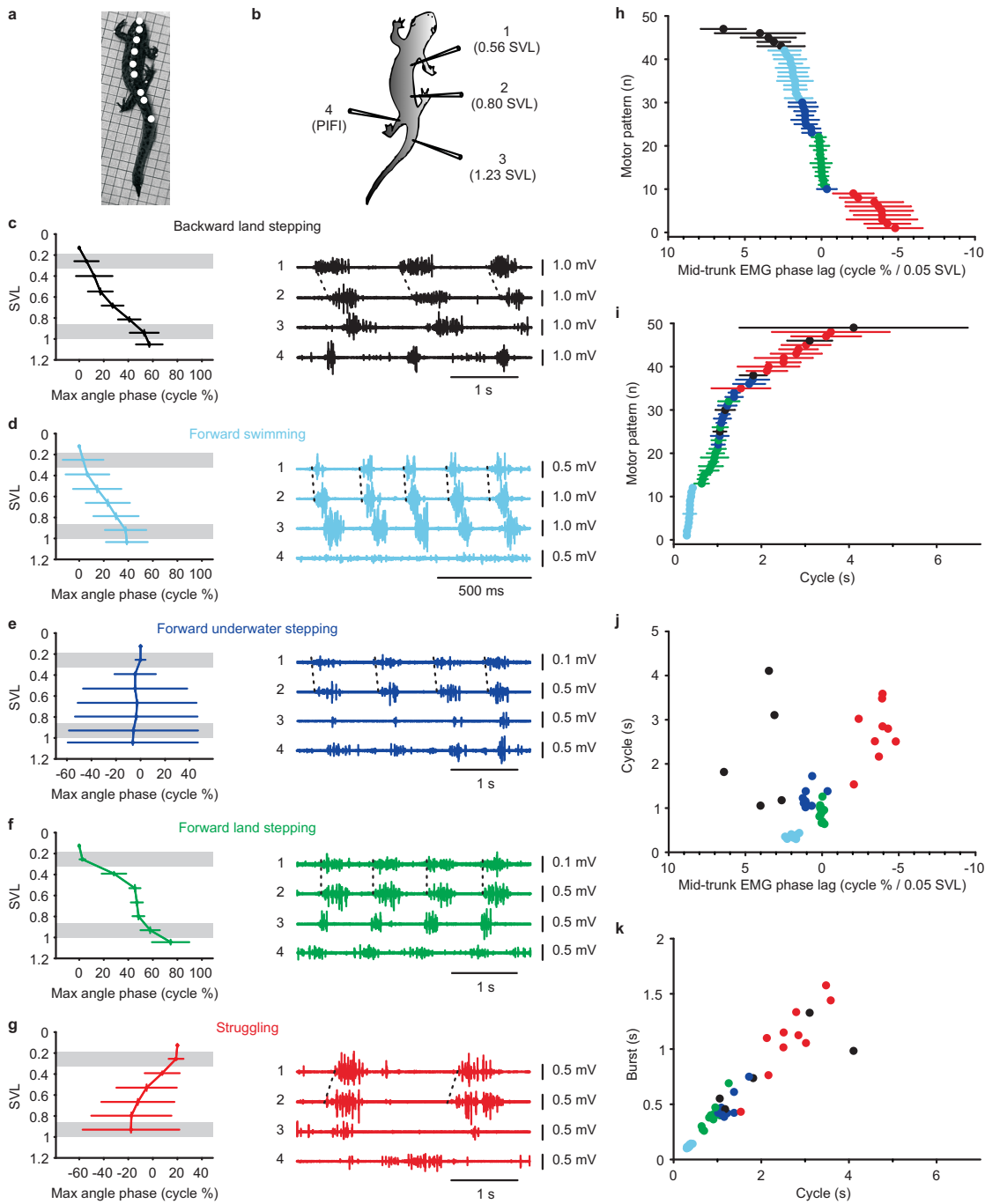


Figure 2.3 – Kinematic and electromyographic patterns for five motor behaviors in the salamander *Pleurodeles waltl*. **Left:** Example kinematic patterns are shown for each motor behavior. The position of the markers is expressed in fractions of the snout-vent length (SVL), in order to normalize the measurements between different animals. The timing of maximal body curvature is indicated as a percentage of the cycle duration. **Middle:** Example EMG patterns are shown for each behavior, for the recording sites indicated at the top. **Right:** The mid-trunk intersegmental phase lags recorded from all individuals are shown sorted by decreasing phase lags (top). Below are shown the sorted cycle durations, the correlation between phase lag and cycle duration, and the correlation of the burst duration with the cycle duration. From Ryczko et al. [in preparation].

## 2.4 Analysis of the *in vitro* Recordings

We summarize here some important observations from recent *in vitro* experiments. We obtained raw electrical recordings from the laboratory of Jean-Marie Cabelguen at INSERM (Bordeaux, France) and proceeded to our own analysis, except for figure 2.5. The recordings were obtained from the ventral roots of isolated spinal cords activated by bath-application of NMDA, as described by Delvolvé et al. [1999].

The recording were processed automatically in Matlab. An example of this process is shown in figure 2.4. The data were smoothed using a cubic spline fit (red line). The local minima and maxima of the spline were used to identify the cycles. In each cycle, the start of the burst was determined by considering a straight line from the local maximum to the local minimum on the left side of the burst. The burst start was set at the point on the spline that lied the furthest away from this line. The end of the burst was calculated in the same way, with the line joining the local maximum to the local minimum on the right side of the burst. The time of the burst was calculated from the centroid of the area enclosed by the burst (circular markers in figure 2.4).

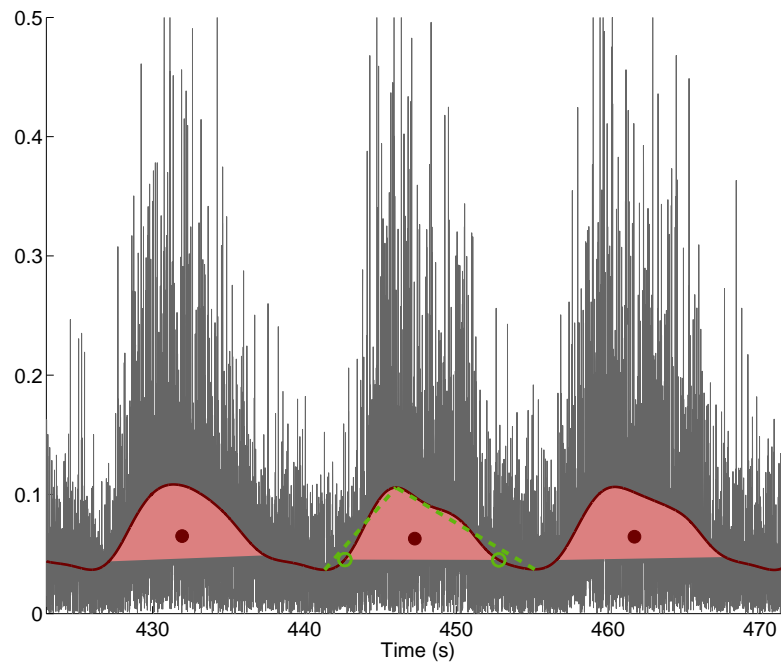


Figure 2.4 – Burst identification in recordings *in vitro*. The raw electrical data are shown in gray. The red line shows the result of a cubic spline filter. The onset and offset of each burst are estimated by tracing a line from the local maximum to the local minima on both sides (green dashed lines) and finding the points on the spline curve that are furthest away from these lines (green open markers). The burst time is calculated as the centroid (red filled marker) of the surface (light red) delimited by the spline curve and the two open markers.

### 2.4.1 Distribution of Phase Lags *in vitro*

There is a great variety of intersegmental phase lags observed *in vitro*. Before looking at the experimental data, we propose some definitions to distinguish between several types of variability.

#### Terminology of Phase Lag Variability

We distinguish the following types of phase lag variability in recordings *in vitro*:

- Between preparations: different recording sessions (whether on the same individual or different ones) give different phase lags. We refer to this as phase lag *diversity*.
- Between ventral roots: in a given preparation, the phase lag can vary along the body. We refer to this as phase lag *inconsistencies*. Conversely, the absence of variability along the cord is referred to as the *uniformity* of phase lags.
- Between cycles: in a given preparation, for two given ventral roots, the phase lag can vary from a cycle to another. We refer to this as *cycle to cycle variability*.

Finally, in modeling experiments, we are interested in the possibility of adjusting the phase lag through simple control signals. We refer to this as phase lag *flexibility*.

We will now look at the different types of variability as exhibited by the experimental data.

#### Phase Lag Diversity

A great variability of phase lags has been observed between different preparations, with values ranging from about -13% to 12%. This range was observed in the whole spinal cord, the isolated mid-trunk and the isolated mid-trunk hemicord, as shown in figure 2.5.

The distribution of phase lags shows three peaks, one in positive lags, one in negative lags, and one around zero. This variability was also observed in preparations which included the brainstem, though only two peaks were reported [Delvolvé et al., 1999].

#### Phase Lag Inconsistencies

A more constrained variability is observed in individual recordings, when considering different electrodes along the spinal cord. Unfortunately, data could be only be recorded simultaneously from four ventral roots. This means that we have at most three phase lag values to compare for a given preparation (when the four electrodes were recording from ipsilateral ventral roots), and in many case we have only one or two values (as some electrodes were used to record from limb nerves or contralateral roots).

Based on those recordings that include four ipsilateral ventral roots, we calculated the distribution of phase lags for each root pair. Results are shown in figures 2.6 and 2.7.

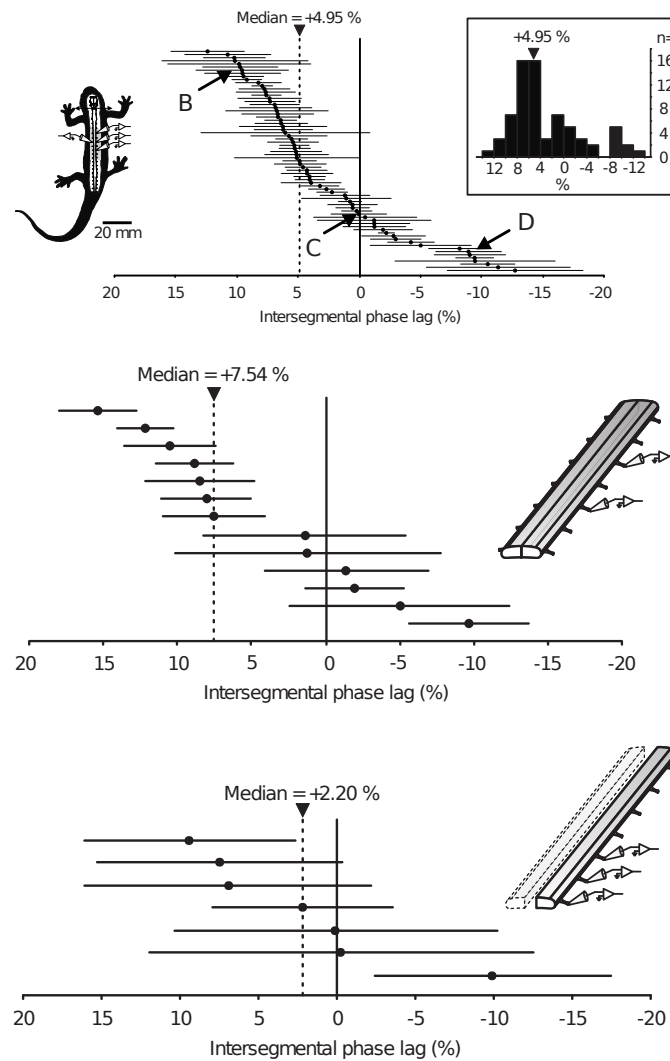


Figure 2.5 – Variability of intersegmental phase lags *in vitro*. Each dot represents the average phase lag for one preparation. Top: whole spinal cord. Center: isolated mid-trunk. Bottom: isolated mid-trunk hemicord. From (Ryczko et al prepa).

Some preparations (e.g. the top right one in figure 2.6) show a significant difference between recording sites. In most cases (e.g. top left in figure 2.6 and top in figure 2.7), recording sites show small differences, consistent with a slight increase or decrease of phase lag along the body. Large differences ( $> 5\%$ ) are rare, and phase lags are normally the same sign for different recording positions (see the upper-left preparation for an exception). After calculating the median phase lag for each pair of ventral roots, we plotted the standard deviation of the medians in figure 2.8. The variability of the median appears to be rather low, with most values below 3%.

## Chapter 2. Experimental Data on the Salamander

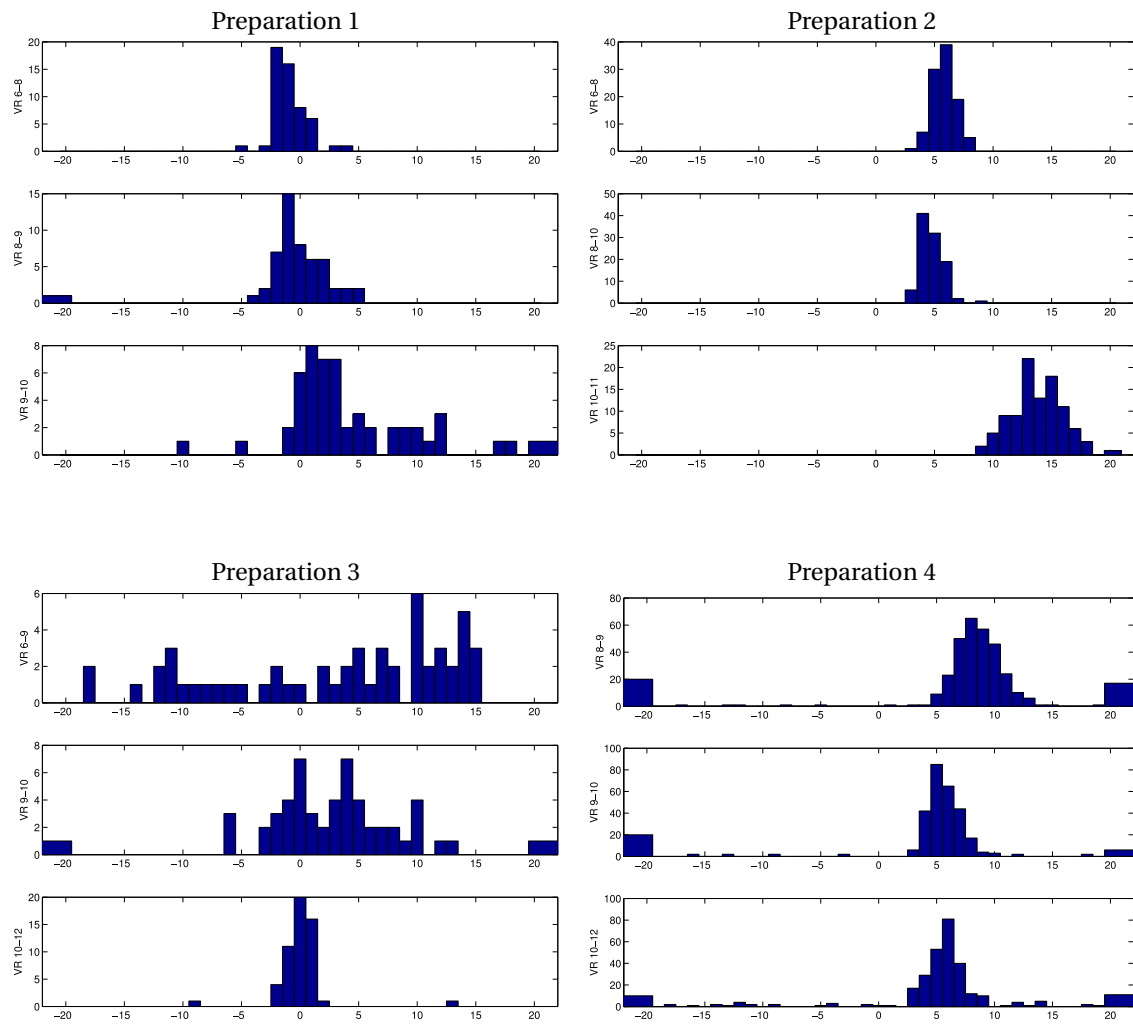


Figure 2.6 – Histograms of intersegmental phase lags for three pairs of ventral roots, in four *in vitro* preparations (first set). Each histogram shows the distribution of cycle to cycle phase lags between two ventral roots, during one recording session.

## 2.4. Analysis of the *in vitro* Recordings

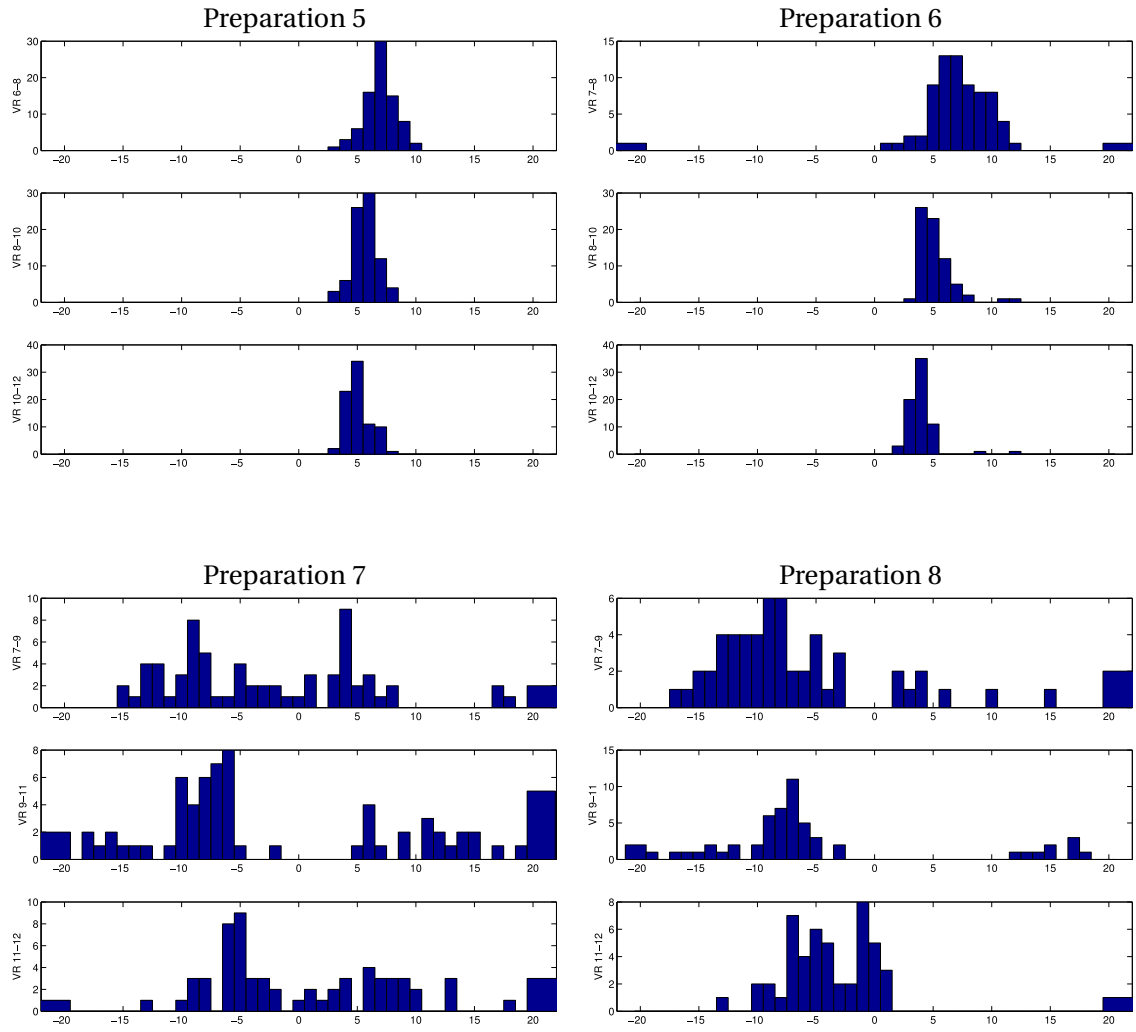


Figure 2.7 – Histograms of intersegmental phase lags for three pairs of ventral roots, in four *in vitro* preparations (second set). Each histogram shows the distribution of cycle to cycle phase lags between two ventral roots, during one recording session.

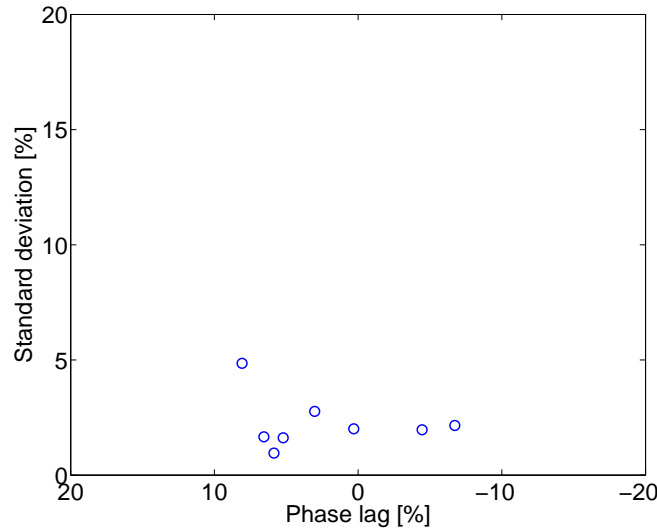


Figure 2.8 – Standard deviation of intersegmental phase lags between pairs of ventral roots, using recordings with four ipsilateral ventral roots.

### Cycle to Cycle Variability

During one recording session, the phase lags show some noise in the form of cycle to cycle variability, but are generally stable: there is no continuous drift. To illustrate this, we show the cycle per cycle phase lags of our two longest recordings in figure 2.9.

There is no drift in phase lag values. As we will see in chapter 4, this observation will be important in deciding between two types of CPG models. There is however a variable amount of noise. To quantify this noise and its variation between recordings, we plotted the standard deviations of the phase lag in figure 2.10. We merged data from all recordings in our possession; one point is plotted for each pair of ventral roots between which a phase lag was calculated. We deemed important to calculate standard deviations on individual pairs of ventral roots, rather than lumping together all phase lags from the same preparation: As presented in the previous section, phase lags from the same preparation can show systematic differences depending on the electrode position, an effect we wanted to exclude from the analysis of cycle to cycle variations.

Cycle to cycle standard deviations are rather high (between 0% and 15%), compared to the standard deviations along the spinal cord (below 3%, see section 2.4.1).

Note that high standard deviations don't necessarily amount to high noise levels: there can be consistent phase lag changes (i.e. the switches described in section 2.4.2) that would lead to high standard deviations. Another factor is illustrated in figure 2.9 (left): in that case, recordings from ventral roots 6 and 10 gave a median intersegmental phase lag of 10.3%. This means an effective phase lag (between the electrodes) of  $4 \times 10.3 = 41.2\%$ . Due to fluctuations, the



cycle to cycle value might get slightly over 50%. In that case, it would be detected as a negative phase lag (e.g. a lag of 52% would be detected as -48%), leading to very big standard deviations. This explains the points at the bottom of figure 2.9 (left).

To exclude these effects, we tried restricting the analysis to data with four ipsilateral ventral roots, where switches happen to be rare, and electrodes are close enough to avoid confusions between positive and negative phase lags. We found the same range of standard deviations (data not shown), suggesting that cycle to cycle variations are indeed greater than variations along the spinal cord.

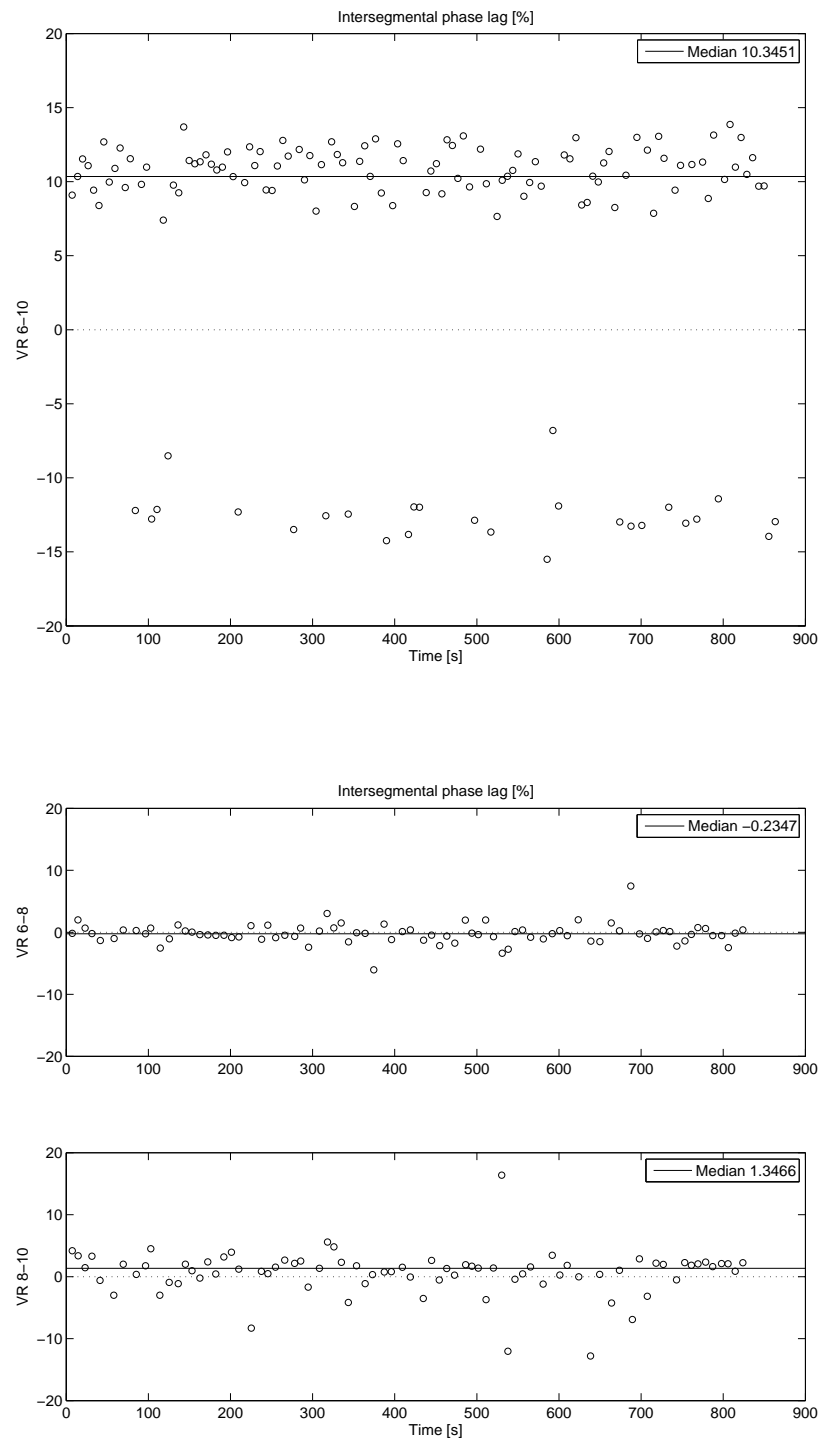


Figure 2.9 – Intersegmental phase lag time series for two long recordings, showing noise but no drift.

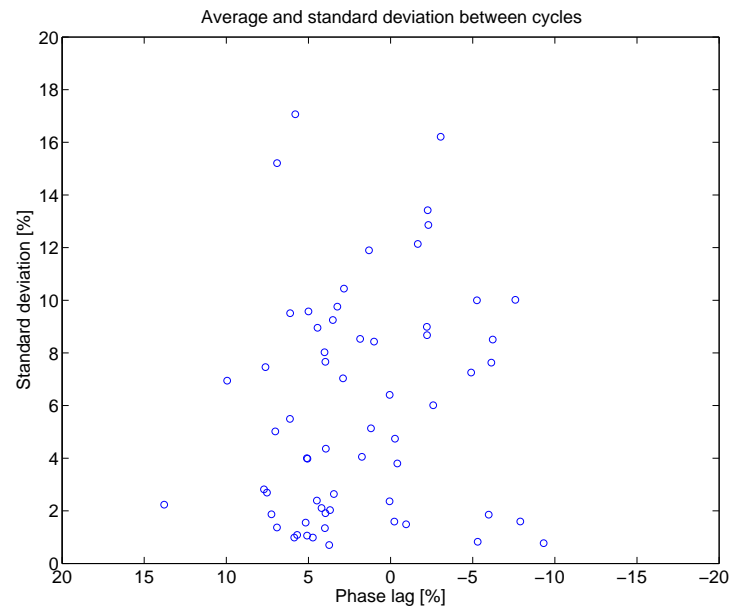


Figure 2.10 – Standard deviation of intersegmental phase lag timeseries. Phase lags calculated from each pair of ventral roots were treated independently (see text for details).

### 2.4.2 Rhythm Switches

An important feature of biological data is that they show spontaneous switches between different phase lag values. Most of the switches share the following characteristics:

- Sign switch: phase lags switch between positive and negative values.
- Correlated period: cycles with positive lags are significantly faster than cycles with negative lag.
- Memory: when switching back, the spinal network recovers the original cycle period and intersegmental phase lag.

We illustrate these points with one nice example in figure 2.11.

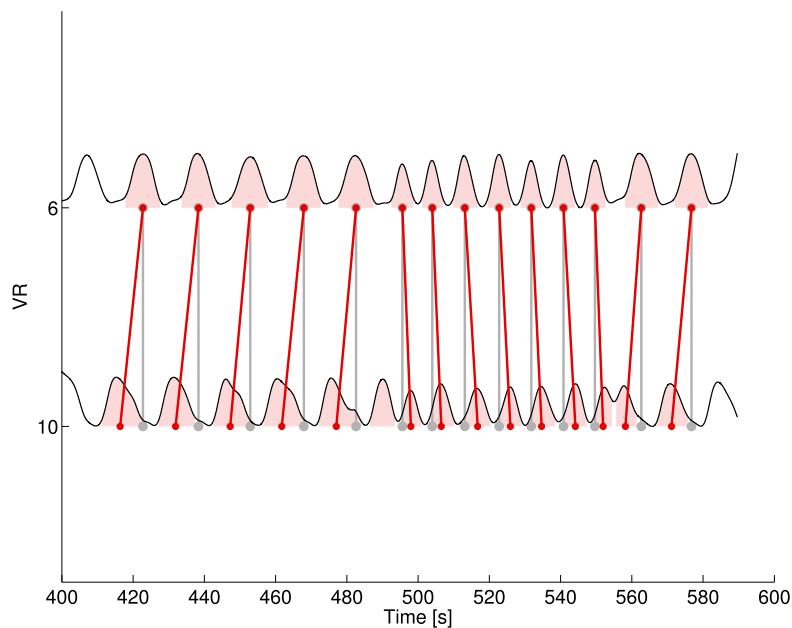


Figure 2.11 – Activity pattern during a back-and-forth switch between negative and positive phase lags. The rhythm accelerates as the lag becomes positive. The network then switches back to the original lag and period.

The cycle to cycle periods, phase lags and duty cycles<sup>5</sup> are shown in figures 2.12, 2.13 and 2.14 respectively. We see a clear correlation between phase lag and period, and the recovery of original values after the back-switch. Interestingly, the duty cycle is virtually not affected by the switch.

---

5. The width of the burst as a percentage of the cycle duration.

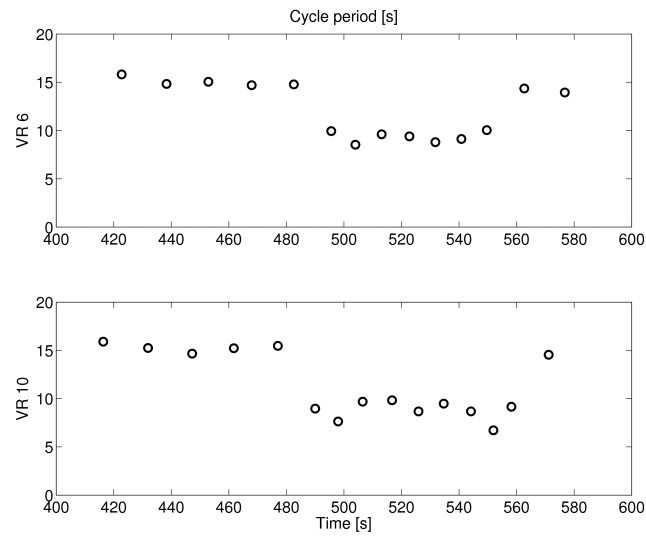


Figure 2.12 – Cycle to cycle periods during the phase lag switch of figure 2.11. Following the second switch, the rhythm returns to its original cycle period.

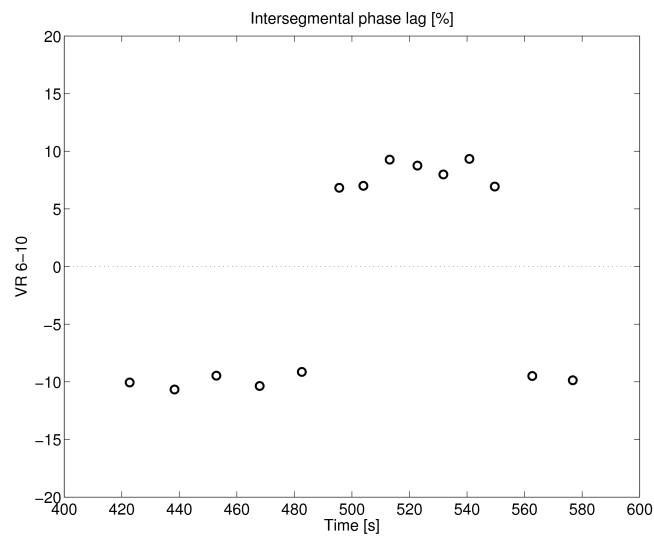


Figure 2.13 – Intersegmental phase lags during the phase lag switch of figure 2.11. Following the second switch, the rhythm returns to its original phase lag.

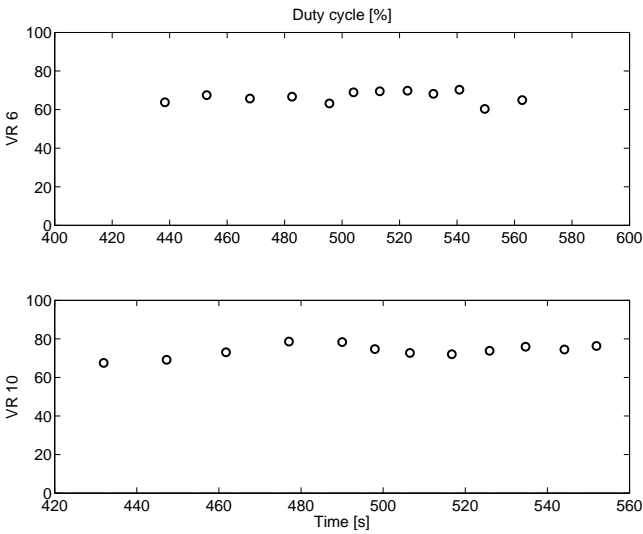


Figure 2.14 – Duty cycles during the phase lag switch of figure 2.11. The duty cycle is almost not affected by the switch.

### 2.4.3 Phase Lag and Frequency

We mentioned in the previous section that there is a strong correlation between phase lag and frequency during spontaneous switches: negative lags are associated with slow rhythms. But is this effect limited to slow and fast rhythms in a given preparation, or is there a more general correlation between phase lag and frequency? We analyzed this effect in a more general context using the recordings in our possession that include four ipsilateral ventral roots. These recordings were chosen primarily because they allow us to calculate the average phase lag based on three values covering most of the mid-trunk. They also have the advantage of showing few lag switches. The median period and phase lag was calculated for each ventral root. Averages and standard deviations were calculated by pooling the medians of the different ventral roots.

Results are shown in figure 2.15 (top). It appears that in these data, the period is a monotonous function of the phase lag. The trend is very clear, but there are few data points (eight). We show the same plot using all data in our possession (i.e. including preparations with less than four ipsilateral recordings) in the bottom panel. The trend is much less clear.

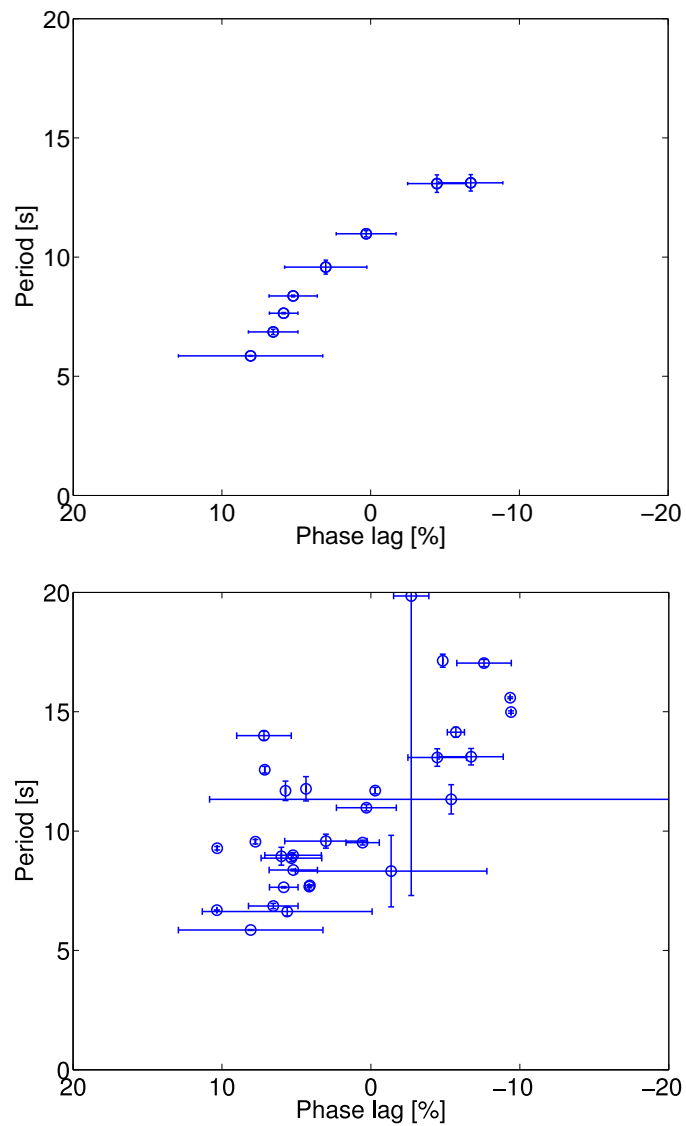


Figure 2.15 – Period as a function of intersegmental phase lag. **Top:** Using recordings with four ipsilateral ventral roots. **Bottom:** Using all available recordings. In both plots, error bars show the variability between ventral roots.



## 3 State of the Art

We give here an overview of past studies that are relevant to the modeling of gait generation and gait transitions in salamanders. We begin with a summary of the models of the lamprey swimming circuitry and body mechanics, which were often used as a source of inspiration for salamander models. We then review previous research on CPG and mechanical models of the salamander. In the last section, we briefly mention related work from robotics.

### 3.1 Lamprey Models

Due in part to its simplicity, the lamprey spinal circuitry has been studied extensively [Buchanan and Grillner, 1987, Grillner et al., 1988, 1991, 1995], giving rise to numerous models of the swimming CPG. These models can be classified according to their level of abstraction. At the lowest level, biophysical models use relatively realistic (e.g. multi-compartment Hodgkin-Huxley) neuron models. Such models can be used to validate our understanding of the physiological processes involved in rhythm generation [Ekeberg et al., 1991, Wallén et al., 1992, Huss et al., 2007, Kozlov et al., 2009]. At an intermediate level, connectionist models use less realistic neuron models such as leaky integrators, abstracting the complexity of internal neuron dynamics to focus on the interneuronal connectivity and how it can account in itself for the generation of different patterns of oscillations [Buchanan, 1992, Williams, 1992, Ekeberg, 1993]. At the highest, most abstract level, the CPG is modeled as a chain of mathematical oscillators, where each oscillator typically represents a whole population of biological neurons grouped in an oscillatory unit. These models are used to investigate very general properties of the network without relying on the details of the biological implementation. Such network properties include the possible dominance of rostrocaudal coupling over caudorostral coupling (or vice versa), and the kind of network structure capable of producing a constant intersegmental phase lag independently of the frequency of oscillations [Kopell, 1995, Williams and Sigvardt, 1995]. These models can also be used to investigate the interactions between the CPG, sensory feedback and descending signals from the brain.

The work of Ekeberg [1993] is notable for combining the neural and musculoskeletal aspects

of locomotion in simulations of the swimming lamprey. Local proprioceptive feedback from axial stretch receptors was present in this study but its effect was not specifically investigated. The role of sensory feedback was addressed in a later study [Ekeberg et al., 1995]. It was found that feedback from the stretch receptors had no significant effect on a normal swimming pattern, but that it had a stiffening effect on the body that could be useful in overcoming perturbations such as when swimming through a region of water with current flowing in the opposite direction. In this case, sensory feedback would help prevent bending of the body, which in absence of feedback causes the animal to turn away from the current barrier. This model of the neural circuits, muscles and stretch receptors was an important source of inspiration for subsequent modeling work on the salamander, including ours.

An area that has been the subject of a lot of research is the relationship between muscle properties, the hydrodynamic forces and the timing between muscle activation and body curvature in fishes. It appears that in most species, the wave of muscle activation travels faster from the head to the tail than the wave of body contraction [Wardle et al., 1995]. This conclusion has been cast into doubt for relying on the assumption that curvature is proportional to deflection from the center line [Katz and Shadwick, 1998], but there is ample evidence in various species, and based on different techniques, that the effect is real [Altringham and Ellerby, 1999].

The phenomenon is documented in the lamprey [Williams et al., 1989] and the salamander [Blight, 1977, Frolich and Biewener, 1992, D'Août et al., 1996]: the delay between muscle activity and body bending gets larger towards the tail. This change of timing along the body has been assimilated to a change of muscle function [Altringham et al., 1993]. The muscle generates positive work when it is activated during the contraction phase, as is the case in the rostral part of the body. It would generate negative work when activated during the stretching phase, which can occur in the caudal part. In that case, the resistance of muscles to stretch helps in transmitting caudally the power generated in the trunk. Altringham et al. [1993] also propose that the larger EMG-kinematic lag in the caudal part optimizes force generation in those muscles.

The observation of an increasing EMG-kinematic lag in many species has triggered a lot of modeling effort to understand its cause and purpose, if any. In a recent study, McMillen et al. [2008] have shown the equivalence of a joint-link model of the lamprey body with passive stiffness and damping and an active torque generated by a muscle model, to a discretized viscoelastic rod with preferred curvature determined by the output of the muscle model. Using the discretized rod, a Hill-type muscle model [McMahon, 1984], and the Taylor model for hydrodynamics [Taylor, 1952], they find that the speed difference between EMG and mechanical waves requires body taper<sup>1</sup> and passive viscoelasticity.

In related work, Tytell et al. [2010] use a 2D Navier-Stokes model for the hydrodynamics, and a simple muscle model based on linear springs that do not resist compression, with an active force term taken directly from the muscle activation dynamics (without velocity or

---

1. I.e. that the body gets thinner towards the tail. But the important point is that the muscles get weaker.

length dependence). No damping is included besides that from water. The muscle model is attached to a mechanical structure that includes normal springs along the notochord<sup>2</sup> as well as perpendicularly to the notochord to connect to the muscles. They find that the speed difference between EMG and mechanical waves during swimming appears when muscles generate low forces relatively to fluid forces. The article highlights the importance of having a good hydrodynamic model. The results obtained with the 2D Navier-Stokes model are in agreement with Lighthill's theory [Lighthill, 1971] and suggest that Taylor's model gives wrong phase relationships between muscle activation and body contraction. However the authors warn that the very good agreement with Lighthill's theory might be an artifact of using a two-dimensional Navier-Stokes model, where vortices can only be shed at the tail tip and not along the dorsal and ventral surfaces. We address the question of the EMG-kinematic lag during salamander swimming in chapter 5. By validating our simulation results with swimming experiments using a real robot, we show that our results do not depend on hydrodynamic simulation artifacts.

### 3.2 Salamander Models

We know of six modeling studies concerning the neural circuits involved in the generation of various gaits of the salamander, and one involved in the neurophysiological details of rhythm generation.

In Ermentrout and Kopell [1994], a chain of phase oscillators was used as an abstract model of a vertebrate's CPG. The ability of the chain to produce stable traveling waves and S-shaped standing waves was investigated analytically and numerically. Nearest-neighbor couplings, designed to induce synchrony, were supplemented by two kinds of long-range couplings: inward coupling from the extremities to the middle of the chain, and outward coupling from the middle to the extremities. Both inward and outward couplings were designed to induce antiphase between the parts that they connected. Their strengths determined the stable patterns of oscillations, which included synchrony, traveling waves, S-shaped standing waves, and anti-waves (two waves traveling in opposite directions in different parts of the chord). The ranges of strengths allowing for stable traveling waves and stable standing waves did not overlap. In other words, traveling and standing waves could be generated with the same network connectivity, but with different coupling strengths. The other models presented next explored other, more realistic possibilities to explain the transitions between traveling and standing waves, in particular without the need for the specific long-range couplings and without the need for changing coupling strengths between modes of locomotion.

In Ijspeert [2001], a connectionist model of the salamander CPG was developed based on leaky integrator neurons. The network was inspired by a model of the lamprey CPG [Ekeberg, 1993], with the major addition of limb centers, represented by two additional segments: one

---

2. Although classified as a vertebrate, the lamprey does not develop vertebrae. It retains instead the embryonic *notochord*, a flexible rod-shaped body, into adulthood.

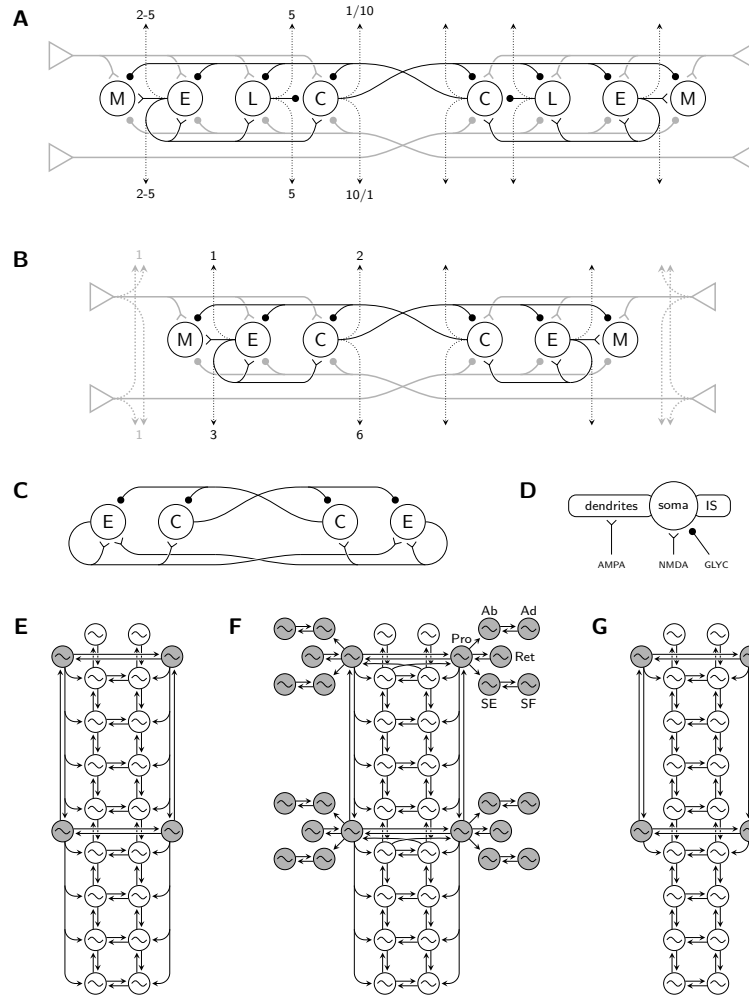


**Figure 3.1 – Models of the salamander spinal circuitry for locomotion.** **A** Segmental network in Bem et al. [2003]. Four populations of leaky integrator neurons are present in the left and right side of the spinal cord: motoneurons (M), excitatory interneurons (E), inhibitory interneurons projecting ipsilaterally (L) and inhibitory interneurons projecting contralaterally (C). Stretch-sensitive edge cells (gray triangles) send excitatory connections to ipsilateral populations and inhibitory connections to contralateral populations. The E and L populations have axons extending ipsilaterally to 2-5 and 5 segments respectively, in both directions. The C population has axons extending to 1 segment rostrally and 10 segments caudally; these extents were reversed in the rostral part of the spinal cord to reproduce EMG recordings of the walking trot. **B** Segmental network in Harischandra et al. [2011], also based on leaky integrator neurons. Both E and C populations have axons extending longer in the caudal direction. **C** Segmental network in Bicanski et al. [2011]. The E populations also project to the contralateral E population. **D** The model in Bicanski et al. [2011] uses Hodgkin-Huxley neurons made of three compartments: the axon's initial segment (IS), the soma that receives NMDA and glycynergic synapses, and the dendrites that receive AMPA synapses. **E** A CPG network with global coupling between limb and axial oscillators, as used in Ijspeert et al. [2005] and Ijspeert et al. [2007]. Axial and limb oscillators are represented in white and gray respectively. The Ijspeert et al. [2005] model has 40 segments while Ijspeert et al. [2007] has 8. **F** A CPG network with global ipsilateral limb->body coupling and local contralateral body->limb coupling, as used in Harischandra et al. [2011]. Each limb is modelled with separate oscillators for the abductor (Ab), adductor (Ad), protractor (Pro), retractor (Ret), knee extensor (KE) and knee flexor (KF) muscles. The model includes 40 segments but only 9 are shown. **G** A CPG network with local coupling between limb and axial oscillators, as used in Ijspeert et al. [2005]. This model includes 40 segments but only 9 are shown.

for the forelimbs and one for the hindlimbs. The segmental network was modeled using six inhibitory interneurons. The range of intersegmental connections was limited to five segments. Forelimbs and hindlimbs projected to all the trunk and tail segments, respectively. A genetic algorithm was used to adjust the synaptic weights of the intrasegmental, intersegmental, and limb-body connections. Standing waves were generated by the network when a tonic excitatory drive was applied to both body and limb oscillators. Traveling waves were released by suppressing the drive to the limb segments.<sup>3</sup> This work therefore served as a proof of concept that a lamprey-like network could be extended with limb CPGs to produce both swimming and walking gaits.

Another study by Bem et al. [2003] focused on reproducing the complexity of the salamander EMG patterns (described in section 2.2) in a model of the lamprey CPG [Ekeberg, 1993]. The connectivity of the model is shown in figure 3.1A. The generation of the walking pattern, with double-bursting in the neck and tail regions, required the reversal of the intersegmental inhibitory connections in the rostral part of the network, as well as an increase of the tonic drive at the girdles and a phasic drive outside the girdle regions. Generation of the swimming pattern also required drive adjustments. Because of its modified connectivity, the rostral part of the network generated a caudorostral wave under uniform tonic excitation. This was compensated for by increasing the tonic drive in the rostral part of the network. Additional increases in regions slightly caudal to the girdles were able to reproduce the discontinuities in the salamander swimming pattern. The same effect could be achieved by suppressing the sensory feedback in the girdle regions.

In Ijspeert et al. [2005], a neuromechanical simulation was used to explore more systematically different potential body-limb CPGs configurations underlying salamander locomotion. In particular, local and global connectivity patterns between the limb and body CPGs were compared. In configurations with local connectivity, the limb oscillators are connected only to the nearest segments of the body (figure 3.1F). With the global connectivity, forelimb oscillators are connected to all trunk oscillators, and hindlimb oscillators to all tail oscillators (figure 3.1D). Inhibitory connections were used between limb oscillators, and between the left and right oscillator of the same segment, in order to induce antiphase behavior. Excitatory connections were used between limb and body oscillators to induce in-phase behavior. Ascending and descending connections were both excitatory and inhibitory, which allowed for arbitrary phase relationships. The simulation results showed that, in the absence of sensory feedback, only the configurations with global coupling can produce standing waves as observed during walking. Local coupling configurations always resulted in traveling waves in the CPG output. However, using these traveling waves as the control signal for the mechanical simulation on the ground still resulted in quasi-standing waves of body undulation. This was attributed to the environment interaction forces on the ground, which differ from interaction forces in water. The addition of sensory feedback then entrained the CPG itself to standing wave-like patterns of oscillations. The discontinuities observed in the rostrocaudal phase lags during

---

3. An inhibitory drive to the limb segments was actually used to prevent slow oscillation in the limb networks

swimming could also be reproduced by making the intersegmental coupling stronger in the rostral direction and setting the girdle segments to slightly lower intrinsic frequencies.

In a subsequent study [Ijspeert et al., 2007], the mechanisms of automatic transitions between swimming and walking were investigated. A network of amplitude-controlled phase oscillators was used, with global connections from limb to body oscillators, and bidirectional connections between nondiagonal limbs (figure 3.1D). This work sought to reproduce the MLR stimulation experiments described in section 2.3, where a switch from low-frequency stepping to high-frequency swimming could be induced by increasing the intensity of the electrical stimulation in the MLR. This was achieved through the introduction of two hypotheses. First, that limb oscillators saturate at high frequencies: They stop oscillating at high levels of stimulation. Second, that for the same level of stimulation, limb oscillators have lower intrinsic frequencies than the body oscillators. Numerical simulations showed that the first hypothesis provides a mechanism for the automatic transition between walking and swimming similar to that observed in MLR stimulation experiments. It also explains why walking frequencies are always lower than swimming frequencies, as shown by kinematic recordings [Frolich and Biewener, 1992]. The second hypothesis explains the rapid increase of frequencies observed when the salamander switches from walking to swimming: During walking, the lower frequency of the limb oscillators slows down the rhythm of the body CPG. When the limb oscillators saturate, the body oscillators suddenly become free to oscillate at their higher intrinsic frequency. This mechanism also explains a gap observed between the walking and swimming frequencies. The second hypothesis was verified *in vitro*: The mid-trunk and limb segments were isolated by transections of the spinal cord, and an identical tonic drive applied pharmacologically to all parts resulted in slower rhythms in the limb segments than in the mid-trunk (see supplementary material in Ijspeert et al. [2007]). In the present thesis, we sought to extend this model to account for the diversity of motor patterns observed *in vitro* and *in vivo*, while retaining the achievements of this study.

This CPG model was tested on *Salamandra robotica*, an amphibious salamander robot capable of swimming and walking and the precursor to the robot used in this thesis. The robot was used to demonstrate that the CPG model can generate forward locomotion with variable speed and heading, as this requires a mechanical body and cannot be studied at the neuronal level alone. The robot also allowed for the quantitative comparison of the gaits generated by the model to the gaits of the animal.

Recently, Harischandra et al. [2010] developed a 3D musculo-mechanical model of the salamander *Pleurodeles waltl*, made of 15 axial segments and three degrees of freedom per leg. The muscle model is a small variation of the linear spring-damper model with variable stiffness used by Ekeberg [1993], that we use in the present work. The model was used to reproduce a walking gait with traveling wave in the trunk, and a walking trot gait with standing wave in the trunk, using predefined muscle activation patterns. The relative role of the trunk and legs in turning was explored. It was found that side-stepping with the legs without trunk-bending was the most efficient for turning in the walking gait, while a combination of side-stepping

and trunk-bending was more efficient during trotting. Trunk bending without side stepping always performed the worst. In a later study [Harischandra et al., 2011], the same model was driven with a spiking neuron-based CPG derived and simplified from the lamprey model of Kozlov et al. [2009]. The axial connectivity of the model is represented in 3.1B. The segmental model is also used for each of the three flexor-extensor or retractor-protractor pairs in each limb, with the E neuron on the flexor or retractor side receiving additional tonic excitation. The connectivity between limb networks and between limb and axial networks is represented in 3.1F. The CPG model coupled to the musculo-mechanical model was used to investigate the role of sensory feedback in generating walking, trotting, and the transitions between these gaits. Axial proprioceptive feedback from putative stretch-sensitive edge cells in the spinal cord was included, as well as excitatory feedback from limb stretch receptors most active at the end of the stance phase. It was found that the trotting gait could easily be generated centrally without sensory feedback, using the global coupling scheme from limb to axial networks as in Ijspeert et al. [2007]. On the other hand, the walking trot required a weakening of these connections to allow for a traveling wave in the trunk. It also required the addition of excitatory feedback to the limb networks from limb and axial stretch receptors, in order for the retractor muscles to display the 75% duty cycle appropriate for walking. The study thus suggests that sensory feedback could play a significant role in the walk-trot gait transition.

Finally, one recent study investigated the neurophysiological mechanisms of rhythm generation specific to the salamander [Bicanski et al., 2011]. This is the most detailed model of the salamander locomotor circuits to date, but it is restricted to the simulation of one segment. The model is built on Hodgkin-Huxley neurons each comprising 3 compartments (figure 3.1D) with up to 7 ionic channels. It is based on a lamprey model [Wallén et al., 1992] but includes some unique features, such as the excitatory connections between the left and right hemisegments (figure 3.1C). The model reproduces rhythmic bursting by simulated NMDA excitation, as well as the behavior of *in vitro* preparations subject to a variety of pharmacological conditions.

### 3.3 Related Work in Robotics

For completeness, we briefly present here other efforts to build salamander robots, and to integrate sensory feedback in robot locomotion in general.

The GEO robot (Lewis [1996], figure 3.2, top right) implements a sprawling posture and includes a single-link flexible spine. The robot was designed for stepping on land only, and was controlled with an abstract CPG model that matched its kinematic structure, such that there was no notion of intersegmental coordination. The Robo-Salamander prototype from Breithaupt et al. [2002] (figure 3.2, bottom right) shows a similar kinematic structure. It was driven by a minimal neural controller evolved using a genetic algorithm to solve a simple walk-to-target task. It is also restricted to land locomotion.

The Chigon robot (Yin et al. [2012], figure 3.2, top left) is a recent amphibious salamander

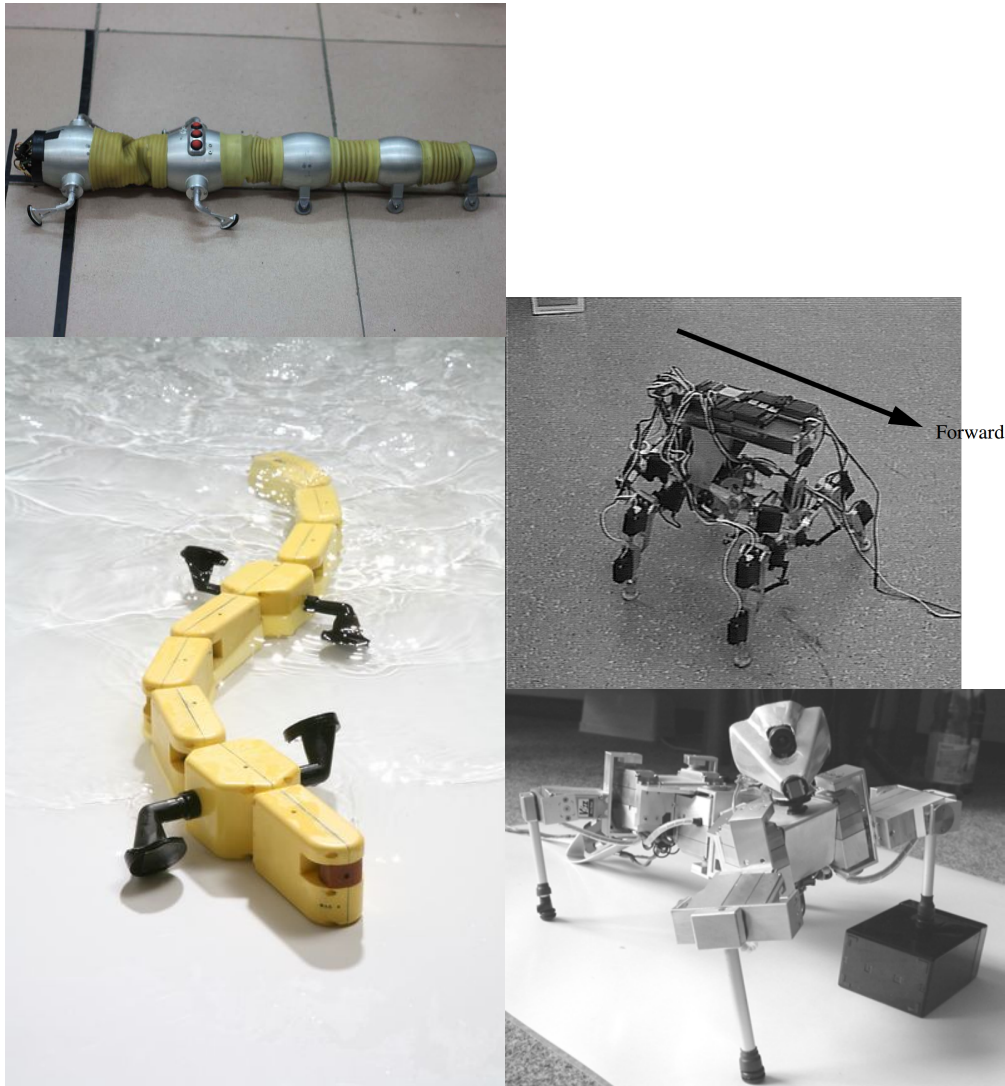


Figure 3.2 – Pictures of previously published salamander robots. **Top left:** Chigon [Yin et al., 2012]. **Bottom left:** Salamandra robotica [Ijspeert et al., 2007]. **Top right:** GEO [Lewis, 1996]. **Bottom right:** Robot-Salamander [Breithaupt et al., 2002].



robot that includes one joint in the trunk and three joints in the tail. It is driven by a sine controller.

The Salamandra robotica robot of Ijspeert et al. [2007] (figure 3.2, bottom left) was the first amphibious salamander robot, and with its successor the Salamandra robotica II, it is still the only amphibious salamander robot with several axial joints in the trunk. This characteristic is important for our work, as we are particularly interested in the coordination of muscles at different levels of the trunk during various aquatic and terrestrial behaviors. For the present work we used Salamandra robotica II, which is described in detail in chapter 7.

Proprioceptive sensory feedback for locomotion in robotics has mostly been used in erect-posture quadrupeds [Kimura et al., 1999, Fukuoka et al., 2003] and in bipeds [Taga et al., 1991, Taga, 1998], where it contributes to the stability of locomotion. A notable exception is the work of Umedachi et al. [2010], who developed a methodology for incorporating local sensory feedback in a distributed controller, based on the *discrepancy function*. In this framework, a deviation between the control signal and the robot motion is fed back to the oscillator-based controller. The form of the feedback term is derived mathematically to act on the phase of the oscillator in a way that reduces the discrepancy between the control signal and the state of the mechanical system. Kano et al. [2010] have applied this methodology to the control of a compliant snake robot moving on ground with variable friction and up a slope. They found that sensory feedback helped in stabilizing the direction of motion and in decreasing the energy consumption.

Also relevant is the work of Aoi et al. [2011], where numerical simulations were used to study sensory feedback-induced gait transitions in a quadruped body driven by coupled phase oscillators. The mechanical model was composed of a front body and a back body connected by a torsional spring-damper system. Each limb was governed by one oscillator and received feedback from a tactile sensor which triggered a resetting of the phase in the oscillator. The couplings between oscillators were such that an antiphase relationship was enforced between the left and right limbs in each body (front and back). The coupling strengths between bodies however were left to zero. It was found that the model could transition from a trotting to a walking gait by increasing the stiffness of the torsional joint.

### 3.4 Outstanding issues

The model of the salamander spinal cord published in Ijspeert et al. [2007], our starting point, was successful in reproducing important features of salamander locomotion, including the generation of traveling waves for swimming and standing waves for stepping, and a mechanism of transition between these gaits similar to that observed in MLR stimulation experiments. However, the model does not reproduce recent experimental data from recordings *in vitro* and *in vivo* that show a high flexibility in the spinal network. It also does not address the role of sensory feedback, the dynamics of muscles and how they interact with the environment. Finally, the mechanisms of selection and transition between behaviors

remains to be explored in the context of a larger repertoire that includes underwater stepping, backward stepping and struggling.

### 3.4.1 A More Flexible Network

In the model of Ijspeert et al. [2007], the formation of standing waves and the gap in frequencies between swimming and stepping are due to the influence of the limb centers on the axial (trunk and tail) centers. In particular, the extensive connections from limb to axial centers, where each forelimb oscillator connects to all the ipsilateral trunk oscillators, mean that limb activity is inseparable from standing waves in the trunk. The axial network is also rather rigid in this model: When limbs are inactive, the CPG produces an intersegmental phase lag of exactly 12.5% (corresponding to a phase lag of 2.5% in the animal<sup>4</sup>).

Recent *in vitro* preparations show a great diversity of phase lags between individuals, with values distributed between -13% and 12% per spinal segment (see section 2.4). This is what we will refer to as the *open-loop* range of intersegmental phase lags. Similarly, recent electromyographic data from swimming, underwater stepping, forward land stepping, backward stepping and struggling salamanders have shown that the intact animal uses different intersegmental phase lags for different behaviors, in a range of roughly -5% to 5% (see section 2.2). This is what we call the *closed-loop* range of phase lags.

The biological data suggest that connections from the limb centers to the axial centers force the frequency but not the phase of trunk and tail oscillators. In terms of couplings, this suggests a strong local coupling of the limbs to only a few oscillators of the trunk and the tail, resulting in the frequency locking of axial oscillators at the girdles, which would entrain other oscillators in the trunk and the tail without restricting the formation of traveling waves.

The design of a flexible CPG network is addressed in chapter 4.

### 3.4.2 The Mechanisms of Regulation

A diversity of intersegmental phase lags is observed *in vitro* and *in vivo*. However the *in vivo* range is significantly smaller (-5% to 5% vs. -13% to 12%), and more importantly, the *in vivo* range represents the union of recordings from different behaviors that are each characterized by a specific phase lag (see section 2.2). For example, EMG recordings show that intact salamanders swim with a specific intersegmental phase lag of 2% to 2.5%.

In the model of Ijspeert et al. [2007], the phase lag is specified explicitly for each ascending and descending coupling. In the absence of limb activity, this intrinsic phase lag is directly reflected in the output of the CPG, and thus in the motor patterns. Generating a specific motor pattern from diverse intrinsic phase lags requires the addition of a mechanism to reduce this

---

4. The model of Ijspeert et al. [2007] includes only 8 segments while the animal has about 40. An intersegmental of 12.5% in the model therefore translates to a values five times smaller in the animal.

variability (i.e. to explain how a large variety of *in vitro* patterns are transformed into more stereotyped *in vivo* patterns).

We show in chapter 5 how a flexible network can be regulated by simple drive signals from the brain and sensory feedback to generate five different behaviors. The role of sensory feedback as a regulation mechanism is explored in more details in chapter 6.

Regarding the regulation by drive signals from the brain, the question remains as to how to properly adjust the drive levels to generate the desired behavior. It is also not clear how these drive levels will interact with sensory feedback in shaping the activity of the CPG.

#### 3.4.3 The Role of the Body Viscoelastic Properties

Another point missing from the model of Ijspeert et al. [2007] is the role of the mechanical properties of muscles and how their interaction with the environment affects the motion of the joints. This is interesting on its own as a part of the locomotion control architecture, but it is also crucial to the modeling of the closed-loop system, where the activity of the CPG is shaped by feedback signals calculated for example from the joint positions.

In chapter 5, we introduce a mechanical model of the salamander that includes virtual muscles, and show what modifications to the muscle parameters are necessary to reproduce different behaviors. The EMG-mechanical delay, which is due to the muscle dynamics, plays an important role in the closed-loop system during swimming. This is further analyzed in chapter 6.

Finally, in chapter 7, we present a distributed robot controller that implements the virtual muscles locally in each robot module, allowing for reduced communications and smaller time-steps.



## 4 Flexible Models of the Isolated CPG

This chapter presents different approaches to the modeling of a flexible salamander CPG network based on coupled abstract oscillators. By flexible, we mean that the network can easily be made to generate arbitrary patterns, i.e. arbitrary intersegmental phase lags and cycle frequencies, in a range that corresponds to recent observations in the animal. The notion of controllability<sup>1</sup> is therefore essential. However we will also strive to design networks that spontaneously generate a variety of patterns, in order to reproduce the diversity observed *in vitro* (see section 2.3). Note that such a network only makes controllability more important.

Regarding the variability of phase lags observed during *in vitro* experiments, we should note that the nature of the excitation could contribute to the variability of the fictive locomotor patterns. Most of the data collected with salamander *in vitro* preparations use NMDA to excite the spinal network (see section 1.1). In the lamprey spinal cord, NMDA-induced rhythms show a variability of phase lags [Matsushima and Grillner, 1992], whereas D-glutamate-induced patterns are very close to EMG patterns recorded on intact lampreys [Wallen and Williams, 1984]. Unfortunately, there is no published evidence of a successful use of D-glutamate to induce fictive swimming in the salamander spinal cord (see Lavrov and Cheng [2004] for D-glutamate-induced limb activity). The extreme phase lags observed *in vitro* might thus be an artifact of NMDA excitation; it would be interesting to see if they can be reproduced using other sources of excitation (e.g. D-glutamate or MLR stimulation). Nevertheless, we chose to aim for models that can reproduce the whole range of phase lags observed with NMDA excitation.

### 4.1 Features Required of the Model

We want our isolated CPG model to reproduce the diversity of phase lags observed *in vitro* (2.3), possibly with a similar distribution. In accordance with the findings in our analysis in

---

1. Controllability has different meanings in different contexts. Here, by controllability we mean the ease with which the activity pattern of the network can be controlled by external inputs such as descending commands from the brainstem.

section 2.4, the phase lags produced by our model should be stable in time and reasonably uniform along the cord. The model should account for the correlation observed between phase lags and frequencies. Ideally, it should also reproduce the spontaneous switches observed in the isolated spinal cord between slow rhythms with negative lags and fast rhythms with positive lags (2.4.2).

Finally, since the variety of patterns observed *in vitro* is reflected in the behaviors of the animal *in vivo*, another concern is to which extent this diversity can be managed e.g. by higher centers in the brainstem, to select a pattern depending on the desired behavior. For example, the model of Ijspeert et al. [2007] allows for the transition between swimming and walking by modulating a single drive signal from the brainstem.

In a first stage, we will consider the axial network in isolation. Once we have a model of the axial network that fits the requirements described above, we will add limb oscillators and look at how they interact with the axial network.

## 4.2 Difficulties with a Previous Model

In the model of Ijspeert et al. [2007], the strong global coupling from limb to axial oscillators imposes a standing wave on the trunk and tail whenever the limbs are rhythmically active. An obvious first step is to revert to a local coupling scheme such as in figure 3.1G. However we will show here that even when relaxing this constraint by considering the isolated axial network, the model is ill-suited to the production of diverse activity patterns.

### 4.2.1 General Approach

A straightforward solution to the problem of generating a diversity of phase lags with the isolated CPG model is to encode this diversity explicitly in the model, by choosing randomly a value for the intersegmental phase bias in successive simulations. In this way it would be trivial to achieve any desired distribution of phase lags. However, such a solution would provide no insight into the mechanisms of intersegmental coordination. More importantly, it provides no mechanism for the brainstem to select a particular pattern, and it clashes directly with the observed correlation between phase lag and cycle frequency. Instead, we will mainly investigate models where the diversity of phase lags is coupled to a diversity of frequencies. This should also help reproducing the spontaneous switches in phase lags and frequencies.

Below, we show various attempts at generating a diversity of phase lags based on the introduction of a random factor in the intrinsic frequencies of the oscillators, which could correspond to some variability in the biological oscillatory neuronal pools. The model used is a variation

of that in Ijspeert et al. [2007], using the following oscillator equations:

$$\begin{aligned}\dot{r}_i &= a(R_i - r_i) \\ \dot{\theta}_i &= 2\pi\nu_i + \sum_{j=1}^N w_{ij}r_j \sin(\theta_j - \theta_i - \phi_{ij}) \\ x_i &= r_i \cos\theta_i\end{aligned}\tag{4.1}$$

with  $r_i$  the oscillator amplitude of oscillator  $i$ ,  $\theta_i$  the phase,  $a$  a gain for the convergence of the amplitude,  $R_i$  the target amplitude,  $\nu_i$  the intrinsic frequency,  $w_{ij}$  and  $\phi_{ij}$  the coupling weights and phase biases, and  $x_i$  the output of the oscillator.  $N$  is the number of oscillators.

In the model of Ijspeert et al. [2007], the oscillator output was  $x_i = r_i(1 + \cos\theta_i)$  (always positive), and the amplitude was controlled by a critically damped second-order differential equation:  $\ddot{r}_i = a\left(\frac{a}{4}(R_i - r_i) - \dot{r}_i\right)$ .

All the results described in the rest of this investigation are based on these equations, with the topology of a single chain of 8 oscillators ( $N = 8$ ), such as one side of the axial network in Ijspeert et al. [2007] (figure 3.1G). We will refer to this model as the *Original Hemicord* model. The hemicord topology was chosen for simplicity—all results apply to the double chain, with the caveat that random effects are attenuated in the double chain (since the two oscillators in each segment average-out the random effects to some extent) so that the amplitude of random processes must be increased in compensation. The gain  $a$  was set to 5 and the target amplitude  $R$  to 1. Due to the simple topology of the network, the only remaining parameters aside from the intrinsic frequencies are the coupling strengths  $w_{i,i+1} = w_{i+1,i} = 10$  between neighboring oscillators, and the phase biases  $\phi_{i,i+1} = -\phi_{i+1,i} = \phi$ . In the following, we will often refer to the wave number  $k$  instead of the phase bias  $\phi$ . It represents the number of waves visible at any time on the body. The two quantities are related by the equation  $k = \frac{N\phi}{2\pi}$ . We will also refer to the phase lag as a percentage, which is always a percentage of the whole cycle, so that  $100\% = 2\pi$ .

#### 4.2.2 Random Intrinsic Frequencies

The first approach we tried was to pick each intrinsic frequency  $\nu_i$  from a random distribution. We chose arbitrarily a flat distribution in the range of 0.5 to 1.5 Hz. An example pattern obtained with this network is shown in figure 4.1. We see important irregularities in the phase lag along the chain of oscillators.

The distribution of phase lags based on 50 simulations is shown in figure 4.2 (left), together with the lag–period plot. The distribution is a sharp peak centered on the nominal phase lag (12.5% for 8 segments with a wave number  $k = 1$ ). The period is almost not affected. The standard deviation is calculated between pairs of ventral roots (using the median value for each pair). It is close to the biological values of figure 2.8.

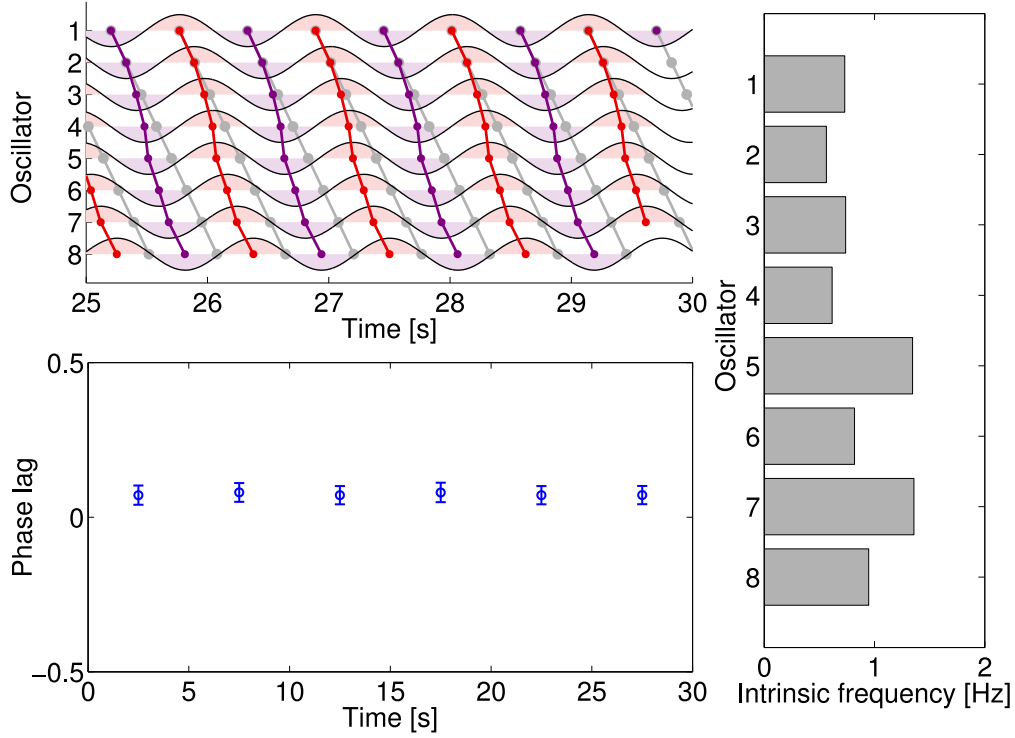


Figure 4.1 – **Top left:** One pattern obtained with the Original Hemicord model and random intrinsic frequencies in (0.5, 1.5) Hz, with intrinsic phase lags of 12.5% and coupling strengths  $w_{ij} = 10$ . Black lines represent the outputs of the oscillators. The centroids of the surfaces delimited by the positive and negative parts of the oscillation (light red and light purple respectively) are used to determine the phase of the oscillation twice per cycle (red and purple circular markers). The phase lags are represented graphically by connecting the markers between neighboring oscillators (red and purple lines). **Bottom left:** Phase lag average and standard deviation over 5 seconds windows, as a fraction of a cycle. **Right:** Intrinsic frequencies for each oscillator.

We corrected for the extreme phase bias by using a nominal phase lag of 0 instead of 12.5% (we could also have used a slightly positive lag). We were also able to obtain a range of phase lags of about -10% to 10%, either by halving the coupling strength, or by doubling the range of random frequencies. Further increases in frequencies or decreases in coupling strengths led to loss of synchronization or unstable rhythms. Results for 100 repetitions with decreased coupling strengths ( $w = 5$ ) are shown in figure 4.3.

The (-10%, 10%) range obtained is close to the biological range, but the inconsistencies (intersegmental variability) are very high, as can be seen from the errorbars. This variability is further illustrated in figure 4.4. Again, the phase lag is very irregular, with positive values in the first half of the chain and negative values in the second half. Tests with the addition of longer couplings up to the 5th nearest neighbors gave better phase lag consistency but in a reduced range (data not shown).



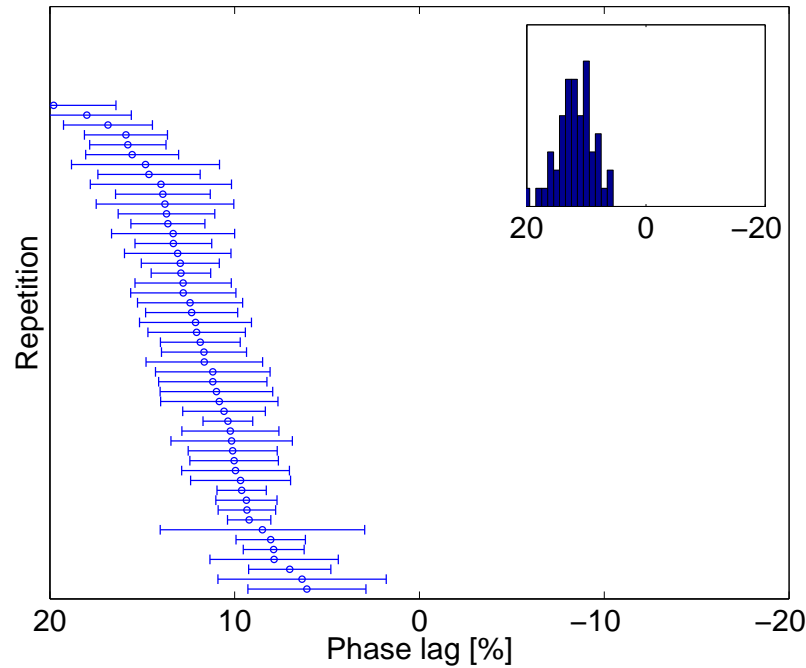


Figure 4.2 – Distribution of intersegmental phase lags in the Original Hemicord model with random intrinsic frequencies. Parameters as in figure 4.1.

### 4.2.3 Flexibility by Brainstem Input

It has been proposed early on [Matsushima and Grillner, 1992] that differences in the uncoupled (intrinsic) frequencies of the oscillators could be used to control the intersegmental phase lag from the brainstem, by provided different levels of excitation to different segments.

We tried modulating the frequency of the most rostral segment to control the phase lag along the spinal cord. We find stable patterns when multiplying the rostral frequency by a factor between 0.5 and 1.5. This allows for some control (up to half a cycle, i.e. a 7% average phase lag with 8 segments), but results in gradients of phase lags. This is illustrated in figure 4.5.

### 4.2.4 Random Walks on the Frequencies

Rather than setting each segment frequency to a random but fixed value, we tried applying damped random walks on these (now time varying) variables. A sample result is given in figure 4.6.

As can be seen, this model has drifting phase lags and frequencies, and thus cannot be controlled by a simple brainstem action on rostral segments. Given these limitations, and the stability of phase lags observed in the animal *in vitro*, we did not explore it further.

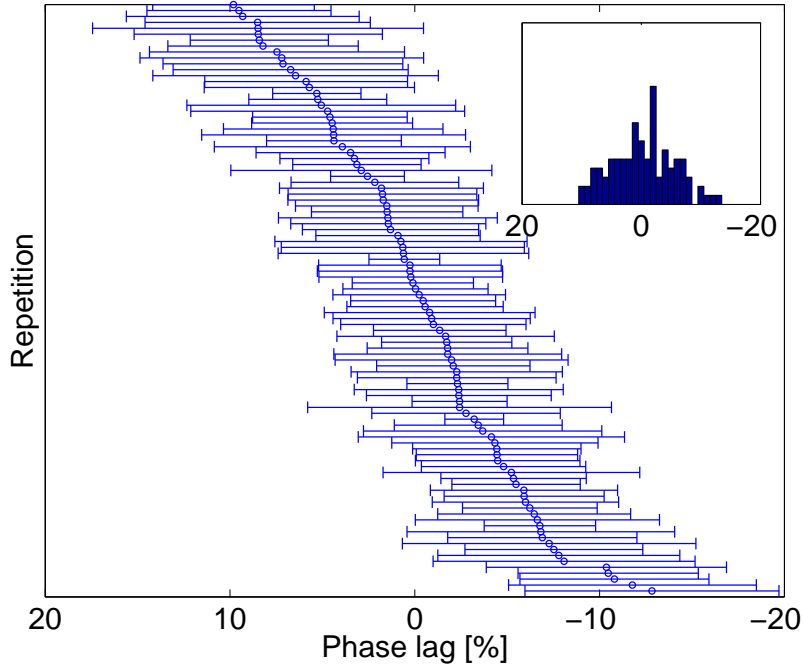


Figure 4.3 – Distribution of intersegmental phase lags in the Original Hemicord model with random intrinsic frequencies,  $w = 5$  and  $k = 0$  (i.e. nominal phase lag of 0).

#### 4.2.5 Conclusions on the Ijspeert et al. [2007] Model

Even in the absence of strong, extensive couplings from limb to axial oscillators, we were unable to generate a diversity of uniform phase lags based on the model from Ijspeert et al. [2007] by playing randomly with the intrinsic frequencies of the oscillators. The diversity of phase lags that we did obtain came at the expense of lag consistency. These results are consistent with the findings of Cohen et al. [1982], which concluded that a chain of oscillators with symmetric ascending and descending couplings requires a very specific adjustment to the intrinsic frequencies in order to maintain a uniform lag: the frequency of the oscillator at one boundary must be adjusted by an amount opposite to the adjustment at the other boundary. While this could be an option for controllability *in vivo*, it can hardly account for the diverse but uniform phase lags observed *in vitro*: no basis exists for such differential excitation in arbitrary portions of the spinal cord.

We note that it remains a possibility that this model with or without extensive couplings from limbs oscillators could generate a range of intersegmental phase lags through the action of sensory feedback. However this is not relevant to the reproduction of the *in vitro* observations.

Following these results, in the rest of this thesis, we investigated models that depart significantly from the model of Ijspeert et al. [2007].

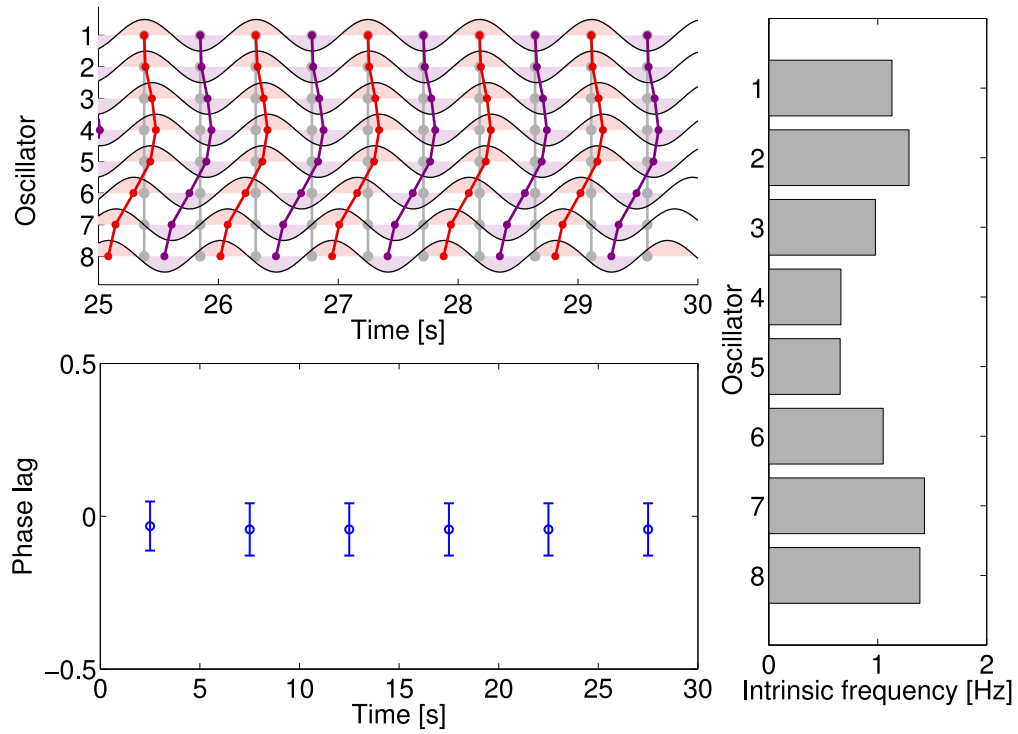


Figure 4.4 – Original Hemicord model with random intrinsic frequencies,  $w = 5$  and  $k = 0$ . See figure 4.1 for a general description. The lower intrinsic frequencies in oscillators 4 and 5 (right panel) lead to a positive phase lag in the first part of the chain (top panel). The relatively higher frequencies of oscillators 6–8 lead to a negative phase lag in the second half of the network. These irregularities of the phase lag along the chain are reflected in the high standard deviations in the bottom panel.

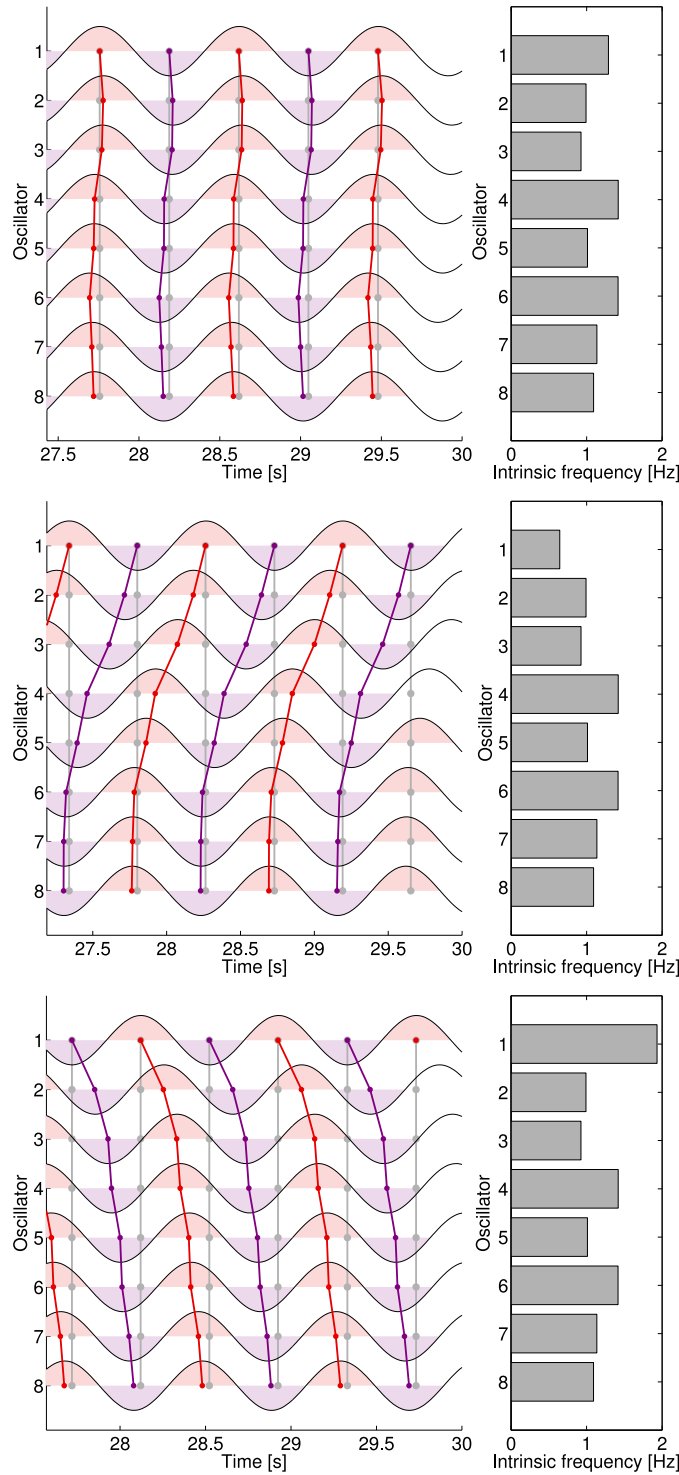


Figure 4.5 – Original Hemicord model with random intrinsic frequencies,  $w = 5$  and  $k = 0$ . **Top:** All oscillators drawing their frequency from the same distribution. **Middle:** Rostral frequency multiplied by 0.5. **Bottom:** Rostral frequency multiplied by 1.5. The different intrinsic frequency of the first oscillator has a strong effect on the phase lag. However this effect attenuates towards the end of the chain, leading to non-uniform phase lags.

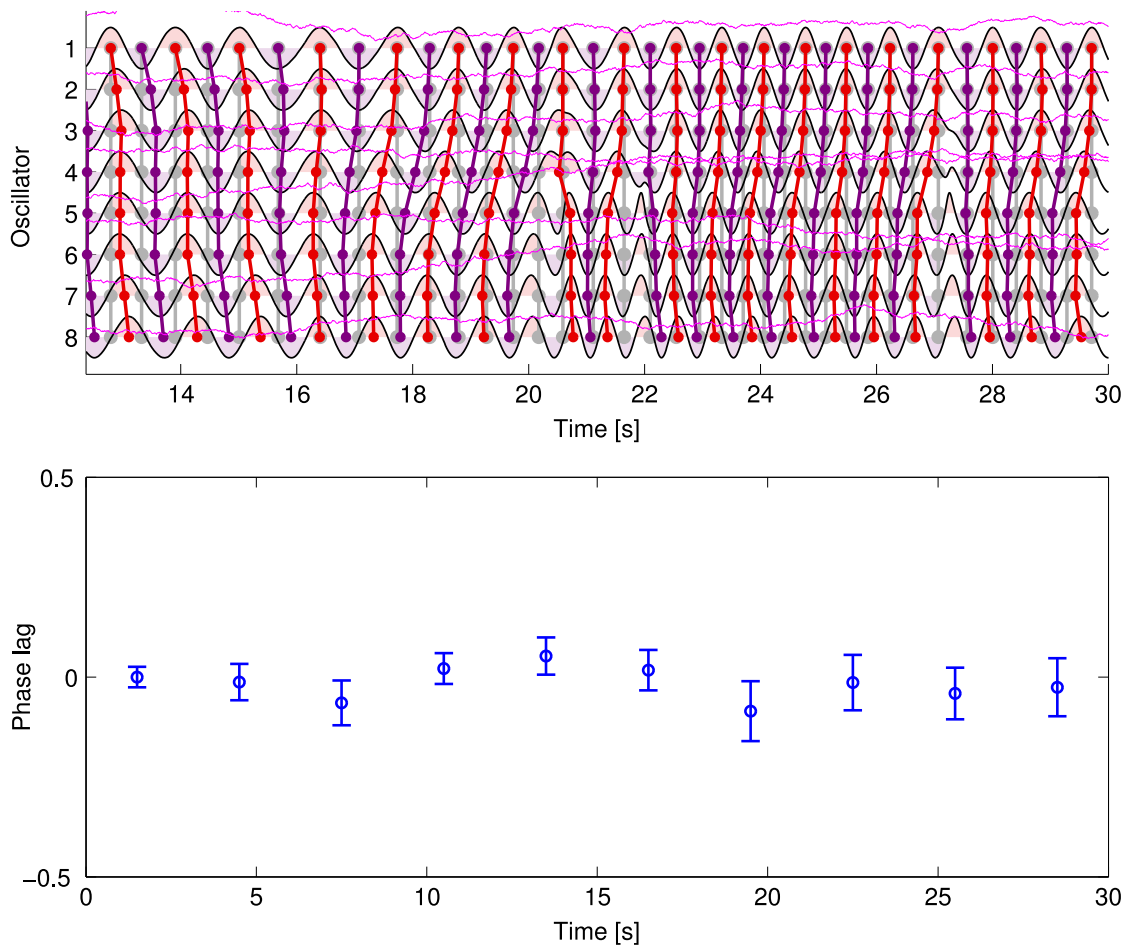


Figure 4.6 – Original Hemicord model with time-varying intrinsic frequencies subject to a damped random walk and with  $k = 0$ . **Top:** Oscillation at each joint, with the fluctuations in the intrinsic frequencies (noisy lines in magenta). Only the last 17 seconds of simulation are shown. **Bottom:** Phase lag average over 5 seconds windows, as a fraction of a cycle, for the whole simulation. The fluctuations in the intrinsic frequencies of the oscillators lead to fluctuations in the intersegmental phase lags.

### 4.3 A Radically Different Approach to Flexibility

Until here, we have tried to build a network with some randomness in the parameters that would set its natural (unforced) intersegmental phase lag to different values. To each set of parameter values (which could vary with time in the case of the random walk) corresponds one stable pattern, the idea being that descending commands from the brain could adjust the parameters to select a different pattern.

But if the objective is to have a flexible network, why should the pattern be determined by the values of the network parameters? Should not the pattern be part of the network *state*, just like the phase, for which the oscillator does not have a natural or preferred value?

In such a network, the role of the intersegmental couplings would not be to establish any given phase lag, but to ensure the *uniformity* of the phase lag—any phase lag—along the body. The initial pattern would then be determined by the initial conditions, i.e. the initial values of the state variables. The phase lag could be altered at any time by perturbing the state variable  $\theta_i$  somewhere in the chain of oscillators. This would cause a modification of the local phase lag which the couplings would then replicate in the rest of the network. In a sense, the network acts as a memory, keeping the phase lag that was applied externally to a part of the network, until the next perturbation.

In the following sections, we investigate couplings that maintain a consistent phase lag along the spinal cord, without constraining the value of the actual phase lag. We call them *flexible couplings*. We first derive different forms of flexible couplings. We show simulation results for some of them in section 4.3.3.

#### 4.3.1 Polar Coordinates

To design a completely flexible coupling, it suffices to use a coupling linear in the phase lag difference, of appropriate sign, and which vanishes for identical phase lags. For example, the following equations describe a flexible hemicord model with descending couplings, as shown in figure 4.7 (left):

$$\begin{aligned}\dot{\theta}_i &= \omega + \phi_i^{i-1} - \phi_{i-1}^{i-2} \\ &= \omega + 2\theta_{i-1} - \theta_{i-2} - \theta_i & i \geq 3 \\ \dot{\theta}_i &= \omega & i = 1, 2\end{aligned}\tag{4.2}$$

with  $\phi_k^j = \theta_j - \theta_k$ .

The coupling is diffusive, as it vanishes when  $\phi_{i-1}^{i-2} = \phi_i^{i-1}$ . The resulting phase lag in the whole chain is determined by the initial conditions: it is the initial phase lag between the first two oscillators. Indeed, these oscillators receive no coupling, so their phase relationship  $\phi_2^1$  will not change, but will be propagated down the chain. Possible values depend on the range of

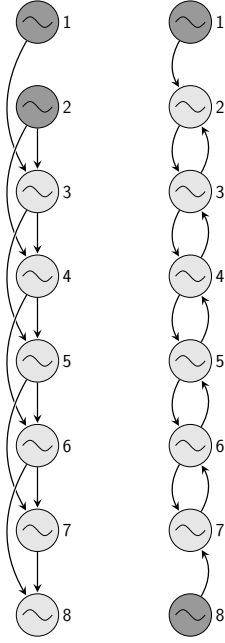


Figure 4.7 – Network topologies for flexible hemicord models. **Left:** Descending coupling scheme. Each oscillator receives projections from its two closest rostral neighbors, except for the first two oscillators (dark gray) which receive no coupling. **right:** Bidirectional coupling scheme. Each oscillator receives couplings from its rostral and caudal neighbors, except for the boundary oscillators (dark gray) which receive no coupling.

initial conditions. With fully random initial phases,  $\phi_2^1$  can take any value in  $(\pi, \pi)$ , and the chain will converge to that.

The corresponding ascending coupling is

$$\begin{aligned}\dot{\theta}_i &= \omega + \phi_{i+2}^{i+1} - \phi_i^{i+1} \\ &= \omega + 2\theta_{i+1} - \theta_{i+2} - \theta_i\end{aligned}\tag{4.3}$$

It appears that a linear combination of these two couplings (even with different weights) is unstable. However we know e.g. from the lamprey entrainment experiments described in chapter 3 that the coupling is bidirectional. We can easily design a bidirectional coupling by making each oscillator a target of its two nearest neighbors, as shown in figure 4.7 (right):

$$\begin{aligned}\dot{\theta}_i &= \omega + \phi_i^{i-1} - \phi_{i+1}^i \\ &= \omega - 2\theta_i + \theta_{i-1} + \theta_{i+1}\end{aligned}\tag{4.4}$$

This coupling has the same properties as the descending and ascending couplings, with one important difference: here, it is the first and last oscillators that receive no coupling. Therefore, absent external inputs, their initial phase relationship  $\theta_1 - \theta_n$  will stay constant and constrain the phase lag along the chain:  $\phi_{i+1}^i = \frac{\theta_1 - \theta_n}{n-1}$  (modulo  $2\pi$ ). With  $\theta_1 - \theta_n \in (pi, \pi] \bmod 2\pi$ , a network with random initial phases generally converges to a uniform phase lag smaller than  $\frac{\pi}{n-1}$ . Higher phase lags are possible but very unlikely, as they require an arrangement of initial phases close to the final pattern of uniform lags. However once the network has stabilized to a small uniform phase lag, it is possible for perturbations to move the phase lag to a higher

value.

Note that this bidirectional coupling is identical to that in Ijspeert et al. [2007] with target phase lag  $\phi = 0$ , except for the first and last oscillators receiving no coupling.

Interestingly, the bidirectional coupling can be combined with the ascending or descending coupling, or both, without losing stability. Their relative weights determines the range of phase lags.

### Sine

Taking the sine of the coupling gives similar properties:

$$\dot{\theta}_i = \omega + \sin(2\theta_{i-1} - \theta_{i-2} - \theta_i) \quad (4.5)$$

The main difference is that phase lags will converge modulo  $2\pi$ , which is desirable.

### Two Sines

We can also take the sine of the two lags separately:

$$\begin{aligned} \dot{\theta}_i &= \omega + \sin\phi_i^{i-1} - \sin\phi_{i-1}^{i-2} \\ &= \omega + \sin(\theta_{i-1} - \theta_i) - \sin(\theta_{i-2} - \theta_{i-1}) \end{aligned} \quad (4.6)$$

This coupling has fixed points at

$$\begin{aligned} \sin\phi_i^{i-1} - \sin\phi_{i-1}^{i-2} &= 0 \\ \sin\phi_i^{i-1} &= \sin\phi_{i-1}^{i-2} \\ \phi_i^{i-1} &= \begin{cases} \phi_{i-1}^{i-2} + 2k\pi & k \in \mathcal{Z}, \text{ or} \\ \pi - \phi_{i-1}^{i-2} + 2k\pi \end{cases} \end{aligned} \quad (4.7)$$

The stability of the fixed points is found by taking the derivative with respect to  $\theta_i$ :

$$\frac{d}{d\theta_i} (\sin(\theta_{i-1} - \theta_i) - \sin(\theta_{i-2} - \theta_{i-1})) = -\cos(\theta_{i-1} - \theta_i) < 0 \text{ if } \phi_i^{i-1} \in \left(-\frac{\pi}{2}, \frac{\pi}{2}\right) \quad (4.8)$$

Thus stable lags are in  $(-\frac{\pi}{2}, \frac{\pi}{2})$ . However, boundary oscillators, which have different connectivity (e.g. upper boundary for descending-only coupling) sometimes synchronize to the second fixed point, with the form  $\pi - \phi_{i-1}^{i-2} + 2k\pi$ .



### 4.3.2 Cartesian Coordinates

It is sometimes desirable to have a dynamical system in Cartesian coordinates—for example to simplify the introduction of Cartesian feedback signals.<sup>2</sup> The flexible coupling in the form of equation (4.5) can be rewritten to Cartesian coordinates. To simplify the notation, we show the development for the third oscillator:

$$\begin{aligned}\dot{\theta}_3 &= \omega + \sin(2\theta_2 - \theta_1 - \theta_3) \\ \dot{r}_3 &= a(R_3 - r_3)\end{aligned}\tag{4.9}$$

Here we include the differential equation governing the amplitude, as per equation (4.1). The steps to rewrite the uncoupled oscillator equations to Cartesian coordinates are detailed in section 5.3.2. Here we concentrate on the coupling term, i.e. the sine of equation (4.9). Using the trigonometric relations

$$\sin(\alpha - \beta) = \sin \alpha \cos \beta - \cos \alpha \sin \beta\tag{4.10}$$

$$\sin 2\alpha = 2 \sin \alpha \cos \alpha\tag{4.11}$$

$$\cos 2\alpha = \cos^2 \alpha - \sin^2 \alpha\tag{4.12}$$

we find

$$\begin{aligned}\sin(2\theta_2 - \theta_1 - \theta_3) &= \sin 2\theta_2 \cos(\theta_1 + \theta_3) - \cos 2\theta_2 \sin(\theta_1 + \theta_3) \\ &= 2 \sin \theta_2 \cos \theta_2 (\cos \theta_1 \cos \theta_3 - \sin \theta_1 \sin \theta_3) - \\ &\quad (\cos^2 \theta_2 - \sin^2 \theta_2) (\sin \theta_1 \cos \theta_3 + \cos \theta_1 \sin \theta_3)\end{aligned}\tag{4.13}$$

and introducing the transformation

$$\begin{aligned}x &= r \cos \theta \\ y &= r \sin \theta\end{aligned}\tag{4.14}$$

we find our coupling term in Cartesian coordinates. Equation (4.9) then becomes

$$\begin{aligned}\dot{x}_3 &= a(R_3 - r_3) \frac{x_3}{r_3} - \bar{\omega}_3 y_3 \\ \dot{y}_3 &= a(R_3 - r_3) \frac{y_3}{r_3} + \bar{\omega}_3 x_3 \\ \bar{\omega}_3 &= \omega_3 + \frac{1}{r_1 r_2^2 r_3} (2x_2 y_2 (x_1 x_3 + y_1 y_3) - (x_2^2 - y_2^2) (x_3 y_1 + x_1 y_3))\end{aligned}\tag{4.15}$$

---

2. By Cartesian signal we mean for example an oscillation such as  $\cos \theta$  rather than a phase such as  $\theta$ .

### Two Sines

Alternatively, we can rewrite the coupling of equation (4.6) in Cartesian coordinates:

$$\begin{aligned}
 \dot{\theta}_3 &= \omega_3 + \sin(\theta_2 - \theta_3) - \sin(\theta_1 - \theta_2) \\
 &= \omega_3 + \sin\theta_2 \cos\theta_3 - \cos\theta_2 \sin\theta_3 - \sin\theta_1 \cos\theta_2 + \cos\theta_1 \sin\theta_2 \\
 &= \omega_3 + \frac{y_2 x_3}{r_2 r_3} - \frac{x_2 y_3}{r_2 r_3} - \frac{y_1 x_2}{r_1 r_2} + \frac{x_1 y_2}{r_1 r_2} \\
 &= \omega_3 + \frac{1}{r_2 r_3} (y_2 x_3 - x_2 y_3) - \frac{1}{r_1 r_2} (y_1 x_2 - x_1 y_2)
 \end{aligned} \tag{4.16}$$

### Direct Cartesian Coupling

It would be interesting to have simpler couplings than the convoluted expressions of equations (4.15) and (4.16). Taking inspiration from the form of e.g. equation (4.4), we can write:

$$\begin{aligned}
 \dot{x}_i &= a(R_i - r_i) \frac{x_i}{r_i} - \omega_i y_i - 2x_i + x_{i-1} + x_{i+1} \\
 \dot{y}_i &= a(R_i - r_i) \frac{y_i}{r_i} + \omega_i x_i - 2y_i + y_{i-1} + y_{i+1}
 \end{aligned} \tag{4.17}$$

or, if we omit the coupling of the oscillator to itself:

$$\begin{aligned}
 \dot{x}_i &= a(R_i - r_i) \frac{x_i}{r_i} - \omega_i y_i + x_{i-1} + x_{i+1} \\
 \dot{y}_i &= a(R_i - r_i) \frac{y_i}{r_i} + \omega_i x_i + y_{i-1} + y_{i+1}
 \end{aligned} \tag{4.18}$$

Numerical simulations show that these two forms give good results (data not shown). In the second case however we get different lags at the boundaries than in the rest of the network. Moreover, the amplitude of the oscillators is affected by the coupling, unless we rescale the coupling term to the local amplitude, which also fixes the lags at the boundaries.

### 4.3.3 Simulation Results

Phase lag histograms for the polar coordinate networks with descending couplings are shown in figure 4.8. The range of initial phase lags can be adjusted by changing the range of random initial phases. Subsequent perturbations however can push the network beyond the plotted range. The exception is the network based on a two-sine coupling, which only admits phase lags between -25% and 25%. This is consistent with our predictions in section 4.3.1.

In networks based on the bidirectional coupling, the phase lag is constrained by the phase difference between the two boundaries. The full range  $(-\pi, \pi)$  between the boundaries translates to an intersegmental phase lag restricted to  $(-\frac{\pi}{N-1}, \frac{\pi}{N-1})$  where  $N$  is the number of segments.

With identical frequencies, these networks can produce a range of perfectly smooth phase lags. We show here results on a network in polar coordinates with descending 2-sines couplings. We can reproduce the physiological range of phase lags by using initial phases in  $(0, 1)$  radians. As shown in figure 4.9, the standard deviation is close to zero.

To introduce some inconsistencies along the spinal cord, we used random values for the intrinsic frequencies of the third and following segments (the frequencies of the first two segments must be identical to avoid phase drifts). Using frequencies in  $(2\pi - 2, 2\pi + 2)$ , we obtained results similar to biological observations (figure 4.10).

The controllability of the network phase lag by adjustments to the intrinsic frequency of the first oscillator is illustrated in figure 4.11. Due to the random initial conditions, the network activity displays a negative phase lag. At time  $t = 10$ s, a positive perturbation is added to the phase derivative of the first oscillator, until  $t = 11$ s. The perturbation changes the phase relationship between the first and last oscillators, causing the network to converge to a new, positive phase lag. This is a significant novelty compared to the model of Ijspeert et al. [2007]: the effect of the perturbation stays in the system after the perturbation ends.

#### 4.3.4 Conclusions on the Flexible Couplings

Networks based on these flexible couplings are very sensitive to perturbations of the phase or frequency of the boundary oscillators. Networks with descending or ascending coupling are very sensitive at the two most rostral or most caudal oscillators, respectively. In all cases, a slight difference in the frequency of a sensitive oscillator leads to a continuous drift in phase lags. This precludes mechanical entrainment of the network frequency (where local sensory feedback affects the frequency of a part of the network), as well as synchronization with e.g. slower limb oscillators.

The flexible model thus better matches the biological data on diversity and inconsistencies than the Original Hemicord models, but its robustness and entrainment properties are not adequate. The model can accommodate noise with zero average, but even slight systematic deviations in the rostral frequencies lead to continuous drifts in phase lags, which are not observed in the animal (section 2.4.1). The observation with rhythm switches that the phase lag reverts to its original value after a second switch is also clearly incompatible with this model.

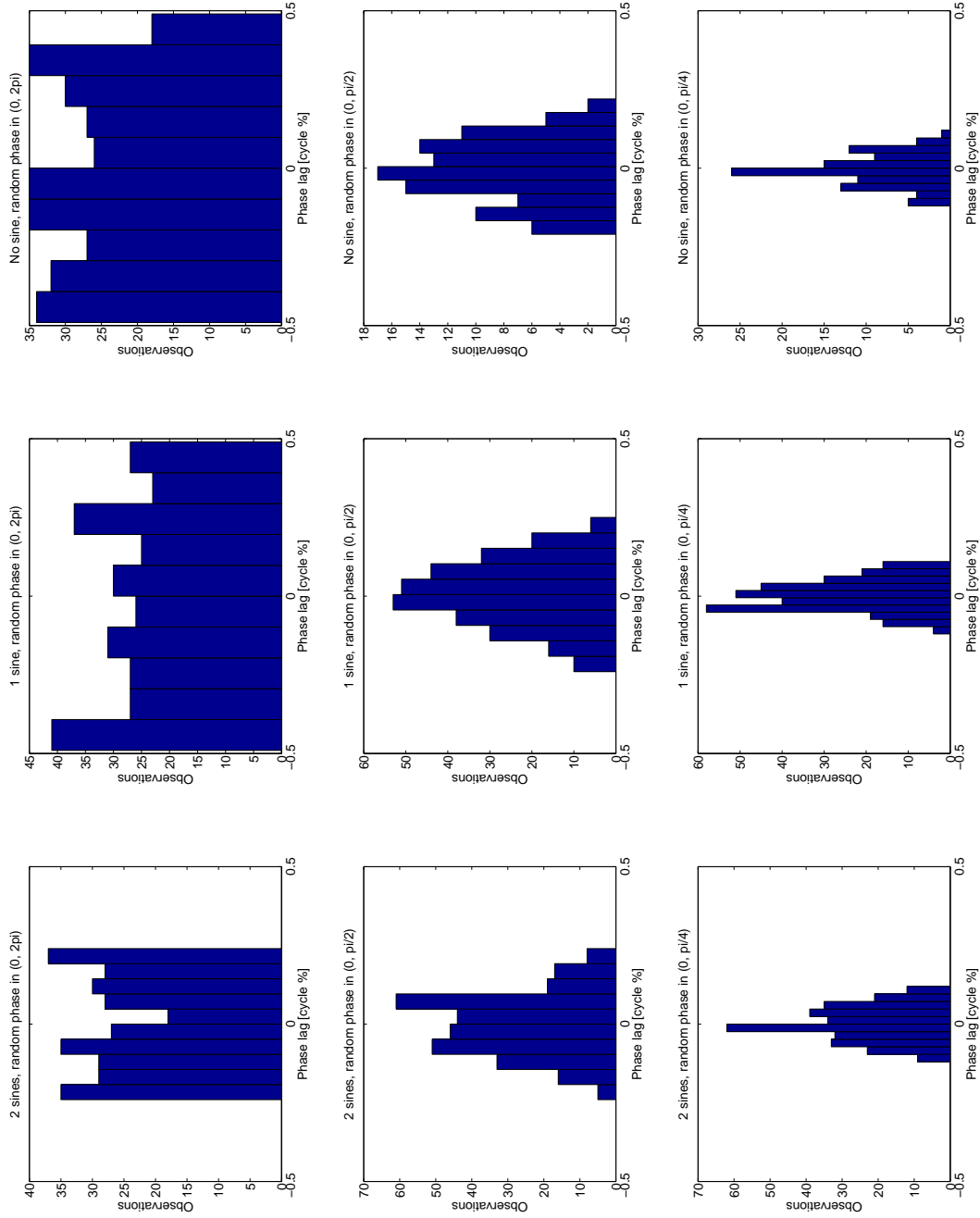


Figure 4.8 – Range of phase lags obtained with intrinsically flexible hemicord networks in polar coordinates using descending couplings. **Left column:** With a network based on the two-sine coupling of equation (4.6). **Middle column:** With a network based on the sine coupling of equation (4.5). **Right column:** With a network based on the coupling of equation (4.2). **Top row:** Using random initial phases in  $(0, 2\pi)$ . **Middle row:** Using random initial phases in  $(0, \pi/2)$ . **Bottom row:** Using random initial phases in  $(0, \pi/4)$ .

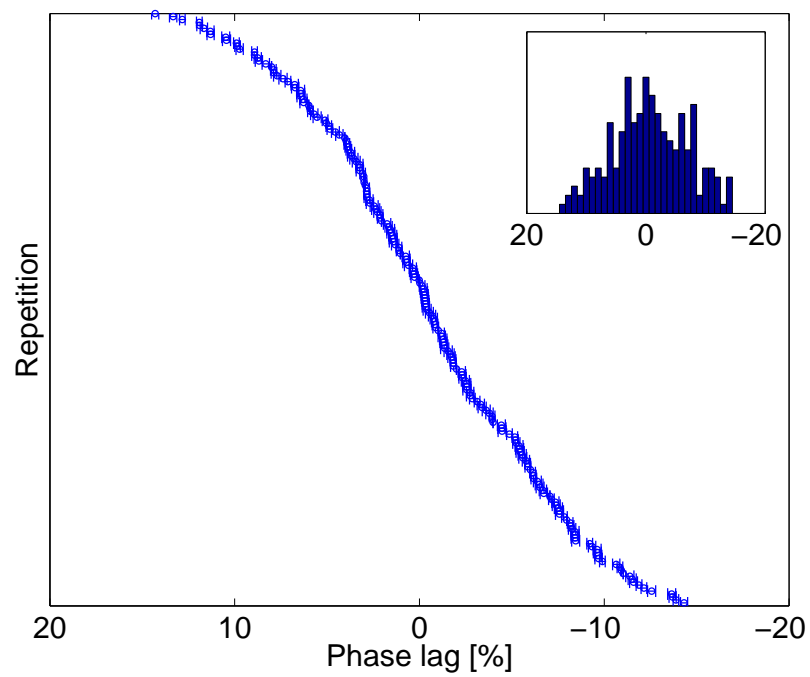


Figure 4.9 – Distribution of intersegmental phase lag in a flexible hemicord network in polar coordinates, with descending 2-sines couplings and random initial phases in  $(0, 1)$ .

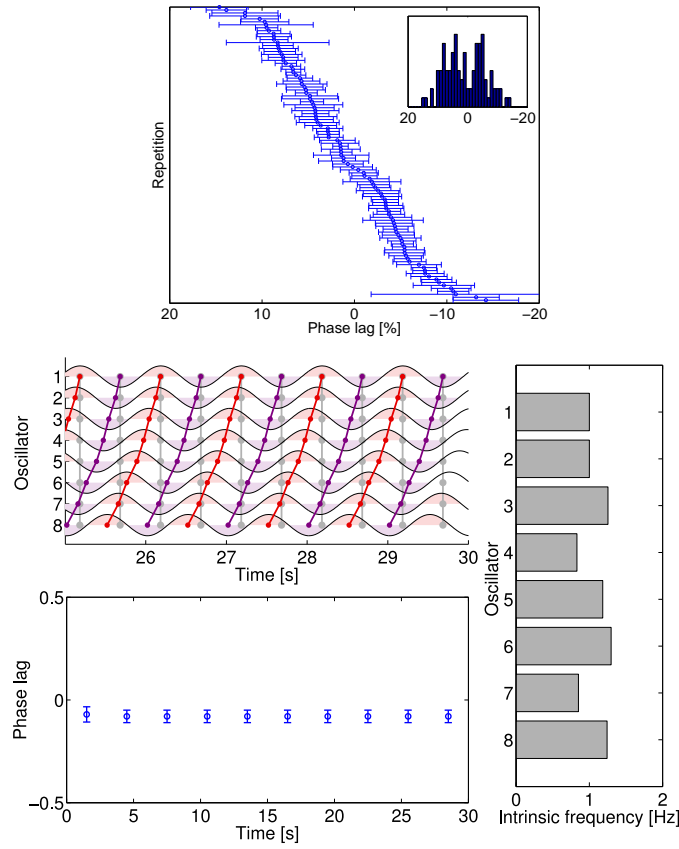


Figure 4.10 – Flexible hemicord network in polar coordinates, with descending 2-sines couplings and random intrinsic frequencies in  $(2\pi - 2, 2\pi + 2)$  for the third and following oscillators. **Top:** distribution of intersegmental phase lags. **Bottom:** One activity pattern.

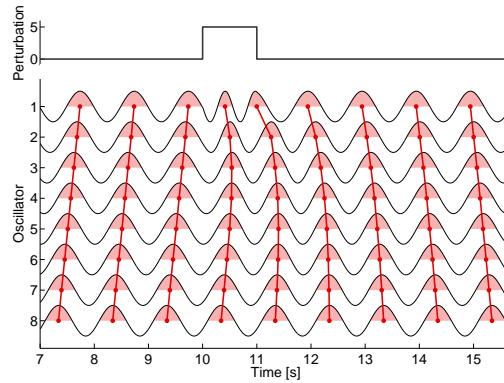


Figure 4.11 – Control of the phase lag in a flexible hemicord network with bidirectional sine coupling, using a transient perturbation of the intrinsic frequency in the first oscillator. **Top:** Perturbation added for 1 second to the phase derivative  $\dot{\theta}_1$  of the first oscillator. **Bottom:** The perturbation temporarily increases the frequency of the first oscillator. This changes the phase relationship between the first and last oscillators, causing the network to switch from a negative to a positive phase lag.

## 4.4 A Flexible Network that is Robust to Variations in Frequencies

We present here our most successful attempt at designing a flexible CPG network. The approach is much more conservative than that of the previous section. It proved successful in modeling the diversity of phase lags observed *in vitro* (including the three peaks of the phase lag distribution), the correlation between phase lag and cycle frequency, and the spontaneous switches between slow and fast rhythms. It also proved easily controllable. We show in chapter 5 how the model was used to reproduce the five salamander behaviors with a salamander robot. In this chapter, we will illustrate the controllability with a simplified model that reproduces the main results of Ijspeert et al. [2007] (section 4.4.5).

The model is based on the findings that the salamander axial CPG is organized as a double chain of oscillators, similar to the lamprey, and that limb segments are intrinsically slower than other segments [Ijspeert et al., 2007]. Compared to the work of Ijspeert et al. [2007], the model was modified to support the range of intersegmental phase lags observed *in vitro*, with and without simultaneous rhythmic activity in the limb centers. The main hypotheses are 1) that limb oscillators project mostly to axial oscillators close to the girdles, as opposed to extensive projections from the limbs to all trunk and tail oscillators 2) that intersegmental couplings are stronger in the rostrocaudal direction, and 3) that limb oscillators saturate at lower excitatory drives than axial oscillators.

### 4.4.1 Design Considerations

Without considering the phase lag switches, the Original Hemicord model with random intrinsic frequencies (section 4.2) has three issues:

- Phase lags are too variable along the spinal cord.
- Phase lags are not flexible enough: changing the activity of rostral segments results in irregular phase lags along the chain.
- There is no correlation between phase lags and frequencies.

We can address these issues by making one important change to the network: breaking the ascending/descending symmetry<sup>3</sup>. Indeed, either adding longer descending connections, or increasing the descending coupling weights is sufficient: in such asymmetric networks, the phase lag can be controlled by tuning the rostral segment frequencies, with no significant increase of the inconsistencies along the spinal cord. The resulting model is closer to recent models of the lamprey CPG, both in terms of coupling scheme and controllability [Kozlov et al., 2009].

As in the work of Kozlov and coauthors, we decided to use a dominantly descending coupling. This has the advantage of making the network controllable through differential excitation of the first segment (closest to the head), which seems more natural than differential excitation

---

3. By symmetric we mean here that the coupling strength and the extent of the projections are identical in the rostral and caudal directions. The Original Hemicord model does include a coupling asymmetry in the phase biases.

of the last segment. Note that there is ample experimental evidence for a coupling asymmetry in the lamprey, but there is conflicting evidence regarding the nature of the asymmetry (i.e. the direction of the dominant coupling) [Hill et al., 2003].

The model was developed using the Codyn framework (<http://www.codyn.net>). The framework provides a language designed for the concise description of coupled dynamical systems. Networks can be exported to raw C files that can be compiled to run on a robot microcontroller. We took advantage of this feature to implement the robot controller described in chapter 7.

### 4.4.2 Model Description

Only the 25 most rostral segments of the salamander spinal cord are modeled, corresponding to the active part of the robot (the caudal half of the robot tail is made of a passive piece of plastic). As in the model of Ijspeert et al. [2007], each hemisegment and each limb is modeled as a phase oscillator with controllable amplitude, and the connections between oscillators are functions of the phase difference between sender and receiver:

$$\begin{aligned}
 \dot{\theta}_i &= 2\pi\nu_i + \sum_j r_j w_{ij} \sin(\theta_j - \theta_i - \phi_{ij}) \\
 \dot{r}_i &= a_i(R_i - r_i) \\
 x_i &= r_i(1 + \cos\theta_i) \\
 \nu_i &= d_i e_i \\
 R_i &= d_i P(d_i, d_i^{th})
 \end{aligned} \tag{4.19}$$

A positive output  $x_i$  for oscillator  $i$  is calculated from the instantaneous phase  $\theta_i$  and amplitude  $r_i$ . The intrinsic frequency  $\nu_i$  is proportional to the oscillator excitability  $e_i$  and to a drive  $d_i$  that represents the excitation from descending pathways. The intrinsic amplitude  $R_i$  increases with increasing drive until it approaches a saturation threshold  $d_i^{th}$  after which it decreases progressively to zero due to the sigmoid function  $P(d, d^{th}) = 1/(1 + e^{b(d - d^{th})})$  with  $b$  the saturation rate. The excitability and saturation threshold of each oscillator is drawn from a Gaussian distribution with different mean for forelimb, hindlimb and axial oscillators. The coupling from oscillator  $j$  to oscillator  $i$  is characterized by a strength  $w_{ij}$  and phase bias  $\phi_i$ . The gain  $a_i$  determines the speed of convergence for the amplitude. Note that the differential equation controlling the amplitude is simplified compared to the oscillator model of Ijspeert et al. [2007] (see section 4.2.1).

The network connectivity is described in figure 4.12 and table 4.1. Other parameter values are provided in table 4.2.

The oscillator and coupling parameters were tuned to obtain the range of intersegmental phase lags and cycle durations observed *in vitro*. Multiple simulations were performed. Some parameters were picked from a Gaussian distribution to reflect the diversity of *in vitro* prepa-



#### 4.4. A Flexible Network that is Robust to Variations in Frequencies

Table 4.1 – Coupling parameters in the asymmetric model

Coupling type	Strength $w_{ij}$	Phase bias $\phi_{ij}$
Intersegmental, rostrocaudal	5	$2\pi \cdot 0.066$
Intersegmental, caudorostral	1	$-2\pi \cdot 0.066$
Intrasegmental, lateral	10	$\pi$
Interlimb, rostrocaudal	3	$\pi$
Interlimb, caudorostral	30	$\pi$
Interlimb, lateral	10	$\pi$
Limb to axial oscillators	30	4
Axial to limb oscillators	2.5	-4

rations. In particular, the parameter that determines the intrinsic frequency of an oscillator as a function of the external drive, and which we call excitability, was picked randomly for each oscillator. Different means were used for the excitability and saturation thresholds of the forelimb, hindlimb and axial oscillator, as shown in table 4.2.

Table 4.2 – Other parameters in the asymmetric model

Name	Symbol	Value
Excitability	$e_i$	$1.1 \pm 0.07$ (axis) $0.8 \pm 0.05$ (forelimbs) $0.5 \pm 0.03$ (hindlimbs)
Drive	$d$	$0.1 \pm 0.01$
Drive random walk conv. factor	$c$	0.001
Drive random walk step size		0.03
Saturation threshold	$d^{th}$	0.3 (axis) $0.09 \pm 0.02$ (limbs)
Saturation rate	$b$	500

#### 4.4.3 Results

We performed 10'000 simulations with the isolated CPG model to have a good approximation of the phase lag distribution. The results are shown in figure 4.13. The model was tuned to reproduce the three peaks in the distribution of intersegmental phase lags with a similar range of values and median. The peaks are centered on phase lags of 6.9%, 1.5% and -7.2%. The model also reproduces the correlation between phase lag and cycle duration (figure 4.14) and the reversible switches between slow and fast rhythms (see section 4.5.1).

### 4.4.4 Discussion

The absence of strong connections from limb oscillators to the mid-trunk (the limbs project only to axial oscillators close to the girdles, hypothesis 1) is important for the flexibility of the CPG: such connections would impose a fixed phase pattern during limb activity [Ijspeert et al., 2007].<sup>4</sup> Removing them allows for the expression of more activity patterns, such as the rostrocaudal wave of activity observed during backward stepping.

The intersegmental phase lag is modulated through adjustments of the frequencies of the uncoupled oscillators. Because rostrocaudal couplings are stronger than caudorostral couplings, a segment will entrain a slower or faster caudal neighbor to its own frequency. However the faster segment will lead the slower one with a delay that increases with the difference in uncoupled frequencies (this delay being in addition to the coupling's natural phase bias). This effect will propagate down the chain of oscillators, such that the frequency and phase lag of the whole chain can be controlled by adjusting two values: the uncoupled frequency of the first segment, and that of the other segments.

This mechanism of phase lag modulation is similar to the *trailing oscillator hypothesis* proposed in a model of the lamprey CPG [Matsushima and Grillner, 1992]. An important difference is that the lamprey model assumes symmetrical rostrocaudal and caudorostral couplings, while we find that the asymmetry of the couplings (hypothesis 2) is important to maintain a uniform phase lag along the chain of oscillators. If the intersegmental couplings were symmetric, the effect of the frequency difference would attenuate as it propagates down the chain, as each segment would not take on the frequency of its rostral neighbor, but a value between that and its own frequency. This attenuation leads to non-uniform phase lags along the chain and must be compensated by adjusting the uncoupled frequency of the first and last segments in opposite amounts [Cohen et al., 1982].

An alternative to this asymmetry between ascending and descending couplings would be to have a different effective coupling strength when accelerating vs. decelerating the target oscillator. For example, when additional excitation is provided to the first segments, a coupling that has a stronger effect when *accelerating* the target oscillator is equivalent to a stronger descending coupling (since the rostral oscillators accelerate their caudal neighbors). However this scheme works only in one direction. To maintain uniform phase lags while decreasing the excitation of the first segments would require a coupling that has a stronger effect when *slowing down* the target oscillator. The asymmetry between ascending and descending intersegmental couplings therefore constitutes the more general solution.

While the abstract nature of the oscillator model makes it easy to reason about the mechanism

---

4. We assume here that global connections from the limb centers to the trunk and the tail are incompatible with the diversity of synchronization patterns observed in salamanders. We conclude that limb centers must connect only locally to the axial centers. However, the functional coupling between limb and axial centers could also be altered dynamically by neuromodulators, allowing the network to switch between different connectivity patterns to produce different behaviors [Harris-Warrick and Marder, 1991]. Modulations of functional coupling in the spinal network by neuromodulators were recently identified in the *Xenopus* [Rauscent et al., 2009].

of phase lag generation, we note that the same principles apply to more detailed models of the spinal cord. For example, Kozlov et al. [2009] built a model of the lamprey CPG based on the Hodgkin-Huxley formalism and found similarly that intersegmental coupling asymmetry was important to generate a uniform phase lag along the cord. There is ample experimental evidence for such asymmetry in the lamprey [Hill et al., 2003].

This basic principle of phase lag modulation, together with the differences in excitabilities and saturation thresholds between forelimb, hindlimb and axial oscillators (hypothesis 3), account for the three peaks in the distribution of phase lags *in vitro*. When all oscillators are active, the hindlimb oscillators slow down the forelimbs, and the strong local connections from limb to axial oscillators slow down the girdle segments, leading to a very low phase lag in the trunk and tail axial networks. This corresponds to the rightmost peak of the distribution. When the hindlimb oscillators saturate, the forelimb oscillators accelerate a bit but continue to slow down the first segments, yielding the phase lags that make up the middle peak of the distribution. When all limb oscillators saturate, the axial network generates the even higher phase lags found in the leftmost peak. This connection between phase lag and frequency also explains the correlation observed between these two measures *in vitro*. The switches between slow and fast rhythms correspond to the transitions between active and saturated limbs. The transitions are triggered by the small fluctuations in the excitatory drive (section 4.5.1, figure 4.18), which represents NMDA excitation in this case.

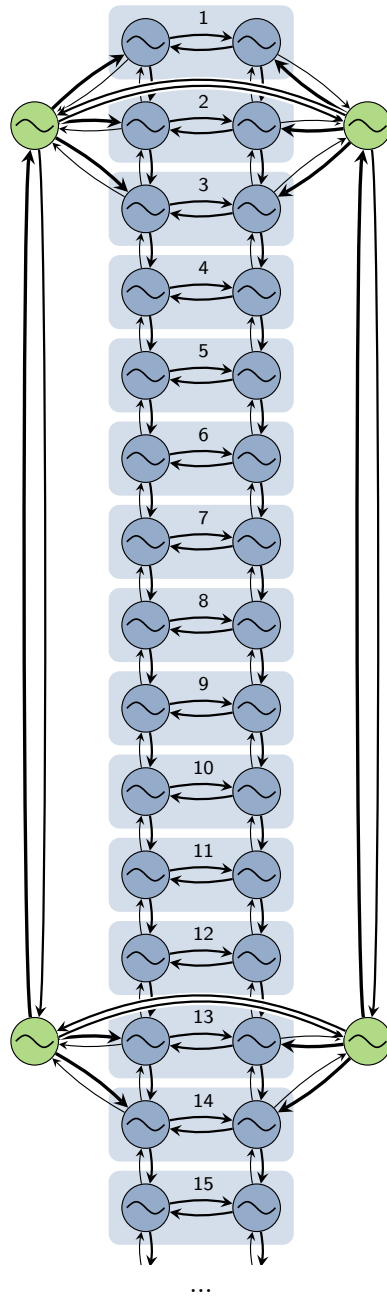


Figure 4.12 – Connectivity of the model with asymmetric intersegmental couplings. Axial and limb oscillators are shown in blue and green respectively. Thicker arrows denote stronger couplings. The full model is made of 25 segments.

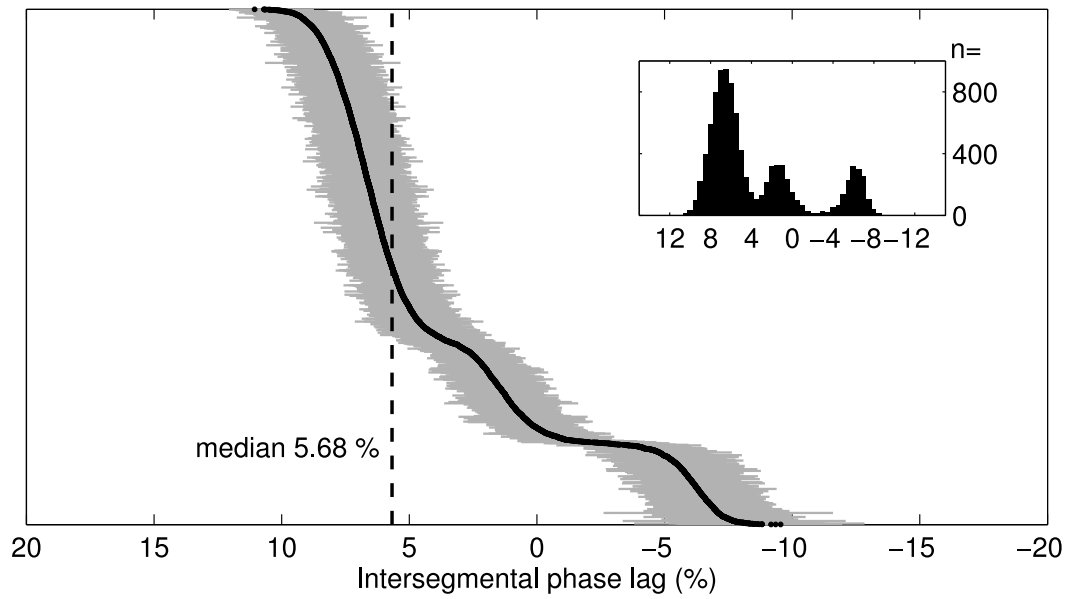


Figure 4.13 – Distribution of intersegmental phase lags in the asymmetric model. The figure shows the result of 10'000 simulations with different random seeds, sorted by decreasing phase lag. For each simulation, the intersegmental phase lags are measured in the mid-trunk and a median value calculated for each pair of ventral roots. The plot shows the average and standard deviation calculated across all mid-trunk ventral roots. The distribution of phase lags is shown in insert.

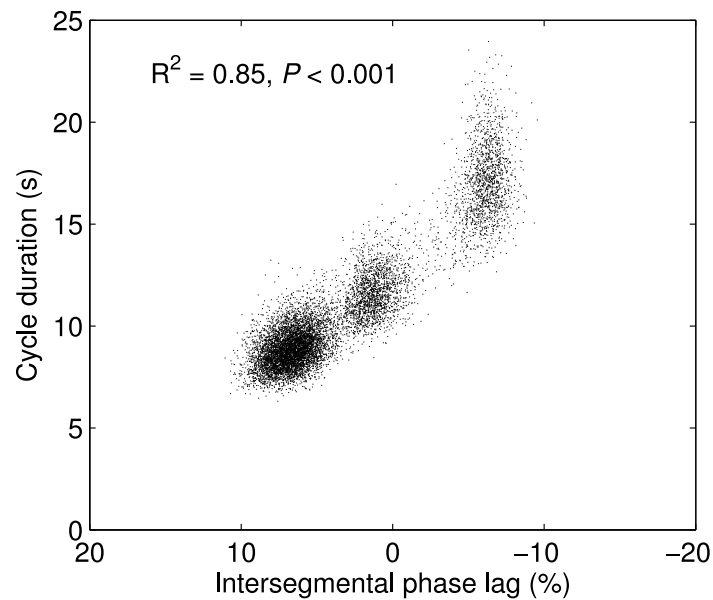


Figure 4.14 – Correlation between intersegmental phase lag and cycle duration in the asymmetric model. Each dot corresponds to one simulation of figure 4.13. The coefficient of determination  $R^2$  of a linear regression and the corresponding  $F$ -test  $P$  value are indicated on the figure.

#### 4.4.5 Application to the Swimming-Walking Transition

The network proposed in section 4.4.2 produces very different intersegmental phase lags depending on the (random) intrinsic frequencies of the oscillators, yet at the same time the phase lag can easily be controlled by using differential excitation of the first and other segments. To illustrate the point, we reproduce the main results of Ijspeert et al. [2007] using a similar network topology: the axial network is made of 8 axial segments, and axial oscillators do not project to limb oscillators (figure 4.15). Compared to Ijspeert et al. [2007], the only significant differences are that limb oscillators project only locally to the axis, and that descending axial connections are stronger than their ascending counterparts.

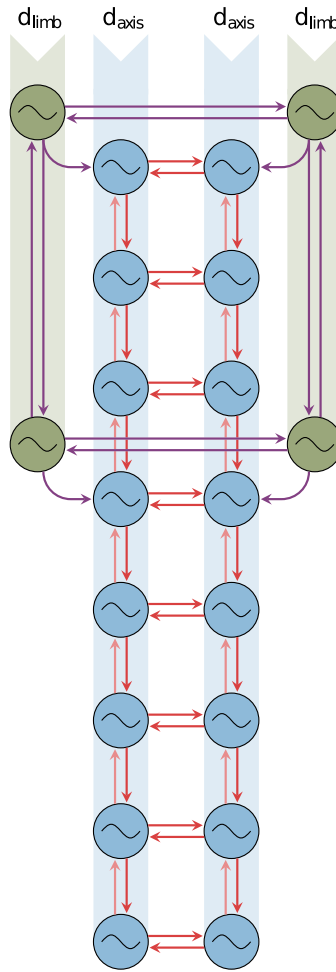


Figure 4.15 – Simplified model with asymmetric couplings. The network is made of a double chain of axial oscillators (blue) with nearest-neighbor couplings, plus 4 oscillators for the limbs (green) that connect locally to the axial oscillators. Limb and axial oscillators receive different drive signals. Couplings from limbs oscillators are the strongest ( $w = 20$ , in purple), followed by descending and ascending couplings ( $w = 5$ , red and  $w = 1$ , light red respectively). The interlimb and intrasegmental phase biases are set to  $\pi$ . Descending and ascending intersegmental phase biases are set to  $\frac{2\pi}{7}$  and  $-\frac{2\pi}{7}$  respectively.

#### 4.4. A Flexible Network that is Robust to Variations in Frequencies

The equations are also simplified; we kept only the parts that are essential to the mechanism of controllability:

$$\begin{aligned}\dot{r}_i &= a(R_i - r_i) \\ \dot{\theta}_i &= 2\pi\nu_i + \sum_{j=1}^N w_{ij}r_j \sin(\theta_j - \theta_i - \phi_{ij}) \\ R_i &= d_i \\ \nu_i &= d_i e_i \\ x_i &= r_i \cos \theta_i\end{aligned}$$

The excitability of limb and axial oscillators is 0.5 and 1 respectively. The saturation of limb oscillators is not shown in the equations; it is implemented simply by setting  $R_i = 0$  in these oscillators when  $d_i \geq 2.5$ .

The principle of phase lag modulation detailed in section 4.4.4 also applies to this network. The phase lag can be controlled by differential drive levels between the limb and axial oscillators: the frequency of the first segments is forced by the strong couplings from the limb oscillators. The lag can thus be controlled by adjusting the drive to the limb oscillators. The controllability of the network is demonstrated in figure 4.16. We see that the frequency and phase lag can be controlled independently when limbs are active, by first setting the limb drive to obtain the desired frequency and then setting the axial drive to obtain the desired phase lag.

Although the network is perfectly controllable through differential activation of the limb and axial oscillators, differential drives are not needed to reproduce the results of Ijspeert et al. [2007]: the swim-to-walk transition can be reproduced while applying a common drive to all oscillators (figure 4.17). When the drive is low, the lower excitability of the limb oscillators causes the first segment to be slowed down, which plays the role of a differential drive. The excitabilities and coupling strengths have been chosen so that the slow down will be in the right amount to yield a standing wave in the trunk and the tail. When the drive goes over 2.5, the limb oscillators saturate and the “differential drive” effect vanishes, which releases the traveling wave and faster rhythm that are natural to the axial network.

We see in figure 4.17 that the phase lag during either swimming or stepping stays the same as the frequency increases.

Note that in contrast to the stereotypical behaviors of figure 4.17, differential activation of axial and limb oscillators in figure 4.16 allow for the production of a wide, continuous range of phase lags.

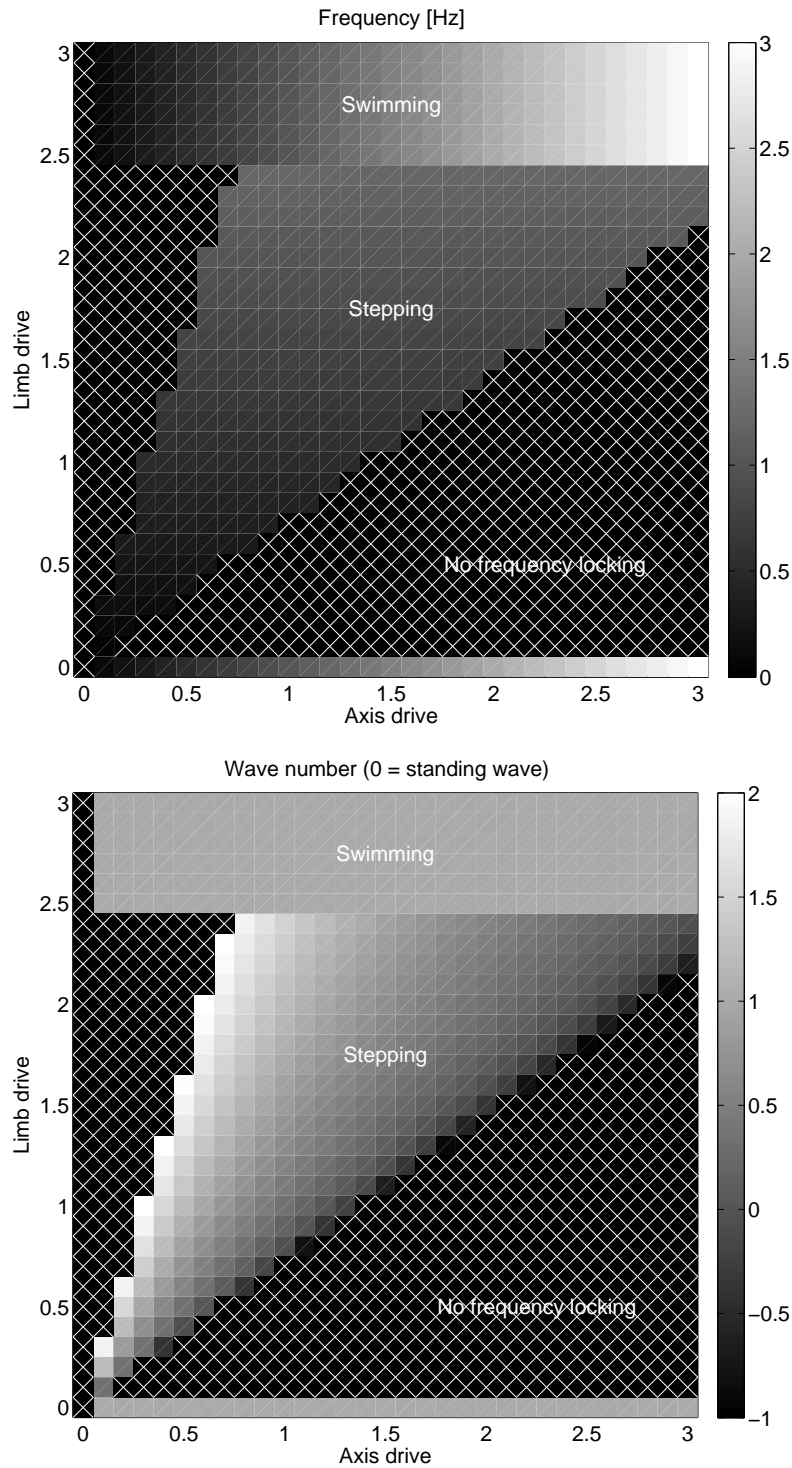


Figure 4.16 – Controllability in the simplified asymmetric model. The cycle frequency increases with increasing limb drive. The intersegmental phase lag decreases with increasing axial drive. Above a drive of 2.5, the limb oscillators saturate and the swimming pattern is released; in this regime the swimming (intrinsic) phase lag is maintained for all values of the axial drive. A clear gap in frequencies is observed between the stepping and swimming regions along the  $d_{axis} = d_{limb}$  line. Black regions with white crosses correspond to cases where the limb and axial frequencies are too far apart for the oscillators to reach frequency locking.



#### 4.4. A Flexible Network that is Robust to Variations in Frequencies

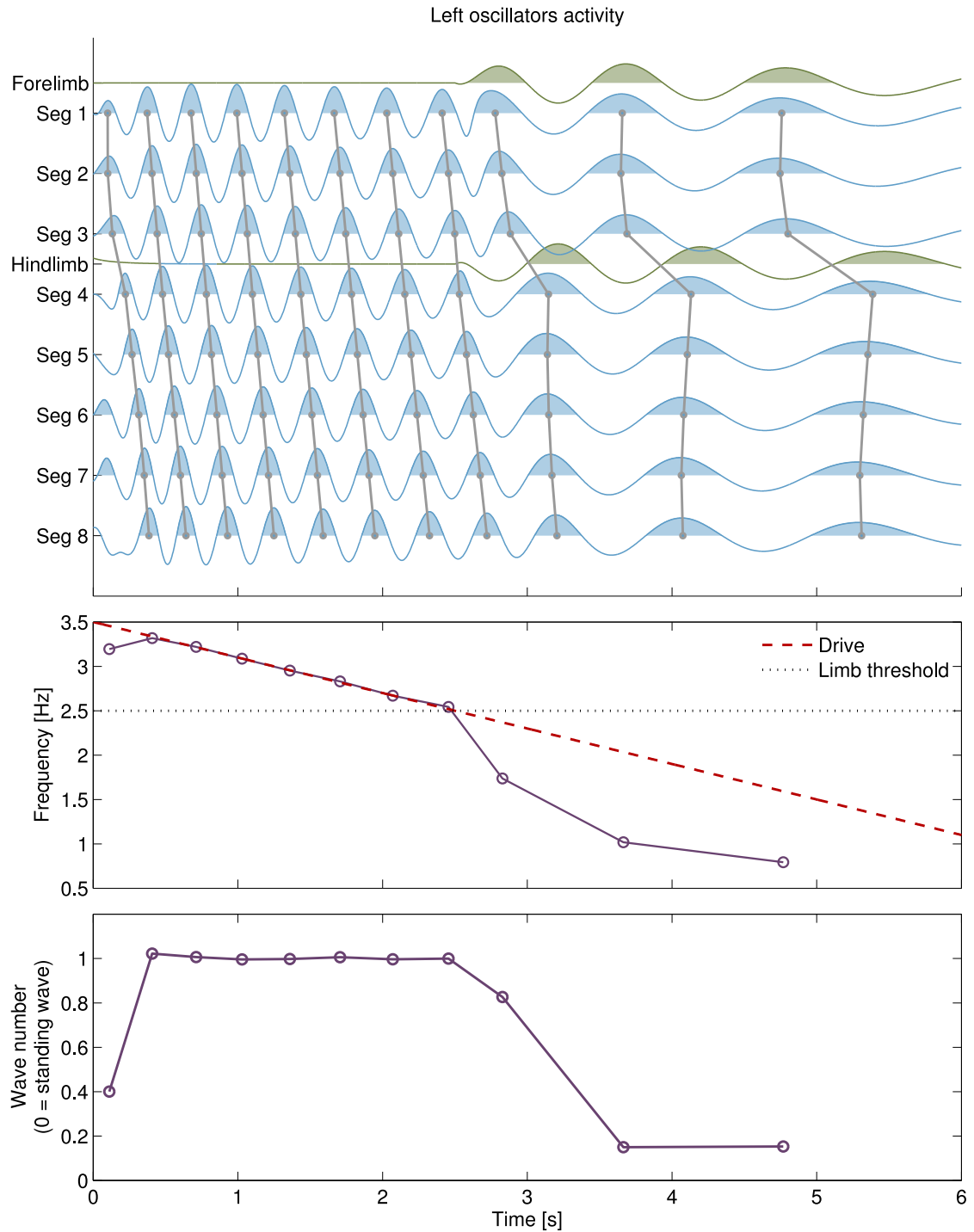


Figure 4.17 – Swim-to-walk transition in the simplified model with asymmetric couplings. **Top:** By using a uniform drive for the whole network and decreasing it linearly from 3.5 to 1, we observe a transition from a swimming pattern (wave number = 1) to a walking pattern (wave number = 0, i.e. standing wave). Axial and limb outputs are shown in blue and green respectively. The timing of each "burst" is calculated from the centroids of the colored patches. **Middle:** The drive and overall network frequencies as functions of time. When the drive gets under 2.5, the limbs come out of saturation and suddenly slow down the network. **Bottom:** As the limbs come out of saturation and slow down the network, the pattern suddenly switches from a traveling wave (wave number = 1) to a standing wave (wave number = 0).

### 4.5 Modeling Spontaneous Rhythm Switches

We propose here different mechanisms that could account for the spontaneous switches observed *in vitro*, between slow rhythms with negative phase lags and fast rhythm with positive phase lags (see section 2.4.2).

We first show that these switches can be a natural consequence of drive fluctuations in the asymmetric model of section 4.4. We then mention an alternative based on loops in the network couplings that might replace or complement the mechanism described for the asymmetric model. Finally, we briefly discuss some other possibilities.

#### 4.5.1 Rhythm Switches in the Asymmetric Model

To produce a switch in the model with asymmetric intersegmental couplings, we need to introduce some stochasticity in the global level of drive. The same drive  $d$  is used for all oscillators, with small fluctuations added in the form of a mean reverting random walk:  $\dot{d} = c(d_0 - d) + \sigma$  with  $d_0$  the drive picked from a Gaussian distribution,  $c$  a convergence factor, and  $\sigma$  a random process yielding positive and negative steps with equal probability. The random walk parameters are given in table 4.2.

The random fluctuations in the drive cause the limb oscillators to go in and come out of saturation. When the limb oscillators are saturated, the axial network displays a traveling wave of activity. When the limb oscillators come out of saturation, they force their slow frequency on the axis, at the same time a drop in frequencies and a switch to negative phase lags. The effect is illustrated in figure 4.18. Note that residual oscillations remain in the limb oscillators even after the switch. This is due to the small size of the drive fluctuation and the fact that limb saturation is not implemented as a discrete event but through a sigmoid (see section 4.4.2). However their influence on the axial oscillators quickly wanes as their amplitude decreases, due to the term  $r_j$  in the coupling in equation (4.19).

#### 4.5. Modeling Spontaneous Rhythm Switches

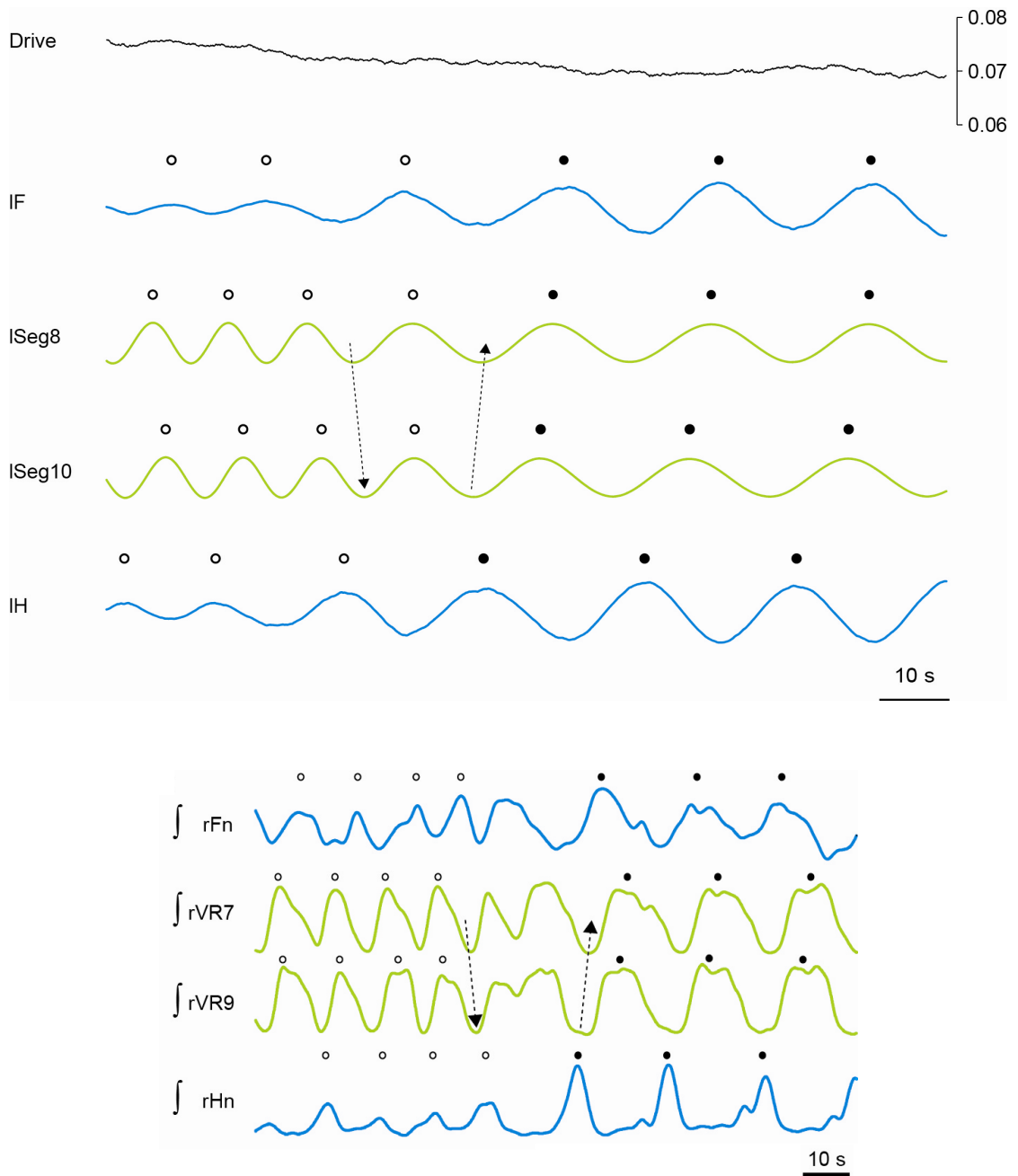


Figure 4.18 – Rhythm switch in the asymmetric model. **Top:** As the drive decreases (top), the limb oscillators (IF and IH for left forelimb and left hindlimb, in blue) come out of saturation, and they start to impose their slow frequency on the axial oscillators (green). The black and white markers indicate the centroids of the slow and fast “bursts” respectively. **Bottom:** Filtered data of a similar switch observed in the animal *in vitro* [Ryczko et al., in preparation].

Table 4.3 – Four regimes in a simple network loop

Phase lag [%]	Period [s]
$-10.68 \pm 0.06$	$24.75 \pm 0.00$
$-3.58 \pm 0.01$	$13.83 \pm 0.00$
$3.62 \pm 0.02$	$9.29 \pm 0.00$
$10.66 \pm 0.01$	$7.16 \pm 0.00$

### 4.5.2 Network Loops

Another possibility to explain the occurrence of rhythm switches is the presence of multi-stability due to coupling loops. It is known that multiple stable regimes, with different phase lags and frequencies, can coexist in neural network loops [Briggman and Kristan Jr, 2008]. Note that a network with this type of multi-stability would be quite sensitive to transient perturbations, which would suffice to radically change the activity pattern. We have not observed this effect with the asymmetric model proposed in section 4.4, despite the presence of network loops through the limb oscillators. However we did observe multi-stability when using some other parameter values, with stronger couplings from axial to limb oscillators.

Here we analyze a simple network loop as a proof of concept. We first show that the network can stabilize around different intersegmental phase lags, with lower phase lags being associated with lower cycle frequencies, as observed in the *in vitro* recordings. We then show that the stable patterns can easily be predicted based on the conditions of 1) frequency locking and 2) loop consistency, i.e. the fact that the sum of the phase lags around the loop must be a multiple of  $2\pi$ .

#### Observations

We considered the network of figure 4.19, made of phase oscillators  $\dot{\theta}_i = 2\pi\nu_i$  and couplings of the form  $\dot{\theta}_i = 2\pi\nu_i + w_{ij} \sin(\theta_j - \theta_i - \phi_{ij})$ . We ran 50 simulations and measured the period and average phase lag. Results sorted by phase lag are shown in figure 4.20.

We found that phase lags and periods were concentrated around four values, listed in table 4.3, with lower phase lags corresponding to longer periods.

#### Period Consistency

Since the intrinsic periods are identical, frequency locking implies that the coupling terms are equal. With our coupling, the coupling value depends on the difference between the desired and actual phase lag: calling this difference  $\Delta\phi$ , the coupling value is  $w \sin \Delta\phi$ . The conditions

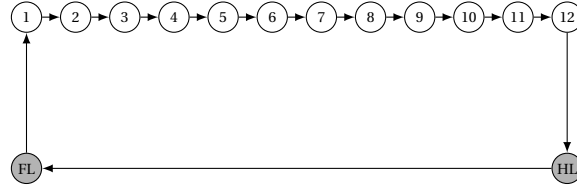


Figure 4.19 – Loop network. All oscillators have the same intrinsic frequency 0.09 Hz. All couplings have the same strength  $w_{ij} = 0.5$  and phase bias  $\phi_{ij} = 0$  except for  $\phi_{FL,HL} = \pi$ .

for all oscillators to have the same frequency are:

$$\begin{aligned} w_{i,i-1} \sin \Delta\phi_{i,i-1} &= w_{HL,n} \sin \Delta\phi_{HL,n} \\ &= w_{FL,HL} \sin \Delta\phi_{FL,HL} \\ &= w_{1,FL} \sin \Delta\phi_{1,FL} \end{aligned} \quad (4.20)$$

with  $i = 2, \dots, n$  ( $n = 12$ ).

### Loop Consistency

The phase lag between an oscillator and itself must be  $0 + 2k\pi$ . Adding the lags over one full loop, we find

$$\begin{aligned} \sum_{i=2}^n (\phi_{i,i-1} + \Delta\phi_{i,i-1}) &+ (\phi_{HL,n} + \Delta\phi_{HL,n}) \\ &+ (\phi_{FL,HL} + \Delta\phi_{FL,HL}) \\ &+ (\phi_{1,FL} + \Delta\phi_{1,FL}) = 0 + 2k\pi \quad k \in \mathcal{Z} \end{aligned} \quad (4.21)$$

### Application

With our values of  $\phi_{ij}$ , equation (4.21) reduces to

$$(n-1)\Delta\phi_{i,i-1} + \Delta\phi_{HL,n} + \Delta\phi_{FL,HL} + \Delta\phi_{1,FL} = \pi + 2k\pi$$

With our equal weights  $w_{ij}$ , equation (4.20) implies that all  $\Delta\phi_{ij}$  are equal (modulo  $2\pi$ , and excluding unstable solutions of the form  $\pi - \Delta\phi_{ij}$ ). We thus have

$$\begin{aligned} (n+2)\Delta\phi &= \pi + 2k\pi \\ \Delta\phi &= \frac{\pi + 2k\pi}{n+2} \\ \dot{\theta} &= 2\pi\nu + w \sin \frac{\pi + 2k\pi}{n+2} \end{aligned}$$

giving the following periods and phase lags:

Phase lag [%]	Period [s]
−10.71	24.76
−3.57	13.83
−3.57	9.28
10.71	7.16

which correspond to the observations in table 4.3.

### 4.5.3 Other Possibilities

There are certainly other ways of modeling rhythm switches. One option would be to have some sort of bistability at the level of the hemisegments or segments themselves, which we could model using oscillators with two limit cycles in the  $(x, y)$  space. Transient perturbations on  $x$  or  $y$  could push the system from one limit cycle to the basin of attraction of the other. Another option would be to have the frequency itself be a state variable with two stable fixed points for a given level of drive. A perturbation of the frequency would then cause a rhythm switch. In both cases, the intersegmental couplings should be designed in a way such that a switch in one oscillator propagates to the rest of the network, since *in vitro* recordings show that the whole preparation switches in one cycle.

We could also model the switch as a bifurcation where one limit cycle replaces another. In this case we would need to add a random process to the bifurcation parameter to have switches occurring randomly. The bifurcation parameter could be shared by all oscillators, allowing the whole network to switch at the same time (this would be similar to what happens in our model with the drive fluctuations and the saturation of the limb oscillators, but with the bifurcation happening at the level of the individual oscillators rather than at the network level).

Finally, multi-stability in the network might be a consequence of delays in the intersegmental couplings [Ermentrout and Ko, 2009]. Even just two phase oscillators coupled as in equation (4.19) show several stable oscillation patterns when delays are introduced in the couplings [Schuster and Wagner, 1989]. We look at this phenomenon in some detail for the implementation of the controller in the robot (section 7.3.3).

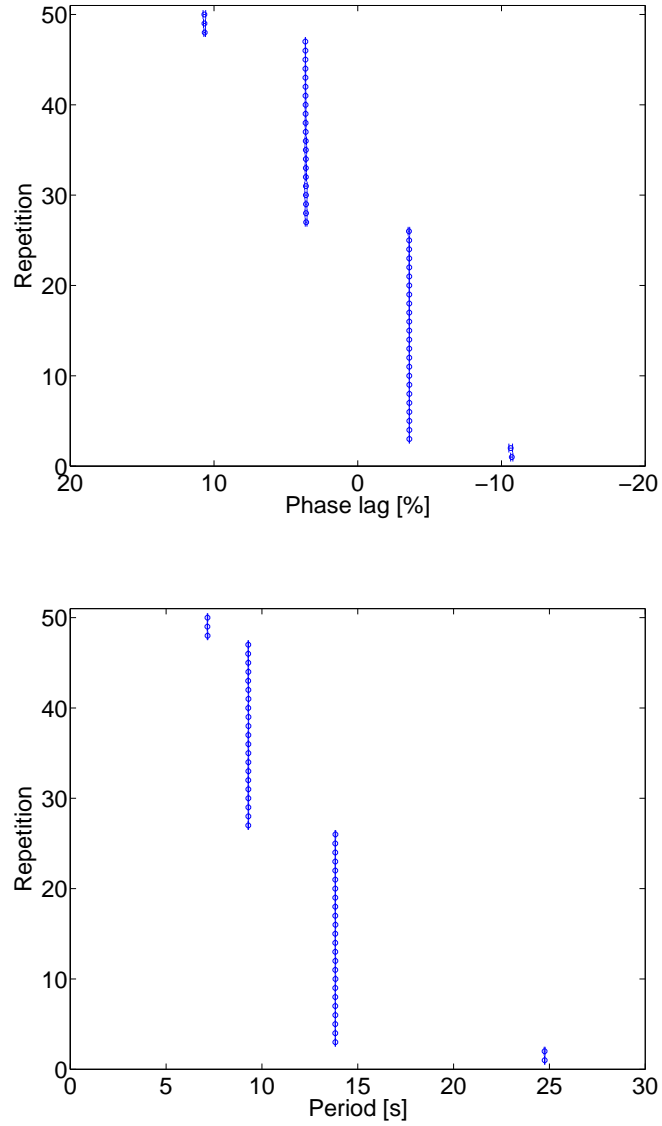


Figure 4.20 – Results for 50 simulations with the loop network of figure 4.19, with  $w_{ij} = 0.5$ ,  $\nu_i = 0.09\text{Hz}$ ,  $\phi_{ij} = 0$  except for  $\phi_{FL,HL} = \pi$ . The network can converge to four different rhythms, depending on the initial conditions.





## 5 The Flexible CPG in its Body: A Diversity of Behaviors

We have seen in chapter 4 that the model with asymmetric intersegmental couplings was successful in reproducing many observations from *in vitro* recordings, including the distribution of intersegmental phase lags and the correlation between phase lag and cycle frequency. The controllability of the network through differential drive signals to the limb and axial oscillators was demonstrated in section 4.4.5.

Our next step was to connect the CPG model to a musculo-mechanical model of the salamander, in order to reproduce the various behaviors observed *in vivo*. The mechanical body also allows for the introduction of sensory feedback in the CPG. The control architecture is shown in figure 5.1. The new components are described in the following sections.

The CPG network equations and parameter values are the same as during simulations of *in vitro* experiments (see equations (4.19) and tables 4.1 and 4.2), except for the drive, saturation thresholds and limb→axis phase bias. These are given in table 5.1. The saturation thresholds were increased from their *in vitro* values to match the higher frequencies observed *in vivo*.

Table 5.1 – CPG parameters adjusted for *in vivo* simulations.

Name	Symbol	Value
Drive	$d$	Behavior dependent
Drive random walk conv. factor	$c$	0
Drive random walk step size		0
Saturation threshold	$d^{th}$	3 (axis) 1.27 ± 0.02 (limbs)

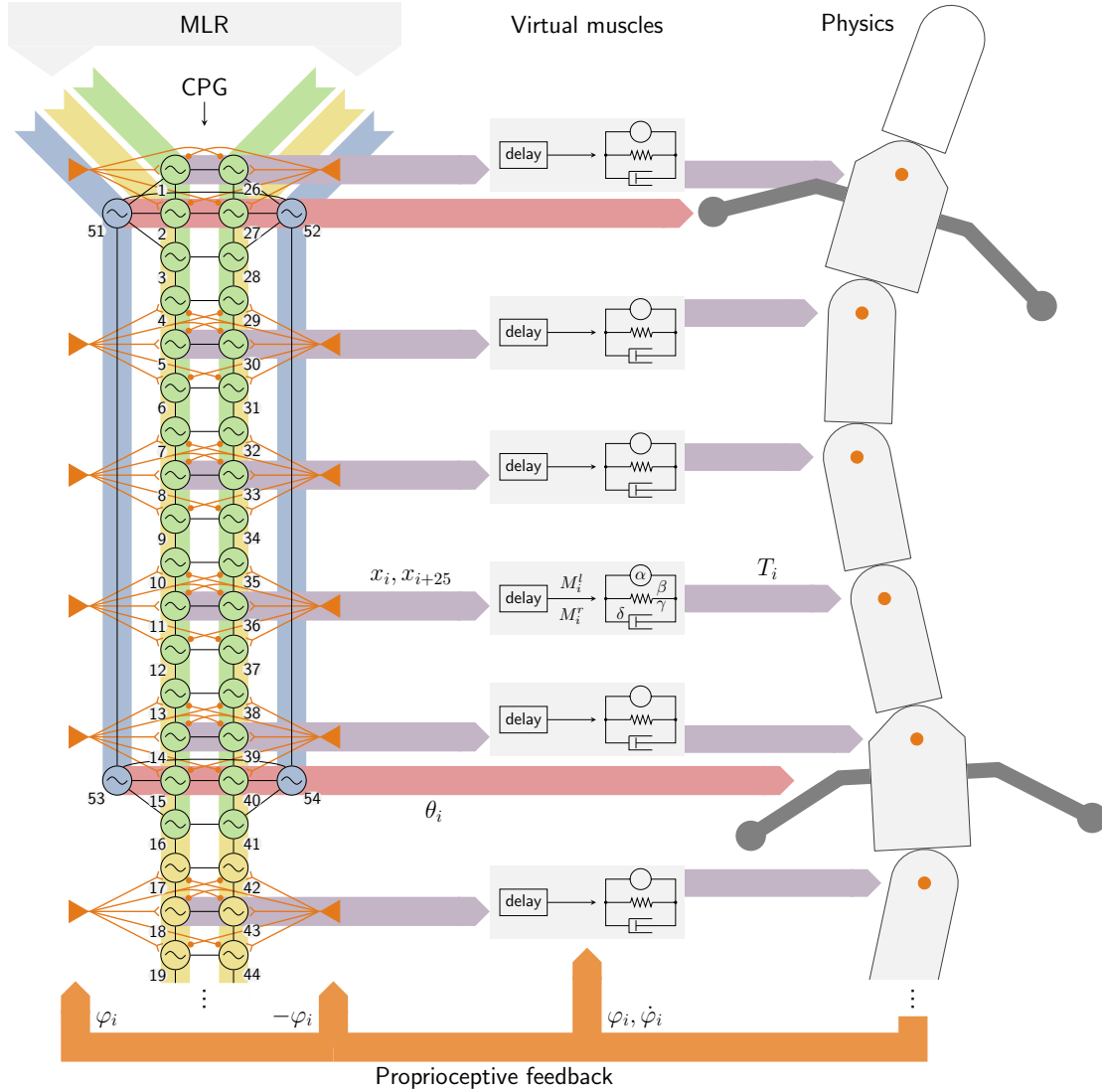


Figure 5.1 – Control architecture for the simulation of *in vivo* behaviors. **Left:** the CPG model is limited to the first 25 segments of the spinal cord, of which 19 are shown in the figure. The axial CPG is represented by a double chain of oscillators (black circles), numbered 1-25 and 26-50 for the left and right sides respectively. The limbs are represented by four additional oscillators, numbered 51-54. Black lines indicate a bidirectional coupling between two oscillators. Each oscillator also receives a drive signal representing excitation from the MLR. Different drives can be applied to the limb oscillators (blue), the trunk segments (green) and the tail segments (yellow). A stretch receptor (orange triangle) on each side of each joint projects ipsilaterally and contralaterally to the three nearest segments. The outputs  $x_i, x_{i+25}$  of one segment close to each joint is used as activation signal for the corresponding muscle (light purple lines, though they look gray on this paper); the phase  $\theta_i$  of each limb oscillator (light red) is used directly as a representation of the desired limb position. **Middle:** a delay is applied to the CPG outputs  $x_i, x_{i+25}$  to generate the left and right muscle activities  $M_i^l, M_i^r$ , to account for the muscle activation dynamics. The muscle model also takes as input the joint position  $\varphi_i$  and velocity  $\dot{\varphi}_i$  to determine the joint torque  $T_i$ , as shown in equation (5.1). **Right:** the torque  $T_i$  is applied at each axial joint (orange circles). The joint positions and velocities are measured and fed back to the muscle model (light orange lines) and the stretch receptors (joint positions only).

## 5.1 Virtual Muscles

In the model of Ijspeert et al. [2007], the output of the CPG oscillators was used as a representation of the desired trajectory of the robot joints. A PD controller was used to adjust the voltage of each motor to follow this trajectory. In the animal however, the output of the CPG is the activity of the motoneurons that innervate the muscles. It is thus more closely related to the joint torque than to the joint position.

Due to the muscle activation dynamics, it can take 20 to 50 milliseconds for the muscle to respond to a motoneuron action potential and adjust its activation state [Loeb and Ghez, 2000]. Even so, the activation state does not in itself determine the force generated by the muscle. The force is a non-linear function of the current state of stretching of the muscle, its current rate of stretching, and the activation [McMahon, 1984]. The dependence on the state and rate of stretching are similar to the effect of a non-linear spring and damper respectively.

The force generated by the muscle at the joint will add to the internal forces due to other muscles and passive body tissues, and to the external forces due to the interactions with the environment. The sum of these forces determines the angular acceleration of the joint and thus its future velocity and position.

From the above it follows that the relationship between the output of the CPG and the motion at the joints is very indirect. Incorporating the dynamics of muscles is therefore necessary to an accurate depiction of locomotion control by the CPG, and doubly so if we want to reproduce a variety of behaviors, between which the interactions with the environment might be very different. It is especially important if we want to investigate the role of sensory feedback in the control loop: because sensory feedback is typically related to the motion of the body, the dynamics of muscles will have a great impact on the shape of the feedback signal, and on its phase relative to the CPG activity.

For all these reasons, we decided to incorporate a muscle model in our control architecture. We use a spring-damper model with variable stiffness, rewritten as a rotational spring-damper system with an active element [Ekeberg, 1993], such that two antagonist muscles are combined in one viscoelastic joint (see figure 5.2):

$$T_i = \alpha(M_i^l - M_i^r) - \beta(M_i^l + M_i^r + \gamma)\varphi_i - \delta\dot{\varphi}_i \quad (5.1)$$

where  $T_i$  is the torque generated by the muscle in joint  $i$ ,  $M_i^l$  and  $M_i^r$  are the left and right muscle activation signals coming from the CPG, and  $\varphi_i$  is the joint angle. The muscle parameters  $\alpha$ ,  $\beta$ ,  $\gamma$  and  $\delta$  represent the active gain, stiffness gain, tonic stiffness and damping respectively. The  $\beta$  and  $\delta$  terms in equation (5.1) represent nonlinear approximations to the dependence of the muscle force on its state and rate of stretching.

In order to minimize the number of parameters, we started by using the same muscle parameter values in all joints. This is of course a gross approximation, and we found that weaker

muscles towards the end of the tail were necessary to maintain a uniform phase lag along the body, as shown in section 5.5. However, taper was not required for uniform lags in the real robot and actually led to poor performance (section 5.8).

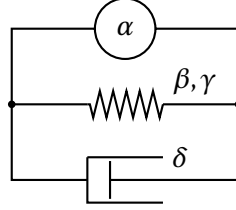


Figure 5.2 – Diagram of the rotational spring-damper muscle model. The parameters  $\alpha$ ,  $\beta$ ,  $\gamma$  and  $\delta$  represent the active gain, stiffness gain, tonic stiffness and damping respectively.

The outputs  $x_i, x_{i+25}$  of the oscillators in selected segments were delayed by 10 milliseconds and the result used as inputs  $M_i^l, M_i^r$  to the muscle model (figure 5.1). The delay was introduced as a minimum to account for the muscle activation dynamics. This was only done in simulation since on the robot, the motor torque controller already introduces a much larger delay of the order of 100 ms (see section 7.2).

### 5.1.1 Relation to a PD Controller

With its linear stiffness and damping properties, our muscle model is similar to the PD controllers typically used for position control in robotics. PD controllers with low stiffness have actually been used as an approximation of virtual muscles in robots [Fukuoka et al., 2003]. Here we explore in more details the similarities and differences between the two systems.

#### The Muscle Model as a PD Controller With Forcing Term

A PD controller attempts to minimize the error  $\tilde{\theta} = \theta - \theta_0$  between some measured variable  $\theta$  and the target value  $\theta_0$ , by adjusting its output  $y$  as a linear combination of the error and its time derivative:

$$y = K_p(\theta - \theta_0) + K_d \frac{d}{dt}(\theta - \theta_0) \quad (5.2)$$

where  $K_p$  and  $K_d$  are the *proportional* and *derivative* gains respectively.

Equation (5.1) has an active part (the  $\alpha$  term) acting against a passive part (the second and

third terms). The passive part can be read as a PD controller. Indeed, introducing

$$\begin{aligned}
 y &= T \\
 \theta &= \varphi \\
 \theta_0 &= \varphi_0 \\
 K_p &= \beta(M_f + M_e + \gamma) \\
 K_d &= \delta
 \end{aligned} \tag{5.3}$$

in equation (5.2), we find the passive part of the muscle model:

$$T = \beta(M_f + M_e + \gamma)(\varphi - \varphi_0) + \delta \frac{d}{dt}(\varphi - \varphi_0)$$

The active part is then acting as a forcing term on the PD controller.

### The Muscle Model as a Variation of the PD Controller

The whole equation of the muscle model can also be considered as a PD controller where the stiffness (proportional gain) and rest position are determined by the motoneuron activities  $M_f$  and  $M_e$ . Introducing

$$\begin{aligned}
 y &= T \\
 \theta &= \varphi \\
 \theta_0 &= \varphi_0 \\
 K_p &= \beta(M_f + M_e + \gamma) \\
 K_d &= \delta \\
 X &= -\frac{\alpha}{K_p}(M_f - M_e)
 \end{aligned} \tag{5.4}$$

in equation (5.1), we find

$$y = K_p(\theta - \theta_0 - X) + K_d \frac{d}{dt}(\theta - \theta_0) \tag{5.5}$$

or

$$y = K_p(\theta - \theta_0 - X) + K_d \frac{d}{dt}(\theta - \theta_0 - X) + K_d \frac{d}{dt}X \tag{5.6}$$

If  $\frac{d}{dt}X = 0$ , then equation (5.6) corresponds exactly to a PD controller with target value  $\theta_0 + X$ . The variable  $X = -\frac{\alpha(M_f - M_e)}{\beta(M_f + M_e + \gamma)}$  thus corresponds to an offset from the original target.

If  $X$  is varied, the muscle model doesn't quite correspond to a PD controller, because of the last term of equation (5.6), or because of the absence of  $X$  in the derivative term of equation (5.5).

In a PD controller, the derivative term reacts to changes in the error  $\theta - \theta_0$ . Changes to the offset  $\theta_0$  would affect the output through both the proportional and derivative terms (see equation (5.2)), whereas in a muscle model with constant  $\theta_0$  and varying  $X$ , changes in the offset  $X$  have no impact on the derivative term (see equation (5.5)); the derivative term only reacts to changes in the actual joint velocity (not the “error velocity”). This corresponds to a damping behavior, whereas the derivative term of the PD controller doesn’t behave exactly like a damping term when the offset  $\theta_0$  is changing. Of course, the target in equation (5.6) of the muscle model could be varied by changing  $\theta_0$  instead of  $X$ , but a nice feature of the muscle model is that both the stiffness and the trajectory are controlled by the muscle activities  $M_f$  and  $M_e$ ,

To summarize, the PD controller damps the motion relative to the target, whereas the muscle model damps the absolute motion. In a PD controller, if the measured and target values move in the same direction but with the target moving faster, the derivative term will have an “anti-damping” effect due to the increasing error. By contrast, in the muscle model, the damping will always counteract the actual motion of the joint.

Let’s express the muscle activities  $M_f$  and  $M_e$  as functions of  $X$  and  $K_p$ . From (5.4) we have

$$\begin{aligned} X &= -\frac{\alpha(M_f - M_e)}{\beta(M_f + M_e + \gamma)} \\ M_f - M_e &= -\frac{X\beta}{\alpha}(M_f + M_e + \gamma) \\ M_f + \frac{X\beta}{\alpha}M_f &= -\frac{X\beta}{\alpha}(M_e + \gamma) + e \end{aligned}$$

and finally

$$M_f = \frac{M_e(1 - \frac{X\beta}{\alpha}) - \gamma \frac{X\beta}{\alpha}}{1 + \frac{X\beta}{\alpha}} \quad (5.7)$$

Inserting (5.7) in the expression of the stiffness  $K_p$  in (5.4), we find:

$$K_p = \frac{2M_e + \gamma}{\frac{1}{\beta} + \frac{X}{\alpha}} \quad (5.8)$$

From (5.8) and (5.7), we find expressions of the muscle activities as functions of the offset  $X$  and stiffness  $K_p$ :

$$\begin{aligned} M_e &= \frac{K_p}{2} \left( \frac{1}{\beta} + \frac{X}{\alpha} \right) - \frac{\gamma}{2} \\ M_f &= \frac{K_p}{2} \left( \frac{1}{\beta} - \frac{X}{\alpha} \right) - \frac{\gamma}{2} \end{aligned} \quad (5.9)$$

Equation (5.9) gives the values of  $M_e$  and  $M_f$  for any desired stiffness  $K_p$ , and as long as  $X$  is kept constant, the muscle model will behave exactly like a PD controller. If  $X$  is varied, the effect of the additional term in equation (5.6) can be mitigated by decreasing the damping  $K_d$  or increasing the stiffness  $K_p$ .

## 5.2 The Mechanical Model in Simulation

The muscle model was used to actuate the joints of a mechanical body in simulation. The idea was to use numerical simulations to explore systematically the muscle and feedback parameter space, then to validate specific results on the robot *Salamander robotica II*. We therefore decided to simulate the robot morphology rather than the morphology of the animal. The robot is described in chapter 7. The geometry and kinematic structure of the robot was closely reproduced, except for the limbs, as shown in figure 5.3. The simulations were performed in the Webots 6 environment (Cyberbotics). The 3D physical simulation is based on Open Dynamics Engine (ODE, [www.ode.org](http://www.ode.org)). The density of the modules was set to  $920 \text{ kg/m}^3$ . The Coulomb friction parameter for the body was set to 0.04, and that of the feet to 0.4. The passive caudal fin was modeled as a chain of 10 small segments with passive stiffness [Grizou, 2011].

Robot controllers in Webots are limited to a time-step of 1 millisecond. However for an accurate simulation of the spring and damping properties of the body, smaller time-steps were necessary: the simulation was numerically stable only with a time-step of 0.5 milliseconds or less. The Webots limitation was bypassed by implementing the muscle model in a physics plugin. Muscle activation signals were sent from the controller (which integrates the CPG model) to the physics plugin using the libwebots framework<sup>1</sup>. The torque calculated as the output of the muscle model was added directly to the joint using the ODE function `dJointAddHingeTorque()`.

The same plugin was also responsible for the calculation of hydrodynamic forces.

### 5.2.1 The Hydrodynamic Model

The hydrodynamic forces were calculated using a recent extension of Lighthill's Elongated Body Theory [Boyer et al., 2008, 2010]. The model is basically the superposition of a 3D Lighthill model with a Taylor-like model for resistive forces. This model has been used successfully to model the hydrodynamics of the *Amphibot III* robot, which is a limbless version of our robot. In that work, the hydrodynamic model coefficients were fitted to the robot using data from a large number of swimming experiments.

We implemented the model in the Webots physics plugin, using the coefficients fitted to Amphibot III. The limbs were modeled as small body segments, without wake.

1. <https://ponyo.epfl.ch/redmine/projects/libwebots>

## Chapter 5. The Flexible CPG in its Body: A Diversity of Behaviors

---

The Archimedes force was initially calculated using a simple approximation of the immersed volume of each segment, and the result applied to the center of mass. This lead to unrealistic behaviors in the model when the robot was coming partially out of water. In particular, an almost fully immersed passive robot would capsize for no apparent reason.

We implemented a more accurate calculation of the Archimedes to remediate this problem, based on the following steps:

1. The intersections between the edges of the parallelepiped<sup>2</sup> and the water surface are calculated.
2. The intersection points are ordered using a simple Gift wrapping algorithm to form the top face of the immersed polyhedron.
3. The volume and centroid of the immersed polyhedron are calculated using Mirtich's formulas [Eberly, 2002].
4. The Archimedes force is calculated from this volume and applied at the centroid.

The polyhedra used in this calculation are represented with a blue overlay on the swimming robot in figure 5.3. Thanks to the more accurate calculation of the Archimedes force, the unrealistic behaviors disappeared. The stability of the robot was also increased when swimming at the surface of water.

---

2. Note that the force is only calculated for the parallelepiped in each module . The final value is multiplied by a constant factor to compensate for the cylindrical volumes that were omitted.



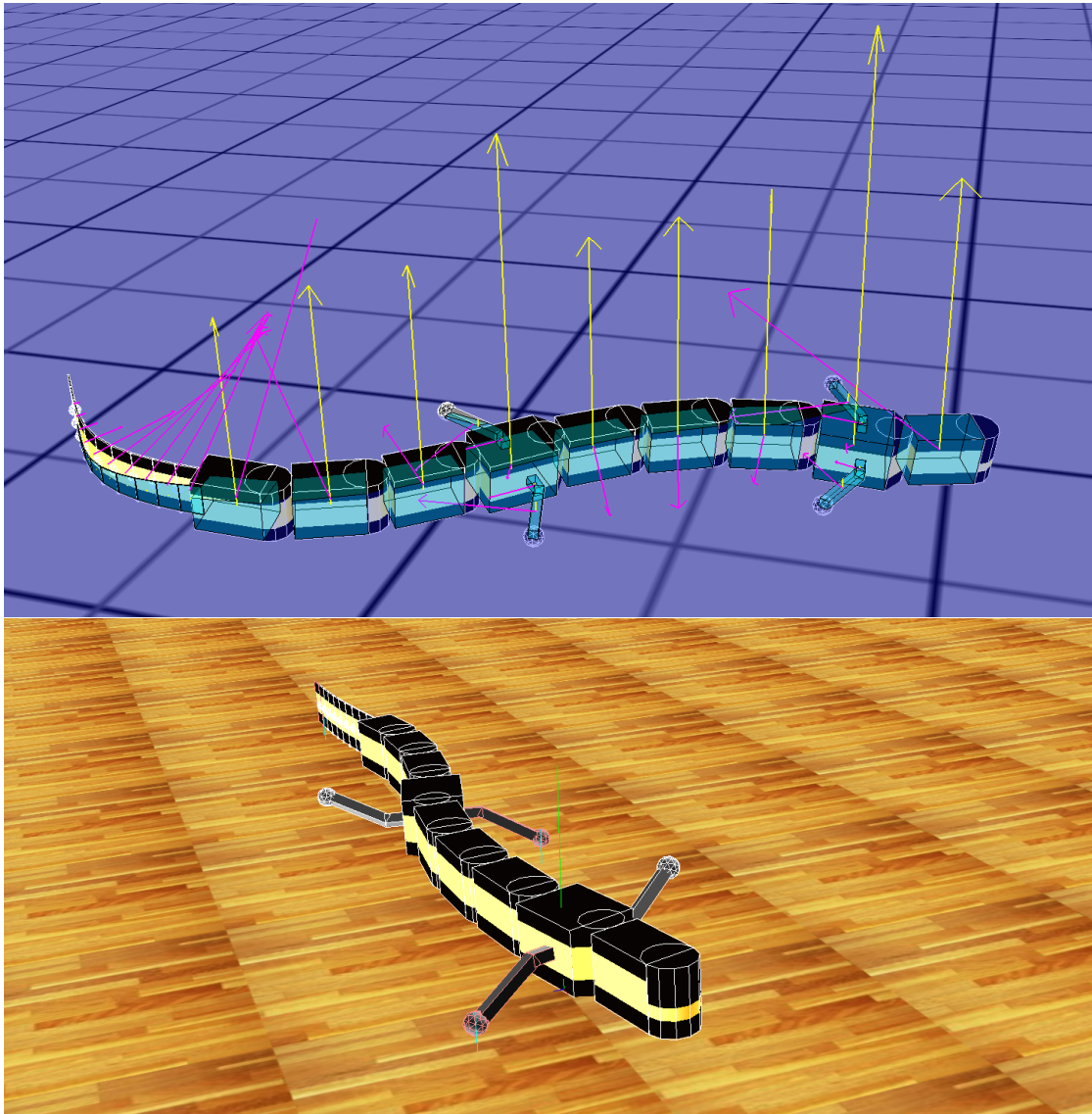


Figure 5.3 – Simulations of swimming and forward land stepping in the Webots environment. In the swimming simulation, the Archimedes and hydrodynamic forces are represented in yellow and magenta respectively (with different scales). A blue overlay on the modules highlights the immersed parts, the volume of which is used to calculate the Archimedes force.

### 5.3 Integrating Local Sensory Feedback in the CPG

Taking the combined model composed of the CPG, the virtual muscles and the mechanical model, we can close the loop by introducing sensory feedback. We first discuss the nature of the feedback that we will use, then the ways of integrating this feedback in the CPG equations.

#### 5.3.1 The Nature of the Feedback

We are specifically interested in local feedback distributed along the body of the animal, in contrast to descending signal feedback from the vestibular system for example. Indeed, it seems particularly interesting to investigate how local feedback interacts with descending commands to shape the activity of the CPG. In choosing a form of sensory feedback to include in the model, we again took inspiration from work on the lamprey. The best documented form of local feedback in the lamprey is probably the feedback from stretch-sensitive edge cells in the spinal cord [Viana Di Prisco et al., 1990]. Cells of similar morphology have been observed in the salamander [Schroeder and Egar, 1990] but their sensitivity to stretching has not been verified. These findings form the basis for the inclusion of proprioceptive feedback in many lamprey and salamander models [Ekeberg, 1993, Ekeberg et al., 1995, Ijspeert et al., 2005, Harischandra et al., 2011], including ours.

The local proprioceptive feedback  $s_i$  for oscillator  $i$  is calculated from the joint angle  $\varphi_i$ :

$$s_i = w_i^{\text{ipsi}} s_i^{\text{ipsi}} + w_i^{\text{contra}} s_i^{\text{contra}} \quad (5.10)$$

with  $s_i^{\text{ipsi}}$  and  $s_i^{\text{contra}}$  the positive part of  $\varphi_i$  and  $-\varphi_i$  respectively, for the left side ( $-\varphi_i$  and  $\varphi_i$  for the right side). The same feedback signal is sent to the 3 segments closest to each joint (see figure 5.1). This leaves segments 3 and 16 without feedback, which is reasonable since the amplitude of the body curvature is smallest at these positions in the animal [Karakasiliotis et al., 2012].

To reduce the number of parameters, we decided to use the same feedback strengths in all segments:

$$\begin{aligned} w_i^{\text{ipsi}} &= w^{\text{ipsi}} \\ w_i^{\text{contra}} &= w^{\text{contra}} \end{aligned} \quad (5.11)$$

We conducted initial tests regarding the relative strengths of ipsilateral and contralateral feedback, and found that the two parameters were mostly redundant for our purpose. We did find that changing their relative values was useful to compensate for varying delays in the control loop (data not shown), but we had no use for this capability. We chose to set:

$$w^{\text{contra}} = -w^{\text{ipsi}} \quad (5.12)$$

#### 5.3.2 Incorporating a Cartesian Feedback in a Polar Oscillator

We incorporate local proprioceptive feedback by reading the joint angle from the simulation and sending it back to the CPG . Given two oscillators in Cartesian coordinates, with state variables  $x_i$  and  $y_i$  for  $i \in 1, 2$ , we know that adding  $x_2$  to  $\dot{x}_1$  for example will allow for the entrainment of oscillator 1 by oscillator 2, provided that their intrinsic frequencies are not too different [Pikovsky et al., 2003]. This motivated our choice to have the feedback act on the CPG like a direct coupling between two Cartesian oscillators, as it should allow us to reproduce another important finding in biology: numerous experimental studies *in vitro* have shown that subjecting the lamprey spinal cord to discrete or periodic bending has a strong effect on the fictive locomotion pattern [McClellan and Sigvardt, 1988, Williams et al., 1990, Kiemel et al., 2003, Tytell and Cohen, 2008]. In particular, periodic bending can entrain the CPG rhythm in a typical a range of 90% to 140% of the resting frequency [Williams et al., 1990, Tytell and Cohen, 2008]. This capability is attributed to the presence of the stretch-sensitive edge cells in the spinal cord. In keeping with the idea of a phylogenetic conservatism between the lamprey and the salamander, we wanted to be able to reproduce this effect in our model.

Note that it would be difficult to have the joint angle signal act on an oscillator like a regular coupling, i.e. another term in the sum of equation (4.19): for this we would need to know explicitly the phase of the joint angle. By using a Cartesian coupling, we avoid this difficulty but create another: we now need to incorporate a Cartesian coupling in a Polar oscillator.

We start with the isolated oscillator equation from the system (4.19),

$$\begin{aligned}\dot{r} &= a(R - r) \\ \dot{\theta} &= \omega\end{aligned}\tag{5.13}$$

with  $\omega = 2\pi\nu$ , and rewrite it in Cartesian coordinates using the transformation

$$\begin{aligned}x &= r \cos \theta \\ y &= r \sin \theta\end{aligned}\tag{5.14}$$

We find generic differential equations for the Cartesian states  $\dot{x}$  and  $\dot{y}$  by taking the time-derivative of (5.14):

$$\begin{aligned}\dot{x} &= \dot{r} \cos \theta - r \dot{\theta} \sin \theta = \frac{\dot{r}}{r} x - y \dot{\theta} \\ \dot{y} &= \dot{r} \sin \theta + r \dot{\theta} \cos \theta = \frac{\dot{r}}{r} y + x \dot{\theta}\end{aligned}\tag{5.15}$$

Introducing (5.13) in (5.15) gives us the Cartesian equations for our oscillator:

$$\begin{aligned}\dot{x} &= \frac{a(R-r)}{r}x - y\omega \\ \dot{y} &= \frac{a(R-r)}{r}y + x\omega\end{aligned}\tag{5.16}$$

with  $r = \sqrt{x^2 + y^2}$ . We can now introduce the Cartesian feedback signal  $s$  in the oscillator:

$$\begin{aligned}\dot{x} &= \frac{a(R-r)}{r}x - y\omega + s \\ \dot{y} &= \frac{a(R-r)}{r}y + x\omega\end{aligned}\tag{5.17}$$

The remaining part of the work is to convert (5.17) back to Polar coordinates. We start with the relation

$$r^2 = x^2 + y^2\tag{5.18}$$

and differentiate with respect to time:

$$\begin{aligned}2r\dot{r} &= 2x\dot{x} + 2y\dot{y} \\ \dot{r} &= \frac{x\dot{x} + y\dot{y}}{r}\end{aligned}\tag{5.19}$$

Replacing  $\dot{x}$  and  $\dot{y}$  from (5.17) gives

$$\begin{aligned}\dot{r} &= \frac{x}{r} \left( \frac{a(R-r)}{r}x - y\omega + s \right) + \frac{y}{r} \left( \frac{a(R-r)}{r}y + x\omega \right) \\ \dot{r} &= \frac{1}{r^2} a(R-r)(x^2 + y^2) + \frac{x}{r}s\end{aligned}\tag{5.20}$$

and using (5.18) and (5.14) we find

$$\dot{r} = a(R-r) + s \cos \theta\tag{5.21}$$

To find the expression of  $\dot{\theta}$  with feedback, we use a linear combination of (5.15),

$$\begin{aligned}\dot{x} &= \frac{\dot{r}}{r}x - y\dot{\theta} & | \cdot (-y) \\ \dot{y} &= \frac{\dot{r}}{r}y + x\dot{\theta} & | \cdot x\end{aligned}$$

which gives us

$$x\dot{y} - \dot{x}y = x^2\dot{\theta} + y^2\dot{\theta} \quad (5.22)$$

$$\dot{\theta} = \frac{x\dot{y} - \dot{x}y}{r^2} \quad (5.23)$$

and introducing  $\dot{x}$  and  $\dot{y}$  from (5.17):

$$\begin{aligned} \dot{\theta} &= \frac{1}{r^2} \left( \frac{xy}{r} a(R-r) + x^2\omega - \frac{xy}{r} a(R-r) + y^2\omega - ys \right) \\ \dot{\theta} &= \frac{x^2 + y^2}{r^2} \omega - \frac{ys}{r^2} \end{aligned} \quad (5.24)$$

and finally, with (5.18) and (5.14):

$$\dot{\theta} = \omega - \frac{s}{r} \sin \theta \quad (5.25)$$

Introducing the new feedback terms from equations (5.21) and (5.25) into the CPG equations of (4.19), we find the CPG equations with feedback:

$$\begin{aligned} \dot{\theta}_i &= 2\pi\nu_i + \sum_j r_j w_{ij} \sin(\theta_j - \theta_i - \phi_{ij}) - \frac{s_i}{r_i} \sin \theta_i \\ \dot{r}_i &= a_i(R_i - r_i) + s_i \cos \theta_i \\ \dot{x}_i &= r_i(1 + \cos \theta_i) \\ \dot{y}_i &= d_i e_i \\ R_i &= d_i P(d_i, d_i^{th}) \end{aligned} \quad (5.26)$$

The influence of this feedback on the dynamics of the CPG is analyzed in detail in chapter 6.

## 5.4 Systematic Exploration of the Muscle and Feedback Parameter Space

The simplicity of our CPG and mechanical models allows us to run tens of thousands simulations in a few days. We were thus able to explore the muscle and feedback parameter spaces systematically, and choose parameter values based on the global picture of the fitness landscapes, rather than by trusting an optimization algorithm.

Rather than exploring the whole six-dimensional space  $(\alpha, \beta, \gamma, \delta, w^{\text{ipsi}}, w^{\text{contra}})$  in one time, we used an iterative process, fixing some parameters while others were varied. Compared with an optimization algorithm, we are not guaranteed to settle on an (locally) optimal value, but we get a better intuition of the effect of each parameter on the dynamics of the system. We show here some results around our final parameter values.

### 5.4.1 Fitness Measurements

In our search for good muscle and feedback parameters, we tried to optimize the following fitness measurements:

1. **Speed:** This is an obvious measure of fitness for any particular gait.
2. **Feedback effect:** This is a rather intuitive, ill-defined fitness. It relates to one of our core motivations: we want to investigate the role of muscle dynamics and sensory feedback in salamander locomotion. Therefore we are interested in parameter values that show an interesting effect of feedback on the CPG, e.g. such that feedback modulates the intersegmental phase lag.
3. **Intersegmental phase lag:** The model is supposed to reproduce the five salamander behaviors described in section 2.2, which are characterized by specific cycle frequencies and CPG and kinematic intersegmental phase lags. We generally have no problem reproducing an arbitrary cycle frequency, but phase lags can be problematic. We want at least that the qualitative differences in phase lags between the five behaviors be reproduced with the model. All the measures of phase lag along the body that we present below are calculated as a lag between two consecutive *segments*, in percentage of a cycle duration. The kinematic phase lags that we measure between two *modules* are always converted to the equivalent intersegmental values. Also, since the biological data at our disposal concerns mostly the mid-trunk, we perform all our measurements on the second, third and fourth axial joints. The fifth joint is excluded as it is under strong mechanical influence from the second girdle.
4. **Periodicity:** When (strong) feedback is introduced in the CPG, periodicity becomes a concern as the CPG pattern can become erratic. We try to avoid aperiodic gaits.
5. **Maximal torques:** Since we want to eventually reproduce our results on the robot, we look for parameter values that stay in its range of operation. Our robot is capable of generating up to 0.7 Nm in each axial joint (see section 7.2).

Regarding the *feedback effect* fitness, our CPG model provides a natural benchmark: the intrinsic intersegmental phase of 6.6% is quite inappropriate for swimming. In an open-loop model we would adjust it through differential drive signals. However we found early on that with appropriate muscle parameter values and feedback strengths, this open-loop CPG pattern could be significantly decreased by sensory feedback, leading to a dramatic increase in swimming speed. However this effect often led to unstable gaits, in the sense that swimming was aperiodic, with transient phases showing poor performance.

We therefore started to explore systematically the parameter space with the swimming gait, looking for a large region where feedback would have the beneficial effect of decreasing the phase lag and at the same time cause no loss of periodicity.

All the tests in this section were made using “average individuals”: the standard deviations of the excitabilities were set to 0. This gave us more reproducible results while searching for

good muscle and feedback parameters. This restriction was relaxed at the time of validating the simulation results on the robot (see section 5.8).

### 5.4.2 Selection of the Muscle Damping Constant

The damping parameter  $\delta$  is critical to the stability of the model. If it is too low, the energy of the system is not sufficiently dissipated and the simulation is mechanically unstable. If it is too high, the simulation becomes numerically unstable, requiring a smaller time-step. This is not a problem with the model per se, but limits the possibilities of exploration of the parameter space depending on the simulation time constraints. In our case the time-step was not the limiting factor, but we found that large damping constants led to decreased performance. This is to be expected, since a high damping amounts to a lot of lost energy.

As explained previously, we focused on the effect of feedback in choosing our parameter values. Figure 5.4 shows a beneficial effect of feedback in a large region of the  $(\beta, w^{\text{ipsi}})$  parameter space (dark regions in the bottom panels), with stronger feedback needed when  $\beta$  (i.e. the stiffness) increases. However only a very small part of this region corresponds to perfectly periodic rhythms (upper right panel).

Figure 5.5 shows the results obtained after increasing the damping constant to 0.1. The periodic region is larger, and the speed a bit lower as expected. Figure 5.6 shows the results for  $\delta = 0.15$ . The periodic region has shrunk again, and the speeds are even lower.

From these observations we decided to set  $\delta = 0.1$ .

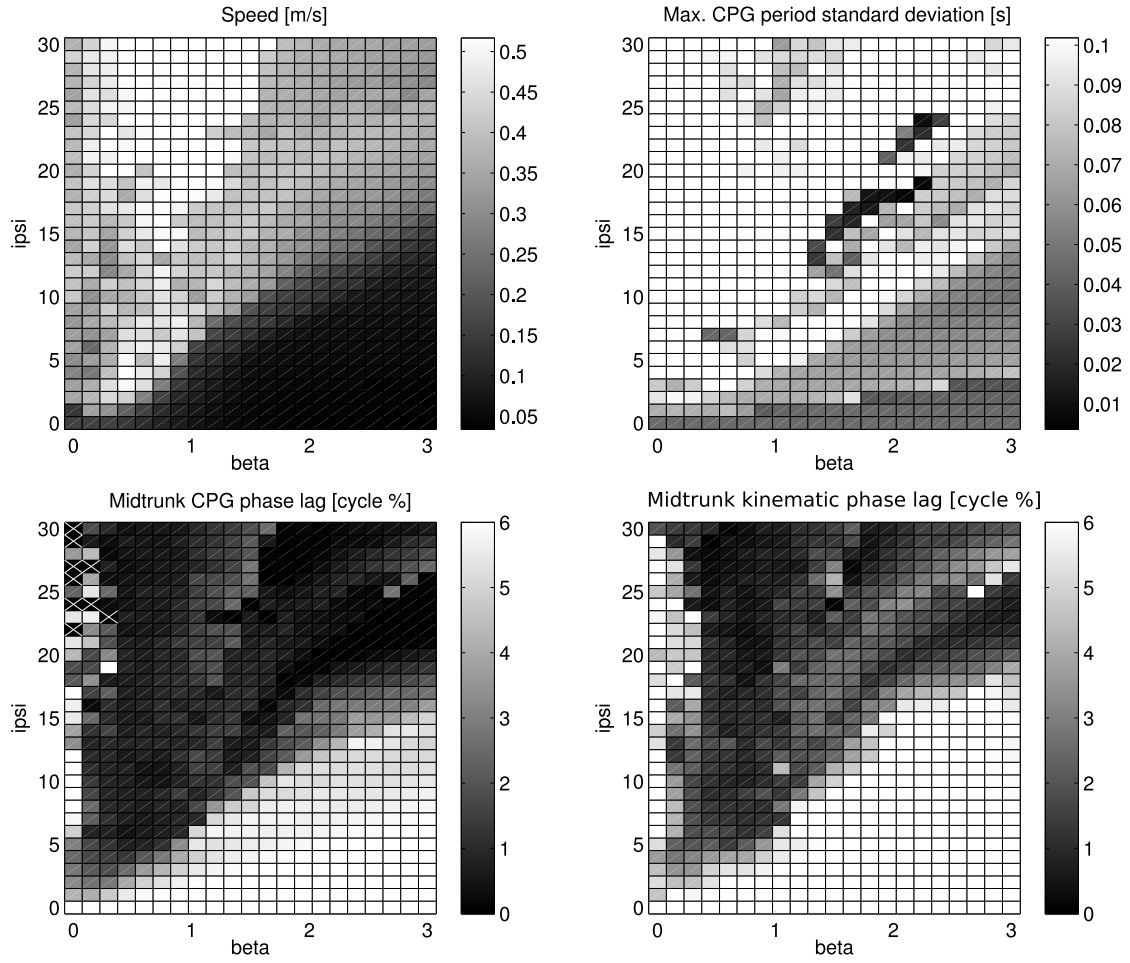


Figure 5.4 – Systematic exploration of the  $(\beta, w^{\text{ipsi}})$  parameter space in swimming simulations with  $\alpha = 0.4$ ,  $\gamma = 0$  and  $\delta = 0.05$ . **Upper left and bottom:** Without feedback  $w^{\text{ipsi}} = 0$ ) the CPG produces patterns with phase lags of 6.6%, leading to very small speeds. Increasing the feedback leads to a drop in the CPG and kinematic phase lags (bottom left and bottom right) and an increase in swimming speed. Higher  $\beta$  values, which correspond to stiffer bodies, require stronger feedback for the same effect on the CPG. **Upper right:** Maximum standard deviation of the cycle period among the oscillators. Only a small region of the parameter space (in black) gives perfectly periodic rhythms.



#### 5.4. Systematic Exploration of the Muscle and Feedback Parameter Space

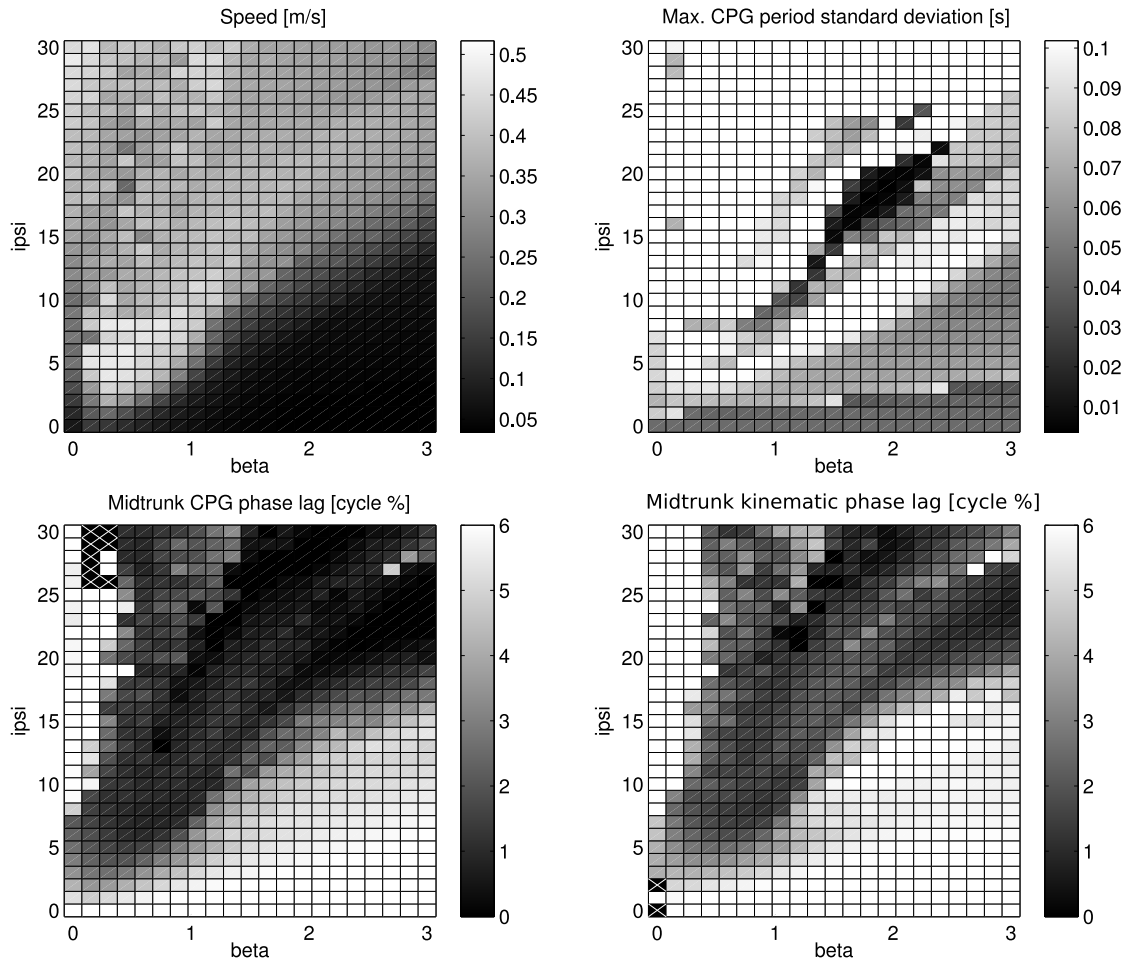


Figure 5.5 – Systematic exploration of the  $(\beta, w^{\text{psi}})$  parameter space in swimming simulations with  $\alpha = 0.4$ ,  $\gamma = 0$  and  $\delta = 0.1$ .

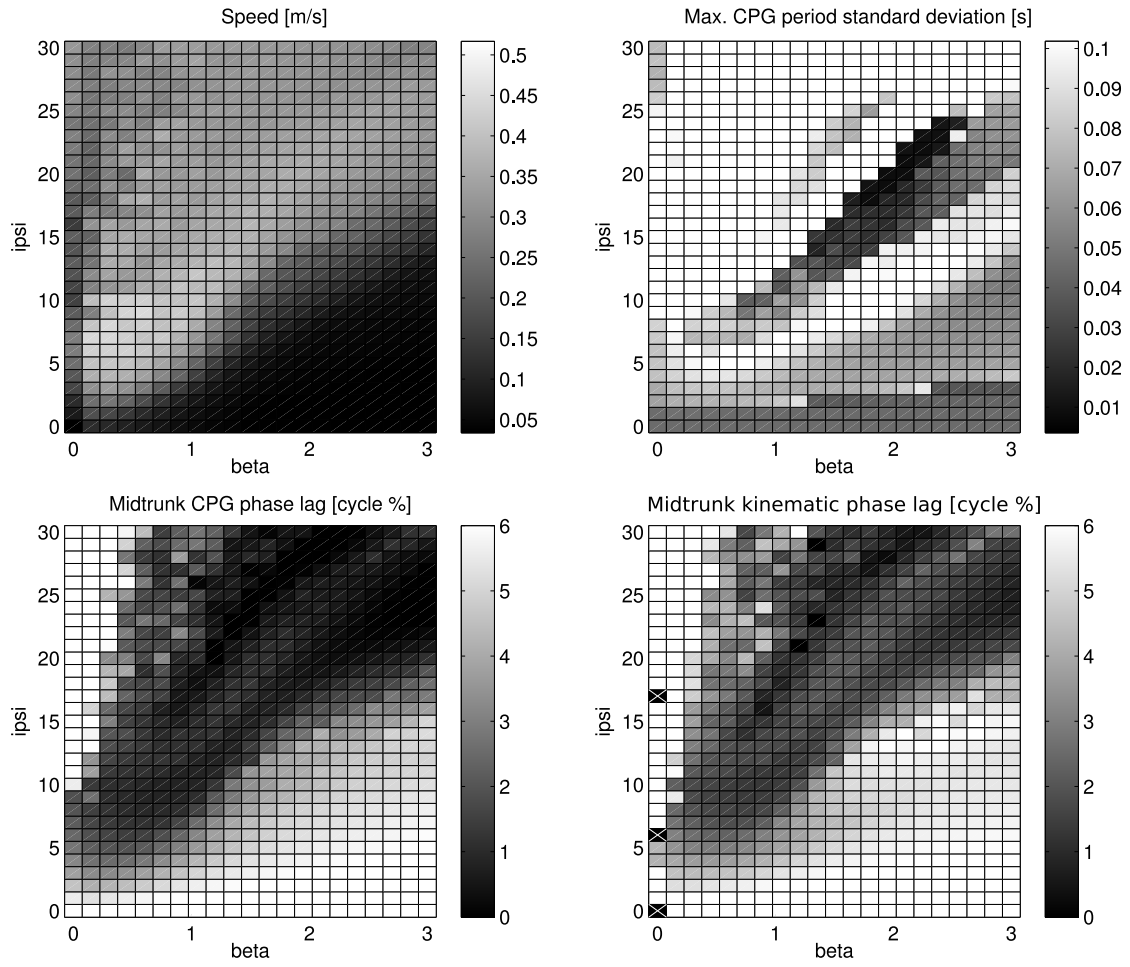


Figure 5.6 – Systematic exploration of the  $(\beta, w^{\text{ipsi}})$  parameter space in swimming simulations with  $\alpha = 0.4$ ,  $\gamma = 0$  and  $\delta = 0.15$ .

### 5.4.3 Selection of the Muscle Stiffness and Feedback Strength

We have seen in the previous section that appropriate feedback strengths depend strongly on the stiffness. We therefore explored the corresponding parameters together.

Figure 5.7 shows the result of a systematic exploration of the  $(\beta, \gamma)$  space with  $w^{\text{ipsi}} = 19$ . These simulations were performed with a drive of 1.34, corresponding to an intrinsic frequency of 1.47 Hz. We first note that in this case  $\beta$  and  $\gamma$  are mostly redundant, as both can be varied to adjust the stiffness. We see again a small region of periodic rhythms (upper right panel, black region) where feedback has a strong effect on the CPG pattern (lower left panel, same area). Looking at the results obtained with  $w^{\text{ipsi}} = 21$  and  $w^{\text{ipsi}} = 24$  (figures 5.8 and 5.9 respectively) we see that a feedback strength of 21 maximizes the size of the periodic region. We therefore set  $w^{\text{ipsi}} = 21$ .<sup>3</sup>

Figure 5.8 also provides us with an optimal stiffness, with a degree of freedom due to the redundancy of  $\beta$  and  $\gamma$ . Remembering that the salamander shows passive tail undulations during underwater stepping (chapter 2), we decided on a small but non-zero value for the tonic stiffness with  $\beta = 1.2$  and  $\gamma = 0.2$ .

---

3. For this level of drive. The scaling of the feedback strength with the drive is addressed in chapter 6.

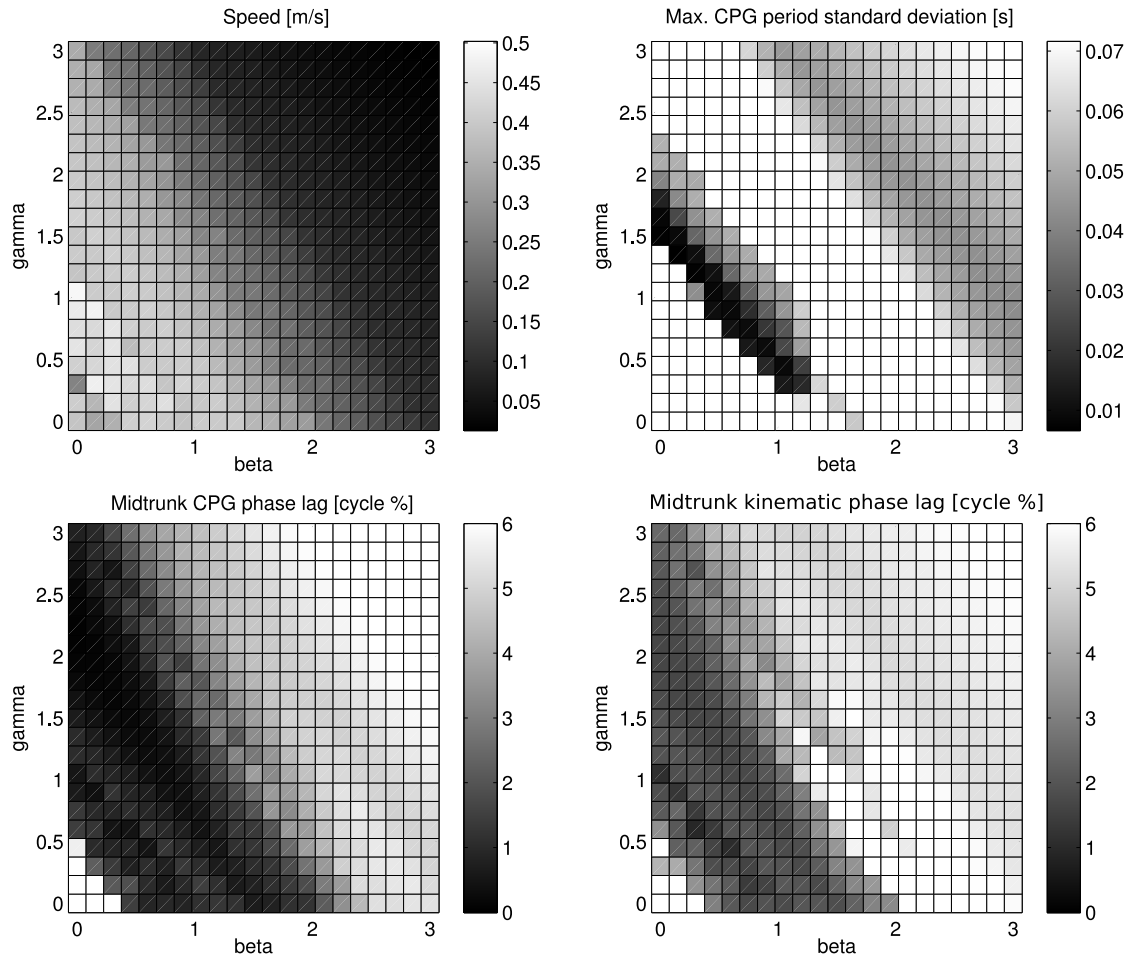


Figure 5.7 – Systematic exploration of the  $(\beta, \gamma)$  parameter space in swimming simulations with  $\alpha = 0.4$ ,  $\delta = 0.1$  and  $w^{\text{ipsi}} = 19$ .

#### 5.4. Systematic Exploration of the Muscle and Feedback Parameter Space

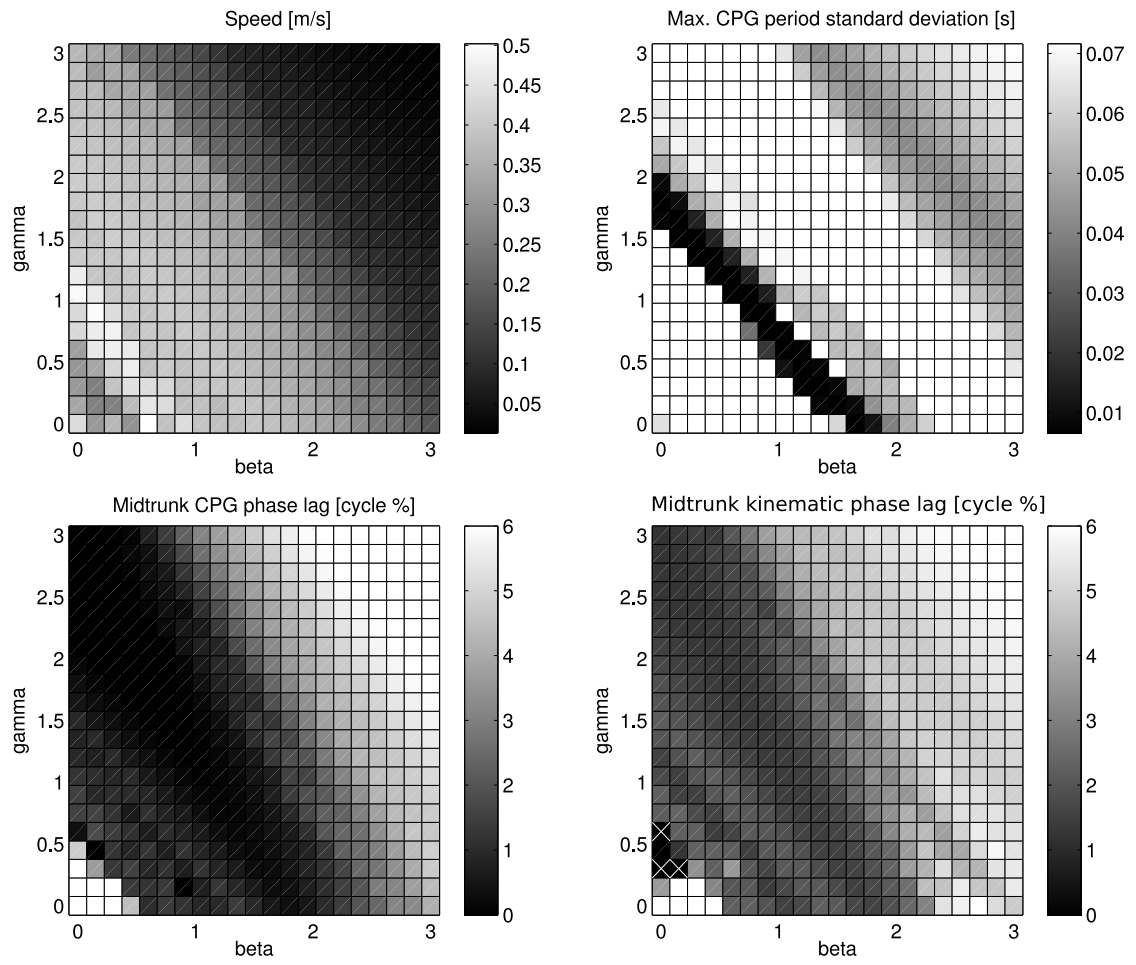


Figure 5.8 – Systematic exploration of the  $(\beta, \gamma)$  parameter space in swimming simulations with  $\alpha = 0.4$ ,  $\delta = 0.1$  and  $w^{\text{ipsi}} = 21$ .

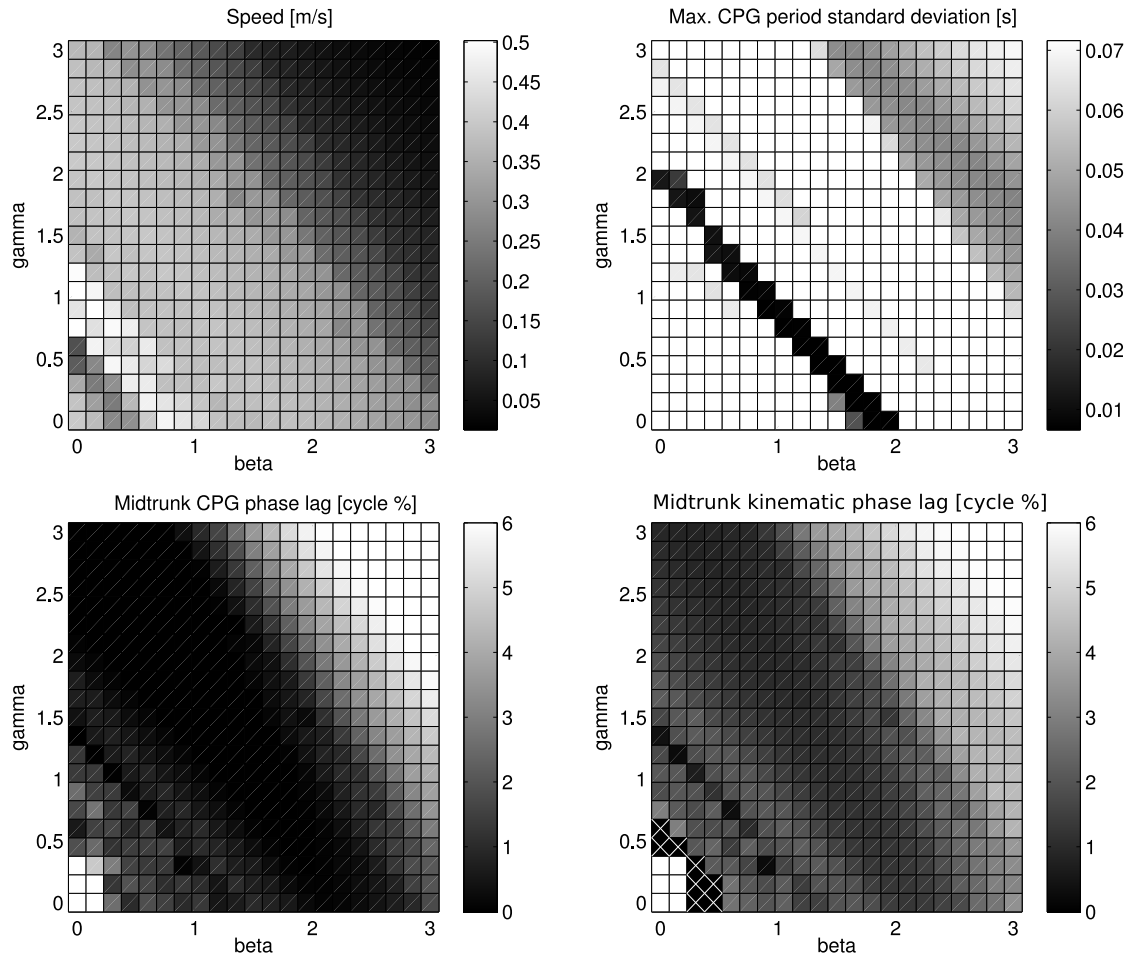


Figure 5.9 – Systematic exploration of the  $(\beta, \gamma)$  parameter space in swimming simulations with  $\alpha = 0.4$ ,  $\delta = 0.1$  and  $w^{\text{ipsi}} = 24$ .

#### 5.4.4 Selection of the Muscle Gain

The active gain  $\alpha$  controls the amplitude of the joint oscillations: larger values allow the muscles to push further on each side at a given cycle frequency. Larger amplitudes (up to a point) lead to higher swimming speeds. Alternatively,  $\alpha$  can be increased together with the stiffness (through either  $\beta$  or  $\gamma$ ) to produce the same joint angles with more rigidity, in order to resist perturbations for example.

The previous results were obtained with an active gain  $\alpha = 0.4$ . This value was selected as a trade-off between the maximization of the speed and the minimization of the muscle torques: the periodic region in figure 5.8 is at the limit of our robot's capabilities, with maximum torques between 0.67 Nm ( $\beta = 1.65$ ,  $\gamma = 0$ ) and 0.85 Nm ( $\beta = 0$ ,  $\gamma = 1.8$ ).

### 5.5 Salamander Behaviors in Simulation

Having selected muscle and feedback parameter values for swimming, our next step was to try and reproduce all five behaviors with the same model. The excitatory drives to the CPG oscillators were tuned to reproduce typical EMG patterns for each behavior, in terms of cycle frequency and intersegmental phase lags. In accordance with the principles of controllability described in section 4.4.5, we were able to reproduce the CPG patterns for the five behaviors using differential activation of only two parts of the network, with one level of drive used for the limb oscillators and another used for the axial oscillators.

The cycle frequencies targeted with the model were set to half that of the EMG recordings. This was chosen to reflect the scaling of locomotion frequency with body mass observed in animals [Bejan and Marden, 2006].

As described in the next section, we found it necessary to introduce body taper in the form of weaker muscles in the tail. This is in agreement with a simulation study of the lamprey from McMillen et al. [2008] which found that taper was necessary to reproduce the CPG-kinematic phase lags observed in the animal. We implemented taper by multiplying the parameters  $\alpha$  and  $\beta$  in modules 6, 7 and 8 by a factor 0.7, 0.5 and 0.3 respectively.

For behaviors involving the limbs, a transfer function on the phase  $\theta_i$  of the limb oscillators was used to adjust the duty factor to 77%, as observed during forward and backward land stepping in the salamander [Ashley-Ross and Lauder, 1997, Ashley-Ross et al., 2009]. An optimal phase bias, in terms of speed, was determined for the limb→body CPG couplings. A value  $\phi_{ij} = 1.83$  was found to be a compromise that gave good performance for underwater stepping as well as forward and backward land stepping.

In the next sections we show typical CPG and kinematic patterns that were obtained, and the adjustments that were sometimes necessary to reproduce a particular behavior.

### 5.5.1 Swimming

Swimming patterns for four conditions are shown in figure 5.10, using the same muscle parameters:  $\alpha = 0.4$ ,  $\beta = 1.2$ ,  $\gamma = 0.2$  and  $\delta = 0.1$ . The drive was set to 1.34, corresponding to an intrinsic frequency of 1.47 Hz.

The bottom-left panel shows the closed-loop pattern obtained with the feedback strength  $w^{\text{ipsi}} = 21$  selected in section 5.4.3, with the same level of drive applied to all oscillators. The local sensory feedback has an accelerating effect on the CPG, increasing the frequency to 1.54 Hz. Apart from a deviation at joint 2, the CPG phase lag is quite uniform along the body. The CPG-kinematic delay increases towards the tail, as observed in the animal (see section 3.1).

The phase lag deviation around joint 2 is due to the absence of sensory feedback in segment 3 (see figure 5.1). As discussed in chapter 6, the absence of feedback leads to a relative decrease of excitation in this segment. This has the effect of increasing the lag between segments 2 and 3. The late oscillation of segment 3 also causes the following segments to be delayed, which explains the high lag between joints 1 and 2 (segments 1 and 5) in the figure. Interestingly, a similar irregularity in the CPG activity has been observed in the animal (see section 2.2). A previous modeling study also found that sensory feedback was a likely explanation [Bem et al., 2003].

The bottom-right panel shows the same simulation with the body taper removed, so that all muscles have the same strength. In this case the muscles in the tail are too strong; the last active joint in particular is seen to catch-up with the CPG, giving a smaller CPG-kinematic lag locally. As explained in chapter 6, this smaller CPG-kinematic lag, close to  $\frac{\pi}{2}$ , has a maximal accelerating effect on the corresponding joints, causing a decrease of the CPG phase lag towards a quasi-standing wave. We note also from the trajectories of the neck joint, at the top, that the first segment is not frequency-locked with the rest of the body. A stable gait without taper would thus require an adjustment to the feedback strength.

In the upper-left panel, we show how large the intersegmental phase lag would be in absence of feedback. This large phase lag can also be decreased by giving less excitation to the first segment than to the rest of the body (here 1.03 and 1.34 respectively).



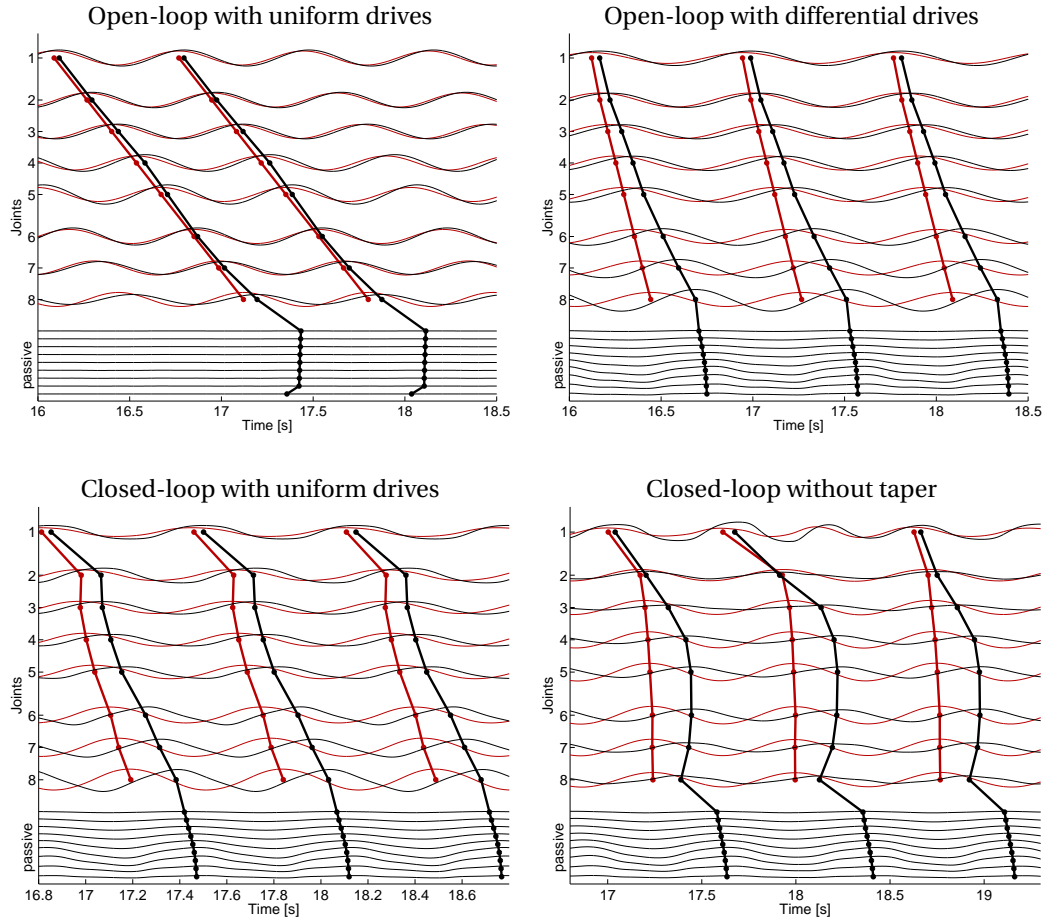


Figure 5.10 – Swimming patterns in simulation. Thin lines represent the left CPG oscillator (red) and kinematic (black) oscillations at each joint. Circular markers are placed at the centroid of the positive half of the oscillation in each cycle. The centroids are used to calculate the phase lag between consecutive modules. The phase lags are proportional to the slope of the thick lines that connect the centroids. **Top left:** With the same drive to all oscillators, the CPG network without feedback produces a very large intersegmental phase lag of 6.6%. **Top right:** Using a 23% lower drive for the first segment gives a much more natural phase lag close to 2%. The kinematic phase lag is significantly higher. **Bottom left:** With a strong sensory feedback, the phase lag is also reduced to about 2% in spite of the uniform drives. Here also the kinematic phase lag is greater than the CPG phase lag. **Bottom right:** Same condition as in the left panel, but with uniform muscle strengths along the body. The absence of taper causes great irregularities at the level of the last active joint.

### 5.5.2 Forward Land Stepping

Good open-loop patterns for forward land stepping were obtained with limb and axial drives of 1.21 and 0.657 respectively (figure 5.11 left). The kinematics however displayed significant deviations from the CPG pattern, which are not observed in the animal. This could be remediated by increasing the tonic stiffness  $\gamma$  from 0.2 to 0.6 (figure 5.11 right). Interestingly, this increased stiffness was not necessary with the robot (section 5.8).

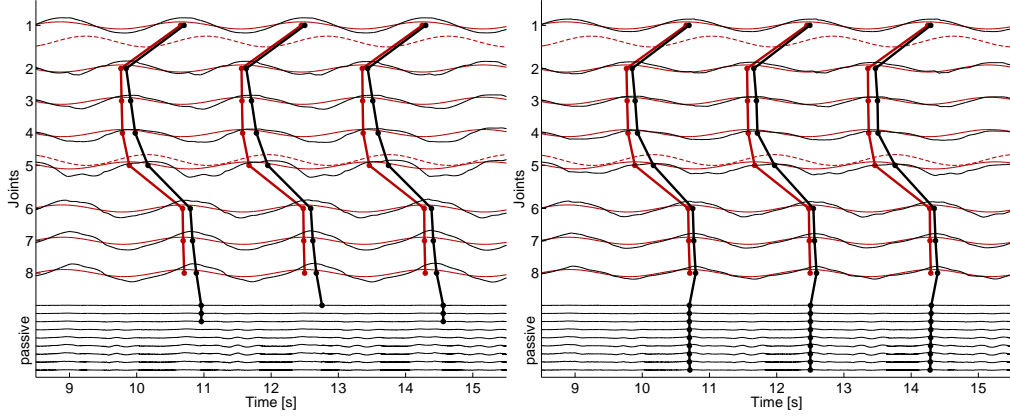


Figure 5.11 – Open-loop forward stepping in simulation. See figure 5.10 for a general description. Here the output of the limb oscillators is shown in dashed red. **Left:** CPG and kinematic patterns using the same muscle parameters as for swimming. **Right:** The kinematic pattern follows the CPG more closely after increasing the tonic stiffness  $\gamma$  from 0.2 to 0.6.

Next, the effect of sensory feedback on forward land stepping was analyzed. Figure 5.12 (top left) shows that without differential drive or feedback, the CPG with active limbs produces backward traveling waves with large negative phase lags. These correspond to the right peak of the *in vitro* distribution of section 4.4.3. However, introducing a similar (but weaker) axial proprioceptive feedback as in swimming has a counter-productive effect. This is illustrated in the top-right panel, using the open-loop pattern of figure 5.11 and setting  $w^{\text{ipsi}} = 1.4$ . The CPG phase lag is again negative. The kinematic pattern deviates significantly from the CPG pattern and shows positive lags.

Since a positive ipsilateral and negative contralateral feedback had a counter-productive effect, we tried inverting the ipsilateral and contralateral weights. With  $w^{\text{ipsi}} = -w^{\text{contra}} = -1.4$ , we get a nearly standing wave in the trunk even when using uniform drives.

Finally, we considered introducing excitatory feedback signals from the limbs, as proposed in [Harischandra et al., 2011]. We used the following simplified expression, introduced directly in the equation for the phase derivative  $\dot{\theta}$  in the limb oscillators:

$$\dot{\theta} = \omega + w^{\text{limb}} \max\left(0, 1 - \frac{|\varphi - \varphi_0|}{\frac{\pi}{2}}\right) \quad (5.27)$$

where  $\varphi$  is the angle of the rotational limb joint and  $\varphi_0$  the angle at the transition from stance

to swing. The feedback is maximal at the end of the stance and decreases linearly on either side until it reaches zero. The rate of decrease is such that the feedback is non-zero for a quarter of the leg rotation.

We found that this limb feedback with a strength  $w^{\text{limb}} = 5$  could almost generate a standing wave in a network with uniform drives (figure 5.12 bottom-right).

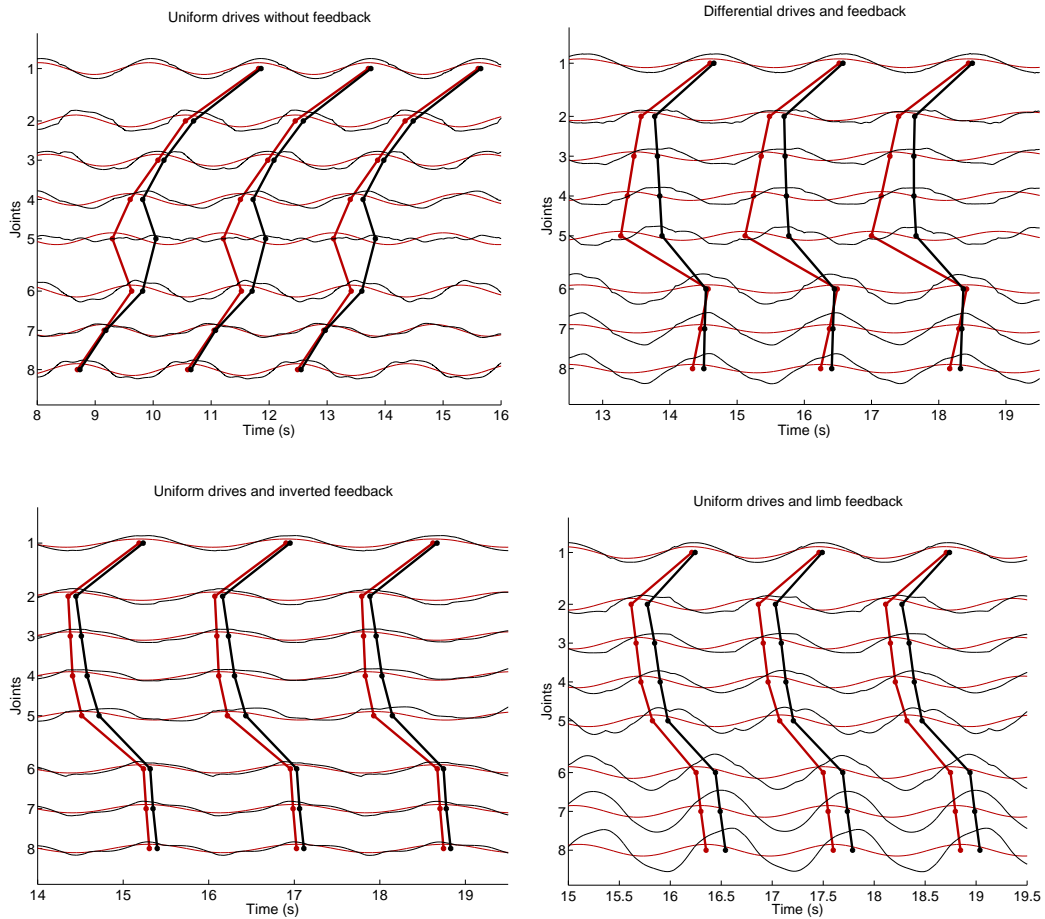


Figure 5.12 – Feedback effect in forward land stepping. In all four cases  $\gamma$  was set to 0.2. In cases of uniform drive, the drive was 0.9. **Top left:** Without differential drive or feedback, the CPG with non-saturated limb oscillators produces caudorostral waves of activity. **Top right:** Using the same drives as in figure 5.11, the axial proprioceptive feedback (here  $w^{\text{ipsi}} = 1.4$ ) has a counter-productive effect of reducing the phase lag. **Bottom left:** Inverting the ipsilateral and contralateral weights (i.e. setting  $w^{\text{ipsi}} = -1.4$ ) leads to an increase in phase lags such that differential drives are not necessary. **Bottom right:** Good patterns can also be obtained with uniform drives using excitatory feedback from the limbs.

We decided to disable sensory feedback when simulating the other behaviors, and use differential activation of the limb and axial oscillators exclusively. It is likely that similar results could be obtained by replacing partially or completely the drive difference with limb sensory feedback.

### 5.5.3 Underwater Stepping

Underwater stepping is particularly interesting due to the passive tail undulations observed in the animal (chapter 2). This behavior required adapting the buoyancy of the robot to keep it at the bottom of the pool. This was achieved by decreasing all Archimedes forces by 8%.

We simulated underwater stepping with active and passive tails (without feedback), using differential drives to the limb and axial oscillators (0.84 and 0.44 respectively) to generate an almost standing wave in the axis, in agreement with the EMG recordings. The passive tail was simulated by setting the drive to zero in the tail oscillators. We then looked at the hydrodynamic forces in both cases. We note that this is an example of a study that was possible in simulation, that we could not have done on the real robot.

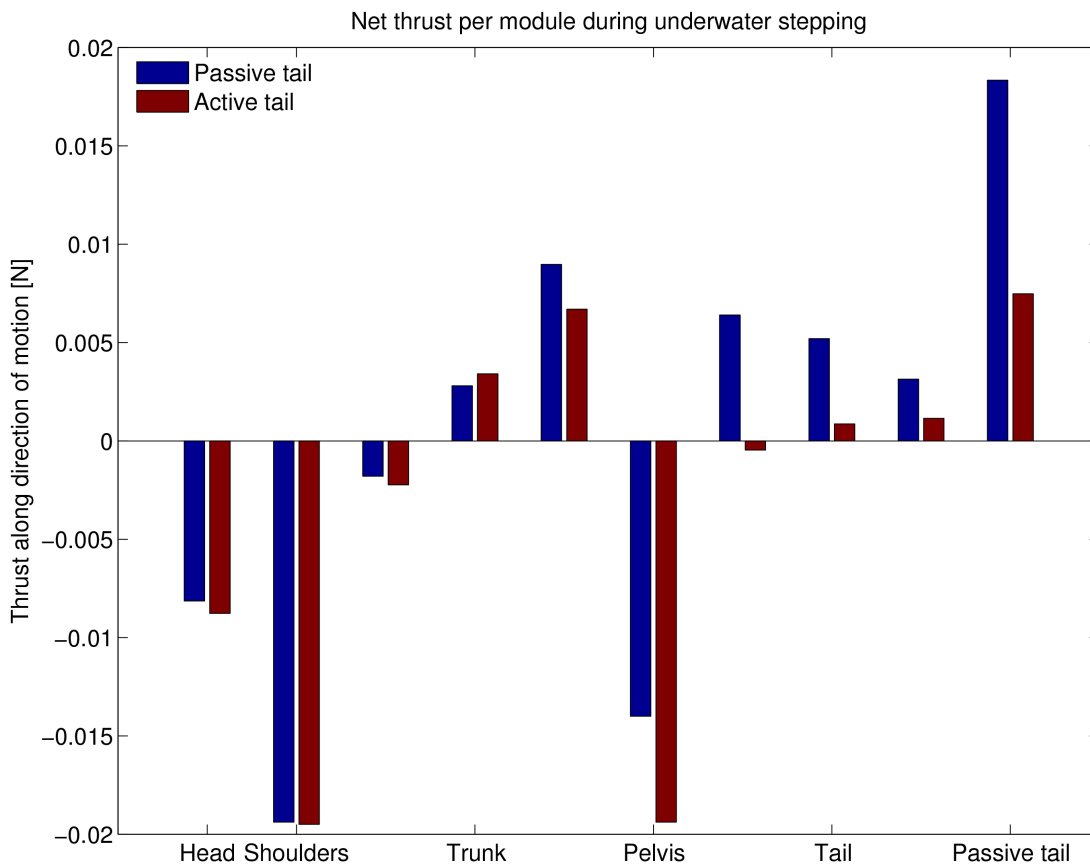


Figure 5.13 – Comparison of hydrodynamic forces during water stepping in simulation with active vs. passive tail.

Figure 5.13 shows the result of this analysis. We see that the passive tail generates much more thrust than the active tail. It actually generates enough thrust to mostly overcome the drag generated in the rest of the body. The low efficiency of the active tail can be understood intuitively: When the tail is passive, the oscillations induced by the almost standing wave in the trunk propagate down the tail, generating a traveling wave that helps moving forward.

When the tail is active, it actively tried to generate a quasi-standing wave, which is not as efficient as the passive traveling wave.

The oscillation patterns in both cases are shown in figure 5.14. The tail oscillations look remarkably similar despite the significant difference observed in hydrodynamic forces.

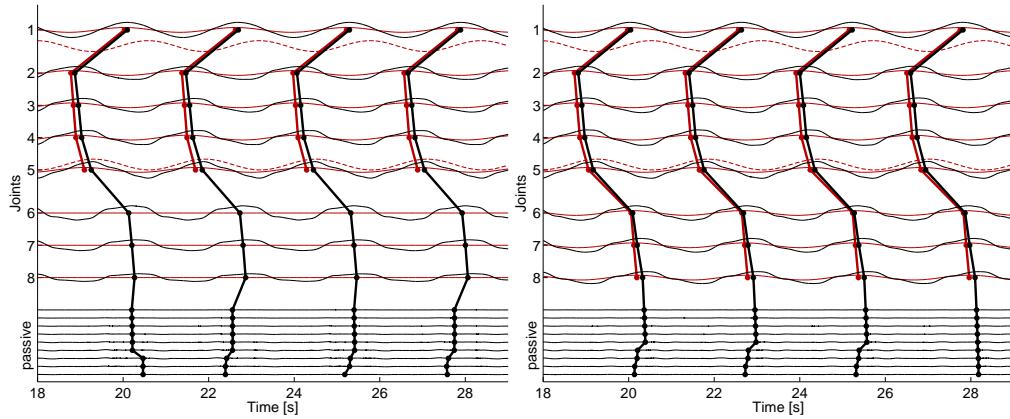


Figure 5.14 – Underwater stepping in simulation. **Left:** Passive tail. **Right:** Active tail.

#### 5.5.4 Backward Stepping

The simulation of backward stepping required two adaptations. First, the direction of rotation of the limbs had to be inverted. This was done by multiplying the phase  $\theta_i$  of the limbs by -1 at the output of the CPG. Second, the muscles had to be made stronger.

Figure 5.15 (left) shows that with the muscle parameters used in the previous behaviors, the CPG fails to impose a traveling wave in the trunk. Good results were obtained by multiplying the muscle gain  $\alpha$  and stiffness  $\beta$  by 10 (right panel). The differential drives were set to 0.51 and 0.22 for the limb and axial oscillators respectively.

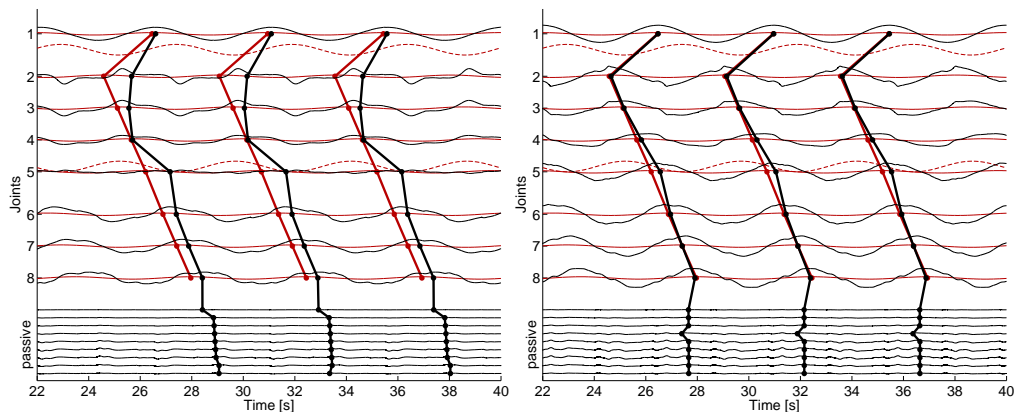


Figure 5.15 – Backward stepping in simulation. **Left:** Normal muscle parameters. **Right:** Muscle gain  $\alpha$  and stiffness  $\beta$  multiplied by ten.

### 5.5.5 Struggling

The simulation of struggling required fixing the hind girdle to the floor. However the robot should be free to adjust its pitch angle depending on the rotation of the limbs. This was implemented in ODE by removing the tail and using a hinge joint between the hind girdle and the world.

Friction between the robot and the floor was reduced by a factor 2, to mirror the experimental conditions with the animal, which was moving on a table covered with oil.

Finally, the simulation of struggling also required stronger muscles, as shown in figure 5.16. We used the same parameters as for backward stepping, multiplying  $\alpha$  and  $\beta$  by a factor 10.

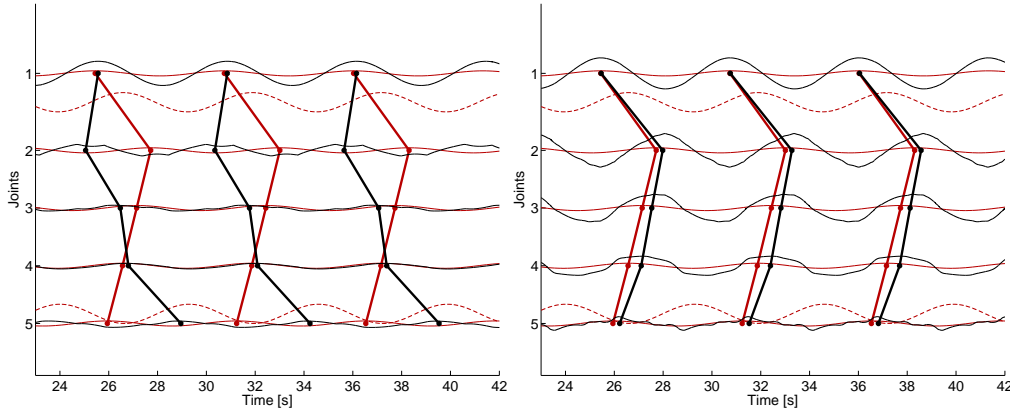


Figure 5.16 – Struggling in simulation. **Left:** Normal muscle parameters. Only five joints are shown as the tail was not simulated. The kinematics deviate wildly from the CPG pattern. **Right:** Muscle gain  $\alpha$  and stiffness  $\beta$  multiplied by ten.

## 5.6 Turning

The study of Ijspeert et al. [2007] showed that turning gaits could be generated by using differential drive signals between the left and right sides in a double chain of oscillators. However it is not obvious to what extent the principle applies to our control architecture based on virtual muscles. It is also not clear how the differential drive between each side would interact with the local sensory feedback.

We did not investigate turning gaits in detail, but we performed a few tests to verify that the left-right differential drive mechanism also works in our model. The results are shown in figure 5.17. We see that the mechanism works very well, with and without feedback. Note that with feedback (right panels), the robot does not swim quite straight even before the turning begins. It appears that the controller with local sensory feedback but no steering is more sensitive to the initial conditions.

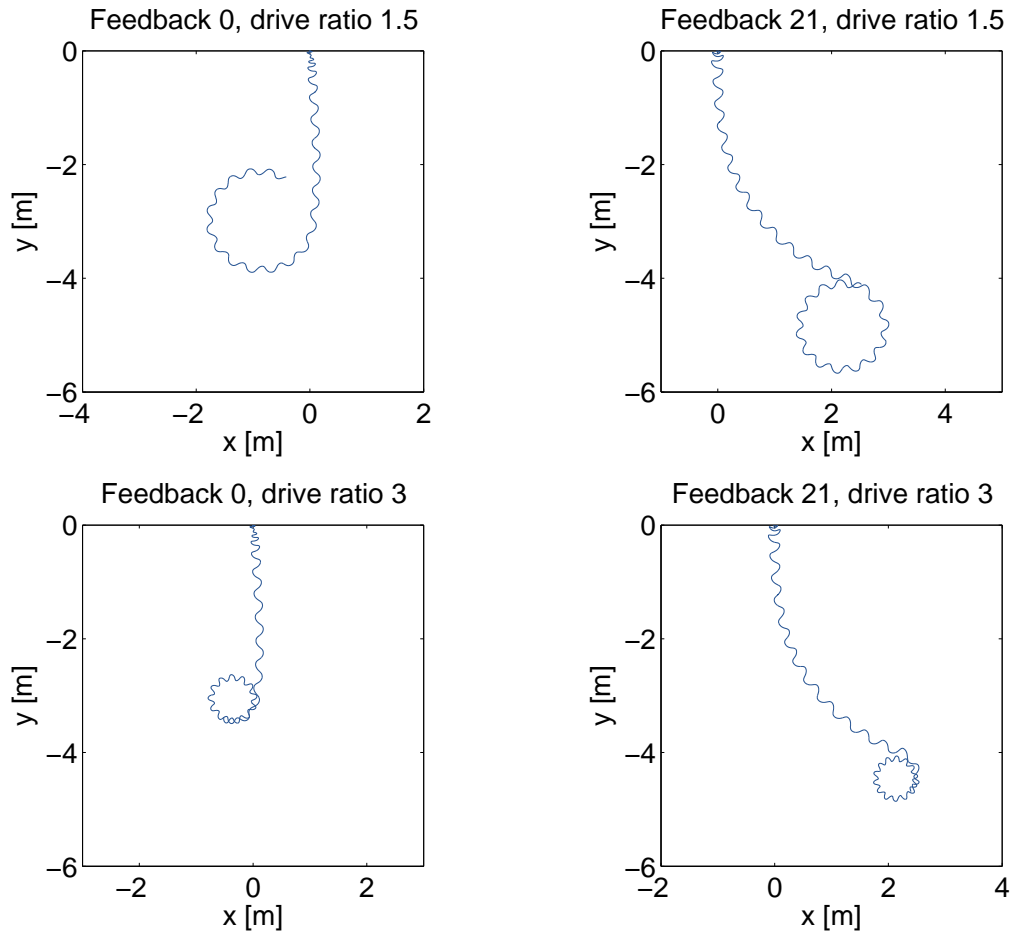


Figure 5.17 – Turning during swimming in simulation. An imbalance in the drives between the left and right chains of oscillators was introduced after 10 seconds of simulation. The trajectory of the head is shown without and with axial proprioceptive feedback (left and right side respectively). In the cases without feedback, a differential drive of 1.03 in the neck vs 1.34 in the rest of the body was used. For the top panels, the drive in the left and right chains of oscillators was multiplied by 1.2 and 0.8 respectively, yielding a ratio of 1.5. For the bottom panels the drives were multiplied by 1.5 and 0.5 respectively (ratio of 3).

## 5.7 Gait Transitions

To conclude the simulation study, we show two transitions from in figure 5.18. For the top panel, differential drives were used for the swimming gait. The forward stepping drives were replaced with the swimming drives after 10 seconds of simulation. For the bottom panel, the forward stepping drives were replaced with a uniform drive, and axial feedback was enabled (it was disabled during forward stepping).

In both cases, the transition is made in about one cycle. However, the open-loop network needs about 7 cycles for the intersegmental phase lags to converge to their final value. The closed-loop network converges in 2 or 3 cycles.



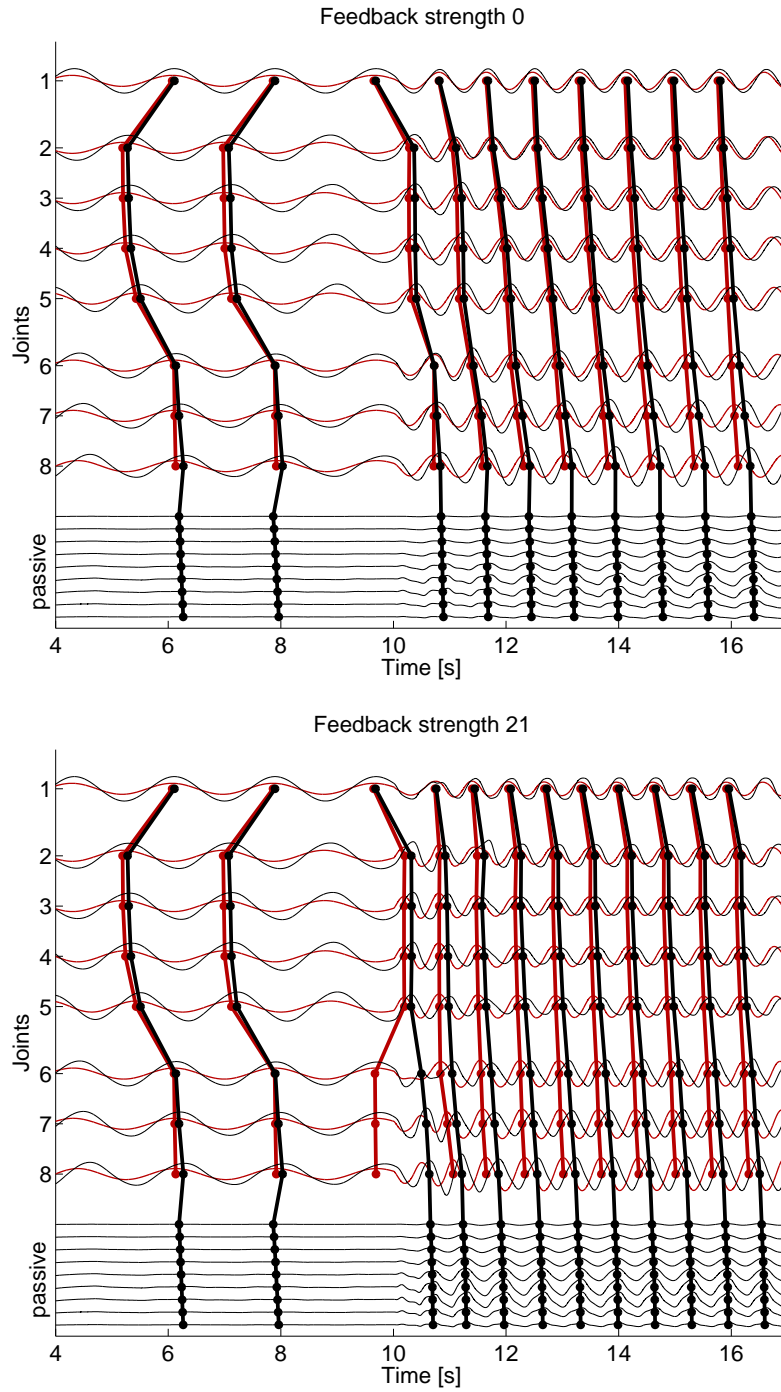


Figure 5.18 – Walk-swim gait transitions in simulation. **Top:** Transition to swimming without feedback. After 10 seconds, the forward stepping drives are replaced with a differential drive of 1.03 in the neck vs 1.34 in the rest of the body. The network needs about 7 cycles to converge to its final phase lag after the transition, as seen from the CPG-kinematic lag in joint 8. **Bottom:** Transition to swimming feedback. After 10 seconds, the forward stepping drive are replaced with a uniform drive of 1.34 and axial feedback is enabled with a strength  $w^{\text{ipsi}} = 21$ . The network needs only 2 or 3 cycles to converge after the transition.



## 5.8 Robot Experiments

We used the CPG model of section 4.4 and the muscle parameters of section 5.4 to drive the robot *Salamandra robotica II* [Crespi et al., 2013]. Chapter 7 describes the robotic platform from a control perspective. The control architecture in figure 7.5 can be compared to that used in simulations, shown in figure 5.1. The speed was measured in each experiment using an external video tracking system described in section 7.4. The tracking system was also used to record the trajectory of each module, in order to calculate the actual intersegmental kinematic phase lag.<sup>4</sup>

The robot model differs from the simulation in three respects. First, the control architecture does not include an artificial delay between the output of the CPG and the input of the virtual muscles, since the PI torque controller already introduces a larger delay (chapter 7). Second, sensory feedback was removed in the neck, as it was destabilizing, leading to aperiodic rhythms. Note that such feedback is presumably weak in the animal, since neck oscillations are very small, while in the robot the neck oscillations are quite large, due to the uniform muscles parameter values along the body that we have assumed for simplicity. A model that reproduces the low amplitude of neck oscillations (for example by increasing the neck stiffness) and that includes neck feedback would presumably give qualitatively similar results. Figure 5.25 shows that the inclusion or exclusion of neck feedback does not change the effect of feedback on the CPG phase lag qualitatively, at least during forward land stepping. The effect of neck feedback during swimming is addressed in chapter 6. The third modification is the removal of the body taper that was used in simulation. As described below, we found that taper in the form of weakened muscles in the tail was not necessary to produce nearly uniform phase lags in the robot, and was actually detrimental to performance and stability.

Two adaptations were made to the robot to reproduce the different behaviors. During underwater stepping, the buoyancy was adjusted by adding 72 g of lead inside the head. During backward stepping, tape was added under the feet to increase slipping, mirroring the conditions of the animal experiments.

As in simulations, the cycle frequencies targeted with the model were set to half that of the EMG recordings. Due to the limits of operation of the robot, the target value for swimming was further lowered down to 1.1 Hz.

Five different “individuals” were modelled with the robot, by initializing the CPG model parameters with different random seeds. The excitatory drives were adjusted for each “individual” and each motor behavior. The same muscle parameter values could be used to reproduce swimming, underwater stepping and forward land stepping, while backward land stepping and struggling required stronger muscles (see table 5.2). The CPG and kinematic patterns obtained with one individual are given in appendix A.

---

4. The actual kinematics differ from the estimation of the motor encoders due to the elasticity of the connectors between the robot modules.

Table 5.2 – Muscle and feedback parameters for robot experiments

Name	Symbol	Value
Feedback strength	$w^{\text{ipsi}}$	10 (swimming)
Muscle strength	$\alpha$	0.5 4 (backward stepping, struggling)
Muscle active stiffness	$\beta$	1.2 12 (backward stepping, struggling)
Muscle tonic stiffness	$\gamma$	0.2
Muscle damping	$\delta$	0.1

We found that compared to the simulations, the muscle gain  $\alpha$  had to be increased on the robot to obtain reasonable amplitudes of oscillation during swimming. The top panel in figure 5.19 shows that a 25% increase of  $\alpha$  had a great impact on the swimming speed. However the tail oscillations were still rather small. We therefore decided to remove the body taper and use the same muscle parameters in the tail as in the trunk. This had an even greater impact on the swimming speed, as can be seen in the figure. It also led to nicer, more periodic gaits, as shown in the bottom-right panel. The bottom-left panel shows that the larger oscillations enhanced the effect of feedback on the intersegmental phase lag, shifting the plot to the left.

During swimming, the same high level of drive could be used for limb and axial oscillators. The strong drive would cause the limb oscillators to saturate. The axial network without sensory feedback would produce a travelling wave with high mid-trunk intersegmental phase lags of  $6.1 \pm 1.4$  %, reflecting the main peak of the *in vitro* phase lag distribution. This is very unlike the 2% EMG phase lag in the animal and leads to poor swimming. The CPG phase lag could be decreased by lowering the drive to the most rostral oscillator, as proposed in models of the lamprey CPG [Kozlov et al., 2009], and as shown in simulation in section 5.5.1. Alternatively, we found that a strong axial proprioceptive feedback could significantly decrease the CPG phase lag (phase lag  $1.9 \pm 1.1$  %), leading to a dramatic improvement in swimming speeds (figure 5.24). The effect of feedback on the intersegmental phase lags is illustrated in figure 5.20. The slope of the lines connecting the circular markers in the figure represents the intersegmental phase lags (with vertical lines corresponding to a phase lag of zero). Before introduction of sensory feedback, the phase lag is too large for the robot to swim efficiently. The introduction of feedback reduces the phase lags to appropriate values. The variability between individuals is also reduced by the introduction of feedback: while the third individual, in red, is an outlier in the open-loop case (dashed lines), it has a phase lag similar to the other individuals in the closed-loop case (solid lines).

The remaining motor behaviors, which involve rhythmic limb activity, required setting the limb→body phase bias to an appropriate value. Systematic tests with steps of 0.5 were conducted to find an optimal limb→body CPG phase bias in terms of speed. The results are shown in figure 5.21. For forward land stepping an underwater stepping, we found a common optimal

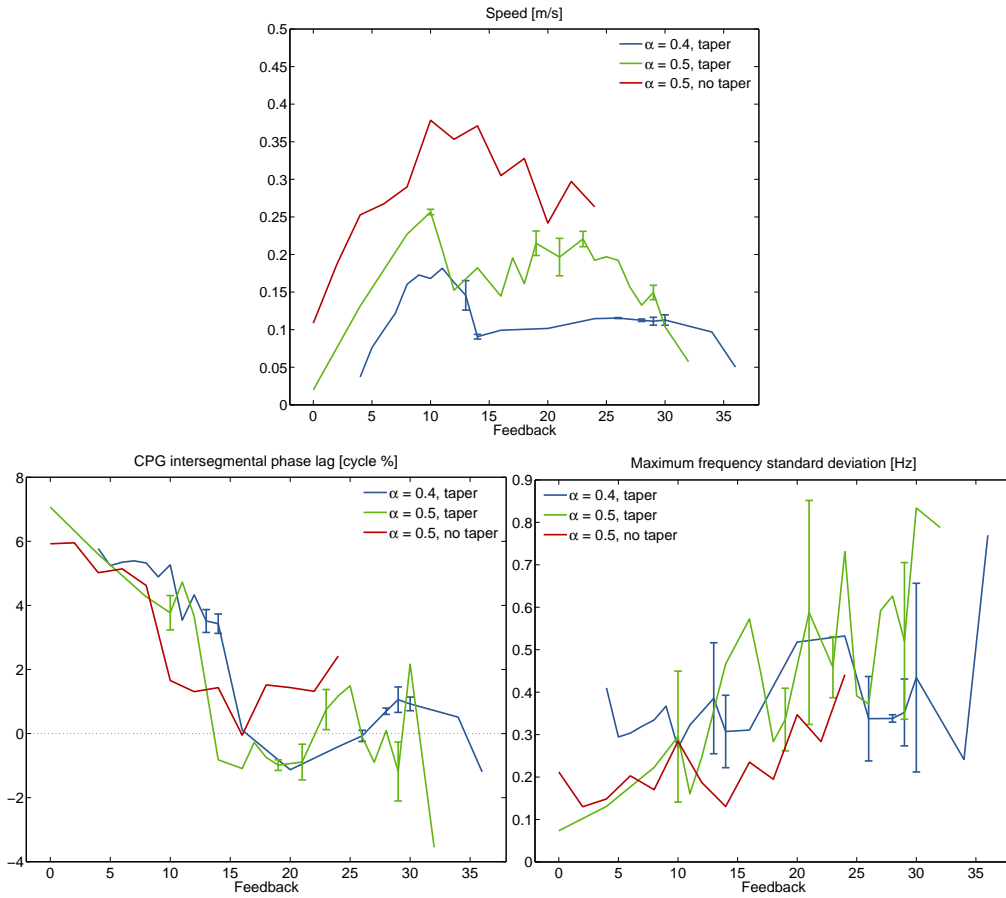


Figure 5.19 – Effect of axial proprioceptive feedback during swimming. Results are shown for three conditions: with the muscle gain  $\alpha = 0.4$  and body taper, as in simulations; with  $\alpha = 0.5$  and body taper; with  $\alpha = 0.5$  and no body taper. The bottom-right plot shows the maximum, among the modules, of the standard deviation of the cycle frequency. We use this quantity as a measure of the gait periodicity.

value  $\phi_{ij} = 4$ . For backward stepping the limb→body phase bias was optimized separately, yielding an optimal value  $\phi_{ij} = 5.5$ .<sup>5</sup>

The behaviors involving rhythmic limb activity were reproduced as in simulation, using differential drive signals between the neck and the rest of the body. The drives used to achieve the various behaviors are shown in figure 5.23. The nearly standing wave produced during underwater stepping (CPG phase lag of  $0.8 \pm 0.3$  %) resulted in slightly slower locomotion than when the tail was left to oscillate passively as observed in the animal. The locomotion speeds for each individual and each behavior are shown in figure 5.24.

The CPG intersegmental phase lags obtained for forward land stepping, backward land stepping and struggling were  $0.3 \pm 0.4$  %,  $3.5 \pm 0.7$  % and  $-4.1 \pm 0.7$  % respectively. The CPG and kinematic phase lags for all individuals and all behaviors are shown in figure 5.22. The CPG intersegmental phase lag was smaller than the kinematic phase lag during swimming, under-

5. A value  $\phi_{ij} = 6$  actually gave slightly better speeds, but was at the edge of the optimal region.

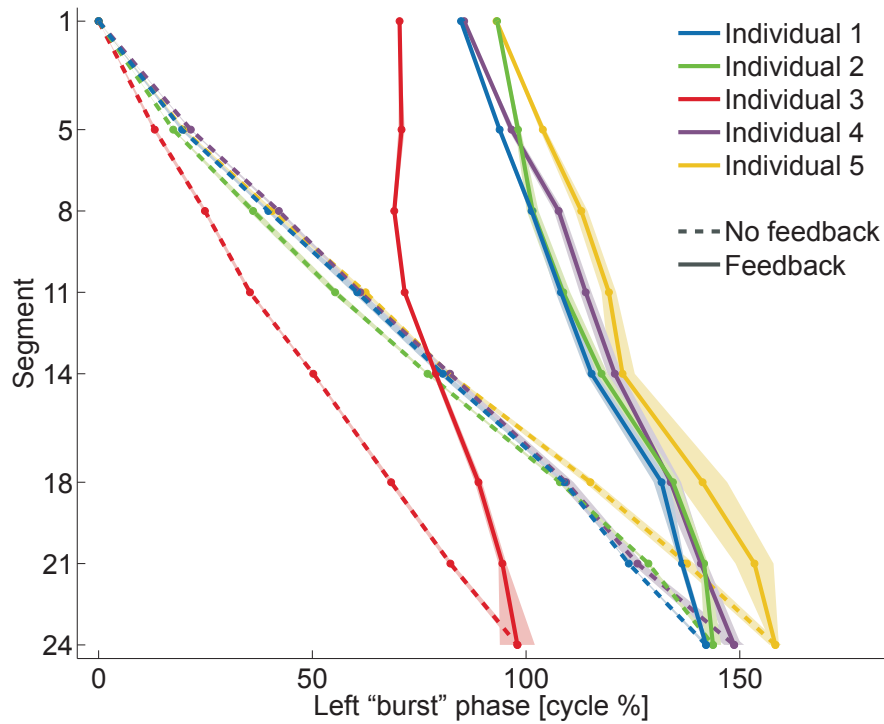


Figure 5.20 – CPG activity pattern during swimming with and without feedback (solid and dashed lines resp.). For experiments with feedback, a strength  $w^{\text{ipsi}} = 10$  was used. Colors correspond to different simulated individuals. The relative position of the ten lines on the horizontal axis is arbitrary. Circular markers show the relative timing of the “bursts” in the left oscillators of 8 CPG segments (the segments used to control the virtual muscles of the 8 robot joints). The lines joining the markers illustrate the phase lags between the robot joints. The open-loop phase lags, which are too large for efficient swimming, are reduced after introduction of sensory feedback. The variability of phase lags between individual is also reduced (the third individual, in red, is an outlier in open-loop but not in closed-loop).

water stepping and forward land stepping. It was larger (in absolute values) during backward stepping and struggling. In all experiments but one, the motor encoders reported a phase lag in between the value calculated with the external video tracking and the CPG phase lag.

Axial proprioceptive feedback similar to that used during swimming was found to have a detrimental effect on rhythm stability during underwater stepping and forward land stepping, with axial and limb oscillators often failing to reach frequency locking. Axial feedback was also found to be counter-productive and decrease the phase lag in trunk during forward land stepping, when differential drives are striving to increase it from negative values towards zero. This is illustrated in figure 5.25, both in presence and in absence of feedback in the neck.

The results shown in figure 5.22, 5.23 and 5.24 were obtained using axial proprioceptive feedback of strength 10 for swimming and only differential drive for the other behaviors.

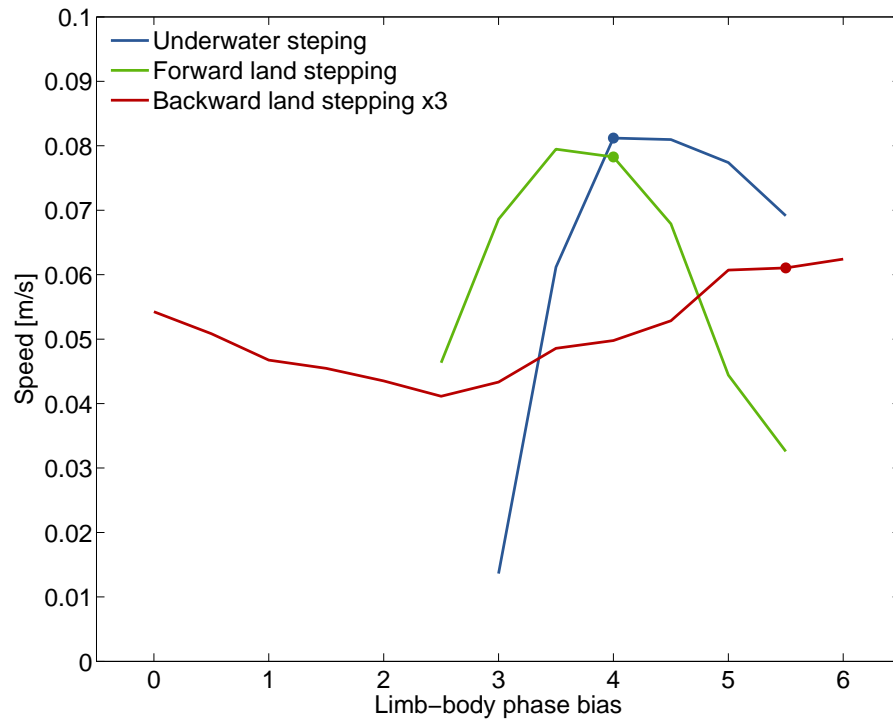


Figure 5.21 – Optimization of the limb→body phase bias in the robot. The tests were performed using an “average individual” where the standard deviation of the oscillator excitabilities was set to 0. The phase bias selected for each behavior is indicated with a circular marker (values in radians). The speeds obtained with backward stepping were multiplied by 3 to increase the legibility of the plot.

## 5.9 Discussion

The robot experiments highlight the controllability of the asymmetric CPG model. During swimming, the lag can be adjusted by changing the drive to the first segment, exactly like in models of the lamprey CPG. Since the natural axial phase lag is around 6%, the drive to the first segment must be reduced to get a lag of about 2%. In the other behaviors, the frequency of the first segments is forced by the strong couplings from the limb oscillators. The lag can thus be controlled by adjusting the drive to the limb oscillators. Since the mid-trunk lag in the isolated network with active limbs is around -7% (rightmost peak of the *in vitro* distribution), the limb drive must be increased compared to the axial drive to achieve a standing wave or a rostrocaudal traveling wave, as shown in figure 5.23.

As discussed in chapter 6, the differential drive principle also applies to the modulation of the intersegmental phase lag by proprioceptive sensory feedback. Sensory feedback often has an excitatory effect on the CPG activity, increasing the locomotion cycle frequency. In our case, during swimming the local proprioceptive feedback in the axis increases the uncoupled frequency of the trunk and tail segments. The first segment receiving no feedback, its uncoupled frequency is comparatively reduced, which leads as expected to a decrease in phase lags, here from  $6.1 \pm 1.4$  % down to  $1.9 \pm 1.1$  % (5.20). The corresponding improvement in

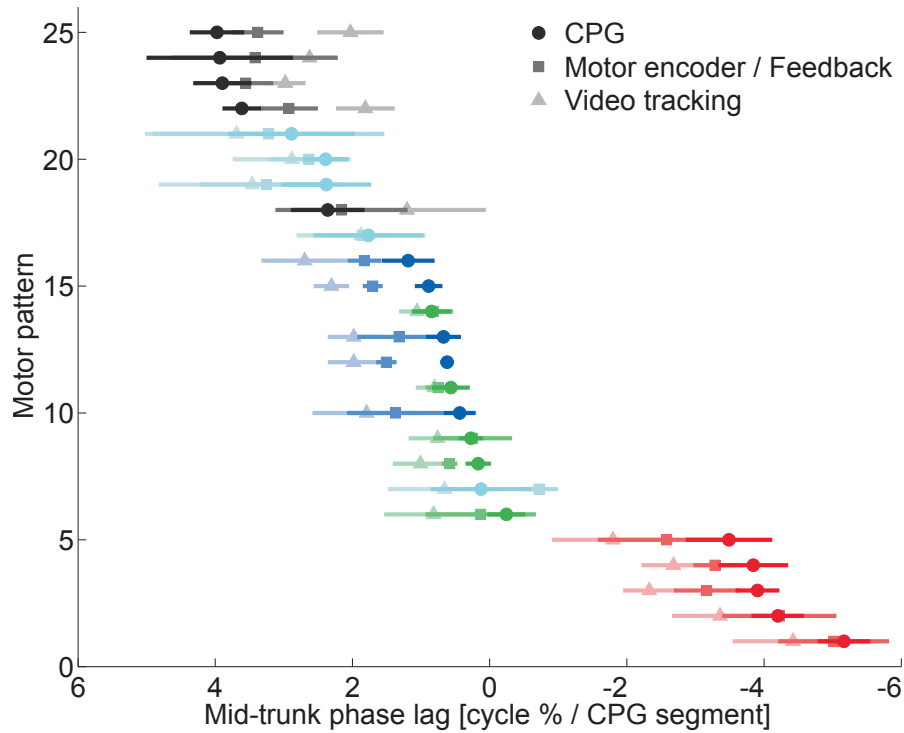


Figure 5.22 – Intersegmental phase lag in the robot mid-trunk in 5 simulated individuals, each reproducing the 5 motor behaviors (black: backward stepping, light blue: swimming, dark blue: underwater stepping, green: forward land stepping, red: struggling). Each line corresponds to one experiment and shows the mean and standard deviation of the CPG and kinematic phase lags. The square and triangular markers show the kinematic lags as calculated from the internal motor encoders and external video tracking respectively. The phase lags are calculated using data from the joints 2, 3 and 4, which represent the robot’s mid-trunk.

swimming speeds is shown in figure 5.24. The same feedback strength was used with the five “individuals”, showing that the effect does not rely on a fine tuning of the feedback strength. However this particular feedback strength did not lead to perfectly periodic swimming in all simulated individuals, as can be seen by the high standard deviation for the speed of the fifth individual in figure 5.24 (yellow).

In the motor behaviors that involved rhythmic limb activity, the excitation from axial proprioceptive feedback, added to the already high intrinsic frequency of the axial oscillators, often prevented them from reaching frequency locking with the slow limb oscillators. When frequency locking did occur, the additional axial excitation was counter-productive, decreasing the phase lag instead of helping to increase it from -7% to 0 or positive values. We investigated other forms of proprioceptive sensory feedback in simulation, and found that using opposite feedback weights, where the oscillator is inhibited by an ipsilateral stretch and excited by a contralateral stretch, could contribute to a slowdown of the axial oscillators and an increase in phase lags. The effect was reproduced on the real robot (figure 5.25), although it was not used to replace the differential drives as in simulation. Alternatively, simulations showed that

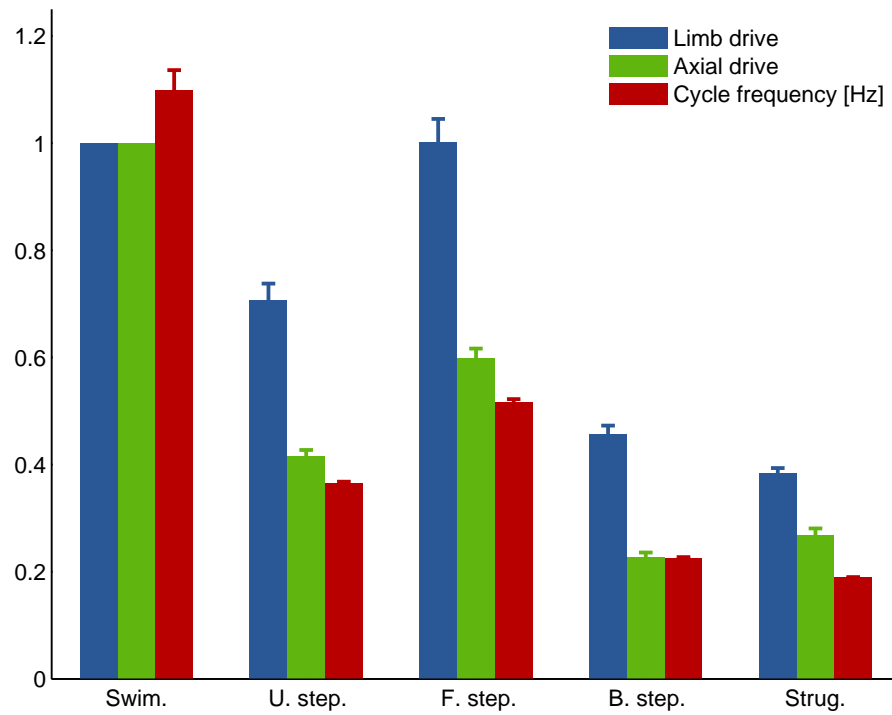


Figure 5.23 – Differential drive signals used to reproduce the 5 motor behaviors, and resulting cycle frequencies. From left to right: swimming with uniform drives and a feedback strength  $w^{\text{ipsi}} = 10$ , underwater stepping, forward land stepping, backward land stepping and struggling. The mean and standard deviation among the 5 individuals is shown for each behavior. The overlap in limb drives between swimming and forward land stepping is due to the reduced drives and limb saturation thresholds used for swimming to accommodate for the robot's limitations.

the extra limb drive could be partially or totally replaced with an excitatory proprioceptive feedback from the limbs, with the same effect of increasing their uncoupled frequency, and thus the intersegmental phase lag (figure 5.12). Such a feedback has been proposed as a way of facilitating the transition from walking to trotting in the salamander [Harischandra et al., 2011].

In the model, descending drives and various forms of proprioceptive feedback thus play a similar role in increasing or decreasing the uncoupled frequency of the oscillators and thereby modulating the intersegmental phase lag.

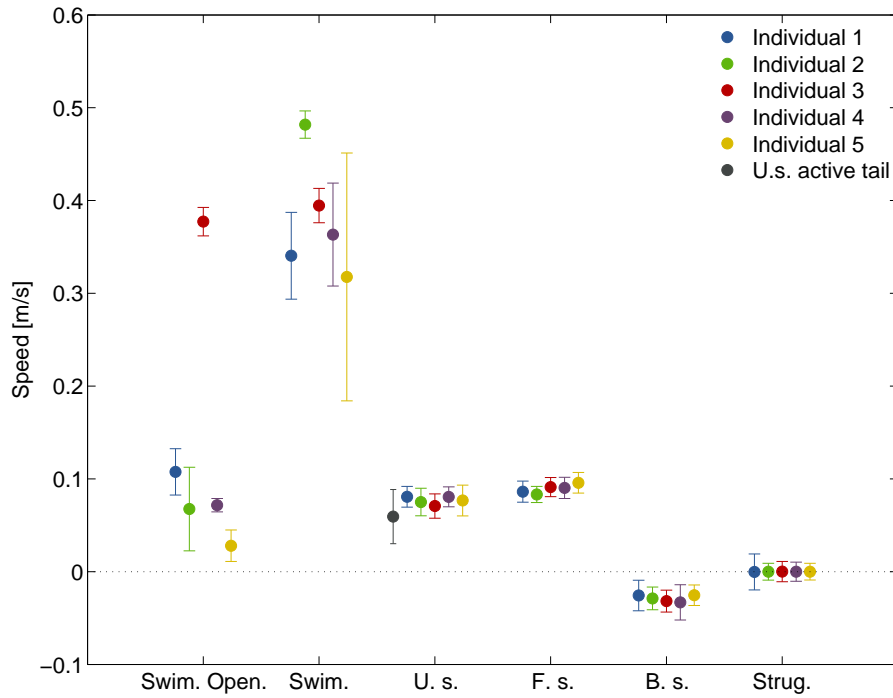


Figure 5.24 – Speed of locomotion in the five individuals for each motor behavior. From left to right: swimming with uniform drives in open-loop, swimming with uniform drives and a feedback strength  $w^{\text{ipsi}} = 10$ , underwater stepping, forward land stepping, backward land stepping and struggling. An additional marker for underwater stepping (gray) shows the speed of an “average” individual <sup>a</sup> using an active tail.

<sup>a</sup>. I.e. a network with the standard deviation of the oscillator excitabilities set to 0.



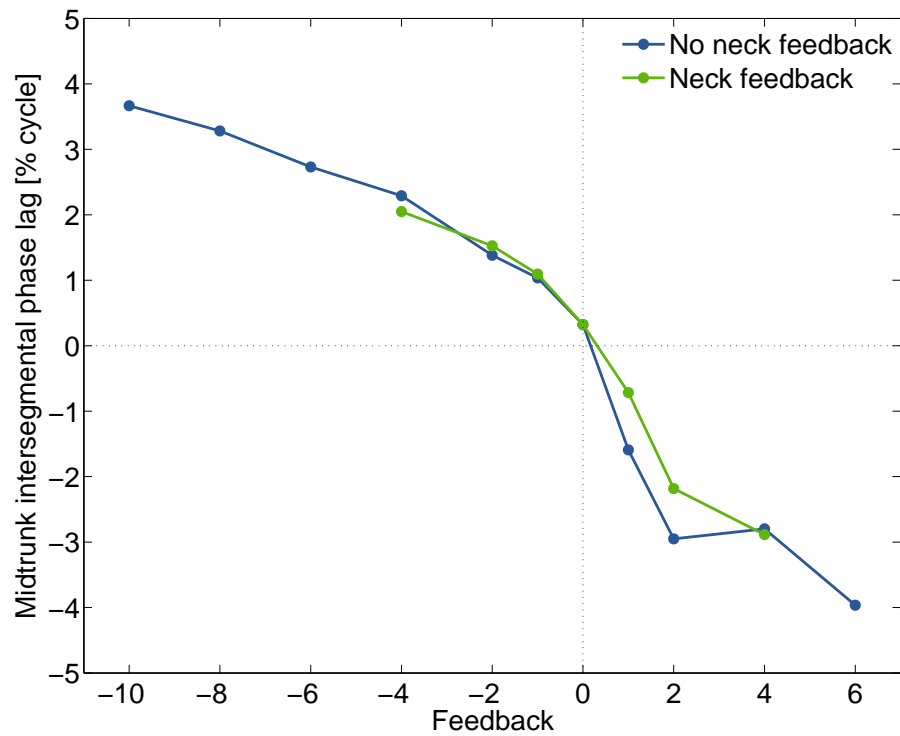


Figure 5.25 – Effect of proprioceptive feedback on the intersegmental phase lag during forward land stepping in an “average” individual where the standard deviation of the oscillator excitabilities was set to 0. The green line shows results obtained with feedback enabled in all joints. The blue line shows results obtained with feedback disabled in the neck. Feedback weights  $w^{\text{ipsi}} \geq 4$  lead to aperiodic rhythms in the tail. Locomotion becomes erratic for  $w^{\text{ipsi}}$  beyond 6.



## 6 Understanding the Effect of Local Sensory Feedback

We have seen in the previous chapter that local proprioceptive feedback has an accelerating effect on the CPG. When the neck receives no feedback, this effect amounts to a differential drive between the neck which is left alone and the trunk and tail which receive additional excitation from the feedback. The mechanism described in section 4.4.4 predicts that this differential excitation will lead to a decrease in intersegmental phase lags, and indeed the phase lag is reduced from over 6% to about 2%, leading to a dramatic improvement in swimming performance. The same mechanism predicts that excitatory limb feedback will lead to an increase in intersegmental phase lags, as observed in simulation (section 5.5.2).

More surprising is the observation of the same phenomenon in presence of neck feedback of the same strength as in the rest of the axial network, as shown in simulation in section 5.5.1. In our tests with the robot, we usually excluded neck feedback because it had an destabilizing effect: many but not all experiments failed to reach a periodic regime. This could presumably be alleviated by adapting the muscle model parameters in the neck to increase stiffness and get lower, biologically more realistic amplitudes of motion. Still, in those cases where a periodic regime was reached, we found again that feedback decreases the intersegmental phase lag and improves swimming performance, as shown in figure 5.25.

Simulations show that the effect is valid over a large range of frequencies, though periodic rhythms are only reached in a rather restricted range of feedback strengths. The appropriate feedback strength  $w^{\text{ipsi}}$  ( $= -w^{\text{contra}}$ ) scales as a quadratic function of the drive  $d$ , and thus of the frequency of locomotion frequency (figure 6.1):

$$w^{\text{ipsi}} \simeq 6.5 d^2 + 7.6 d \quad (6.1)$$

Even more surprising, simulations show that while a large open-loop CPG phase lag is decreased by feedback, a zero or negative open-loop phase lag is actually increased. Figure 6.2 (top) shows the effect of local sensory feedback on a variety of open-loop patterns. The simulations were repeated with a feedback strength  $w^{\text{ipsi}} = -w^{\text{contra}} = 21$  (solid lines). The range

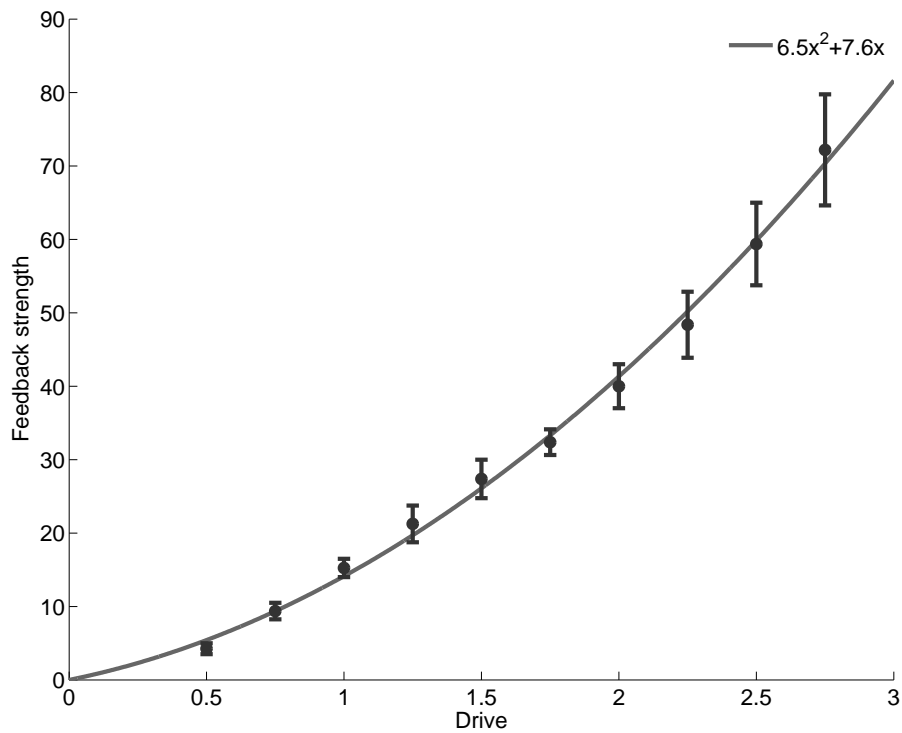


Figure 6.1 – Scaling of appropriate feedback strength with the drive during swimming. The vertical bars indicate the range of feedback strengths that allow for stable, periodic swimming at each drive level. The ranges of weak feedback strengths that give stable swimming without significant modulation of the CPG pattern are not represented. The light gray line represents a quadratic fit of the range center (circular marker) at each level of drive.

---

of CPG intersegmental phase lags was reduced from (-10%, 10%) to (-1.0%, 1.5%). This had a dramatic effect on the speed (bottom panel): In the open-loop case, the speed had a strong dependence on the CPG phase lag, with an optimum around lags of 1.3%. In the closed-loop case however the speed is almost constant for intrinsic (open-loop) CPG lags between -2% and 8%. Even with an intrinsic lag of -10%, the speed is still 46% of the maximum speed, after correcting for the different swimming frequencies.

We remember from the previous chapter that without neck feedback, a feedback-induced increase of the uncoupled frequency in the rest of the body amounts to a differential drive that decreases the intersegmental phase lag. We can get a similar but weaker differential excitation in presence of neck feedback, if we assume that for some reason, feedback does not accelerate as much the neck oscillators as the rest of the axial network. This would explain the right half of figure 6.2 (top). In the left half of the figure, however, the CPG lag is *increased* by feedback. This suggests the neck oscillators get *more* feedback-induced acceleration than the rest of the axial network in this case. More generally, the figure suggests that feedback-induced acceleration in the neck is inversely proportional to the intrinsic CPG phase lag.

A consequence of the intersegmental coupling asymmetry is that the frequency of the network is mostly determined by the frequency of the first oscillators. The feedback-induced acceleration of oscillators in the trunk and the tail therefore has almost no effect on the network frequency. The acceleration of the neck oscillators however results in an acceleration of the whole network. If the hypotheses made in the previous paragraph are correct, we expect the neck frequency, and therefore the whole network frequency, to increase with decreasing CPG phase lags. This is exactly what we observe in figure 6.2 (bottom): the closed loop frequency, in solid purple, increases almost linearly with decreasing CPG phase lags.

Figure 6.2 provides a clue towards understanding this relationship between intrinsic CPG phase lag and feedback-induced acceleration in the neck. In the top panel, the separation between the solid red and blue lines represents the difference in speed between the CPG and kinematic traveling waves. A small separation means that both waves travel almost at the same speed, so that the CPG-kinematic lag is almost constant along the body. A large separation means that the kinematic wave is much slower than the CPG wave, so that the CPG-kinematic lag increases from the head to the tail.

The linear increase of the network frequency towards the left (i.e. at high negative CPG phase lags) in the bottom panel is mirrored in the increase of the CPG-kinematic wave speed difference in the top panel. This suggests that the distribution of CPG-kinematic lags along the body plays an important role in the effect of sensory feedback on the CPG. This is a nice example where the body dynamics together with sensory feedback act as a beneficial filter that “corrects” suboptimal CPG phase lags.

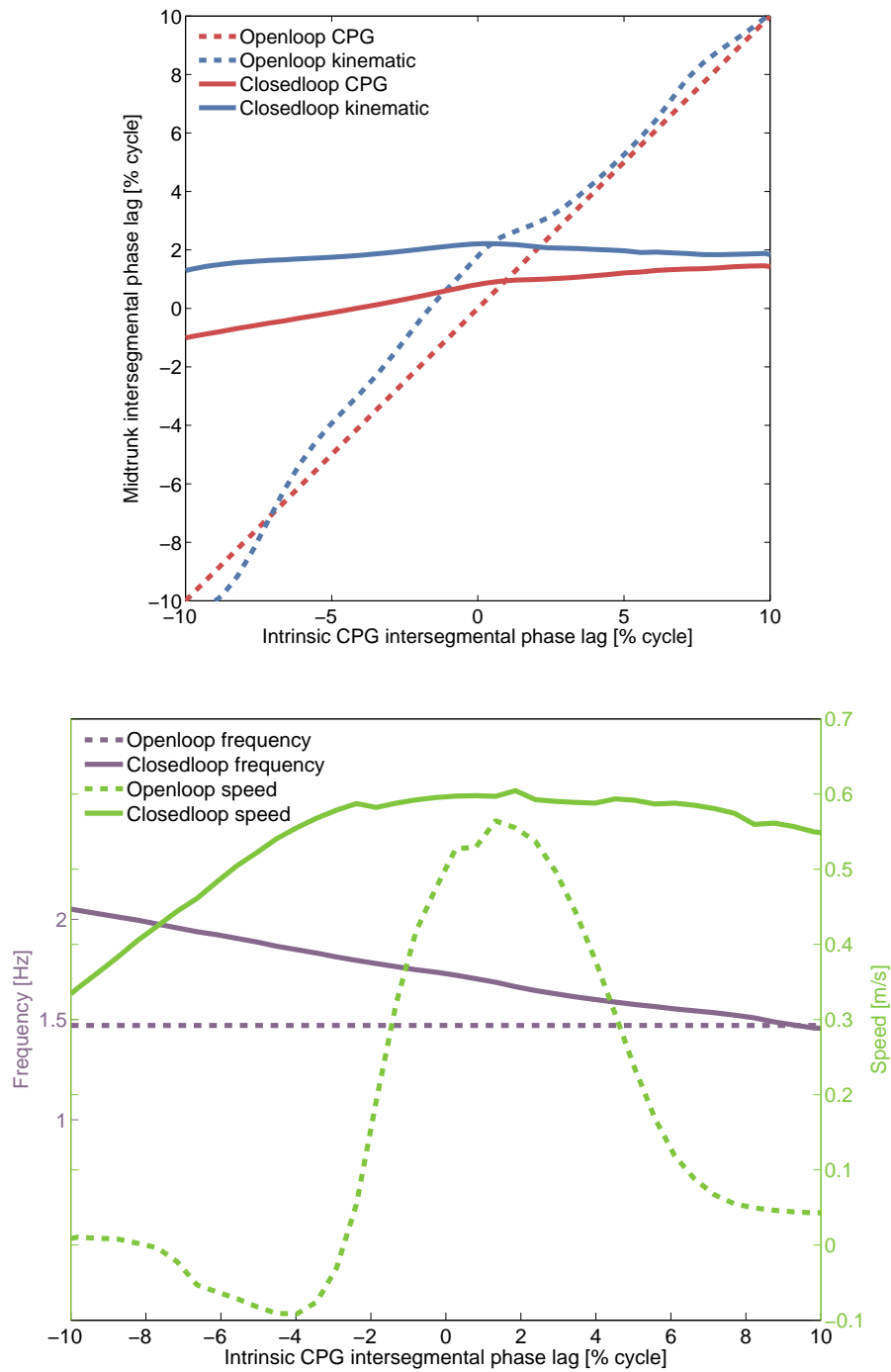


Figure 6.2 – Effect of local sensory feedback on a variety of open-loop patterns in presence of neck feedback during swimming. **Top** 40 simulations were made with CPG intersegmental phase biases ranging from -10% to 10%, without sensory feedback (dashed lines). The simulations were repeated with a feedback strength  $w^{\text{ipsi}} = -w^{\text{contra}} = 21$  (solid lines). **Bottom** The frequency (purple) and swimming speed (green) in the open-loop and closed-loop conditions

## 6.1 A Mathematical Analysis

To further our understanding of the effect of feedback and confirm our hypotheses, we go back to the equations of the CPG established in section 5.3.2. Rewriting the single oscillator equation without couplings, we find

$$\begin{aligned}\dot{r} &= a(R - r) + s \cos \theta \\ \dot{\theta} &= 2\pi\nu - \frac{s}{r} \sin \theta \\ x &= r(1 + \cos \theta)\end{aligned}\tag{6.2}$$

with  $\nu$  the intrinsic frequency and  $s$  the feedback signal. We write  $\phi_{\text{cpg}}^{\text{kin}}$  the CPG-kinematic lag, i.e. the fraction of a cycle by which muscle compression lags behind muscle activation. Since the CPG output  $x$  varies as  $\cos \theta$ , the kinematic state varies as  $\cos(\theta - \phi_{\text{cpg}}^{\text{kin}})$ . And since the feedback signal is positive (excitatory) not when the muscle is compressed but when it is stretched, it is in antiphase with the kinematics and varies as  $\cos(\theta - \phi_{\text{cpg}}^{\text{kin}} + \pi)$ . We will use the following approximation:

$$s \sim A \cos(\theta - \phi_{\text{cpg}}^{\text{kin}} + \pi)$$

where  $A$  is a constant representing the amplitude of the feedback signal, which depends on the amplitude of the joint rotation and the feedback weights. We can rewrite the differential equations of (6.2) as

$$\begin{aligned}\dot{r} &= a(R - r) + A \cos(\theta - \phi_{\text{cpg}}^{\text{kin}} + \pi) \cos \theta \\ \dot{\theta} &= 2\pi\nu - \frac{A}{r} \cos(\theta - \phi_{\text{cpg}}^{\text{kin}} + \pi) \sin \theta\end{aligned}$$

To calculate the average effect of feedback on  $\dot{r}$ , we integrate the added term over a whole period:

$$\frac{1}{2\pi} \int_0^{2\pi} A \cos(\theta - \phi_{\text{cpg}}^{\text{kin}} + \pi) \cos \theta d\theta = -\frac{A}{2\pi} \int_0^{2\pi} \cos(\theta - \phi_{\text{cpg}}^{\text{kin}}) \cos \theta d\theta$$

and using the trigonometric identity  $\cos \alpha \cos \beta = \frac{1}{2}(\cos(\alpha - \beta) + \cos(\alpha + \beta))$ :

$$\begin{aligned}-\frac{A}{2\pi} \int_0^{2\pi} \cos(\theta - \phi_{\text{cpg}}^{\text{kin}}) \cos \theta d\theta &= -\frac{A}{4\pi} \int_0^{2\pi} \cos(-\phi_{\text{cpg}}^{\text{kin}}) + \cos(2\theta - \phi_{\text{cpg}}^{\text{kin}}) d\theta \\ &= -\frac{A}{4\pi} \left( \theta \cos \phi_{\text{cpg}}^{\text{kin}} + \frac{\sin(2\theta - \phi_{\text{cpg}}^{\text{kin}})}{2} \right) \Big|_0^{2\pi} \\ &= -\frac{A}{2} \cos \phi_{\text{cpg}}^{\text{kin}}\end{aligned}\tag{6.3}$$

The system will converge to an amplitude such that  $\dot{r} = 0$ :

$$a(R - r) - \frac{A}{2} \cos \phi_{\text{cpg}}^{\text{kin}} = 0$$

$$r = R - \frac{A}{2a} \cos \phi_{\text{cpg}}^{\text{kin}}$$

The amplitude will be decreased by the feedback for a CPG-kinematic lag in  $\phi_{\text{cpg}}^{\text{kin}} \in (-\frac{\pi}{2}, \frac{\pi}{2})$ , and increased otherwise. In particular, the amplitude is maximally decreased by feedback when the CPG and kinematics are in phase, and maximally increased when they are in antiphase.

Similarly, the average effect on  $\dot{\theta}$  is

$$\frac{1}{2\pi} \int_0^{2\pi} -\frac{A}{r} \cos(\theta - \phi_{\text{cpg}}^{\text{kin}} + \pi) \sin \theta d\theta = \frac{A}{2\pi r} \int_0^{2\pi} \cos(\theta - \phi_{\text{cpg}}^{\text{kin}}) \sin \theta d\theta$$

and using the identity  $\sin \alpha \cos \beta = \frac{1}{2}(\sin(\alpha - \beta) + \sin(\alpha + \beta))$ :

$$\begin{aligned} \frac{A}{2\pi r} \int_0^{2\pi} \cos(\theta - \phi_{\text{cpg}}^{\text{kin}}) \sin \theta d\theta &= \frac{A}{4\pi r} \int_0^{2\pi} \sin \phi_{\text{cpg}}^{\text{kin}} + \sin(2\theta - \phi_{\text{cpg}}^{\text{kin}}) d\theta \\ &= \frac{A}{4\pi r} \left( \theta \sin \phi_{\text{cpg}}^{\text{kin}} - \frac{\cos(2\theta - \phi_{\text{cpg}}^{\text{kin}})}{2} \right) \Big|_0^{2\pi} \\ &= \frac{A}{2r} \sin \phi_{\text{cpg}}^{\text{kin}} \end{aligned} \tag{6.4}$$

The feedback-induced acceleration of the oscillator is maximal for a CPG-kinematic lag  $\phi_{\text{cpg}}^{\text{kin}} = \frac{\pi}{2}$ . The feedback can also have a decelerating effect, which is maximal when  $\phi_{\text{cpg}}^{\text{kin}} = \frac{3\pi}{2}$ . The effect of feedback vanishes for CPG-kinematic lags of 0 or  $\pi$ . The amplitude of the effect, either accelerating or decelerating, is proportional to the feedback amplitude and inversely proportional to the oscillator amplitude.

The effect of feedback in the abstract oscillator model can be conceived as the entrainment of the CPG by a “feedback oscillator”. The dependency of the feedback effect on the CPG-kinematic lag is then quite intuitive. An illustration for the case  $\phi_{\text{cpg}}^{\text{kin}} = \frac{\pi}{2}$  is given in figure 6.3. The figure also shows how the phenomenon relates to burst initiation and termination in a spiking model.



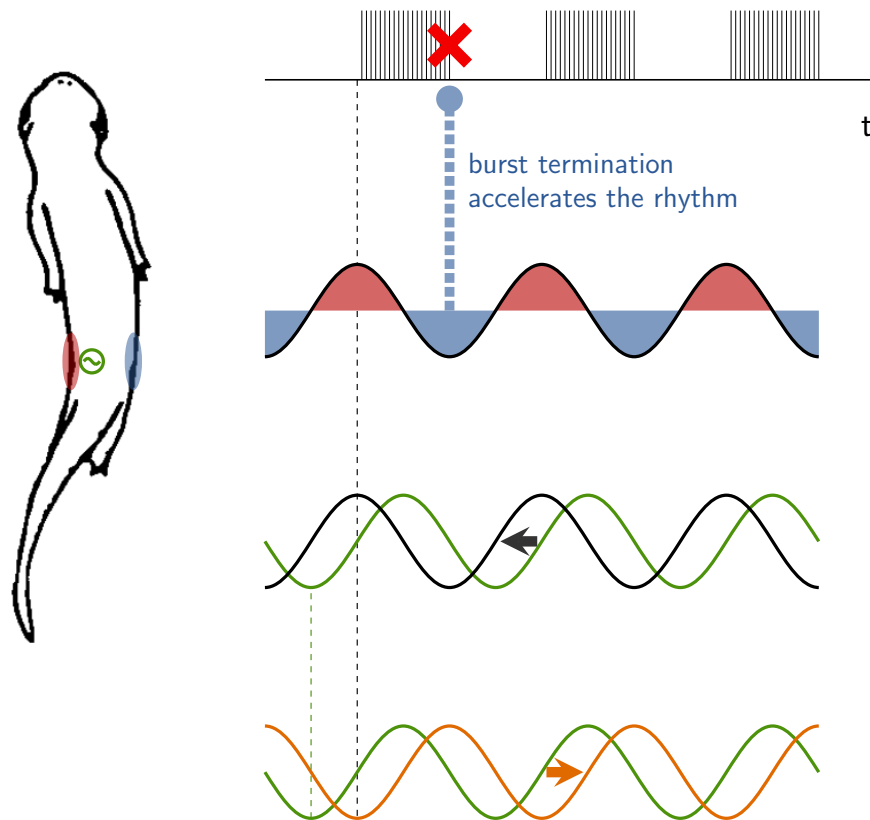


Figure 6.3 – Local effect of sensory feedback. **Left:** A hemisegment (green) receives excitatory feedback (red) during stretching of the ipsilateral side and inhibitory feedback (blue) during stretching of the contralateral side. **Right:** Effect of sensory feedback on the frequency in a hypothetical spiking CPG model and in the abstract oscillator model. The bursts in a spiking model (top) correspond to the positive parts of the sine wave in the abstract oscillator model (green line). The feedback signal (blue in the inhibitory phase and red in the excitatory phase) is in antiphase with the kinematic wave of compression (orange). Here there is a CPG-kinematic lag of  $\frac{\pi}{2}$  (orange arrow) corresponding to the feedback being in advance by  $\frac{\pi}{2}$  with respect to the CPG oscillation. In this configuration the entrainment of the CPG oscillator by feedback (black arrow) has the strongest accelerating effect. In the bursting model the same acceleration occurs due to the early termination of bursting by inhibitory feedback (dashed blue) and the early burst initiation promoted by excitatory feedback (not shown). Salamander schematic from Delvolvé et al. [1997].

## 6.2 Contributions to Feedback-Induced Modulations of Phase Lags

Based on the insight provided by the mathematical analysis in the previous section, we investigated how the CPG-kinematic lag, the feedback amplitude and the oscillator amplitude affect the uncoupled frequency of the oscillators at each joint. We picked three simulations among those represented in figure 6.2, corresponding to intrinsic CPG intersegmental phase lags of 6.6%, 0% and -2%. To distinguish the different contributions to the oscillator acceleration, we used the phase and feedback signals from each simulation to calculate, based on equation (6.2), a hypothetical acceleration that does not depend on the oscillator amplitude:

$$\dot{\theta}_i = 2\pi v_i - s_i \sin \theta_i \quad (6.5)$$

We calculated the average of the acceleration  $-s_i \sin \theta_i$  at each joint over the course of the simulation. The result is shown in figure 6.4, where the blue line represents the actual feedback-induced acceleration and the green lines the hypothetical acceleration based on equation (6.5). The hypothetical accelerations were normalized to match the actual acceleration at the first joint. Finally we calculated a second hypothetical acceleration based on equation (6.5), after normalizing the feedback signals  $s_i$  to remove the effect of different feedback amplitudes along the body. The result is shown as red lines on the figure.

We first observe that the blue line in each panel on the left confirms the hypotheses made at the beginning of this chapter: the feedback-induced acceleration at the neck is lower than in the rest of the body in the case of high intrinsic CPG phase lags (top panel), while in the case of zero phase lag (middle panel) or negative phase lag (bottom panel), the acceleration is higher at the neck.<sup>1</sup> This will provide the differential excitation that explains the decrease of phase lag in the first case and the increase of phase lag in the other cases. The stronger acceleration in the neck is also reflected in the closed-loop frequency of the network: while the intrinsic frequency of the oscillators was 1.47 Hz in all three cases, the actual CPG frequency was  $1.54 \pm 0.03$  Hz,  $1.72 \pm 0.02$  Hz,  $1.78 \pm 0.02$  Hz in the top, middle and bottom panels respectively.

The top-left panel shows what happens in the case of a very high intrinsic CPG phase lag, such as during the robot swimming experiments with the five simulated individuals (figure 5.20). We see that the dominant contribution to the differential excitation between the neck and the rest of the axial network comes from the increasing CPG-kinematic lag (the red marker at the neck is much lower), as seen in the right panel: the CPG-kinematic lag is almost zero in the neck, and close to  $\frac{\pi}{2}$  in the tail. These correspond to minimal and maximal feedback effects respectively, according to equation (6.4). An increasing feedback amplitude towards the tail also helps maintain a high level of acceleration in that part of the network. This increasing feedback amplitude can be read from the larger kinematic amplitudes in the right panel. The

---

1. In the middle panel, the acceleration at the second joint is actually even higher, but this only affects the phase lag between the first and second joints; the oscillators at the second joint will take on the frequency of the first segment anyway, which is what matters in determining the phase lag between the successive segments down the chain. The irregularity at the second joint, also apparent in the right panels, is discussed in section 5.5.1.

## 6.2. Contributions to Feedback-Induced Modulations of Phase Lags

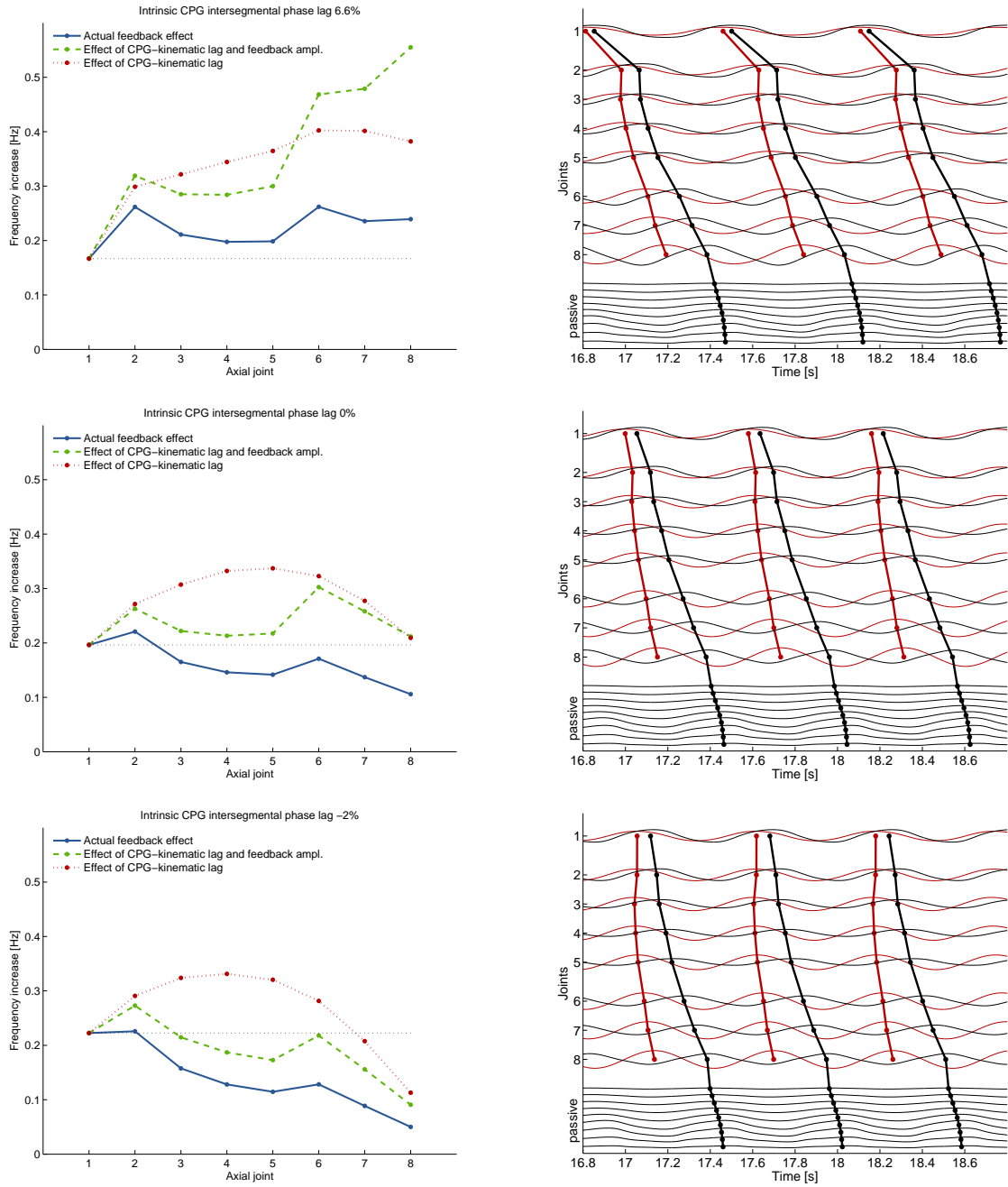


Figure 6.4 – Contributions to the feedback-induced acceleration at each joint during swimming, for intrinsic CPG phase lags of 6.6% (top), 0% (middle) and -2% (bottom). **Left:** In each case the figure shows the actual acceleration at each joint (blue), a hypothetical acceleration if oscillator amplitudes were uniform along the body, normalized to the actual acceleration at the first joint (green), and a hypothetical acceleration if both oscillator amplitudes and feedback amplitudes were uniform along the body, similarly normalized (red). **Right:** The CPG (red) and kinematic (black) oscillation patterns show an increasing CPG-kinematic lag along the body in each case. The CPG-kinematic lag reaches about  $\frac{\pi}{2}$  and  $\pi$  in the top and bottom panels respectively.

actual feedback effect (blue line) is more constant along the body than the hypothetical effect based on equation (6.5). This tells us that the indirect influence of feedback on frequency that goes through the modulation of the oscillator amplitude—the  $r$  in the denominator in equation (6.2)—tends to counteract the higher excitation in the trunk and the tail.

With an intrinsic CPG phase lag of 0% (middle panel), the effect of the CPG-kinematic lag still tends to give more excitation in the trunk than in the neck. Alone, this effect would cause the CPG phase lag to become negative, but it is counterbalanced by the effect of the feedback amplitude, which is lower in the trunk ( $9.2^\circ$  in joint 4 compared to  $14.2^\circ$  in the neck). The determining factor in giving more excitation to the neck than the rest of the body, is the effect of feedback on the oscillator amplitude (see the difference between green and blue lines).

Finally, with a negative intrinsic CPG phase lag of -2% (bottom panel), the CPG-kinematic lag tends to decrease the phase lag in the trunk (more excitation given than in the neck) and increase it in the tail. From the shape of the red curve and based on equation (6.4), we can predict that the CPG-kinematic lag will be close to  $\frac{\pi}{2}$  at joint 4, and close to  $\pi$  at the last joint. This is confirmed by the oscillation traces in the right panel. The actual lag values in degrees are  $94^\circ$  and  $161^\circ$  respectively. Here also the higher excitation due to the CPG-kinematic lag in the trunk is compensated by the lower feedback amplitude. The effect of feedback on the oscillator frequencies explains the counter-intuitive observation that a negative lag is transformed into a positive one thanks to the body dynamics and sensory feedback.

### 6.3 Conclusion

We have seen that local sensory feedback modulates the CPG phase lag towards the optimal values for swimming: a large range of phase lags between -10% to 10% is reduced to a range of -1% to 1.5%. However this whole reduced range of phase lags is appropriate for forward swimming only thanks to the mechanical properties of the body. As shown in figure 6.2 (top), the range of kinematic phase lags is further reduced to between 1.3% and 1.9% (the solid blue line is flatter than the red). This contribution of the body mechanics is also apparent in open-loop, where the speed is positive even with CPG phase lags of -2%. The mechanical asymmetry, mostly due to the passive tail, makes it very hard for the robot to swim backwards.

The effect of local sensory feedback on the uncoupled oscillator frequency is not straightforward. It depends on the CPG-kinematic phase lag, the oscillator amplitude and the feedback (i.e. kinematic) amplitude, as apparent in equation (6.4). But according to equation (6.3), the oscillator amplitude itself is increased or decreased by the feedback, in an amount that is function of the feedback amplitude and CPG-kinematic phase lag. Moreover, the direct effect of feedback on the oscillator frequency is maximal when the CPG-kinematic lag is  $\frac{\pi}{2}$ , while the indirect effect on the frequency, through the oscillator amplitude, is maximal when the CPG-kinematic lag is  $\pi$ .

The magnitude of the feedback effect is proportional to the feedback amplitude and inversely

proportional to the oscillator amplitude. We might expect these two dependencies to compensate for each other, as the feedback amplitude follows the kinematic amplitude, which we expect to increase when the oscillator amplitude and therefore the muscle activation increases. The analysis of three examples in section 6.2 show that they do not compensate for each other.

During swimming, the dominant contribution to the shaping of the CPG activity pattern by feedback depends on the intrinsic CPG intersegmental phase lags. For a high intrinsic CPG phase lag of 6.6%, the dominant factor is the speed difference between CPG and kinematic waves. For an intrinsic CPG phase lag of 0%, the modulation of the oscillator amplitude, which indirectly affects the acceleration of the oscillators, plays an important role. For an intrinsic lag of -2%, a lower feedback amplitude in the trunk plays a dominant role in this part of the body, while the effect of the increasing CPG-kinematic lag dominates in the tail.

It is then far from obvious how the feedback will affect the uncoupled frequency in each segment along the body axis. However, once the effect on the uncoupled oscillator frequencies is known—and that applies also to limb feedback—the differential drive mechanism allows us to infer the overall impact on the intersegmental phase lags. In this sense a common framework can be used to understand the interaction between descending drives and sensory feedback and how they affect the CPG pattern.



## 7 Robotic Platform

In this chapter, we present the robot platform used to reproduce the five salamander motor behaviors mentioned in chapter 2. Particular focus is given to the implementation of a distributed controller for the CPG model and virtual muscles.

### 7.1 Robot Hardware

The hardware of *Salamandra robotica II* is described in detail in Crespi et al. [2013]. We give only a brief description of the robot mechanics, and mention a modification to the electronics that was necessary to the implementation of our controller.

#### 7.1.1 Mechanical Design

The robot is made of a head module, eight active modules and a passive tail (figure 7.1). Each module actuates an axial joint with motion restricted to the horizontal plane; the two girdle modules also include rotational joints for the limbs. The full robot is 111 cm long and weighs 2.48 kg.



Figure 7.1 – The *Salamandra robotica II* amphibious robot. The axes of rotations for each degree of freedom are shown with dashed lines. The dimensions of the head, trunk and tail modules are  $A = 9.5$  cm,  $B = 4.7$  cm and  $C = 5.8$  cm. The girdle modules have the same dimensions except for the width, which is 6.4 cm. From [Crespi et al., 2013].

The modules have LEDs on the covers which were used to track the robot's motion with external video cameras (see section 7.4).

### 7.1.2 Electronics

One important modification was brought by Alessandro Crespi to the design described in Crespi et al. [2013]: the electronics was upgraded to include in every module an LPC2129 ARM7TDMI microcontroller such as that already present in the head. The ARM microcontroller, running at 60 MHz, is much more powerful than the PIC18F2580 available in the original design; in particular it is able to integrate in real time a subset of our CPG model using floating-point emulation, while the PIC18 would only support fixed-point arithmetic. The added calculation power was required for the implementation of the fully distributed controller described in section 7.3.

A PID controller capable of driving a motor in position, velocity or torque control is implemented on a separate PIC16 microcontroller. The PID controller is used as a PI torque controller for the axial joints and as a PD position controller for the rotational leg joints.

Inter-module communication is made over a single CAN bus running at 1 Mbps that connects all the modules and the head. Communications internal to a module, such as between the ARM microcontroller and the PID controller, are made over a local I<sup>2</sup>C bus running at 400 kbps.

## 7.2 Characterization of the PI Torque Controller

The PI torque controller was characterized to verify its linearity, operational range and response time. The  $P$  and  $I$  gains of the PI torque controller were hand-tuned before the calibration based on a trade-off between response time and stability. We thank Dustin Li for doing much of the work in these calibration experiments.

Before proceeding with the characterization of the PI controller, we needed to establish the conversion factors that would allow us to convert between the SI units used in simulation and the internal units of the PI controller. We calculated theoretical values for these factors and compared them to empirical data. Details are given in appendix B.

### 7.2.1 Static Calibration

We show in figure 7.2 the results of the static torque calibration. Different torques were sent as setpoints, and were read back from the PI controller (green line).<sup>1</sup> The actual torque exerted on the environment was measured using a linear dynamometer and a measure of the lever arm (blue line). Measurements were repeated 4 times for each setpoint value.

---

1. The PI controller needs an estimate of the torque to calculate an error term. The estimation is based on a measure of the electrical current flowing through the motor.



## 7.2. Characterization of the PI Torque Controller

The actual torque is close to the estimation of the PI controller for setpoints up to a stagnation level of 0.7 Nm. The PI controller however only sees a stagnation at 0.9 Nm.

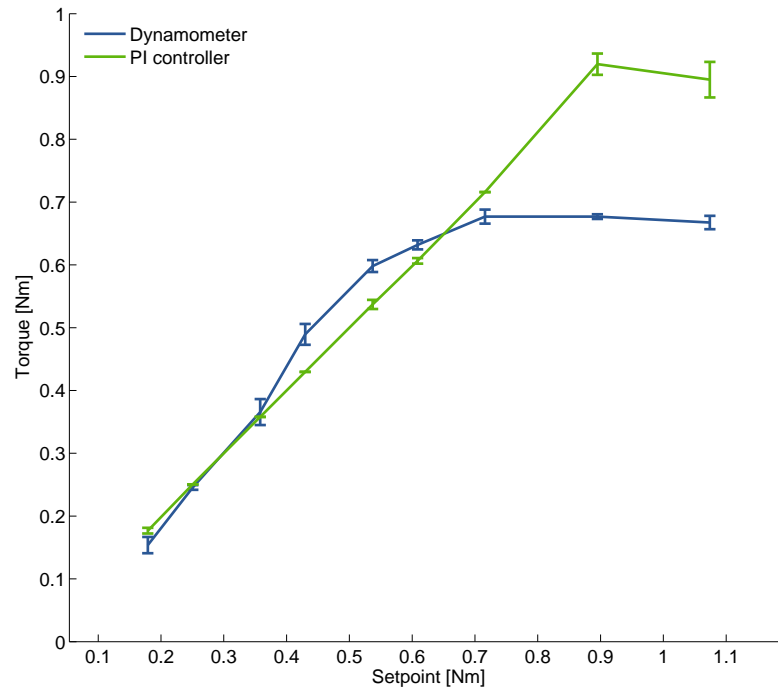


Figure 7.2 – Torque calibration on The *Salamandra robotica II* amphibious robot. The PI controller estimation of torque based on a measure of the current (green) is compared to the actual torque measured with a dynamometer (blue).

### 7.2.2 Lag between Setpoint and Torque

We also looked at the behavior of the PI controller in the case of time-varying torques. We were most interested in estimating the lag between the setpoint signal and the actual torque. This lag is particularly important in the context of a closed-loop controller, as adding a delay in the control loop can have a significant effect on the dynamics of the system.

A rectified sine torque signal was generated in the head with a time-step of 30 ms and sent to a module PI controller over the CAN bus. A read-back of the value was requested from the head immediately afterwards. The PIC18 microcontroller in the module relays the communications from the head over the local I2C bus to the PIC16 microcontroller that implements the PI torque controller.

Rectified sines were used to allow for a condition where the module periodically pulls a spring. Experiments were also conducted with the module held in a fixed position. The results for the two conditions with various amplitudes and frequencies are shown in figure 7.3. We see that the response of the PI controller is similar in all conditions.

The setpoint-torque lag was measured at the points where the signals were crossing their

median values. We found a lag of  $123 \pm 19$  ms. Note that given the magnitude of the time-steps and the communication delays between the head and the module PI controller, this method can only give an upper bound for the setpoint-torque lag.

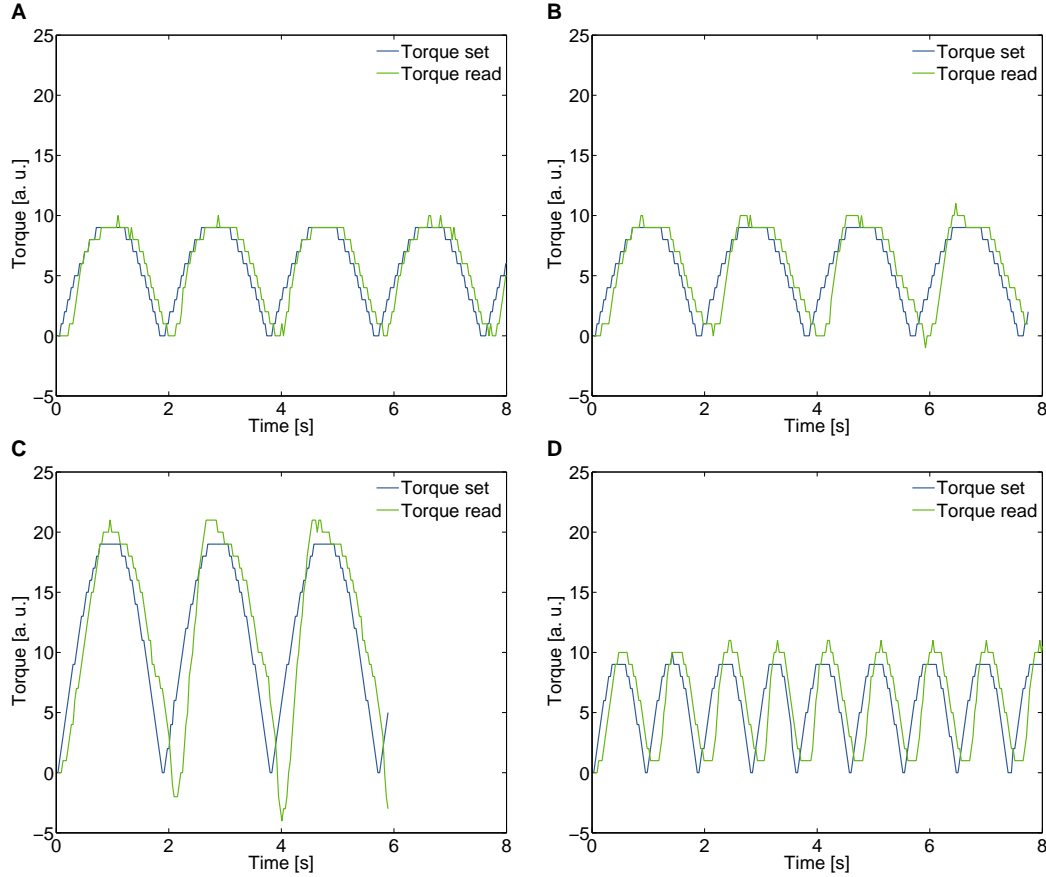


Figure 7.3 – Rectified sine setpoints and torque values read back from the PI controller. The torques are in arbitrary units. **A:** 0.5 Hz oscillations, module a held in fixed position. **B:** 0.5 Hz, module attached to a spring. **C:** 0.5 Hz oscillations, double amplitude, module attached to a spring. **D:** 1 Hz oscillations, module held in a fixed position.

As described in section 7.3, we eventually decided to distribute the robot controller in all the modules, in part to remove communication delays. We also eventually increased by a factor of 2 the  $P$  gain of the PI torque controller. Figure 7.4 shows the setpoint and read-back values obtained during an actual swimming experiment with the distributed controller. We find a setpoint-torque lag of  $51 \pm 1$  ms.

## 7.2. Characterization of the PI Torque Controller

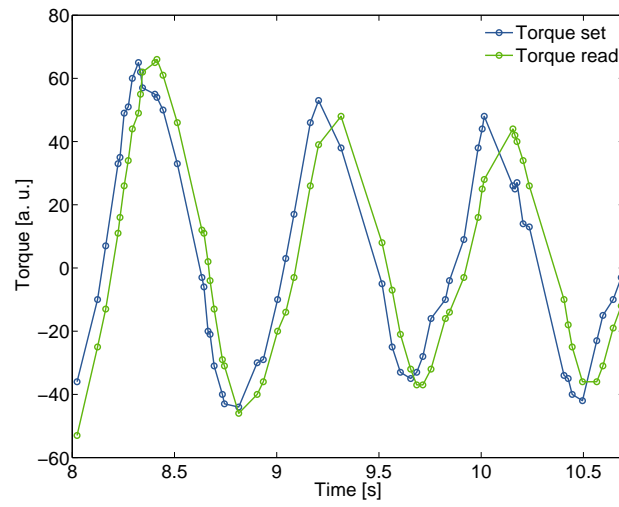


Figure 7.4 – Torque setpoints and values read back from the PI controller in the robot swimming with the muscle model at 1.1 Hz.

### 7.3 A Distributed Robot Controller

The CPG and muscle models used in the robot are the same as those used in simulation and presented in section 4.4 and chapter 5. The only difference, apart from the distributed nature of the robot implementation, is that delays between the outputs of the CPG and the inputs to the muscle model are not included in the robot controller (compare figures 5.1 and 7.5). As we have seen in section 7.2.2, the PI torque controller already introduces a larger delay than the 10 ms that were used in simulation as a minimum to account for the muscle dynamics. The delay of about 50 ms in the robot is actually closer to the biological values which are typically in the 20-50 ms range.

The robot control software is distributed: each module implements its part of the CPG and the muscle model for the axial joint, as shown in figure 7.5. Communications between modules are restricted to drive signals from the head and couplings between adjacent modules and between the two girdles. For example, the second girdle module sends at every time-step over the CAN bus the states  $r_i, \theta_i$  for oscillators 13, 38, 16, 41, 53 and 54.

The small CPG network in each module was implemented by isolating the relevant part of the network described in section 4.4. We used the `cdn-rawc` tool distributed with the Codyn framework to generate raw C files from the high level network description. These files can be compiled directly to run on the ARM microcontroller. A header file exposes a simple API to get and set CPG states and to perform an integration step with the specified time-step.

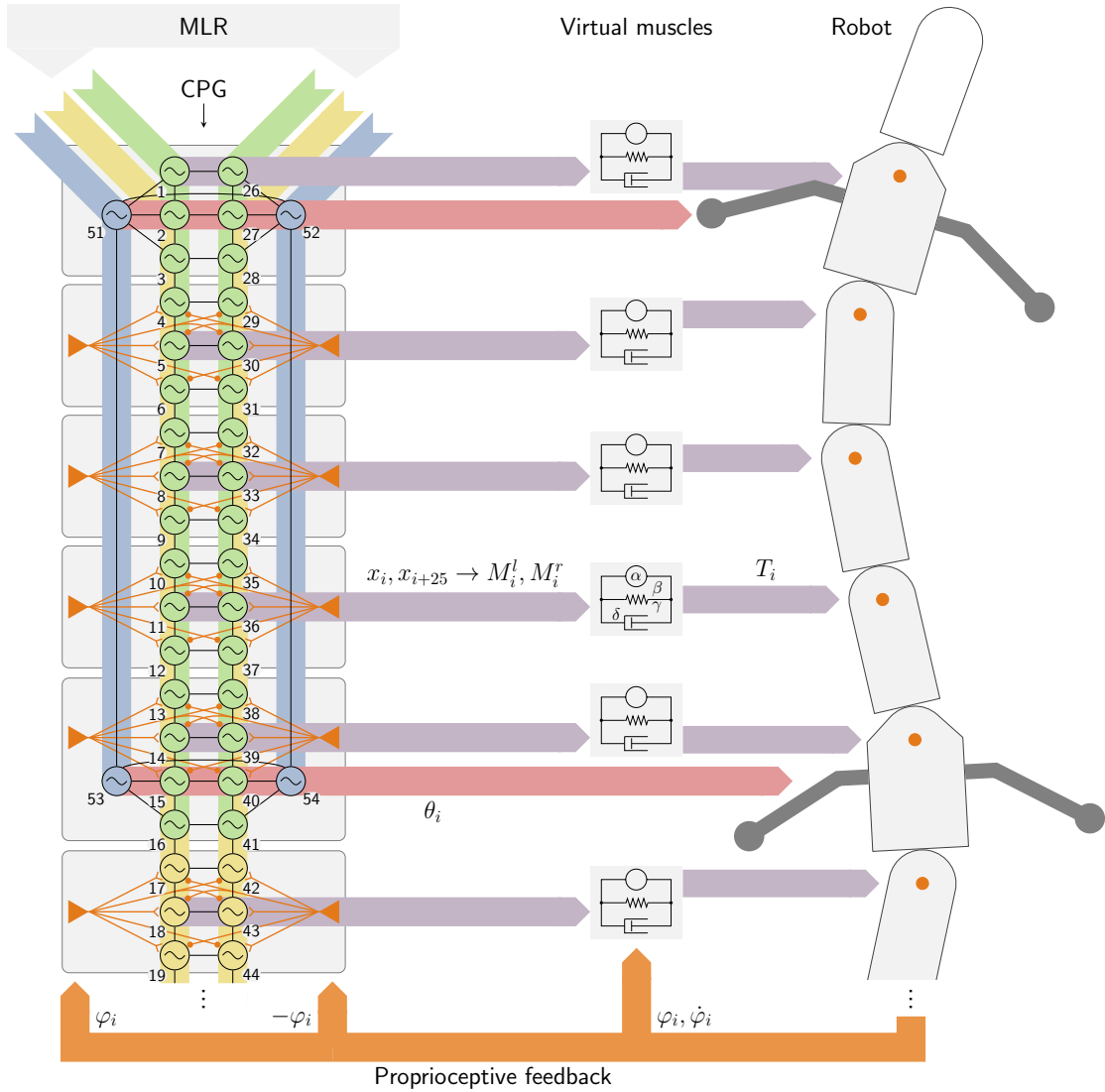


Figure 7.5 – Control architecture for experiments with *Salamandra robotica II*. **Left:** the CPG model is limited to the first 25 segments of the spinal cord, of which 19 are shown in the figure. The axial CPG is represented by a double chain of oscillators (black circles), numbered 1-25 and 26-50 for the left and right sides respectively. The limbs are represented by four additional oscillators, numbered 51-54. Black lines indicate a bidirectional coupling between two oscillators. Each oscillator also receives a drive signal representing excitation from the MLR. Different drives can be applied to the limb oscillators (blue), the trunk segments (green) and the tail segments (yellow). The network is divided in eight groups (gray rectangles, only 6 shown in the figure), corresponding to the eight axial joints of the robot. There is a stretch receptor (orange triangle) on each side of each trunk and tail group. The stretch receptors project ipsilaterally and contralaterally to the three nearest segments. The outputs  $x_i, x_{i+25}$  of one segment from each group is used as activation signal for the corresponding muscle (light purple lines); the phase  $\theta_i$  of each limb oscillator (light red) is used directly as a representation of the desired limb position. **Middle:** The CPG outputs  $x_i, x_{i+25}$  are fed directly as muscle activities  $M_i^l, M_i^r$  to the virtual muscles. The muscle model also takes as input the joint position  $\varphi_i$  and velocity  $\dot{\varphi}_i$  to determine the joint torque  $T_i$ , as shown in equation (5.1). **Right:** the torque  $T_i$  is applied at each axial joint (orange circles). The joint positions and velocities are measured and fed back to the muscle model (light orange lines) and the stretch receptors (joint positions only).

### 7.3.1 First Implementation

In the first implementation of the controller, the state of each oscillator was sent in its own CAN packet. This was due to the states  $r_i, \theta_i$  being internally represented as 32-bit floats, and to the CAN protocol restricting the payload of a packet to a maximum of 8 bytes (64 bits). Packets were sent in extended CAN frames, which include a 29-bit packet identifier. The identifier was used to include packet meta-data, such as the index of the sending module and the type of the packet. An example identifier is:

0x05000301

where 0x05 is a constant identifying a coupling packet, 0x03 identifies the sender as the third module, and 0x01 specifies the type of the coupling packet. Simple modules were sending 4 types of packets: up-left, up-right, down-left and down-right, corresponding to the four oscillators whose state had to be transmitted. Girdle modules had two more packet types for the limb oscillators.

Initial tests were conducted with a chain of 7 simple (non-girdle) modules and a simplified CPG model with symmetrical coupling weights and a uniform intrinsic phase lag of 5% along the chain. The recorded pattern however displayed strongly non-uniform phase lags, with a sharp decrease towards the end of the chain. This is illustrated in figure 7.6 (left) using the output of the left oscillator from the middle segment of each module (see figure 7.5).

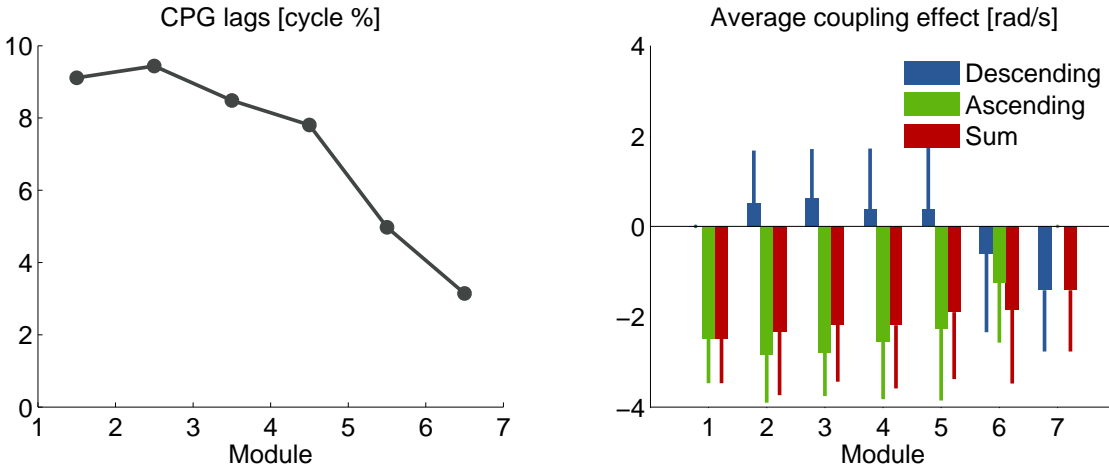


Figure 7.6 – Phase lags and average coupling effects in the first implementation of the distributed controller. **Left:** The intersegmental phase lags calculated from the middle segment of each module, as a percentage of the cycle duration. **Right:** Average effect of the ascending and descending couplings on the on the left oscillator of the middle segment in each module. The values shown correspond to the coupling terms in the sum of equation (4.19), averaged over the whole recording. The red bars show the net effect of both coupling types.

Analyzing the effect of ascending and descending couplings on the middle segment (figure 7.6 right), we see that the ascending couplings have a strong slow-down effect on all but the last

module, where they are absent. The descending couplings partially compensate for this effect in most modules, but cause a further slow-down in the last two. The net effect (red) is a decreasing slow-down towards the tail. As expected from the principles outlined in section 4.4.4, the lesser slow-down in the more caudal segments is mirrored by smaller phase lags in the left panel: the higher uncoupled frequency of the last segments allow them to “catch up” and decrease the lag from their rostral neighbors.

We will see in section 7.3.3 that the slow-down is a consequence of delays in communication between the modules. Figure 7.6 (right) suggests that ascending couplings are on average more delayed than descending couplings. This is certainly a consequence of packets with a higher identifier having a lower priority on the CAN bus. Caudal modules, which have a higher module index, will send packets with higher identifiers.

Ideally, the priority of the packets on the CAN bus should not affect significantly the performance of the controller. But with the four coupling packets described above, and if we assume four additional packets used for data logging and debugging (as was the case during our tests), a robot with eight modules would send 64 packets over the CAN bus at every time-step. Each packet carries a 64-bit payload and 64 bits of additional data for the CAN protocol. At a time-step of 10 ms, these numbers give a total of 819'200 bits per second, which is not very far from the theoretical maximum for the bus running at 1 Mbps. It is therefore likely that two modules will try to send packets at the same time, delaying the delivery of lower priority packets.

We have also observed a high rate of transmission errors on the CAN bus whenever the ARM microcontroller in the modules is active. We could not confirm whether this was due to a software error or to a deficiency in the hardware CAN controller.

For all these reasons, it is desirable to minimize the number of packets sent on the bus, and to increase the robustness of the distributed controller to communication issues. We describe our solutions in the next section.

#### 7.3.2 Second Implementation

The first change we brought to the controller to mitigate the effect of communication delays was to introduce coupling extrapolation. For each type of coupling, we use the data from the two latest coupling packets, and their times of arrival, to extrapolate in the receiver the current value of sender's state variables. A simple linear extrapolation is quite accurate, thanks to the explicit representation of the sender's phase  $\theta_i$  in the coupling packet (the phase is expected to grow linearly while the amplitude is expected to stay constant most of the time). This change leads to a dramatic improvement of the controller, as can be seen in figure 7.7. The phase lag is now almost uniform along the body (left panel) and the effect of the couplings on the frequency of the oscillators has almost vanished (right panel).

While the distributed controller performed acceptably after the introduction of coupling

extrapolation, we still observed a lot of error frames on the CAN bus, which translated to difficulties when communicating with the modules from the head, for example to change model parameters. We therefore decided to decrease the number of coupling and debug packets. We were able to halve the number of packets by sending every floating-point number such as  $r_i$  and  $\theta_i$  as a 16-bit float.<sup>2</sup> These half-floats still provide an absolute precision beyond 0.001 for numbers between -4 and 4, which is the case of our small amplitudes. The phases also fit into this range after wrapping to  $(\pi, \pi)$  (see section 7.3.4).

The effect of coupling extrapolation and of reducing the number of coupling packets can be visualized in figure 7.9 (left). Coupling extrapolation provides the biggest benefit in terms of attenuating the slow-down effect; the reduction from 8 to 4 coupling packets per time-step provides a small additional attenuation.

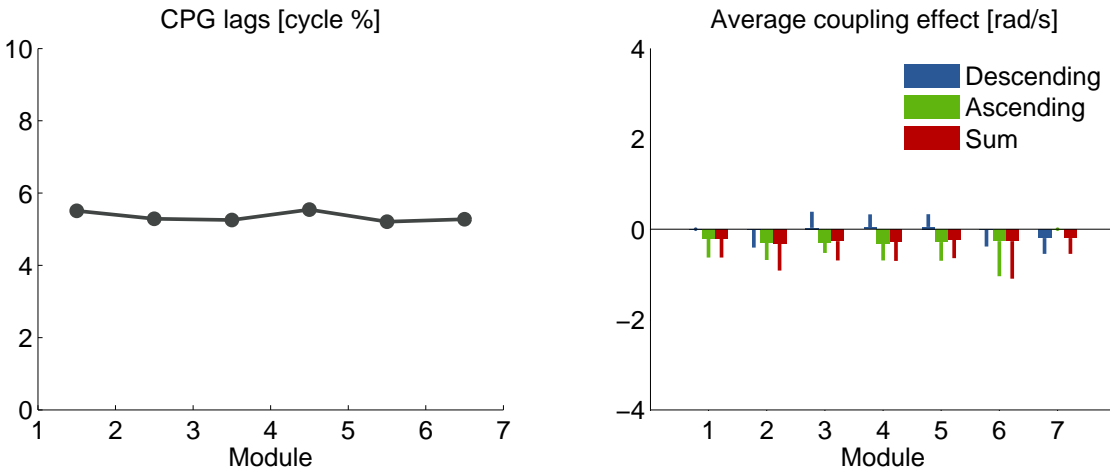


Figure 7.7 – Phase lags and average coupling effects in the distributed controller with coupling extrapolation. See figure 7.6 for details.

The communication improvements following a decrease of the number of CAN packets are also illustrated in figure 7.9.

### 7.3.3 CPG Slow-down Induced by Communication Delays

A slow-down induced by communication delays has been observed for example in a two-dimensional grid of phase oscillators with sine couplings [Niebur et al., 1991]. Here we look at the simple case of two phase oscillators with diffusive couplings of strength  $w$ :

$$\begin{aligned}\dot{\theta}_1 &= \omega + w \sin(\theta_2 - \theta_1 - \phi) \\ \dot{\theta}_2 &= \omega + w \sin(\theta_1 - \theta_2 + \phi)\end{aligned}\tag{7.1}$$

We can drop the phase biases  $\phi$  without loss of generality. A simple change of variable  $\theta_2 =$

2. Recent versions of the GNU GCC compiler for the ARM architecture have built-in support for storing numbers in 16-bit floats, using the `__fp16` data type. Calculations however are always made with 32-bit floats.



$\tilde{\theta}_2 + \phi$  gives

$$\begin{aligned}\dot{\theta}_1 &= \omega + w \sin(\tilde{\theta}_2 - \theta_1) \\ \dot{\tilde{\theta}}_2 &= \dot{\theta}_2 = \omega + w \sin(\theta_1 - \tilde{\theta}_2)\end{aligned}\tag{7.2}$$

A synchronous solution of this system with zero phase lag between  $\theta_1$  and  $\tilde{\theta}_2$  corresponds to a frequency-locked solution of (7.1) with phase lag  $\phi$ . In the rest of this section we will look for in-phase solutions of (7.2), writing  $\theta_2$  instead of  $\tilde{\theta}_2$  to keep the notation simple. Introducing a delay  $\tau$  in the couplings, we have

$$\begin{aligned}\dot{\theta}_1(t) &= \omega + w \sin(\theta_2(t - \tau) - \theta_1(t)) \\ \dot{\theta}_2(t) &= \omega + w \sin(\theta_1(t - \tau) - \theta_2(t))\end{aligned}\tag{7.3}$$

In-phase solutions correspond to the case

$$\theta_i(t) = \Omega t + \theta_0 + 2k_i\pi \quad k_i \in \mathcal{N}\tag{7.4}$$

where  $\Omega$  is the actual angular frequency  $\dot{\theta}_i$  of the oscillations:  $\dot{\theta}_i = \Omega$ . Introducing (7.4) in (7.3), we find that  $\Omega$  is determined by the following equation:

$$\Omega = \omega + w \sin(-\Omega\tau)\tag{7.5}$$

Earl and Strogatz [2003] have given a criterion for the stability of these solutions:

$$w \sin'(-\Omega\tau) = w \cos(\Omega\tau) > 0\tag{7.6}$$

The criterion applies to a wide range of topologies, but unfortunately not to finite chains of more than 2 oscillators. The relation (7.5) can be rewritten as an equation in  $x = \Omega\tau$ :

$$-\frac{1}{w\tau}x + \frac{\omega}{w} = \sin x$$

We cannot solve the equation analytically, but we can see that the solutions are the intersections between  $y = \sin x$  and a line of slope  $-\frac{1}{w\tau}$  and horizontal intercept  $\omega\tau$ , as shown in figure 7.8. According to (7.6), the stable solutions are the intersections that fall on a rising part of the sine.

For a given delay  $\tau$ , the coupling strength  $w$  determines the slope of the line and therefore the number of intersections in such a way that stronger couplings will yield more solutions. We see that with a positive coupling strength, a stable solution  $\Omega\tau = x_0$  is guaranteed if  $\omega\tau < \frac{\pi}{2}$ . This solution always satisfies  $\Omega\tau < \omega\tau$ . In other words, the delayed couplings lead to stable oscillations at a frequency lower than the intrinsic value  $\omega$ , which explains the slow-down we

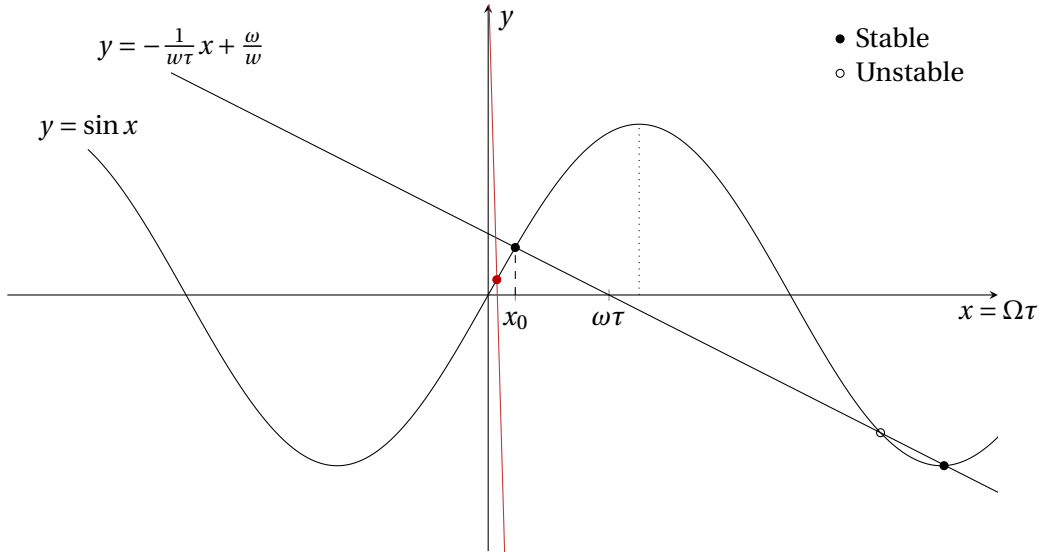


Figure 7.8 – Solutions of the in-phase synchronous oscillations with coupling delays. The stable solution at  $x = x_0$  is always present if  $w$  is positive and if the horizontal intercept  $\omega\tau$  satisfies  $\omega\tau < \frac{\pi}{2}$ . In red, an approximation of the situation in the robot controller, with a delay  $\tau = 10$  ms and a coupling strength  $w = 5$ . Adapted from Earl and Strogatz [2003].

observe on the robot.

If we assume coupling delays of 25 ms, the condition  $\omega\tau < \frac{\pi}{2}$  implies that we are guaranteed to have the stable, slow solution for any intrinsic frequency lower than  $\frac{1}{2\pi\tau} \cdot \frac{\pi}{2} = 10$  Hz. The actual frequency of the oscillations will depend on the coupling strength, with stronger couplings yielding slower rhythms.

The coupling strengths and communication delays in the robot are actually pretty small in terms of the stability analysis shown in figure 7.8. In red, we show an example for a delay of 10 ms and a coupling strength  $w = 5$ . We are clearly in a region of the parameter space where the slow rhythm is the only stable solution for in-phase oscillations.

The analysis presented here does not formally apply to a finite chain of more than two oscillators. Simulations show that the slow-down effect is stronger in longer chains of oscillators (data not shown). This is intuitive since the total coupling strength received by an oscillator increases with the length of the chain: In the case of two oscillators, each receives only one projection. In a long chain, all but the boundary oscillators receive two.

The analysis also assumes that all couplings are identical, and in particular that the delays are the same for all couplings. This is not the case in the robot, where couplings between two segments are delayed only if they cross the module boundaries, which happens for about a third of the intersegmental couplings (see figure 7.5). Finally, the analysis assumes a single chain of oscillators, but simulations show that the slow-down effect is the same in a double

chain, if the connections between left and right oscillators are without delay (apart from the delay due to the integration time-step) as is the case in the robot.

With these limitations in mind, we can use equation (7.5) to get an estimation of the intersegmental coupling delays based on the intrinsic frequency  $\omega = 2\pi \cdot 1$  and the observed frequency  $\Omega$ . The results are shown in figure 7.9 for different conditions.

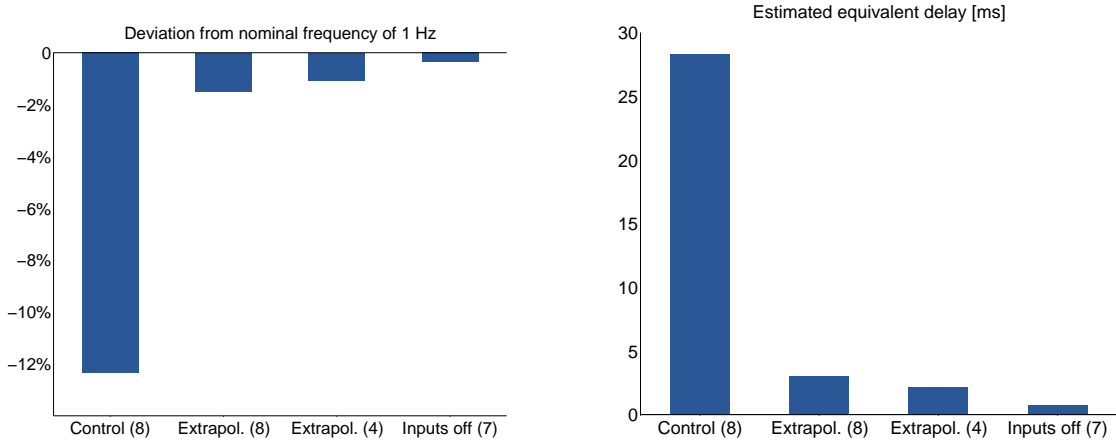


Figure 7.9 – CPG slow-down induced by communication delays, and estimation of equivalent uniform delays. The robot was made of seven simple (non-girdle) modules and used a time-step of 10 ms. The number of CAN packets sent by each module at every time-step is indicated in parentheses. **Left:** The median deviations from the nominal frequency of 1 Hz, among all data from all modules, are indicated for 4 conditions: before and after implementing coupling packet extrapolation (first two bars), after reducing the number of emitted CAN packets from 8 to 4 (third bar), and after disabling the processing of input packets (fourth bar). **Right:** Equivalent delays in a chain of two oscillators, that give the same slow-down according to equation (7.5).

### 7.3.4 Controller Time-Step

In the full robot, one step of the controller loop takes  $6.8 \pm 0.4$  ms to run in girdle modules and  $5.0 \pm 0.6$  ms in other modules. These numbers were measured in the case of girdle modules sending 3 coupling packets and 4 debug packets at each step (2 coupling packets and 3 debug packets for the other modules). Of these, the CPG integration step and muscle model in a simple (non-girdle) module take about 2.1 ms and 1.7 ms respectively. The number for the muscle model includes the time for setting the desired torque and reading the torque, position and velocity.

Initial tests with a CPG oscillating at 1 Hz showed that the computation time of one time-step increased dramatically after about 30 seconds (figure 7.10). This turned out to be caused by the trigonometric functions of the C math library, the execution time of which depends on the value of their arguments. For example, it appears that the  $\sin()$  function takes much more time to execute for an argument greater than some critical value around  $2\pi \cdot 30 \approx 188$ .<sup>3</sup> The problem was solved by implementing phase-wrapping in the CPG, to have  $\theta_i \in (-\pi, \pi)$  at all

3. The effect can be reproduced on a PC. Using the Embedded GNU C library version 2.15 (libc6 package

times. Phase wrapping also has the advantage of maintaining a high absolute precision even when the phase is encoded as a 16-bit floating-point number (see section 7.3.2).

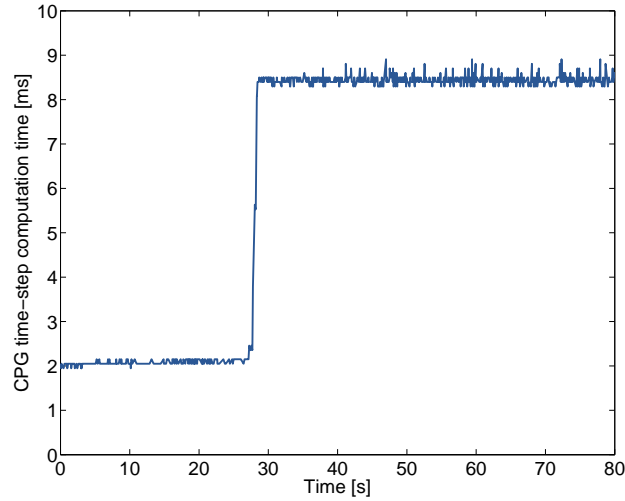


Figure 7.10 – Real-time duration of a CPG integration step using unwrapped phases. With a CPG oscillating at 1 Hz, the computation duration increases dramatically after about 30 seconds.

For the reproducibility of results, it is desirable that the muscle model perform consistently, and that the CPG show consistent numerical accuracy, even when minor changes are made to the controller. We therefore decided against running the model with the smallest possible, variable time-step. We chose to use a fixed time-step of 10 ms, and let the controller sleep for the amount of time required to reach this duration.

We note that a time-step of 10 ms was made possible thanks to the distributed nature of the controller. Given the computation time of over 2 ms for the CPG integration step in each module, a centralized controller running in the head would need over 16 ms to compute one step of the CPG model, not counting the time for communications between the head and the modules.

### 7.3.5 Concluding Remarks

In the present configuration where all the modules communicate with each other over the same CAN bus, the benefits of the distributed controller in terms of communication bandwidth are limited. The next revision of the robot should include direct serial communication channels between adjacent modules. The benefits of the distributed controller design will then be fully realized. Still, as we have seen in section 7.3.4, the distributed architecture allows us to integrate the CPG with a smaller time-step by sharing computations among the modules.

The architecture also shows an obvious advantage for the virtual muscle model, which can run

---

version 2.15-0ubuntu10.3 on Ubuntu 12.04) on an AMD64 architecture, the duration of a call to the `sin()` function increases sharply for operands greater than 201.05.

in a fast local loop rather than requiring the transmission of the joint position, velocity and desired torque at every step over the CAN bus. It also increases the robustness of the muscle model by avoiding the reliance on the CAN bus and its high rate of communication errors.

Finally, we can expect the architecture to greatly improve the robustness of the controller to communication faults. For example, a simulation study with a snake robot showed that a distributed controller with local sensory feedback could maintain a proper coordination between the joints even when all communications were cut [Watanabe et al., 2009]. We still have to characterize the behavior of our controller in such scenarios.

### 7.4 External Video Tracking

The robot joint positions can be read from the motor encoders at each time-step. However this gives no information about the speed of locomotion. To measure the speed, we use an external video tracking system based on two Basler A622F cameras located 2 meters above the pool (for swimming) or track (for other behaviors). The setup is shown in figure 7.11.

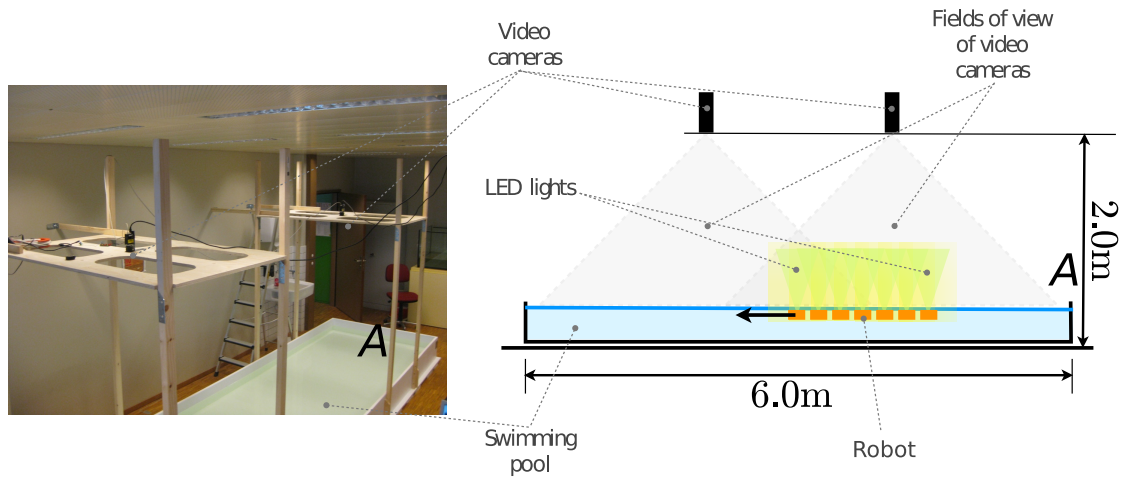


Figure 7.11 – External video tracking setup. Two cameras are placed two meters above a 600x150x30 cm pool, such that their overlapping fields of view cover the whole length of 6 m. Image courtesy of Mathieu Porez.

The cameras record the positions of the LEDs on the cover of each module at a rate of 15 images per second, with an accuracy of  $\pm 1$  cm. By merging the data collected by the two cameras, we are able to cover a track length of 6 meters.

The video tracking system is also used to get a second estimation of the joint position. Due to the compliance in the connectors between the robot modules, the position read from the motor encoders cannot be trusted to reflect accurately the angle between the modules. The joint angles are calculated by fitting in each frame the kinematic chain of the robot to the positions of the LEDs.

## 8 Conclusion

We designed a flexible CPG model that reproduces the main features of recordings from isolated salamander spinal cords, including the distribution of intersegmental phase lags, the correlation between phase lags and cycle frequencies, and the spontaneous switches between slow and fast rhythms. The same model with minimal adjustments was used successfully to reproduce the five motor behaviors documented in the animal,<sup>1</sup> first in simulation and then on a robot. The robot tests for each behavior were conducted with five different “individuals”, that is, using CPG networks with different values for the parameters that determine the intrinsic frequency of each oscillator. This allowed us to reproduce the variability of muscle activation patterns observed in the animals.

The model proved highly controllable: the five different behaviors could be reproduced using only two different levels of excitatory drive, one for the limb oscillators and one for the axial oscillators. The controllability also allowed for the compensation of the differences between the simulated individuals: each individual, using its own set of drive levels, could reproduce all CPG patterns.

We found that local proprioceptive feedback can have a strong optimizing effect on the CPG activity pattern during swimming: while the simulated individuals would produce very different CPG activity patterns in absence of feedback, some of them very inappropriate for swimming, they all showed good swimming performance after the introduction of sensory feedback of equal strength in all individuals. We showed in simulation that feedback, together with the viscoelastic properties of the body, could reduce a range of intrinsic CPG intersegmental phase lags as wide as  $(-10\%, 10\%)$  to a range of kinematic phase lags of  $(1.3\%, 1.9\%)$ , all very appropriate values for swimming.

Thanks to the abstract level of modeling, we were able to analyze mathematically the effect of sensory feedback on the oscillator frequency, and highlighted the role of the increasing CPG-mechanical delay along the body in the stabilization of the swimming gait by sensory feedback. This finding also highlights the importance of muscle dynamics during swimming,

---

1. Swimming, underwater stepping, forward land stepping, backward land stepping and struggling.

and in particular in the understanding of the CPG-muscles-environment-feedback loop. The increasing delay between muscle activation and body curvature along the body of fishes has been the focus of a lot of research, but it is the first time to our knowledge that it is shown to interact with local sensory feedback in a way that is beneficial for locomotion. We note that all these results could not have been obtained without an integrated modeling approach.

Our findings are also original in that they provide a common framework for reasoning about the modulation of the CPG activity pattern by sensory feedback, descending commands from the brainstem and differences in intrinsic cycle frequencies in different parts of the network. Our work relies heavily on the principles outlined by Matsushima and Grillner [1992], but highlight the importance of an asymmetry between ascending and descending intersegmental couplings.

The model of course has its limits. For example, we could not find an expression for the axial proprioceptive feedback that would be appropriate in all of the five salamander motor behaviors considered. We found instead that good stepping gaits were produced by exchanging the ipsilateral and contralateral feedback weights compared to swimming. As far as we know, there is no biological evidence for such an inversion of the effect of feedback between locomotor modes. The model was more successful in the integration of excitatory proprioceptive feedback in the limbs. We found in simulation that such feedback could partially or totally replace the need for a differential drive between limb and axial oscillators during forward land stepping.

From a robotic perspective, our work led to the implementation of a completely distributed controller. This distributed architecture allowed us to minimize the communications between the robot modules and to decrease the CPG integration time-step by distributing the computation cost. This also led to an enhanced response time of the muscle model. We note that this distributed architecture shows an interesting similarity with biology. In animals also, the computation cost is distributed along the body in the numerous segments of the spinal cord, and local proprioceptive feedback loops allow for fast responses. Regarding the virtual muscles, it would be interesting to investigate how their energy consumption compares with a position controller generating a similar gait.



---

## **Final Words**

We have investigated at a very high level the principles that govern the shaping of the muscle activation patterns in the salamander, using abstract phase oscillators, a linear muscle model and a gross approximation of the animal morphology. Our purpose was to explore the phenomena that arise from the interaction between these simple elements. We think that our project was successful in uncovering a general principle of interaction between the CPG, the descending drives from the brainstem and local sensory feedback. However we should note that our simple model cannot tell us what actually happens in the real, complex system. It can only suggest possibilities, phenomena that these simple principles could underlie in the animal. More accurate modeling work and experiments are required to verify whether the principles we describe here still hold in a more realistic model. A first step would be to try and reproduce our results with a similar model, but using a more concrete implementation of the CPG, for example based on a spiking neuron model.

We should also mention that we only addressed a few aspects of the problem of locomotion control in the salamander. Much work remains to be done even at our level of modeling, for example on the coordination of muscles in the limbs, on the generation of discrete movements and on the integration of other sensory feedback modalities.



# A CPG and Kinematic Patterns in Robot Experiments

We show here the CPG and kinematic patterns obtained with the robot for the five salamander behaviors described in chapter 2. We only show the patterns obtained with the first simulated individual, and only one for each behavior (out of three).

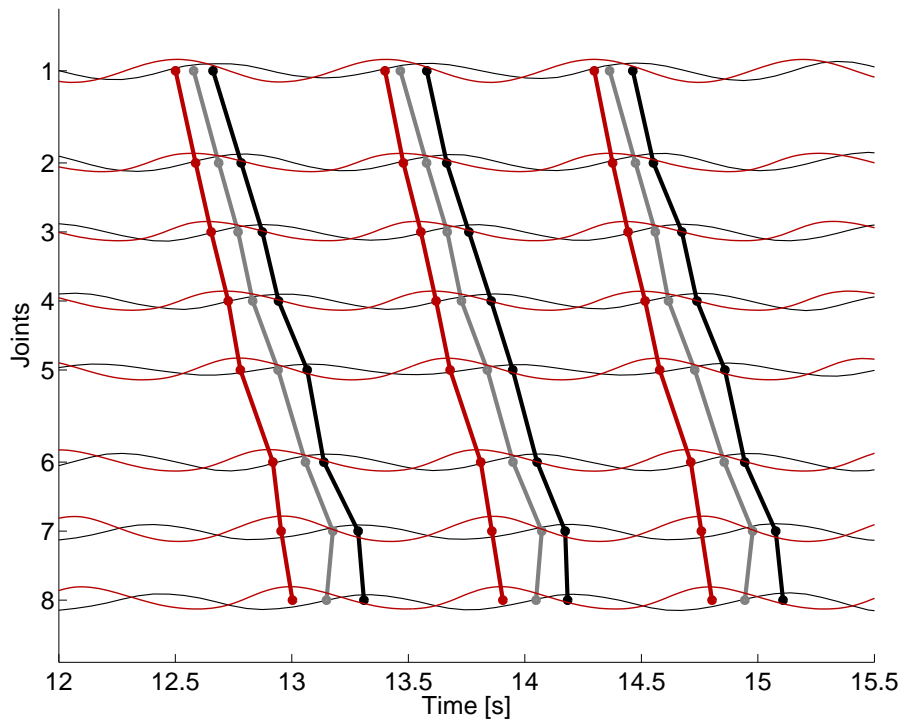


Figure A.1 – Swimming pattern obtained with the first simulated individual, with feedback  $w^{\text{ipsi}} = 10$ . CPG oscillations and joint oscillations reconstructed from the external video tracking data are shown in thin red and black lines respectively. Circular markers show the centroids of the positive halves of the oscillations, which were used to calculate the phase lags between the joints, as shown by the thick red and black lines. The centroid and phase lags are also shown, in gray, for the joint angles read from the motor encoders.

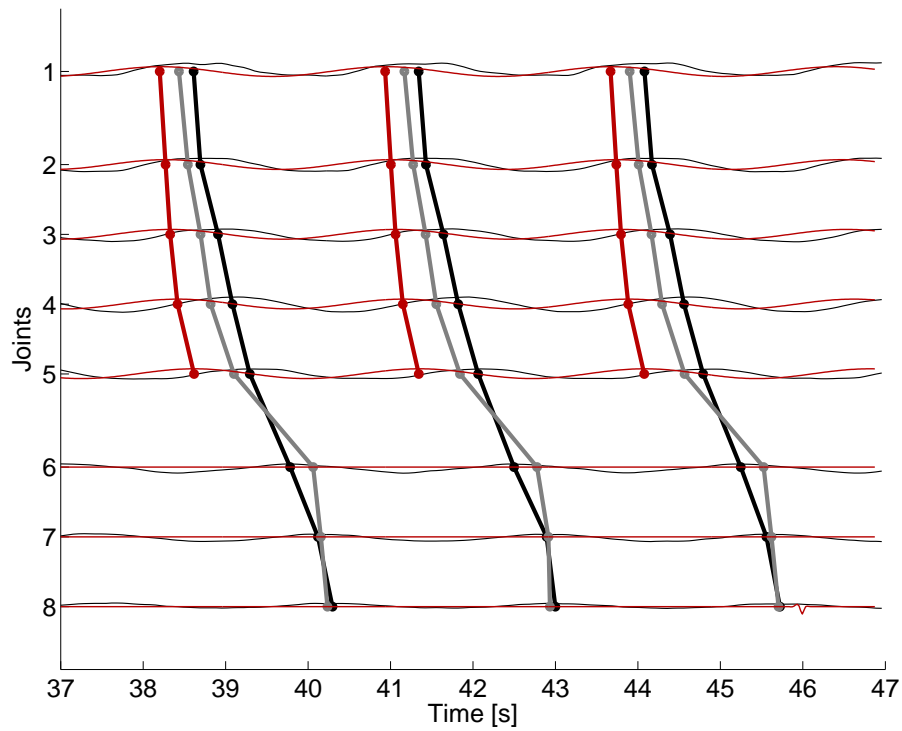


Figure A.2 – Underwater stepping pattern obtained with the first simulated individual.

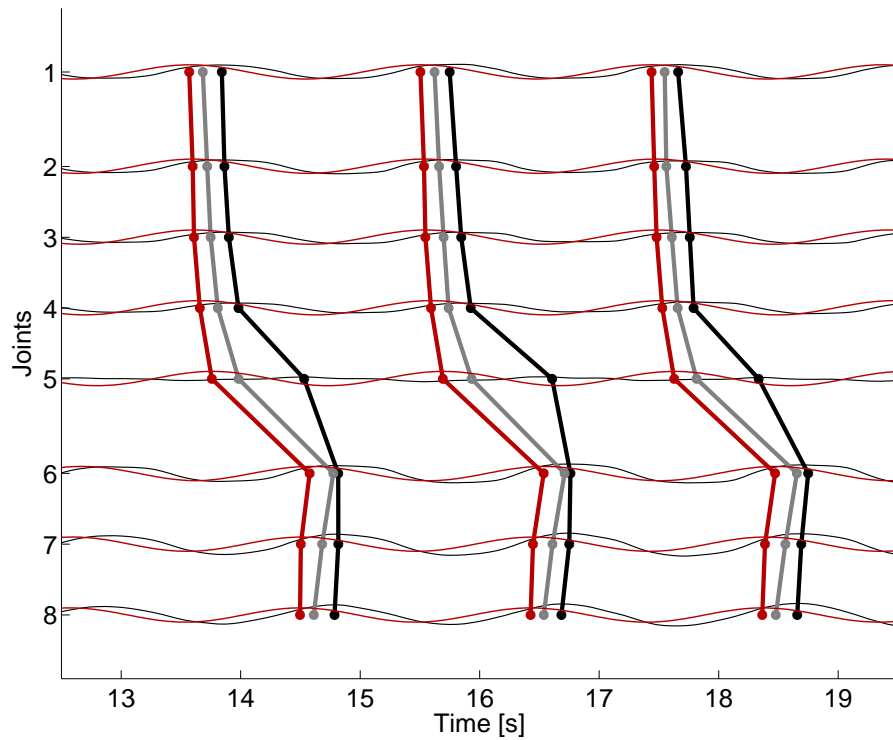


Figure A.3 – Forward land stepping pattern obtained with the first simulated individual.

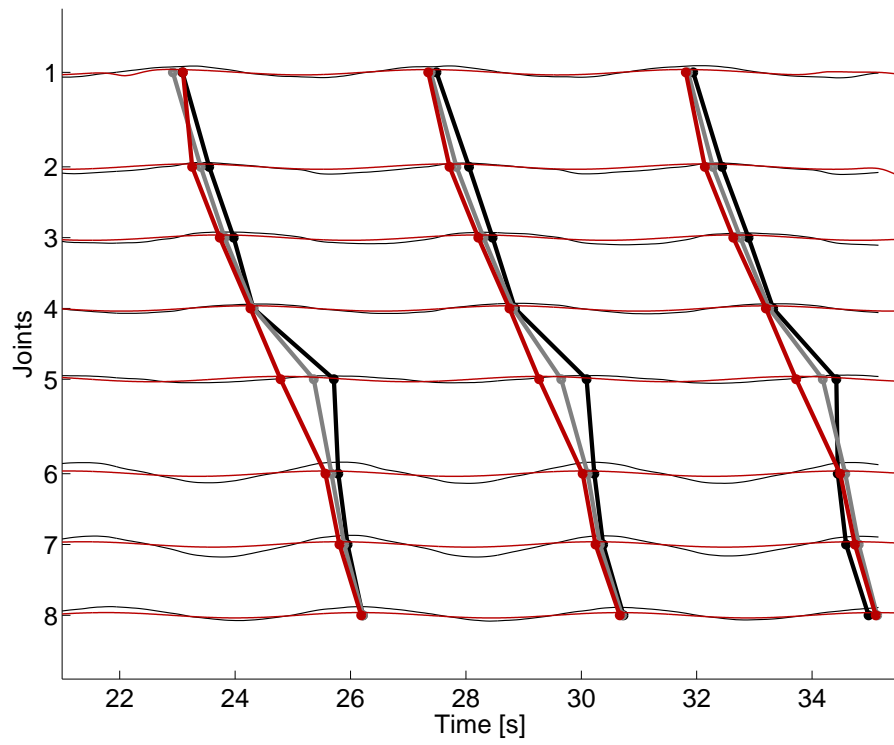


Figure A.4 – Backward stepping pattern obtained with the first simulated individual.

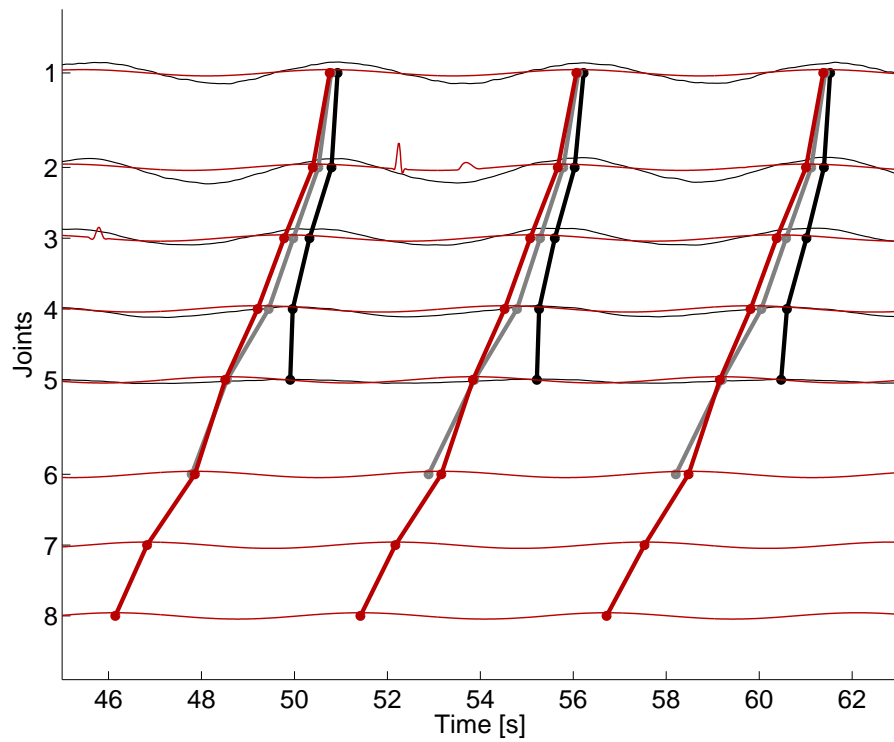


Figure A.5 – Struggling pattern obtained with the first simulated individual. The glitch in the CPG oscillation in joint 2 is probably due to corrupted CAN packets in the communication between the robot modules.



# B Conversion Factors for Internal Robot Units

We give here for reference the detail of the calculation of the factors used to convert from the SI units used in simulation to the internal units of the PI torque controller used on *Salamandra II*.

## B.1 Position Units

The motor encoder emits 512 pulses per revolution. A 32 bits register  $\varphi_{32}$  gives the position of the motor as a count of the number of pulses from the rest position, ie.  $\varphi_{32} = 512$  corresponds to a motor rotation of 360 degrees. The value of  $\varphi_{32}$  is divided by  $2^{d_{\text{pos}}}$ , and the least significant byte of the result is stored in an 8 bit register  $\varphi_8$ . In our robots, we have  $d_{\text{pos}} = 7$  for the body joints and  $d_{\text{pos}} = 8$  for the legs.

The conversion factors for the motor rotation  $\varphi_m$  are given in the following table:

	$\varphi_m$ [deg]	$\varphi_m$ [rad]
1 $\varphi_8$ unit (body)	$\frac{360 \cdot 2^7}{512} = 90.0$	1.57
1 $\varphi_8$ unit (leg)	$\frac{360 \cdot 2^8}{512} = 180.0$	3.14

For the joint rotation, one has to incorporate the reduction factor  $R$  of the gearbox. The following table gives the conversion factors from  $\varphi_8$  to the joint rotation  $\varphi_{\text{joint}} = \frac{\varphi_m}{R}$ . Empirical values are given in the last two columns.

Joint type	$R$	$\varphi_8$	$\varphi_{\text{joint}}$ calculated		$\varphi_{\text{joint}}$ measured	
			[deg]	[rad]	[deg]	[rad]
Axis	135	1	0.667	0.0116	0.680	0.0119
Leg	90	1	2	0.0349		

### B.2 Torque Units

The motor torque  $\tau_m$  is calculated from a measure of the motor current  $I$ , using the motor constant  $k$ :

$$I = \frac{\tau_m}{k}$$

The current is measured from the voltage drop  $V_I$  through a resistor  $R_I$ :

$$V_I = R_I I$$

It is the input voltage of an amplifier (AD628) which leads to the following output voltage  $V_{\text{ampl}}$ :

$$V_{\text{ampl}} = V_I \left( 1 + \frac{R_1}{R_2} \right) \cdot 0.1$$

The resistors are selected such that  $V_{\text{ampl}} \in [-2.5, 2.5]$  V. The voltage is then shifted by 2.5 V to match the PIC A/D converter input range of  $[0, 5]$  V:

$$V_{\text{PIC}} = V_{\text{ampl}} + 2.5 \text{ V}$$

The voltage  $V_{\text{PIC}}$  is digitalized into an integer such that  $[0, 5]$  V maps to  $\{0, 1, \dots, 1024\}$ . Subtracting the *torque bias* 512 from this value to undo the shift of 2.5 V gives the 16 bits signed torque measurement<sup>1</sup>:

$$\tau_{16} = \frac{V_{\text{PIC}}}{5 \text{ V}} \cdot 1024 - 512$$

or when putting it all together:

$$\tau_{16} = \frac{R_I \frac{\tau_m}{k} \left( 1 + \frac{R_1}{R_2} \right) \cdot 0.1 + 2.5 \text{ V}}{5 \text{ V}} \cdot 1024 - 512$$

---

1. In practice the shift is not exactly 2.5 V and the torque bias can be adjusted accordingly.



which reduces to

$$\tau_{16} = \frac{R_I \frac{\tau_m}{k} \left(1 + \frac{R_1}{R_2}\right) \cdot 0.1}{5V} \cdot 1024$$

The 8 bits register  $\tau_8$  is obtained by dividing  $\tau_{16}$  by  $2^{d_{\text{torque}}}$ . In our case  $d_{\text{torque}} = 2$ , so we have  $\tau_{16} = \tau_8 \cdot 4$ .

Using our values  $k = 3.46 \text{ mNm/A}$ ,  $R_1 = 50 \text{ k}\Omega$  and  $R_2 = 1 \text{ k}\Omega$ , we find the following conversion factors for the motor torque:

	$R_I [\Omega]$	$\tau_m [\text{mNm}]$
1 $\tau_{16}$ unit	0.05	0.0663
1 $\tau_8$ unit	0.05	0.265

And with the gearbox reduction, we have the following conversions for the joint torque  $\tau_{\text{joint}}$ :

Joint type	R	$\tau_8$	$\tau_{\text{joint}} [\text{mNm}]$
Axis	135	1	35.8
Leg	90	1	23.9

### B.3 Speed Units

The speed measurement is updated every  $h$  seconds, where  $h$  is the sampling time. It is determined by the value of the 16 bits sampling time register  $h_{16}$ :

$$h = h_{16} \cdot 1.6 \mu s$$

In our case  $h_{16} = 16 \cdot 2^8 + 124 = 4220$  ( $h_{16}^{\text{MSB}} = 16$ ,  $h_{16}^{\text{LSB}} = 124$ ) and we have  $h = 6.75$  ms.

For the speed, the measure is simply the number of encoder pulses received during this sampling time. It is kept in a 16 bits register  $\omega_{16}$ , and in an 8 bits register  $\omega_8$  after division by  $2^{d_{\text{speed}}}$ . In our case,  $d_{\text{speed}} = 3$  for the body and  $d_{\text{speed}} = 1$  for the legs. Since a complete revolution corresponds to 512 pulses, the motor speed is  $\omega_m = \frac{\omega_{16}}{h} \cdot \frac{2\pi}{512}$  rad/s, and we have the following conversion factors:

	$\omega_m$ [deg/s]	$\omega_m$ [rad/s]
1 $\omega_8$ unit (body)	833	14.5
1 $\omega_8$ unit (leg)	208	3.64

Applying the gearbox reduction, we have the following joint speeds:

Joint type	R	$\omega_8$	$\omega_{\text{joint}}$	
			[deg/s]	[rad/s]
Axis	135	1	6.17	0.108
leg	90	1	2.31	0.0404

## Bibliography

- J.D. Altringham and D.J. Ellerby. Fish swimming: patterns in muscle function. *Journal of Experimental Biology*, 202(23):3397–3403, 1999.
- J.D. Altringham, C.S. Wardle, and C.I. Smith. Myotomal muscle function at different locations in the body of a swimming fish. *Journal of experimental biology*, 182(1):191–206, 1993.
- S. Aoi, T. Yamashita, and K. Tsuchiya. Hysteresis in the gait transition of a quadruped investigated using simple body mechanical and oscillator network models. *Physical Review E*, 83(6):061909, 2011.
- M. A. Ashley-Ross. Hindlimb kinematics during terrestrial locomotion in a salamander (*dicamptodon tenebrosus*). *Journal of Experimental Biology*, 193:255–283, 1994.
- M. A. Ashley-Ross and B. F Bechtel. Kinematics of the transition between aquatic and terrestrial locomotion in the newt *taricha torosa*. *Journal of Experimental Biology*, 207:461–474, 2004.
- M. A. Ashley-Ross and G. V. Lauder. Motor patterns and kinematics during backward walking in the pacific giant salamander: evidence for novel motor output. *Journal of Neurophysiology*, 78:3047–3060, 1997.
- M.A. Ashley-Ross, R. Lundin, and K.L. Johnson. Kinematics of level terrestrial and underwater walking in the california newt, *taricha torosa*. *Journal of Experimental Zoology Part A: Ecological Genetics and Physiology*, pages 240–257, 2009.
- A. Bejan and J.H. Marden. Unifying constructal theory for scale effects in running, swimming and flying. *Journal of Experimental Biology*, 209(2):238–248, 2006.
- T. Bem, J. M. Cabelguen, O. Ekeberg, and S. Grillner. From swimming to walking: a single basic network for two different behaviors. *Biological Cybernetics*, 88:79–90, 2003.
- A. Bicanski, D. Ryczko, J.-M. Cabelguen, A.J. Ijspeert, et al. Modeling axial spinal segments of the salamander central pattern generator for locomotion. *BMC Neuroscience*, 12(Suppl 1): P157, 2011.
- A. R. Blight. The muscular control of vertebrate swimming movements. *Biological Reviews*, 52(2):181–218, 1977.

## Bibliography

---

- Q. Bone, R. Ridge, and KP Ryan. Stretch receptors in urodele limb muscles. *Cell and Tissue Research*, 165(2):249–266, 1976.
- F. Boyer, M. Porez, A. Leroyer, and M. Visonneau. Fast dynamics of an eel-like robot—comparisons with navier–stokes simulations. *Robotics, IEEE Transactions on*, 24(6): 1274–1288, 2008.
- F. Boyer, M. Porez, and A. Leroyer. Poincaré–cosserat equations for the lighthill three-dimensional large amplitude elongated body theory: Application to robotics. *Journal of nonlinear science*, 20(1):47–79, 2010.
- K. Brändle and G. Székely. The control of alternating coordination of limb pairs in the newt (*triturus vulgaris*). *Brain Behav. Evol.*, 8:366–385, 1973.
- R. Breithaupt, J. Dahnke, K. Zahedi, J. Hertzberg, and F. Pasemann. Robo-salamander - an approach for the benefit of both robotics and biology. In *CLAWAR 2002*, 2002.
- KL Briggman and WB Kristan Jr. Multifunctional pattern-generating circuits. *Annu. Rev. Neurosci.*, 31:271–294, 2008.
- J. T. Buchanan. Neural network simulations of coupled locomotor oscillators in the lamprey spinal cord. *Biological Cybernetics*, 66:367–374, 1992.
- J. T. Buchanan and S. Grillner. Newly identified ‘glutamate interneurons’ and their role in locomotion in the lamprey spinal cord. *Science*, 236:312–314, 1987.
- J. M. Cabelguen, C. Bourcier-Lucas, and R. Dubuc. Bimodal locomotion elicited by electrical stimulation of the midbrain in the salamander *notophthalmus viridescens*. *The Journal of Neuroscience*, 23(6):2434–2439, 2003.
- J. Cheng, R. B. Stein, K. Jovanovic, K. Yoshida, D. J. Bennett, and Y. Han. Identification, localization, and modulation of neural networks for walking in the mudpuppy (*necturus maculatus*) spinal cord. *The Journal of Neuroscience*, 18(11):4295–4304, 1998.
- J. Cheng, K. Jovanovic, Y. Aoyagi, D. J. Bennett, Y. Han, and R. B. Stein. Differential distribution of interneurons in the neural networks that control walking in the mudpuppy (*necturus maculatus*) spinal cord. *Ex. Brain Res.*, 145(2):190–198, 2002.
- S. Chevallier, M. Landry, F. Nagy, and J. M. Cabelguen. Recovery of bimodal locomotion in the spinal-transected salamander, *pleurodeles waltlii*. *Eur. J. Neurosci.*, 20:1995–2007, 2004.
- A. H. Cohen and P. Wallen. The neural correlate of locomotion in fish. "fictive swimming" induced in a in vitro preparation of the lamprey spinal cord. *Exp. Brain Res.*, 41:11–18, 1980.
- A. H. Cohen, P. J. Holmes, and R. Rand. The nature of coupling between segmented oscillations and the lamprey spinal generator for locomotion: a mathematical model. *J. Math. Biol.*, 13: 345–369, 1982.

- A. Crespi, K. Karakasiliotis, A. Guignard, and A.J. Ijspeert. Salamandra robotica ii: An amphibious robot to study salamander-like swimming and walking gaits. *IEEE Transactions on Robotics*, 2013.
- S. Daan and T. Belterman. Lateral bending in locomotion of some lower tetrapods. *Proc. ned. Akad. Wetten. C.*, 71:245–266, 1968.
- K. D'Août, P. Aerts, and F. de Vree. The timing of muscle strain and activation during steady swimming in a salamander, *ambystoma mexicanum*. *Netherlands Journal of Zoology*, 46: 263–271, 1996.
- B. M. Davis, J. L. Ayers, L. Koran, J. Carlson, M. C. Anderson, and S. B. Simpson. Time course of the salamander spinal cord regeneration and recovery of swimming: HRP retrograde pathway tracing and kinematic analysis. *Experimental Neurology*, 108:198–213, 1990.
- S. M. Deban and N. Schilling. Activity of trunk muscles during aquatic and terrestrial locomotion in *ambystoma maculatum*. *Journal of Experimental Biology*, 212(18):2949–2959, 2009.
- I. Delvolvé, T. Bem, and J. M. Cabelguen. Epaxial and limb muscle activity during swimming and terrestrial stepping in the adult newt, *Pleurodeles Waltl*. *Journal of Neurophysiology*, 78: 638–650, 1997.
- I. Delvolvé, P. Branchereau, R. Dubuc, and J. M. Cabelguen. Fictive rhythmic motor patterns induced by NMDA in an in vitro brain stem-spinal cord preparation from an adult urodele. *Journal of Neurophysiology*, 82:1074–1077, 1999.
- J. Duysens and H.W.A.A. van de Cromment. Neural control of locomotion; part 1: The central pattern generator from cats to humans. *Gait & Posture*, 7(2):131–141, 1998.
- M.G. Earl and S.H. Strogatz. Synchronization in oscillator networks with delayed coupling: a stability criterion. *Physical review. E, Statistical, nonlinear, and soft matter physics*, 67(3 Pt 2):036204, 2003.
- D. Eberly. Polyhedral mass properties (revisited), 2002. URL <http://www.geometrictools.com/Documentation/PolyhedralMassProperties.pdf>.
- J. L. Edwards. The evolution of terrestrial locomotion. In M. K Hecht, P. C. Goody, and Hecht B. M., editors, *Major patterns in vertebrate evolution*, pages 553–577. Plenum Press, 1976.
- Ö. Ekeberg. A combined neuronal and mechanical model of fish swimming. *Biological Cybernetics*, 69:363–374, 1993.
- Ö. Ekeberg, P. Wallén, A. Lansner, H. Traven, L. Brodin, and S. Grillner. A computer-based model for realistic simulations of neural networks i: The single neuron and synaptic interaction. *Biological Cybernetics*, 65:81–90, 1991.

## Bibliography

---

- Ö. Ekeberg, A. Lansner, and S. Grillner. The neural control of fish swimming studied through numerical simulations. *Adaptive Behavior*, 3(4):363–384, 1995.
- B. Ermentrout and T.W. Ko. Delays and weakly coupled neuronal oscillators. *Philosophical Transactions of the Royal Society A: Mathematical, Physical and Engineering Sciences*, 367 (1891):1097–1115, 2009.
- B. Ermentrout and N. Kopell. Inhibition-produced patterning in chains of coupled nonlinear oscillators. *SIAM Journal of Applied Mathematics*, 54(2):478–507, 1994.
- D. Floreano and C. Mattiussi. *Bio-inspired artificial intelligence: theories, methods, and technologies*. The MIT Press, 2008.
- L. M. Frolich and A. A. Biewener. Kinematic and electromyographic analysis of the functional role of the body axis during terrestrial and aquatic locomotion in the salamander *ambystoma tigrinum*. *Journal of Experimental Biology*, 62:107–130, 1992.
- Y. Fukuoka, H. Kimura, and A. H. Cohen. Adaptive dynamic walking of a quadruped robot on irregular terrain based on biological concepts. *The International Journal of Robotics Research*, 3–4:187–202, 2003.
- K. Q. Gao and N. H. Shubin. Late jurassic salamanders from northern china. *Nature*, 410: 574–577, 2001.
- S. Grillner and P. Wallen. Central pattern generators for locomotion, with special reference to vertebrates. *Annual review of neuroscience*, 8(1):233–261, 1985.
- S. Grillner, J. T. Buchanan, P. Wallén, and L. Brodin. Neural control of locomotion in lower vertebrates. In A. H. Cohen, S. Rossignol, and S. Grillner, editors, *Neural control of rhythmic movements in vertebrates*, pages 1–40. Jon Wiley & Sons, 1988.
- S. Grillner, P. Wallén, and L. Brodin. Neuronal network generating locomotor behavior in lamprey: Circuitry, transmitters, membrane properties, and simulation. *Annual Review of Neuroscience*, 14:169–199, 1991.
- S. Grillner, T. Degliana, Ö. Ekeberg, A. El Marina, A. Lansner, G. N. Orlovsky, and P. Wallén. Neural networks that co-ordinate locomotion and body orientation in lamprey. *Trends in Neuroscience*, 18(6):270–279, 1995.
- S. Grillner, A. P. Georgopoulos, and L. M. Jordan. Selection and initiation of motor behavior. In P. S. G. Stein, S. Grillner, A. Selverston, and D. G. Stuart, editors, *Neurons, networks and motor behavior*. MIT press, 1997.
- S. Grillner, P. Wallén, K. Saitoh, A. Kozlov, and B. Robertson. Neural bases of goal-directed locomotion in vertebrates—an overview. *Brain Research Reviews*, 57(1):2–12, 2008.
- S. Grillner et al. The motor infrastructure: from ion channels to neuronal networks. *Nature Reviews Neuroscience*, 4(7):573–586, 2003.

- J. Grizou. Modeling the salamander swimming gait with virtual muscles on a robotic platform. Master's thesis, EPFL, Lausanne, Switzerland, 2011.
- N. Harischandra, J.-M. Cabelguen, and Ö. Ekeberg. A 3d musculo-mechanical model of the salamander for the study of different gaits and modes of locomotion. *Frontiers in Neurorobotics*, 4, 2010.
- N. Harischandra, J. Knuesel, A. Kozlov, A. Bicanski, J.-M. Cabelguen, A.J. Ijspeert, and Ö. Ekeberg. Sensory feedback plays a significant role in generating walking gait and in gait transition in salamanders: A simulation study. *Frontiers in Neurorobotics*, 5, 2011.
- R. M. Harris-Warrick and E. Marder. Modulation of neural networks for behavior. *Annual review of neuroscience*, 14(1):39–57, 1991.
- A.A.V. Hill, M.A. Masino, and R.L. Calabrese. Intersegmental coordination of rhythmic motor patterns. *Journal of neurophysiology*, 90(2):531, 2003.
- M. Huss, A. Lansner, P. Wallén, A. El Manira, S. Grillner, and J.H. Kotalleski. Roles of ionic currents in lamprey cpg neurons: A modeling study. *Journal of neurophysiology*, 97(4): 2696–2711, 2007.
- A. J. Ijspeert. A connectionist central pattern generator for the aquatic and terrestrial gaits of a simulated salamander. *Biological Cybernetics*, 84(5):331–348, 2001.
- A. J. Ijspeert, A. Crespi, and J. M. Cabelguen. Simulation and robotics studies of salamander locomotion: Applying neurobiological principles to the control of locomotion in robots. *NeuroInformatics*, 3(3):171–196, 2005.
- A. J. Ijspeert, A. Crespi, D. Ryczko, and J. M. Cabelguen. From swimming to walking with a salamander robot driven by a spinal cord model. *Science*, 315(5817):1416 – 1420, 2007.
- T. Kano, T. Sato, R. Kobayashi, and A. Ishiguro. Decentralized control of serpentine locomotion that enables well-balanced coupling between phasic and tonic control. In *Proceedings of IROS2010*, Taipei, 2010.
- K. Karakasiliotis, N. Schilling, J.-M. Cabelguen, and A. J. Ijspeert. Where are we in understanding salamander locomotion: biological and robotic perspectives on kinematics. *Biological cybernetics*, pages 1–16, 2012.
- S.L. Katz and R.E. Shadwick. Curvature of swimming fish midlines as an index of muscle strain suggests swimming muscle produces net positive work. *Journal of theoretical biology*, 193 (2):243–256, 1998.
- T. Kiemel, K. M. Gormley, L. Guan, T. Williams, and A. H. Cohen. Estimating the strength and direction of functional coupling in the lamprey spinal cord. *Journal of Computational Neuroscience*, 15:233–245, 2003.

## Bibliography

---

- H. Kimura, S. Akiyama, and K. Sakurama. Realization of dynamic walking and running of the quadruped using neural oscillators. *Autonomous Robots*, 7(3):247–258, 1999.
- N. Kopell. Chains of coupled oscillators. In M. A. Arbib, editor, *The handbook of brain theory and neural networks*, pages 178–183. MIT Press, 1995.
- A. Kozlov, M. Huss, A. Lansner, J.H. Kottleski, and S. Grillner. Simple cellular and network control principles govern complex patterns of motor behavior. *Proceedings of the National Academy of Sciences*, 106(47):20027, 2009.
- I. Lavrov and J. Cheng. Activation of nmda receptors is required for the initiation and maintenance of walking-like activity in the mudpuppy (*necturus maculatus*). *Canadian journal of physiology and pharmacology*, 82(8-9):637–644, 2004.
- M. A. Lewis. *Self-organization of locomotory controllers in robots and animals*. PhD thesis, Faculty of the Graduate School, University of Southern California, August 1996.
- MJ Lighthill. Large-amplitude elongated-body theory of fish locomotion. *Proceedings of the Royal Society of London. Series B. Biological Sciences*, 179(1055):125–138, 1971.
- G.E. Loeb and C. Ghez. The motor unit and muscle action. *Principles of neural science*, pages 674–694, 2000.
- M. MacKay-Lyons. Central pattern generation of locomotion: A review of the evidence. *Phys. Ther.*, 82(1):69–83, 2002.
- T. Matsushima and S. Grillner. Neural mechanisms of intersegmental coordination in lamprey: local excitability changes modify the phase coupling along the spinal cord. *J. of Neurophysiology*, 67:373–388, 1992.
- A. D. McClellan and K. A. Sigvardt. Features of entrainment of spinal pattern generators for locomotor activity in the lamprey spinal cord. *J. Neurosci.*, 8:133–145, 1988.
- T.A. McMahon. *Muscles, reflexes, and locomotion*. Princeton University Press, 1984.
- T. McMillen, T. Williams, and P. Holmes. Nonlinear muscles, passive viscoelasticity and body taper conspire to create neuromechanical phase lags in anguilliform swimmers. *PLoS Computational Biology*, 4(8), 2008.
- E. Niebur, H.G. Schuster, and D.M. Kammen. Collective frequencies and metastability in networks of limit-cycle oscillators with time delay. *Physical review letters*, 67(20):2753–2756, 1991.
- R. Nieuwenhuys, H.J. Donkelaar, and C. Nicholson. *The central nervous system of vertebrates*, volume 1. Springer Verlag, 1998.
- R. Pfeifer, M. Lungarella, and F. Iida. Self-organization, embodiment, and biologically inspired robotics. *Science*, 318(5853):1088–1093, 2007.



- J. Piatt. Regeneration of the spinal cord in the salamander. *Journal of Experimental Zoology*, 129(1):177–207, 1955.
- Arkady Pikovsky, Michael Rosenblum, and Jürgen Kurths. *Synchronization: a universal concept in nonlinear sciences*, volume 12. Cambridge university press, 2003.
- A. Rauscent, J. Einum, D. Le Ray, J. Simmers, and D. Combes. Opposing aminergic modulation of distinct spinal locomotor circuits and their functional coupling during amphibian metamorphosis. *The Journal of Neuroscience*, 29(4):1163–1174, 2009.
- P. J. Roos. Lateral bending in newt locomotion. In *Proc. Ned. Akad. Wetten. Ser. C*, volume 67, pages 223–232, 1964.
- S. Rossignol, R. Dubuc, and J.-P. Gossard. Dynamic sensorimotor interactions in locomotion. *Physiological Reviews*, 86:89–154, 2006.
- D Ryczko and R Dubuc. The multifunctional mesencephalic locomotor region. *Current pharmaceutical design*, 2013.
- D. Ryczko, V. Charrier, A. Ijspeert, and J.M. Cabelguen. Segmental oscillators in axial motor circuits of the salamander: distribution and bursting mechanisms. *Journal of neurophysiology*, 104(5):2677–2692, 2010a.
- D. Ryczko, R. Dubuc, and J. Cabelguen. Rhythmogenesis in axial locomotor networks: an interspecies comparison. *Prog. Brain Res*, 187:189–211, 2010b.
- D. Ryczko, J. Knüsel, A. Crespi, S. Lamarque, A. Mathou, A. J. Ijspeert, and J.-M. Cabelguen. Rich motor behaviors: the spinal cord as a puppet with strings. in preparation.
- D. M. Schroeder and M. W. Egar. Marginal neurons in the urodele spinal cord and the associated denticulate ligaments. *The Journal of Comparative Neurology*, 301:93–103, 1990.
- H. G. Schuster and P. Wagner. Mutual entrainment of two limit cycle oscillators with time delayed coupling. *Prog. Theor. Phys*, 81(5):939–945, 1989.
- G. Székely and G. Czéh. Organization of locomotion. In *Frog Neurobiology, a Handbook*, pages 765–792. Springer Verlag, Berlin, 1976.
- G Taga. A model of the neuro-musculo-skeletal system for anticipatory adjustment of human locomotion during obstacle avoidance. *Biological Cybernetics*, 78(1):9–17, 1998.
- G. Taga, Y. Yamaguchi, and H. Shimizu. Self-organized control of bipedal locomotion by neural oscillators in unpredictable environment. *Biological Cybernetics*, 65:147–159, 1991.
- G. Taylor. Analysis of the swimming of long and narrow animals. *Proceedings of the Royal Society of London. Series A. Mathematical and Physical Sciences*, 214(1117):158–183, 1952.

## Bibliography

---

- E.D. Tytell and A.H. Cohen. Rostral versus caudal differences in mechanical entrainment of the lamprey central pattern generator for locomotion. *Journal of neurophysiology*, 99(5): 2408–2419, 2008.
- E.D. Tytell, C.Y. Hsu, T.L. Williams, A.H. Cohen, and L.J. Fauci. Interactions between internal forces, body stiffness, and fluid environment in a neuromechanical model of lamprey swimming. *Proceedings of the National Academy of Sciences*, 107(46):19832–19837, 2010.
- T. Umedachi, K. Takeda, T. Nakagaki, R. Kobayashi, and A. Ishiguro. Fully decentralized control of a soft-bodied robot inspired by true slime mold. *Biological Cybernetics*, 102(3):261–269, mar 2010.
- G. Viana Di Prisco, P. Wallén, and S. Grillner. Synaptic effects of intraspinal stretch receptor neurons mediating movement-related feedback during locomotion. *Brain Research*, 530: 161–166, 1990.
- P. Wallen and T.L. Williams. Fictive locomotion in the lamprey spinal cord in vitro compared with swimming in the intact and spinal animal. *The Journal of physiology*, 347(1):225–239, 1984.
- P. Wallén, Ö. Ekeberg, A. Lansner, L. Brodin, H. Traven, and S. Grillner. A computer-based model for realistic simulations of neural networks ii: The segmental network generating locomotor rhythmicity in the lamprey. *J. of Neurophysiology*, 68:1939–1950, December 1992.
- C. Wardle, J. Videler, and J. Altringham. Tuning in to fish swimming waves: body form, swimming mode and muscle function. *Journal of experimental Biology*, 198(8):1629–1636, 1995.
- W. Watanabe, T. Sato, and A. Ishiguro. A fully decentralized control of a serpentine robot based on the discrepancy between body, brain and environment. In *IEEE/RSJ International Conference on Intelligent Robots and Systems, 2009. IROS 2009*, pages 2421–2426, 2009.
- B. Webb. Robots in invertebrate neuroscience. *Nature*, 417:359–363, 2002.
- M. Wheatley, M. Edamura, and R. B. Stein. A comparison of intact and in-vitro locomotion in an adult amphibian. *Experimental Brain Research*, 88:609–614, 1992.
- M. Wheatley, K. Jovanovic, R. B. Stein, and V. Lawson. The activity of interneurons during locomotion in the in vitro necturus spinal cord. *Journal of Neurophysiology*, 71(6):2025–2032, 1994.
- T. L Williams. Phase coupling by synaptic spread in chains of coupled neuronal oscillators. *Science*, 258:662–665, 1992.
- T. L. Williams and K. A. Sigvardt. Spinal cord of lamprey: generation of locomotor patterns. In M. A. Arbib, editor, *The handbook of brain theory and neural networks*, pages 918–921. MIT Press, 1995.

- T. L. Williams, K. A. Sigvardt, N. Kopell, G. B. Ermentrout, and M. P. Rempfer. Forcing of coupled nonlinear oscillators: studies of intersegmental coordination in the lamprey locomotor central pattern generator. *J. of Neurophysiology*, 64:862–871, 1990.
- T.L. Williams, S. Grillner, V.V. Smoljaninov, P. Wallen, S. Kashin, and S. Rossignol. Locomotion in lamprey and trout: the relative timing of activation and movement. *Journal of Experimental Biology*, 143(1):559, 1989.
- X. Yin, C. Wang, and G. Xie. A salamander-like amphibious robot: System and control design. In *Mechatronics and Automation (ICMA), 2012 International Conference on*, pages 956–961. IEEE, 2012.



# Curriculum Vitae

**Jeremie Knuesel**

Born 2 May 1983

Email: [knuesel@gmail.com](mailto:knuesel@gmail.com)

## Experience

Swiss Federal Institute of Technology (EPFL), Lausanne 2008 – 2013  
**Biorobotics Laboratory**

PhD thesis on the modeling of locomotor circuits in the salamander spinal cord using an amphibious salamander robot.

- Design and implementation of an isolated spinal cord model as a dynamical system of coupled oscillators based on experimental data
- Development and optimization of a three-dimensional mechanical simulation of a salamander robot for swimming and stepping underwater and on land
- Integration of the spinal cord model and mechanical simulation using virtual muscles and proprioceptive sensory feedback
- Implementation and testing of the spinal cord model and virtual muscles on a salamander robot using a distributed controller

Morgan Stanley Capital International (MSCI), Geneva, London 2006 – 2007  
**Quantitative Equity Research Group**

Research and development on the MSCI Global Investable Market Indices from a historical / back-calculation perspective.

- Construction and improvement of the historical indices for several countries
- Development and consolidation of tools for historical simulations and data analysis

Swiss Federal Institute of Technology (EPFL), Lausanne May – Sep 2006  
**Laboratory of Computational Neuroscience**

Research on the effects of stress and genetic background on meta-parameter dynamics in reinforcement learning models.

- Development of a reinforcement learning model for a Morris water navigation task

Institute of Applied Radiology (IRA), Lausanne Jul – Aug 2004

- Qualification of gamma-cameras for medical imaging
- Analysis of the signal-to-noise ratio in a Positron Emission Tomography installation

## Education

Swiss Federal Institute of Technology (EPFL), Lausanne

PhD student in the Biorobotics laboratory 2008 – 2013

Master of Science in Physics 2001 – 2005

Maturity (University entrance): science, Burier (Switzerland) 1998 – 2001

Awards in mathematics and chemistry

## Journal publications

J. Knuesel, A. Bicanski, D. Ryczko, J.-M. Cabelguen and A. Ijspeert. *A flexible salamander spinal network for locomotion, modeled at two levels of abstraction*. Integr Comp Biol (to appear).

A. Bicanski, D. Ryczko, J. Knuesel, N. Harischandra, V. Charrier, Ö. Ekeberg and A. J. Ijspeert. *Decoding the mechanisms of gait generation in salamanders by combining neurobiology, modeling and robotics*. Biol Cybern, 1-20, 2013.

N. Harischandra, J. Knuesel, A. Kozlov, A. Bicanski, J.-M. Cabelguen, A. Ijspeert and Ö. Ekeberg. *Sensory feedback plays a significant role in generating walking gait and in gait transition in salamanders: a simulation study*. Frontiers in neurorobotics, 5, 2011.

## Conference publications

A. Bicanski, J. Knuesel, D. Ryczko, J.-M. Cabelguen and A. Ijspeert. *Flexible control of phase lag, frequency and locomotor mode in the salamander spinal cord modeled at multiple levels of abstraction*. Society for Neuroscience, Program 788.15, Abstr. RR8, 2012.

J. Knuesel, and A. J. Ijspeert. *Effects of muscle dynamics and proprioceptive feedback on the kinematics and CPG activity of salamander stepping*. BMC Neuroscience, 12(Suppl 1), P158, 2011.

G. Lukšys, J. Knüsel, D. Sheynikhovich, C. Sandi and W. Gerstner. *Effects of Stress and Genotype on Meta-parameter Dynamics in Reinforcement Learning*. NIPS 19, 937, 2007.

## Book chapter

J. Knuesel, J.-M. Cabelguen and A. Ijspeert. *Decoding the mechanisms of gait generation and gait transition in the salamander using robots and mathematical models*. Motor Control: Theories, Experiments and Applications, 417-450, 2010.

## Symposium talk

J. Knuesel, K. Karakasiliotis, A. Crespi, D. Ryczko, J.-M. Cabelguen and A. J. Ijspeert. *Gait transitions between swimming and walking in salamander: lessons from numerical modeling and robotics*, Annual meeting of the society for Integrative and Comparative Biology (SICB), San Francisco, 2013.